Viscoelastic Flow of Polymer Solutions Around Arrays of Cylinders: Comparison of Experiment and Theory

by

Alice Weimin Liu

B.S.E., Chemical Engineering,University of Waterloo (1992)

Submitted to the Department of Chemical Engineering
in partial fulfillment of the requirements for the degree of

Doctor of Philosophy

at the

MASSACHUSETTS INSTITUTE OF TECHNOLOGY

June 1997

Author .....
Department of Chemical Engineering
May 30, 1997

Certified by .....
Robert C. Armstrong
Professor of Chemical Engineering
Thesis Supervisor

Certified by .....
Robert A. Brown
Professor of Chemical Engineering
Thesis Supervisor

Accepted by .....
Robert E. Cohen
Graduate Officer, Department of Chemical Engineering

Viscoelastic Flow of Polymer Solutions Around Arrays of Cylinders: Comparison of Experiment and Theory

by

Alice Weimin Liu

Submitted to the Department of Chemical Engineering
on May 30, 1997, in partial fulfillment of the
requirements for the degree of
Doctor of Philosophy

Abstract

Viscoelastic flow past a periodic array of cylinders has received considerable attention in the past several years because it is a simple model system for polymeric flow in a porous media, which is of interest for such engineering applications as enhanced oil recovery and composite and textile coating operations. Here, we examine through both simulations and experiments the flow of polymer solutions around a periodic, linear array of cylinders.

Finite element simulations are performed with three different constitutive models: the Giesekus model, the FENE-P model, and the Chilcott and Rallison model. All three models treat the macromolecules as dumbbells consisting of two point mass beads connected by a spring immersed in a Newtonian solvent. In the Giesekus model, intramolecular forces are described by a Hookean spring, whereas a finitely extensible spring whose modulus is given by a Warner approximation is used in both the FENE-P and Chilcott-Rallison models. Hydrodynamic drag on the beads is taken to be anisotropic for the Giesekus model and isotropic for the other two models, which differ subtly in their approximate treatment of the nonlinear force law.

Calculations for steady two-dimensional flows are presented. For closely spaced cylinders, the flow is separated between adjacent cylinders; this is not the case for more widely spaced cylinders. In both array arrangements, the structures of the stress and molecular extension fields predicted by all three models are qualitatively similar. A "birefringent strand" of highly stretched polymer molecules, which appears to emanate from the rear stagnation point of a cylinder in a widely spaced cylinder array ($L = 6, H = 2$), strengthens as flow rate increased. For a closely spaced cylinder array ($L = 2.5, H = 2$), the presence of a flow recirculation between neighboring cylinders eliminates the wake extensional flow. The drag force on the cylinders differs among the constitutive models. For the constant viscosity models, a minimum in the drag force enhancement factor, χ occurs at $We \leq 1$, and for the shear thinning models, χ is monotonically decreasing with increasing We.

Experimental studies included examination of the creeping motion of a highly elastic, constant viscosity 0.31% polyisobutylene (PIB) in polybutene (PB) and tetradecane (C14) Boger fluid flowing past the linear array. A two-color laser Doppler velocimeter and force/torque

transducer were used for pointwise velocity and force measurements. Excellent agreement was obtained between the measured steady streamwise velocity field and the numerical predictions. As the volumetric flow rate was increased, flow transitions were observed in both widely spaced ($L = 6, H = 2$), and closely spaced ($L = 2.5, H = 2$) cylinder arrays. The steady periodic 2D flow underwent a transition to 3D transient flow, whereby equally spaced v_z fluctuations appeared along the length of the cylinder. In the widely spaced cylinder array, a sequence of local flow transitions occurred in the wake of the first, second, third, and subsequent cylinders were observed. Flow transitions between interior cylinders, where the flow resembles that past an an infinite array of cylinders, did not occur until a critical $We_{crit} = 1.36$. Whereas in the closely spaced array of cylinders, the flow transition took place in the entire array at the critical $We_{crit} = 1.53$. The temporal and spatial extent of the velocity fluctuations were characterized in both geometries.

The drag and lift forces on the cylinder were also monitored as the Weissenberg number increased. Although the flow underwent a transition at critical We in both flow geometries, the measured drag force was time independent. The measured drag forces agreed extremely well with the Newtonian results at low flow rates, $We \leq 0.6$, for both geometries. Drag enhancement relative to the Newtonian case was first noted prior to any flow transition, and the deviations increased with increasing We. Because none of the viscoelastic constitutive models accurately describe the stress-strain relationships in complex flow geometries, the models failed to predict the drag enhancement prior to the flow transition. For a perfectly centered cylinder, lift force is zero. The lift force on the cylinder was non-zero for large We because the cylinders were not mounted exactly in the center of the channel, and the flow was not symmetric about the centerplane.

Thesis Supervisor: Robert C. Armstrong
Title: Professor of Chemical Engineering

Thesis Supervisor: Robert A. Brown
Title: Professor of Chemical Engineering

Acknowledgments

This thesis is dedicated to my beloved parents, Flora and Edward, and my dearest sister Julia and brother Tom. I thank them for their love and care, encouragement and support. I especially want to thank my parents for their great influence on me. Their vision of a good education for me has motivated me through the years. I want to thank my sister and brother for just being there for me when I needed it. Without them, this thesis would not be possible.

After five years at MIT, it finally comes to an end. I am grateful to have had the chance to come to MIT and work with the best and brightest students and faculty. There were times when I wanted to give up, but my determination and faith, and the encouragement and support of my family and friends gave me the strength to continue. I would like to thank every one of you for making this thesis possible.

I want to thank the members of my thesis committee, Profs. Greg Rutledge and Gareth McKinley, and my thesis advisors, Profs. Robert Armstrong and Robert Brown, for their feedback and criticism of my work. It was a truly great learning experience to work with both Bobs. I also want to acknowledge the National Science Foundation and 3M for providing financial support for this research; and the MIT Supercomputer Facility and the Pittsburgh National Supercomputer Center for providing computational resources.

I want to thank David Bornside for his continuous help, understanding, encouragement, thoughtful advice, and humor (though at times it was difficult to grasp). It was a truly wonderful experience to get to know David, and I thank him for everything that he has done. I am indebted to David for the development of computational tools without which this thesis would have been difficult to complete.

I want to express my gratitude to Peter Morley for his continuous help and encouragement. Without his help, my experiments would not have proceeded so smoothly.

I would like to thank my fellow members of the Bob and Bob research group. I thank Nina for proofreading part of this thesis. It was truly delightful to work and socialize with her. I will definitely miss the coffee hours. I want to thank Radha for all her help, advice, and suggestions over the years. I also want to thank everyone in 246, 256, and 125: Aleksey,

David, Fred, Garette, Howard, Hua, Indranil, Jeff, Junsuo, Jason, Lars, Mark, Mike, Mori, Talid, Todd and Sureshkumar.

My time at MIT was truly educational, I gained not only knowledge but also the ability to communicate with others. I had the opportunity to meet all of the professors, support staff, and graduate students. I want to express my thanks and respect for Profs. Karen Gleason, Klavs Jensen, and Howard Brenner; support staff members Arline, Molly, Darline, Linda, Janet, Elaine, Maria, Carol, Emmi and Fran for their patience with me over the past five years. I will definitely miss my daily visit to headquarters, the student office, and the accounting office. Probably I will miss most the privilege of visiting the dean's office, I want to thank Carol for accommodating me all these times.

During the last five years, I was able to make a lot of friends. I was so lucky to get to know so many wonderful people and build long-lasting friendships. I want to thank Jane for her company. I will definitely miss the Mocha Blasts at ABP. I am so grateful to have had the chance to get to know her better during the final stages of my stay. I want to thank her for proofreading part of my thesis. There are so many friends that I want to thank, and I will definitely miss every single one of you. I want to thank Gerald for his assistance in the lab; it was helpful to have him around. Without his help, I would have had to have weight training. I want to thank Yanqing and her husband for their help over the years; my friends Katarina, Susan, Michelle, Ken, Nancy, I-Ming, Marilyn, Inn, and Rick; my roomates Helen, Marci, and Sumei; and my undergraduate friends Brad, and Betty. I also want to thank Hugh MacDonlad, John Tsuo and Charles Wu for their love, support, and encouragement over the years.

I will always remember MIT - the people and the places. It was the place where I grew and matured, expanded my horizons, and discovered a whole new world. Now, it is time to move on. After all, tomorrow is another day!

Contents

1 Introduction 27

1.1 Polymer relaxation time 27

1.2 Characteristics of non-Newtonian fluids 29

1.3 Motivation 34

2 Literature Review 40

2.1 Newtonian flow past cylinders and spheres 41

2.1.1 Creeping flow around a falling sphere 41

2.1.2 Newtonian flow around a cylinder 42

2.1.3 Flow around a two-dimensional array of cylinders 45

2.2 Viscoelastic flow around cylinders and spheres 48

2.2.1 Viscoelastic creeping flow around spheres 49

2.2.2 Viscoelastic creeping flow around cylinders 50

3 Governing equations for viscoelastic flows 52

3.1 Conservation equations 53

3.2 Constitutive equations from dumbbell models 55

4 The finite element method 63

4.1 Basic concepts of FEM 64

4.2 FEM for solving the Stokes problem 70

4.3 Methods for solving hyperbolic equations 73

4.3.1 SU formulation 74

4.3.2 SUPG method 75
4.4 Solving viscoelastic constitutive equations 75
4.4.1 The viscous formulation 76
4.4.2 The explicitly elliptic momentum equation (EEME) method 77
4.4.3 The elastic viscous split stress (EVSS) methods 79
4.4.3.1 The EVSS method 80
4.4.3.2 The EVSS-G method 82
4.4.3.3 The DEVSS-G method 83

5 Viscoelastic flow around a periodic, linear array of cylinders 86
5.1 A literature survey on viscoelastic flow around cylinders 87
5.2 Problem formulation 92
5.2.1 Flow geometry 92
5.2.2 Governing equations and boundary conditions 93
5.2.3 Constitutive equations 94
5.2.4 Rheological Properties for Giesekus, FENE-P, and Chilcott-Rallison Models 98
5.2.4.1 Steady Simple Shear Flow 98
5.2.4.2 Steady planar elongational flow 98
5.3 Computational methods 99
5.4 Numerical results 104
5.4.1 Flow around a single cylinder ($L = \infty$) 104
5.4.1.1 Newtonian fluid 104
5.4.1.2 Viscoelastic models 104
5.4.2 Cylinders spaced far apart ($L = 6.0$) 108
5.4.2.1 Newtonian fluid 108
5.4.2.2 CR model 109
5.4.2.3 FENE-P model 113
5.4.2.4 Giesekus model 115
5.4.3 Cylinders spaced close together ($L = 2.5$) 117

5.4.3.1 Newtonian fluid 117
5.4.3.2 CR model 117
5.4.3.3 FENE-P model 122
5.4.3.4 Giesekus model 123
5.4.4 Drag force on the cylinders 124
5.4.4.1 Single cylinder 124
5.4.4.2 Widely spaced cylinder array ($L = 6$) 126
5.4.4.3 Closely spaced cylinder arrays ($L = 2.5$) 129
5.5 Summary on viscoelastic flow around a linear arrray of cylinders 132

6 Viscoelastic flow around a 2D Array of Cylinders **134**
6.1 Flow geometry and dimensionless numbers 135
6.2 Flow around a linear periodic array of cylinders ($L = 2.4, H = 1.2$) 135
6.2.1 Newtonian fluid 135
6.2.2 Viscoelastic models 139
6.3 Flow around a square array of cylinders ($L = 2.4, H = 1.2$) 140
6.3.1 Newtonian fluid 140
6.3.2 Inertialess flow of viscoelastic fluid with $\beta = 0.59$ 140
6.3.3 Inertialess flow of viscoelastic fluid with $\beta = 0.1$ 144
6.3.4 Flow with inertia 145
6.4 Flow around a staggered array of cylinders ($L = 2.4, H = 2.4$) 146
6.4.1 Newtonian flow 147
6.4.2 Viscoelastic flow 147
6.5 Flow around a staggered array of cylinders ($L = 3.4, H = 1.7$) 148
6.5.1 Newtonian flow 148
6.5.2 Viscoelastic flow 149
6.6 Drag force on the cylinder 151
6.6.1 Newtonian fluid 151
6.6.2 Effect of array arrangements 152
6.6.3 Effects of model parameters 154

6.6.4 Effect of inertia 155
6.7 Summary on flow around arrays of cylinders 157

7 Experimental methods **159**
7.1 Fluid characterization 159
7.1.1 Rheological Methods 159
7.1.1.1 Simple shear flow 160
7.1.1.2 Shearfree flow 165
7.1.2 Fluid Rheology 170
7.2 Flow Geometry 175
7.3 Laser Doppler Velocimetry 180
7.4 Direct drag force measurement 184
7.4.1 Fundamentals of strain gauges 185
7.4.2 Force transducer 190
7.4.3 Mounting of Nano transducer for drag force measurements 192

8 Experimental investigation of viscoelastic flow around a linear array of cylinders **198**
8.1 Flow in a rectangular channel 200
8.2 Creeping flow in widely spaced cylinder arrays, $L = 6, H = 2$ 203
8.2.1 Steady flow in a widely spaced cylinder array, $L = 6, H = 2$ 203
8.2.1.1 Effects of off-centering on flow kinematics from FEM calculations 205
8.2.1.2 Effects of elasticity on flow past the cylinder 205
8.2.2 Flow transition in linear array of cylinders 209
8.2.2.1 Viscoelastic flow transition in a confined cylinder 213
8.2.2.2 Flow transition in a widely spaced cylinder array ($L = 6, H = 2$) 213
8.3 Creeping flow in closely spaced cylinder arrays ($L = 2.5$, $H = 2$) 230
8.3.1 Steady flow in closely spaced cylinder arrays ($L = 2.5$, $H = 2$) 230

8.3.2 Flow transition in closely spaced cylinder arrays ($L = 2.5$, $H = 2$) . . 231
8.4 Drag force on a cylinder 247
8.4.1 Single cylinder flow 247
8.4.2 Drag behavior in widely spaced cylinder arrays 253
8.4.3 Closely spaced array of cylinders ($L = 2.5, H = 2$) 263

9 Conclusions **269**

Bibliography **278**

List of Figures

1-1 Shearing flow between two parallel plates. The top plate is moving at velocity v and the bottom plate is stationary. The arrows between the two plates represent the local fluid velocity, v_x. 28

1-2 Qualitative difference between polymer and Newtonian fluids. (a) "Shear thinning" phenomena. (b) Normal stress difference. (c) Fano flow. (d) Elastic recoil. 30

1-3 Viscoelastic flow behavior in complex flow geometries. (a) Flow in a channel obstructed by an antisymmetric array of cylinders. (b) Two spheres falling along the centerline of a cylinder. (c) Flow in the four-roll mill-Uebler effect. 33

1-4 Schematic diagram of a commercial PVC extrusion that can be decomposed into a number of simpler subproblems. (McKinley, 1991) 35

2-1 Viscoelastic flow around a linear array of cylinders constrained in a planar slit. The centrally mounted cylinder has a radius of a, the channel width is $2b$, and the center-to-center cylinder spacing is l. A local Cartesian coordinate system is defined at the origin of each cylinder. 41

3-1 Simple mechanical models for polymer solutions whereby polymer is dissolved in a Newtonian solvent continuum. (a) Multi-bead-rod Kramers chain model, and (b) Multi-bead-spring Rouse chain model. 56

3-2 A simple elastic dumbbell model. 57

3-3 Spring modulus, Hookean versus finitely extensible non-linear spring models. 57

5-1 Flow past a linear, periodic array of cylinders confined symmetrically between parallel plates. The cylinders each have radius R_c, and the geometry is specified by the cylinder-to-cylinder spacing L_c and the channel half height H_c. The unit cell on which computations are done is shaded. 93

5-2 Interbead spring force $F^{(c)}$ for Hookean and FENE springs. 96

5-3 Viscometric properties for the Giesekus, FENE-P, and CR models with model parameters of $\beta = 0.59$, $\alpha = 10^{-2}$, and $Q_0 = 10$. (a) Viscosity; the dimensionless viscosity for both the Giesekus and FENE-P models approaches 0.59 at infinite shear rate. (b) First normal stress coefficient. (c) Second normal stress coefficient. (d) Average squared molecular extension. 100

5-4 Planar elongational flow behavior for the Giesekus, FENE-P, and CR models with model parameters of $\beta = 0.59$, $\alpha = 10^{-2}$, and $Q_0 = 10$. (a) Dimensionless elongational viscosity η_1. (b) Mean squared molecular extension as a function of elongation rate $\dot{\varepsilon}$. 101

5-5 Finite element meshes used for calculations of viscoelastic flow around a linear, periodic array of cylinders with $L = 6, H = 2$. 103

5-6 Solution fields for Newtonian flow around a single cylinder in a channel with gap $H = 2$. (a) Ten equally spaced contours are shown for the streamlines. Twenty equally spaced contours between the minimum and maximum values are shown for (b) the normal stress τ_{xx} and (c) the shear stress τ_{xy}. The region shown is for $x \in [-5, 5]$ and $y \in [0, 2]$. In each plot the maximum and minimum locations are denoted by the symbols '$\times$' and '$\bullet$', respectively. . . . 105

5-7 Axial velocity v_x along the symmetry line for flow around a single cylinder in a channel with $H = 2$ (a) upstream and (b) downstream of the cylinder. Results are for $We = 1.0$. 105

5-8 Comparisons of (a) axial normal stress τ_{pxx} and (b) average molecular extension for flow around a single cylinder with $H = 2$ at $We = 0.5$ for the Chilcott-Rallison, FENE-P, and Giesekus models. 107

5-9 Comparison of the average molecular extension at $We = 1.0$ for flow around a single cylinder with $H = 2$. 108

5-10 Solution fields for Newtonian fluid flow around a periodic array of cylinders with $L = 6$ and $H = 2$. (a) Ten equally spaced streamlines; Twenty equally spaced contours between the minimum and maximum values are shown. (b) and (c) are the components of the extra stress τ_{xx} and τ_{xy}. 109

5-11 Molecular extension characterized by $<Q^2>$ across a couple of elements midway between the cylinder and wall for mesh M4 and the more refined mesh M5. The region shown is $x \in [0, 0.2]$ and $y \in [1.45, 1.55]$. 110

5-12 Evolution of v_x for the CR model with $Q_0 = 10$ (a) along the symmetry line $y = 0$; (b) v_x across the periodic boundary $x = 3.0$. 111

5-13 Contours of the (a) axial normal stress τ_{pxx}, (b) normal stress τ_{pyy} (c) shear stress τ_{pxy}, and (d) molecular extension $<Q^2>$ for the CR model with $Q_0 = 10, \beta = 0.59$ at $We = 0.7$. 111

5-14 Contours of the (a) axial normal stress τ_{pxx} and (b) molecular extension $<Q^2>$ for the CR model with $Q_0 = 10$ and $\beta = 0.59$ at $We = 2.0$ for a periodic cylinder array with $L = 6$ and $H = 2$. 112

5-15 Molecular extension along several streamlines close to the symmetry plane for the CR model with $Q_0 = 10$ and $\beta = 0.59$. The streamlines are shown in (a) and are identified by their y-location (y_{-3}) at the left edge of the computational domain, $x = -3$: $y_{-3} = 10^{-3}$, $y_{-3} = 5 \times 10^{-3}$, $y_{-3} = 2.5 \times 10^{-2}$, and $y_{-3} = 5 \times 10^{-2}$. $<Q^2>$ for (b) $We = 0.7$ and (c) $We = 2.0$. (d) $<Q^2>$ across the channel at several locations downstream from the cylinder for $We = 2.0$. 114

5-16 The effect of Q_0 on molecular extension for the CR model with fixed $\beta = 0.59$ and $We = 2.0$. (a) and (b) correspond to $<Q^2>$ for $Q_0 = 5$ and 15, respectively. The maximum value on the color scale corresponds to a fully extended dumbbell in each figure. 115

5-17 Contours of the (a) axial normal stress τ_{pxx} and (b) molecular extension $<Q^2>$ for the FENE-P model with $Q_0 = 10$ and $\beta = 0.59$ at $We = 2.0$ for a periodic cylinder array with $L = 6$ and $H = 2$. 115

5-18 Contours of the (a and c) axial normal stress τ_{pxx} and (b and d) molecular extension $<Q^2>$ for the Giesekus model with $\alpha = 10^{-2}$ and $\beta = 0.59$ at $We = 0.7$ (a and b) and 2.0 (c and d) for a periodic cylinder array with $L = 6$ and $H = 2$. 116

5-19 Creeping flow of a Newtonian fluid around a linear, periodic array of cylinders with spacing $L = 2.5$ and $H = 2$. (a) Stream function. The zero streamfunction is the darker curve; there are 10 equally spaced contours from 0 to the maximum and 5 equally spaced contours from the minimum to 0. (b) Normal stress τ_{xx}. (c) Shear stress τ_{xy}. For the stress contours there are 20 equally spaced contour lines between the minimum and maximum values marked on the plots. 118

5-20 Strength of the flow recirculation, characterized by ψ_{min}, in an array with $L = 2.5$ and $H = 2$ for the CR model with $Q_0 = 10$ and $\beta = 0.59$. The value $\psi_{max} = 2.0$, so that the average velocity across the channel is unity. 119

5-21 Contours of the (a) normal stress τ_{pxx}, (b) normal stress τ_{pyy}, (c) shear stress τ_{pxy}, and (d) average molecular extension $<Q^2>$ for flow around closely spaced cylinder arrays ($L = 2.5, H = 2$). Results are for the CR model with $Q_0 = 10$ and $\beta = 0.59$ at $We = 0.5$. 120

5-22 Comparison of $<Q^2>$ along selected streamlines for the CR model with $Q_0 = 10$ and $\beta = 0.59$ at $We = 1.0$ for cylinder spacings of $L = 2.5$, $L = 6.0$, and $L = \infty$. In all cases, $H = 2.0$. At $x = 0.0$, the streamlines pass through (a) $y = 1.10$ and (b) $y = 1.25$. 121

5-23 Contours of the (a) normal stress τ_{pxx} and (b) average molecular extension $<Q^2>$ for flow around closely spaced cylinder arrays ($L = 2.5, H = 2$). Results are for the CR model with $Q_0 = 10$ and $\beta = 0.59$ at $We = 2.0$. 122

5-24 Dependence of $<Q^2>$ on We for the FENE-P model with $Q_0 = 10$ and $\beta = 0.59$. (a) $We = 0.5$; (b) $We = 2.0$. 123

5-25 Dependence of $<Q^2>$ on We for the Giesekus model with $\alpha = 10^{-2}$ and $\beta = 0.59$. (a) $We = 0.5$; (b) $We = 2.0$. 123

5-26 Evolution of the viscoelastic drag enhancement χ with We for viscoelastic flow around a confined, single cylinder with $H = 2$. Model parameters are chosen as $\beta = 0.59$ and $1/\alpha = Q_0^2 = 100$. The Oldroyd-B (OLDB) model corresponds to $Q_0^2 \to \infty$. The points marked by an '×' on the Giesekus and '+' on the FENE-P curves were obtained on a computational domain of $x \in [-25, 25]$. All other results are for a domain $x \in [-15, 15]$. 126

5-27 Convergence of the dimensionless Newtonian drag force $F_{D,N}$ on a cylinder in a linear, periodic array with $L = 6$ and $H = 2$ with decreasing mesh size h_D. The computed $F_{D,N}$ per unit length is made dimensionless with $\eta_0 <v>$. The best fit polynomial to the numerical data is also shown. 127

5-28 Comparison of viscoelastic drag enhancement χ for different viscoelastic constitutive equations for flow in a widely spaced array of cylinders ($L = 6, H = 2$). The model parameters are $\beta = 0.59$ and $Q_0^2 = 1/\alpha = 100$. Results are obtained with mesh M4. 128

5-29 Dependence of the viscoelastic drag enhancement χ on molecular extensibility for the Chilcott-Rallison and Giesekus models in flow around a periodic array of cylinders ($L = 6, H = 2$). (a) CR model with fixed $\beta = 0.59$ but variable Q_0; (b) Giesekus model with fixed $\beta = 0.59$ and variable α. 129

5-30 Comparison of the viscoelastic drag enhancement χ for the Chilcott-Rallison, FENE-P, and Giesekus models for two degrees of molecular extensibility: (a) $Q_0^2 = 1/\alpha = 100$; (b) $Q_0^2 = 1/\alpha = 400$. In all cases $L = 2.5, H = 2$, and $\beta = 0.59$. 131

5-31 (a) Dimensionless form drag and (b) friction drag force on a cylinder in a linear, periodic array with $L = 2.5, H = 2$, $\beta = 0.59$, and $Q_0^2 = 1/\alpha = 400$. . 131

6-1 Flow past (a) a linear periodic array of cylinders confined symmetrically between parallel plates; (b) a square array of cylinders; and (c) a staggered array of cylinders. The cylinders each have radius R_c, and the geometry is specified by the horizontal cylinder-to-cylinder spacing L_c and the vertical spacing H_c. The unit cell on which computations are done is shaded. 137

6-2 Finite element meshes used for calculations of viscoelastic flow around various flow geometries. Meshes M1, M2 and M3 are used for flow around a linear periodic or square array of cylinders with $L = 2.4$ and $H = 1.2$, and meshes M4 and M5 are used for flow around staggered array of cylinders. 138

6-3 Evolution of axial velocity v_x (a) along the centerline line $x = 1.0$ and $x = 1.4$ correspond to the rear and front stagnation points respectively; (b) across the periodic boundary at $x = 1.2$, for flow around a linear periodic array of cylinders in a channel with $H = 1.2$; (c) $<Q^2>$ across the periodic boundary for the Giesekus model with $\alpha = 10^{-2}$ and $\beta = 0.59$. 140

6-4 (a) Axial velocity vx across the periodic boundary at $x = 1.2$; (b) $<Q^2>$ across the periodic boundary. Results are for flow around a square array of a Giesekus fluid with $\alpha = 10^{-2}$ and $\beta = 0.59$ cylinders with $L = 2.4$ and $H = 1.2$.142

6-5 Dependence of $<Q^2>$ on We for the Giesekus model with $\alpha = 10^{-2}$ and $\beta = 0.59$. (a) $We = 0.2$; (b) $We = 0.5$, flow around a square array of cylinders with $L = 2.4$ and $H = 2$. Importance of wake extensional flow on axial normal stress τ_{pxx} for the Giesekus model for (c) $We = 0.2$ and (d) $We = 0.5$. 143

6-6 Effects of β on stream function and molecular extension for the CR model with $Q_0 = 10$ at $We = 0.5$ for a square array of cylinders with $L = 2.4$ and $H = 1.2$. (a)-(b) $\beta = 0.1$ and (c)-(d) $\beta = 0.59$. 145

6-7 Effects of inertia on flow and pressure fields for a Giesekus model ($\alpha = 10^{-2}, \beta = 0.59$) flow around a square array of cylinders; comparisons are made at fixed $De = 0.5$. The streamfunction, ψ, and periodic pressure, p_p contours shown in (a)-(b) correspond to $Re = 1.0$, and (c)-(d) are for $Re = 17.0$.146

6-8 Contours of the (a) average molecular extension, $<Q^2>$, and (b) polymeric normal stress, τ_{pxx} for viscoelastic flow around a staggered array of cylinders ($L = H = 2.4$). Results are for the Giesekus model with $\alpha = 10^{-2}$ and $\beta = 0.59$ at $We = 0.5$. 148

6-9 Solution fields for Newtonian fluid flow around a staggered array of cylinders with $L = 3.4, H = 1.7$. Twenty equally spaced contours between the minimum and maximum values are shown. (a) Streamfunction, ψ; (b) and (c) are components of the extra stress τ_{xx} and τ_{xy}. 149

6-10 Contours of the average molecular extension $<Q^2>$ for flow around a staggered array of cylinders ($L = 2H = 3.4$). Results are for the Giesekus model with $\alpha = 10^{-2}$ and $\beta = 0.59$ at $We = 0.5$. 150

6-11 Maximum molecular extension, $<Q^2>_{max}$ for the (a) CR, (b) Giesekus, and (c) FENE-P models with model parameters of $\beta = 0.59$ and $1/\alpha = Q_0^2 = 100$, flowing around various cylinder arrays with a porosity of 45.5%. (d) compares the degree of molecular extension predicted by all three models in a square array of cylinders. 151

6-12 Effects of array arrangement on the viscoelastic drag enhancement χ with We for (a) CR model and (b) Giesekus model fluids flow around these geometries. Model parameters are chosen as $\beta = 0.59$ and $1/\alpha = Q_0^2 = 100$. 153

6-13 Effects of model parameters on the drag enhancement c for viscoelastic flow around a square array of cylinders with $L = 2.4$ and $H = 1.2$ (a) $\beta = 0.1$ and (b) $\beta = 0.59$, and $1/\alpha = Q_0^2 = 100$. Dependence of the viscoelastic drag enhancement χ on molecular extensibility for the Chilcott-Rallison and Giesekus models in flow around square array of cylinders. (c) CR model with fixed $\beta = 0.1$ but variable Q_0; (d) Giesekus model with fixed $\beta = 0.1$ and variable α. 155

6-14 Effect of inertia on the drag force per unit length of cylinder for Newtonian and viscoelastic fluids (Giesekus, FENE-P and CR models) flow around a square array of cylinders with $L = 2.4$ and $H = 1.2$ and model parameters $\beta = 0.59$ and $1/\alpha = Q_0^2 = 100$. 156

6-15 Contribution of pressure to drag force in terms of fraction of form drag, for viscoelastic flow around a square array of cylinders, different symbols denotes different constitutive models, 'o' for Giesekus model, "+" for FENE-P model and "Δ" for the CR model, model parameters $\beta = 0.59$ and $1/\alpha = Q_0^2 = 100$ at fixed $We = 0.5$. 157

7-1 Schematic diagrams for (a) cone-and-plate and (b) parallel-plate flow geometries. 160

7-2 Onset and growth of the purely elastic instability observed in the 0.31 wt% PIB fluids in a cone-and-plate geometry with $\theta_0 = 10°$, the direction of rotation of the upper conical fixture is counterclockwise. 163

7-3 Onset and growth of the purely elastic instability observed in the flow of 0.31 wt% PIB fluids in a coaxial parallel disk with $R/H = 20$. 166

7-4 Schematic diagrams of the most commonly used extensional flow arrangements. (a) Approximately homogeneous stretching method; (b) Meissner apparatus; (c) spin-line rheometer; (d) contraction flows; (e) opposed jet rheometer (Armstrong and McKinley, 1995). 167

7-5 Opposed jet rheometer. (a) a photograph of the RFX rheometer (Rheometircs) used in characterizing the elongational behavior of the 0.31 wt% PIB/PB/C14 fluids and (b) a sketch of the flow field (Armstrong and McKinley, 1995). . . 169

7-6 (a) Viscosity $\eta(\dot{\gamma})$ and first normal stress coefficient $\Psi_1(\dot{\gamma})$ under steady-state conditions. (b) Dynamic viscosity $\eta'(\omega)$ and $2\eta''(\omega)/\omega$ for small amplitude oscillatory shear flow. Solid symbols of '•' and '▲' represent measurements for the original 0.31 wt% PIB/PB/C14 fluid, prior to being introduced into any flow cell, and the symbols '□' and '▽' denote results for the degraded fluid used in this work. 172

7-7 Apparent Trouton ratio for 0.31 wt% PIB/PB/C14 solutions from an opposed jet rheometer. The symbol '•' denotes measurements for the "original" sample, and '□' and 'o' represent data collected for the "degraded 1" fluid after flow past single cylinder experiments performed by Byars (1995), and "degraded 2" fluid is the "degraded 1" solution after being used in the present work. 174
7-8 Design of flow geometry for investigating viscoelastic flow around a linear array of cylinders. 176
7-9 Streamwise velocity scan along the length of the cylinder (a) at $z = -21R$ upstream of the first cylinder at $We(\dot{\gamma}) = 1.2$ and (b) at the center of the periodic boundary between the second and third cylinders at $We(\dot{\gamma}) = 1.1$ prior to flow transition. The side walls are located at $x/R = \pm 20$. 177
7-10 Schematic diagram of the experimental system. 179
7-11 Geometric arrangement for a typical 'dual-beam' laser Doppler velocimeter and its interpretation in terms of the 'fringe model' (McKinley, 1991). 182
7-12 Wheatstone bridge circuit. 187
7-13 (a) construction of bonded-wire-type strain gauge (Crandall *et al.* , 1978); (b) strain gauge nomenclature (Omega encyclopedia, 1996). 188
7-14 (a) Overall features of the Nano force transducer; (b) schematic drawing of internal configuration of the Nano F/T (Photographs from Assurance Technologies Inc.). 191
7-15 Mechanical layout for the Nano F/T transducer (Assurance Technologies Inc.). 193
7-16 Cantilever design for mounting of the cylinder to the Nano F/T transducer for drag force measurements on the cylinder. 195
7-17 Cantilever mounting of the Nano F/T at the end of the cylinder for drag force measurements in a linear array of cylinders. 197

8-1 Viscoelastic flow around a linear array of cylinders. A cylinder of radius R is centrally mounted in a rectangular channel with a width of $2H_c$. A local Cartesian coordinate system is defined with its origin at the center of each cylinder. The z-axis is the streamwise flow direction, the y-axis is the transverse direction, and the x-axis is along the length of the cylinder. 199

8-2 Streamwise velocity $v_z(x, 0, -15R)$ measured along the neutral x-direction fifteen radii upstream of the first cylinder. The symbol '⊙' represents the tracker LDV scan from $x = -25R$ to $x = 25R$, the symbol '○' corresponds to the pointwise Nicolet LDV measurements at $We = 0.66$, and the symbol '△' represents the pointwise streamwise velocity taken at $We = 0.49$. 201

8-3 Streamwise velocity $v_z(x, 0, 3R)$ along the length of the cylinder at the center of the periodic boundary $\zeta = 3$ downstream of the fifth cylinder at $We = 0.66$. The symbol '●' represents the tracker LDV scan from $x = -25R$ to $x = 25R$, with the side walls are located at $x = \pm 20R$, and the symbol '○' corresponds to the pointwise Nicolet LDV measurements at $We = 0.66$. 202

8-4 Parabolic fully developed channel flow $v_z(0, y, -15R)$ fifteen radii upstream of the first cylinder. The dimensionless streamwise velocity $v_z(y)/ <v_z>$ in the transverse direction is represented by the symbol '○' at $x = -8R$, the symbol '□' at the channel center, $x = 0$, and the symbol '×' at $x = 10R$ at $We = 0.78$. The solid line is the predicted solution for fully developed channel flow. 204

8-5 Transverse velocity profiles of the dimensionless axial velocity $v_z/ <v_z>$ for an OLDB model with $\beta = 0.59$, 0.5% off-centering in the positive y direction at $We = 0.5$. 206

8-6 Effects of off-centering on the streamwise velocity scan in the streamwise direction at $\nu = \pm 1$. The straight line is the centered case, and the dotted lines are for the 0.5% off-centering in the positive direction at $We = 0.5$. The fluid moves faster at $\nu = 1$ than $\nu = -1$ at all ζ positions. 207

8-7 Streamwise velocity along symmetry plane for viscoelastic flow around a widely spaced cylinder array. (a) Measurements at $We = 0.22$, and (b) $We = 0.48$. . 210

8-8 Streamwise velocity across the midway between neighboring cylinders at (a) $We = 0.22$ and (b) $We = 0.5$. 211

8-9 Modification of the streamwise velocity across the channel at (a) $z = 2.5R$ downstream of the sixth cylinder, and (b) $z = -2R$ upstream of the seventh cylinder in a widely spaced cylinder array. 212

8-10 Elastic wake instability for 0.31 wt% PIB/PB/C14 solution flowing past a confined cylinder with an aspect ratio of $H = 2$. The flow is from top to bottom. Above a critical flow rate, video-imaging shows the formation of a steady cellular structure in the downstream wake of the cylinder at $We = 0.5$ and $Re = 0.028$ (McKinley *et al.* , 1993). 214

8-11 Critical condition for flow transition in a single cylinder flow. (a) The Deborah number, $De_{crit} = \lambda(\dot{\gamma}) < v_z > /R$, and (b) the wavelength at the three-dimensional flow instability, λ_x, as a function of cylinder radius to half-channel width ratio, R/H (Byars, 1995). 215

8-12 Streamwise velocity profile, $v_z(x, 0, -2.5R)$ across the width of the channel at fixed $y = 0$ and $z = -2.5R$ upstream of the second cylinder as the Weissenberg number is increased from $We = 0.51$ to 1.14. 218

8-13 Axial extent of the flow instability at $We_{1,crit} = 1.14$ (a) downstream of the first and (b) upstream of the second cylinders in a widely spaced cylinder array. All streamwise velocity scans were carried out at $y = 0$. 'd1' indicates data collected downstream of the first cylinder, and 'u2' indicates a region upstream of the second cylinder. The instability has an unique wavelength of $3.5R \pm 0.5R$. 219

8-14 (a) Power spectrum of spatial fluctuations in the streamwise velocity $v_z(x, 0, -2.5R)$ measured at $z = -2.5R$ upstream of the second cylinder at the critical $We_{1,crit} = 1.14$. (b) Time series of the streamwise velocity $v_z(0, 0, -2.5R)$ at $z = -2.5R$ upstream of the second cylinder. 220

8-15 Streamwise velocity profile, $v_z(x, 0, -2.5R)$ across the width of the channel at fixed $y = 0$ and $z = -2.5R$ upstream of the third cylinder as the Weissenberg number is increased from $We = 0.51$ to 1.28. 222

8-16 Power spectrum of spatial fluctuations in the streamwise velocity $v_z(x, 0, -2.5R)$ measured at $z = -2.5R$ upstream of the third cylinder at (a) the second critical Weissenberg number, $We_{2,crit} = 1.19$, (b) and third critical Weissenberg number, $We_{3,crit} = 1.28$. (c) time characteristic of the second flow transition at $We_{2,crit} = 1.19$. 223

8-17 Streamwise velocity profile, $v_z(x)$, along neutral x-axis at fixed $y = 0$ and $z = -2.5R$ upstream of the fifth (u5), sixth (u6), seventh (u7) and eighth (u8) cylinders at critical Weissenberg number, $We_{crit} = 1.36$, where the flow in the entire linear array undergoes a transition. The wavelengths of the instabilities are $\lambda_{x,u5} = \lambda_{x,u6} = \lambda_{x,u7} = \lambda_{x,u8} = 6.33 \pm 0.91\ mm = 4.0R \pm 0.6R$. 224

8-18 Streamwise velocity at a fixed point $(0, 0, -2.5R)$ upstream of the seventh cylinder as a function of time at critical $We_{crit} = 1.36$. 226

8-19 Spatial extent of the flow instability in a widely spaced linear array of cylinders. $v_z(x)$ is plotted for $y = 0$ and (a) $z = 1.5R$ to $3R$ downstream of the sixth cylinder and (b) $z = -3R$ to $-1.5R$ upstream of the seventh cylinder. Wavelength of the instability: $\lambda_{x,\zeta=-1.5} = 4.4R \pm 0.6R$, $\lambda_{x,\zeta=1.5} = 3.0R \pm 0.3R$, $\lambda_{x,\zeta=\pm2} = \lambda_{x,\zeta=\pm2.5} = 4.0R \pm 0.6R$, and $\lambda_{x,\zeta=\pm3} = 3.5R \pm 0.5R$ (c) $v_z(x)$ is plotted for $z = -2.5R$ upstream of the seventh cylinder and $y = 0$ to $0.8R$ at critical $We_{crit} = 1.36$. Wavelength is $\lambda_{x,y<0.8} = 4.0R \pm 0.6R$. 227

8-20 (a) $v_x(x)$ profiles along the neutral x-axis at $y = 0$ and $z = -2.5R$ upstream of the sixth cylinder at the critical flow transition $We_{crit} = 1.36$ in a linear array of cylinders. (b) The FFT spectrum used to resolve the x-component instability. 229

8-21 Streamwise velocity profile across $\zeta = 1.25$ mideway between two adjacent cylinders at $We = 0.37$ in a closely spaced cylinder array. The symbols '□', ▲', and 'o' denote measurements downstream of the first, second, and fifth cylinders, respectively. The solid line corresponds to the Newtonian calculations with 0.25% off-centering in the negative y-direction. 232

8-22 Streamwise velocity profile across the channel. The symbols '▲' and 'o' denote measurements at $-1.05R$ upstream of the sixth, and $1.25R$ downstream of the fifth cylinder, respectively at $We = 0.54$. The symbol '□' corresponds to data at $We = 0.72$ obtained $z = 1.25R$ downstream of the seventh cylinder. The solid line corresponds to the Newtonian calculations with 0.25% off-centering in the negative y-direction. 233

8-23 Streamwise velocity profile at fixed y. The solid line is for Newtonian results and the dotted line corresponds to viscoelastic calculations with 0.25% off-centering in the negative y direction. (a) $v_z / < v_z >$ along $y = R$. (b) $v_z / <v_z>$ along $y = 1.35R$. The symbols 'o', '△' and '□' denote measurements between the second and third, the third and forth, the fifth and sixth cylinders, respectively, at $We = 0.45$. The symbol '◆' corresponds to $We = 0.54$. . . . 234

8-24 Streak photographs of 0.25 wt% PIB/PB/Kerosene Boger fluid flow through a 2-D square array of cylinders with a void fraction of 70% (from Chmielewski & Jayaraman, 1993). The flow is from left to right. (a) At $Re = 0.039$ and $We = 0.31$, the flow is essentially Newtonian. (b) At $Re = 0.19$, $We = 1.59$, the flow is asymmetric and time periodic. The recirculation regions oscillate up and down, as can be seen from the recirculation region behind several cylinders. 235

8-25 The time evolution of the streamwise velocity, $v_z(t)$ at a fixed point $(0, 0.68R, z = 1.25R)$ downstream of the first cylinder, as the Weissenberg number is increased from $We = 0.68$ to 1.53. 237

8-26 The FFT power spectrum used to resolve the time period of the instability at a fixed point $(0, 0.68R, 1.25R)$ downstream of the first cylinder at $We = 1.53$. 238

8-27 The streamwise velocity profile, $v_z(x)$, along the length of the cylinder at fixed $y = 0.68R$ and $z = 1.25R$ downstream of the first cylinder as the Weissenberg number is increased from $We = 0.68$ to 1.53. 240

8-28 The FFT power spectrum used to resolve the spatial period of the instability at fixed $y = 0.68R$ and $z = 1.25R$ downstream of the first cylinder at $We = 1.53$. 241

8-29 Extent of viscoelastic instability in a closely spaced cylinder array. The streamwise velocity, v_z is monitored at $x = 0$, $y = 0.3R$ to $1.32R$ and $z = 1.25R$ downstream of the sixth cylinder at $We = 1.53$. 242
8-30 The FFT spectrum used to resolve the time period of the flow instability at $(0, 0.68R, 1.25R)$ downstream of the sixth cylinder at $We = 1.53$. 243
8-31 (a) The time evolution of v_x at $(0, 0.68R, 1.25R)$ downstream of the sixth cylinder at $We = 1.53$. (b) The FFT power spectrum used to determine the time period in (a). 245
8-32 The spatial period of v_z and v_x along the length of the cylinder at $y = 0.68R$ and $z = 1.25R$ downstream of the sixth cylinder at $We = 1.53$. 246
8-33 Calibration curve for mounting of F/T transducer at the end of a cylinder of radius $R = 3.175$ mm and half channel height to cylinder radius, $H/R = 2$. . 248
8-34 Drag force on a confined cylinder with an aspect ratio of $H = 2$. The symbol '□' denotes measured drag force with error bars in We and F_D. 'Newtonian', 'FENEP', 'Giesekus', 'CR' and 'OLDB' denote Newtonian, FENE-P, Giesekus, CR and Oldroyd-B FEM calculations. Model parameters for viscoelastic calculations are $\beta = 0.59$ and $Q_0^2 = 1/\alpha = 100$. 250
8-35 Lift force on a confined cylinder with a channel to cylinder ratio of $H = 2$. . 252
8-36 (a) Evolution of drag and lift forces on the cylinder during startup, steady-state, and shutdown. Experiments take place for 0.31 wt% PIB/PB/C14 fluid flowing around a single, confined cylinder at $We = 0.67$. (b) Enlargement of evolution of the drag and lift forces during startup. 254
8-37 Calibration curve for mounting of F/T transducer at the end of the seventh cylinder in a linear array of cylinders. 255
8-38 (a) Experimental protocol for increments of pressure at an interval of 450 seconds. (b) Drag force on the cylinder as a function of time as the pressure increases from 4 psi to 8 psi. 257
8-39 (a) Mean flow rate as a function of pressure drop. (b) Drag force on the cylinder as a function of pressure drop. 258
8-40 Drag response on a cylinder in a widely spaced cylinder array ($L = 6, H = 2$). 260

8-41 Lift force on a cylinder in a widely spaced array of cylinders. The symbols '□' and '△' denote experimental and OLDB FEM predictions with 0.5% off-centering with $\beta = 0.59$. 261

8-42 Streamwise velocity across the minimum gap between the cylinder and the channel wall. The symbol '□' denotes velocity measurements at fixed $x = 0$, $z = 0$ (the center of the fifth cylinder) and $We = 0.68$. The black and green lines corresponds to the Newtonian and OLDB FEM calculations at $We = 0.84$. 264

8-43 (a) Evolution of the drag and lift forces on the cylinders during startup, steady-state, and shutdown. The valve begins to open at $t = 0$, and is fully open at $t = 7\,s$. The experiment was carried out for a 0.31 wt% PIB/PB/C14 fluid flowing around a linear array of cylinders at $We = 1.3$. (b) Evolution of the drag and lift forces on the cylinder during startup. 265

8-44 Drag force on a cylinder in a closely spaced array. The symbol '□' denotes experimental data points with error bars for both We and drag force measurements. Different colors correspond to the Newtonian, FENE-P, OLDB, CR, and Giesekus FEM calculations. 267

8-45 Lift force experienced by the seventh cylinder in a closely spaced array. The symbol '□' denotes experimental data points with error bars for both We and force measurements. 268

List of Tables

5.1 Drag force per unit length of cylinder for Stokes flow past a single cylinder in a channel. H is the dimensionless channel half-gap, and the drag force is made dimensionless with the product of viscosity and average velocity, $\eta_0 <v>$. 125

5.2 Convergence of dimensionless drag force on a cylinder for the Oldroyd-B model with $\beta = 0.59$ flowing around a linear, periodic array of cylinders with $L = 6$ and $H = 2$. The dashed entries indicate that the calculations can not be continued to higher We with the given mesh. 129

6.1 Convergence of the dimensionless Newtonian drag force per unit length of cylinder $F_{D,N}$ on a cylinder in different cylinder arrangements with a fixed porosity of 45.5%. The drag force is made dimensionless with the product of viscosity and average velocity, $\eta_0 <v>$. 152

7.1 Representative gauge factor for various grid materials. 189

7.2 Specification for the Nano F/T transducer (Assurance Technologies Inc.) . . 192

8.1 Fraction of fluid flow through the wider gap ($y > 0$) as a function of z position ($z = 0$ is the center of each cylinder). Cylinders are misplaced by 0.5% of the channel width with the wider gap distance in the positive y direction. The reported volume fractions are for OLDB model fluid calculations $\beta = 0.59$. . 208

9.1 Critical conditions for the onset of a wake instability in linear cylinder arrays. 271

Chapter 1

Introduction

1.1 Polymer relaxation time

Rheology, defined as the *science of deformation and flow of matter*, is an important scientific and engineering discipline. The term "rheology" was coined by Professor Bingham of Lafayette College, Indiana, in 1929. Today, rheology is essentially composed of three areas: biorheology, polymer rheology and suspension rheology.

The classical theory of elasticity is used to describe solids. Hooke's law states that the force on an object is proportional to its deformation, so that doubling the tension of a spring doubles its extension. Once a force is applied to a Hookean solid, the material reaches a deformed state, beyond which no further movement of the material is detected.

The behavior of liquids is in sharp contrast to the behavior of solids. Under an applied stress, liquids flow. Isaac Newton postulated that the shear stress on a fluid is proportional to the rate of shear and the constant of proportionality is the viscosity (see Fig. 1-1). In the nineteenth century, Navier and Stokes independently derived a consistent three-dimensional theory that described the momentum balance in a viscous Newtonian liquid. The fundamental assumptions of the Navier-Stokes equations are that the fluid is isotropic and the components of stress are linearly related to the velocity gradients. The Navier-Stokes governing equations have been used extensively in the area of fluid mechanics to describe the flow behavior of many common fluids, such as water, oil, and air.

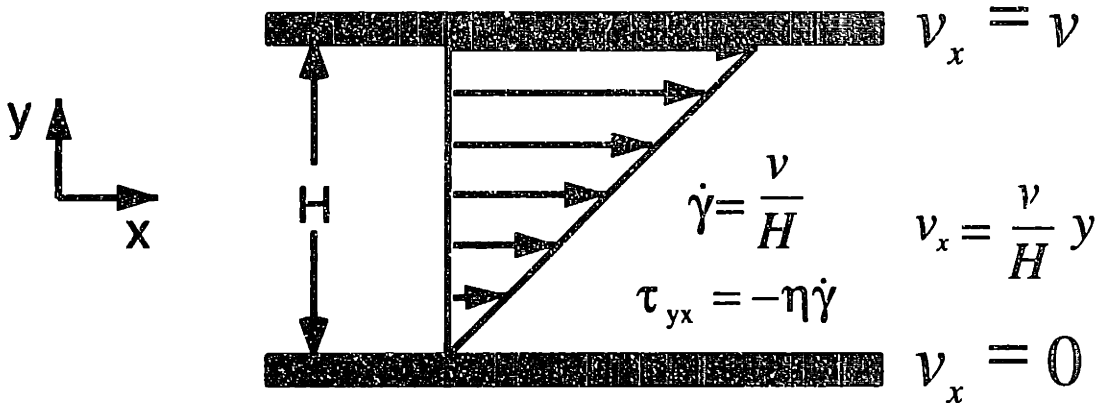

Figure 1-1: Shearing flow between two parallel plates. The top plate is moving at velocity v and the bottom plate is stationary. The arrows between the two plates represent the local fluid velocity, v_x.

In between the solid and liquid extremes lie viscoelastic materials, possessing both elastic and viscous properties. Although rheology is defined as the study of the flow and deformation behavior of all matter, Newtonian fluid mechanics and classical elasticity theory are not traditionally regarded as branches of rheology. More specifically, rheology is the study of complex materials, such as polymer solutions and melts, and suspensions. A silicone material, nicknamed "Silly Putty", is one of the most commonly known examples of viscoelasticity. A ball of silly putty will bounce when dropped on the floor, but if you let the ball sit on a surface it forms a puddle, given sufficient time. Thus, its physical characteristics depend on the time scale of observation, with solid-like behavior over a short time period and liquid like behavior over a long time scale. Professor Marcus Reiner conceived the idea of using the Deborah number, *De*, to describe the time scale in rheology. Professor Reiner's choice of this name comes from a quote in the book of Judges 5:5 where Deborah sang "...The mountains flowed before the Lord, ...". The Deborah number is used to characterize the non-Newtonian behavior of the fluid, and is defined as the ratio of relaxation time of a

material (λ) to the characteristic time of the flow (t_c) i.e.

$$De \equiv \frac{\lambda}{t_c} \tag{1.1}$$

In the limit of $De \to 0$, the fluid behaves like a Newtonian liquid, whereas for $De \to \infty$ the material is a Hookean elastic solid. For $De \approx 1$, elastic effects in the flow become significant.

1.2 Characteristics of non-Newtonian fluids

Polymer solutions and melts are typical examples of viscoelastic materials that are widely available in our daily lives. The term "polymers" refers to materials that are made up of long, covalently-bonded molecules. Naturally existing polymers have been around since life began, and range from biological polymers such DNA and proteins, to natural fibers such as cotton, silk and wool. Synthetic polymers have grown enormously in use over the past fifty years because they are relatively cheap and easy to manufacture, along with having desirable properties like chemical inertness, and low density. For example, polymethyl-methacrylate (PMMA) has good optical clarity, low density and superior mechanical properties to glass, and therefore is a common replacement for glass in airplane windows.

The difference in molecular chain length between the monomer and polymer leads to the striking qualitative difference in the flow behavior. In this section, we summarize the significant differences between the flow behavior of viscoelastic fluids and Newtonian liquids (Bird *et al.* 1987). In particular, we discuss five different features that distinguish Newtonian from viscoelastic liquids: shear thinning in the viscosity, normal stress differences, elongational viscosity, yield stresses and fading memory.

The viscosity of a Newtonian fluid is only a function of temperature and pressure; it is independent of shear rate. The viscosity of a polymer solution depends on shear rate with the viscosity decreasing as shear rate increases; this phenomenon is often referred as shear thinning. The effects of shear thinning can be demonstrated by the dropping sphere and draining experiments (Bird *et al.* 1987) shown in Fig. 1-2(a). Two identical spheres are falling at the same rate in both the Newtonian and polymeric solutions. This seems to

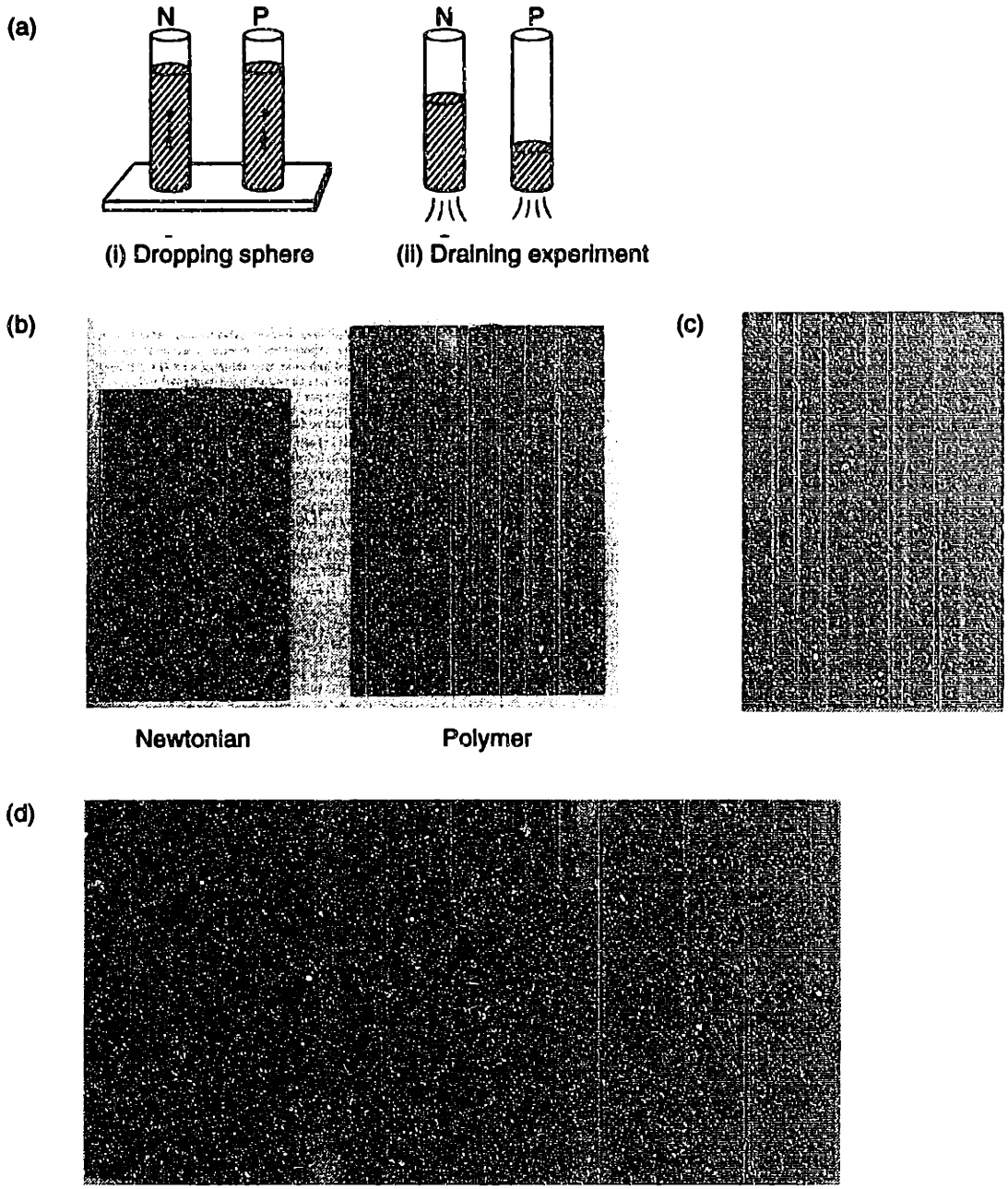

Figure 1-2: Qualitative difference between polymer and Newtonian fluids. (a) "Shear thinning" phenomena. (i) An identical sphere falls at the same rate through each column of fluid, but (ii) the polymer drains faster than the Newtonian fluid. (b) Normal stress difference. Rotating rod in a Newtonian liquid (glycerin) shows a vortex; polymer solution (polyacrylamide in glycerin) climbs up the rod. (Photographed by Dr. F. Nazem, Rheology Research Center, University of Wisconsin Madison.) (c) Fano flow. The 0.75 wt% aqueous solution of Polyox WSR 301 is held in a dish. A thread is produced by raising the dish, with the surface of the liquid just below the orifice. Fluid is drawn into the chamber by applying a vacuum pressure and the reservoir is slowly lowered. (Photographed by Dr. M.C. Couch, University of Wales, Aberystwyth.) (d) Elastic recoil. An aluminum soap solution is poured from a bottle into a beaker. The column of liquid is cut cleanly using a pair of scissors, and much of the liquid above and below the cut point recoils back into the upper and lower bottles respectively (From A.S. Lodge, Elastic Liquids, Academic Press, 1964, p.238).

suggest that the two fluids will drain at the same rate. In reality, the polymeric solution drains faster than the Newtonian material.

Polymer solutions also demonstrate normal stress differences. More accurately polymers exhibit normal stress; for incompressible liquids, we can only measure the differences in the normal stresses. For a unidirectional shear flow, there are two normal stress differences defined as $N_1 = \tau_{11} - \tau_{22}$ and $N_2 = \tau_{22} - \tau_{33}$, where 1, 2 and 3 are coordinates along the flow direction, the gradient of the velocity, and neutral direction, respectively (Bird *et al.* , 1987). For a Newtonian fluid, $N_1 = N_2 = 0$, but for a polymer solution, neither N_1 nor N_2 is zero. These non-zero normal stress components are a direct consequence of the competition between polymer molecules tending to align and become stretched along the streamwise direction, and the attempt of the polymer chains to relax to their equilibrium orientations. The rod-climbing experiment shown in Fig. 1-2(b) is caused by normal stress differences. Rotating rods are inserted into two beakers. One contains a Newtonian liquid and the other a polymeric solution. The Newtonian fluid is pushed outward by the centrifugal force, and a dip in the liquid surface is formed near the center of the beaker. In contrast, the polymeric liquid moves in the opposite direction, it gets pushed toward the center of the beaker and climbs up the rod. In this case, the streamlines are closed circles and the first normal stress difference produces a resultant force pointing inwards against the centrifugal force.

Polymer solutions also exhibit an extensional viscosity that is a function of extension rate. Polymer molecules tend to align in the direction of flow, and this often results in a substantial increase in the elongational viscosity of the fluids. The Fano flow (Fig. 1-2(c)), which is taken from Boger and Walter (1993), is a classical demonstration. A dish of 0.75 wt% Polyox aqueous solution is placed right below the orifice, and fluid is drawn into the chamber by applying a vacuum pressure. When the dish is slowly lowered, a thread of fluid is produced.

Some fluids also may have a yield stress, which means that the fluid will not flow unless the stress exerted on the material is above some critical value. Typical examples of fluids with a yield stress are toothpaste, paints, mayonnaise, and greases.

Another important characteristic of polymer solution is fading memory. Polymer molecules remember past deformation. The time scale for such a memory defines the relaxation time

of the material. Also, long polymer chains do not respond immediately to externally applied force. This delayed response is characterized by the relaxation time, λ. As an example, for a Newtonian liquid such as water, λ is around 10^{-13} seconds, but for a polymeric solution, λ is in the order of 10^{-2} to 10^{2} seconds. A commonly observed example is elastic recoil (Fig. 1-2(d)). For example an aluminum soap solution is poured from a bottle into a beaker, and the column of liquid is cut using a pair of scissors. The liquid above the cut then recoils back into the bottle (Lodge, 1964). Thus, the polymer material has a memory of its deformation history.

Fig. 1-3 shows the striking qualitative difference between the Newtonian and polymeric fluids in complex flow geometries; this is due to the combination of the differences mentioned earlier. In Fig. 1-3(a) (Walter and Jones, 1988), the photographs compare the flow of an aqueous solution of xanthan gum (highly shear thinning) and an aqueous solution of polyacrylamide (large extensional viscosity), past an antisymmetric array of cylinders. The fluid flows from left to right. For the xanthan gum solution, a substantially larger fraction of fluid flow passes through the narrow channels that the geometric ratio of gap widths. In contrast, for the polyacrylamide solution, the dominating extensional viscosity results in a larger fraction of fluid passing through the wider gap that the geometric ratio of gap widths. Figure 1-3(b) shows two spheres falling along the centerline of a cylinder filled with viscoelastic liquid. Depending on the initial separation distance between the spheres, the spheres can either move closer or farther apart over time, in contrast to the Newtonian case, where the separation distance remains constant. This may be due to the presence of a 'negative' wake (Bird *et al.* , 1987). The Uebler effect in Fig. 1-3(c) is another interesting example where an air bubble (or solid particle) is entrapped in a converging flow of a 1 wt% polyacrylamide aqueous solution (Michel, 1973). Due to buoyancy forces, the air bubble rises when the cylinders are stationary. If the cylinders are rotated as shown, the bubble remains at a stationary elevation.

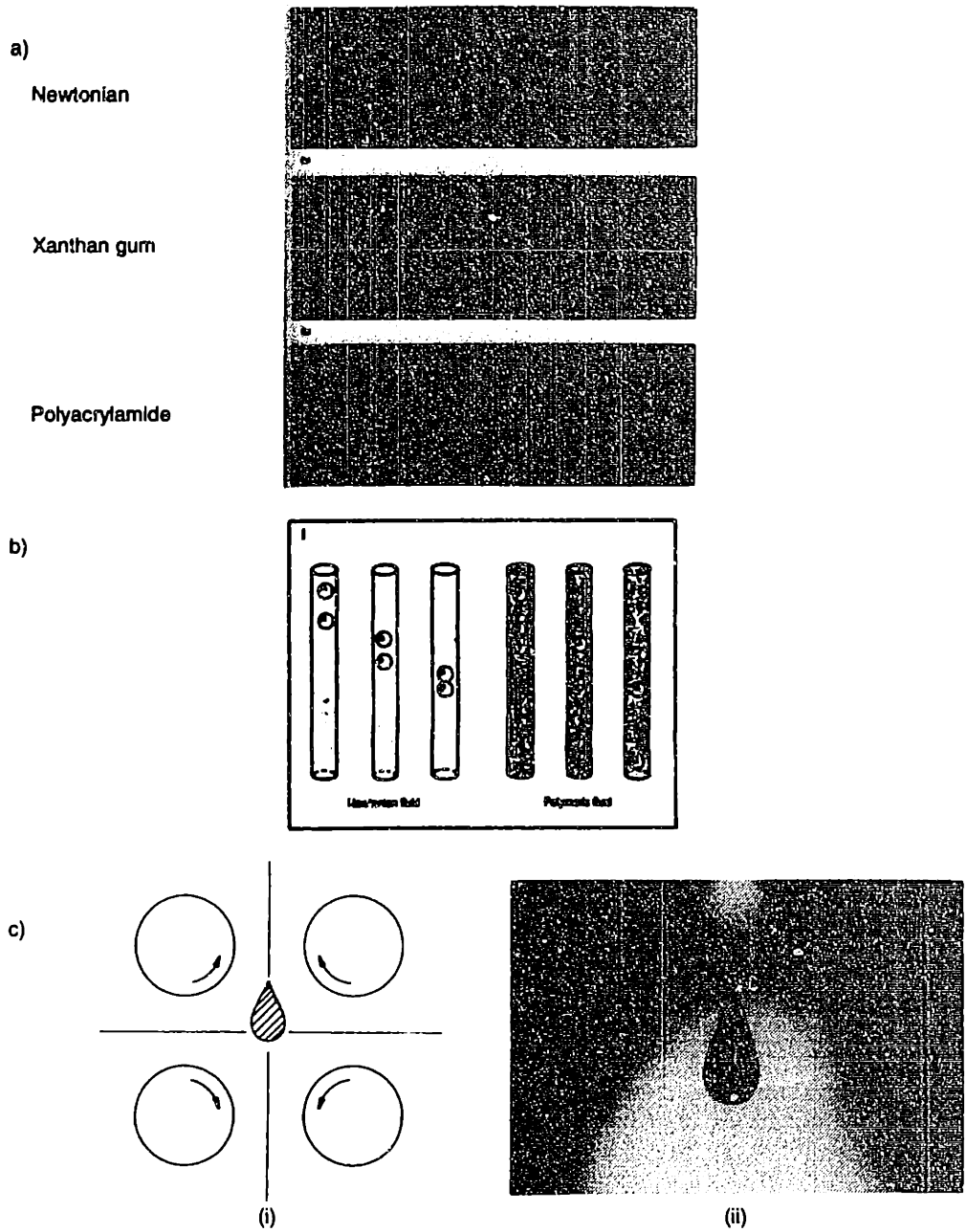

Figure 1-3: Viscoelastic flow behavior in complex flow geometries. (a) Flow in a channel obstructed by an antisymmetric array of cylinders. The flow is from left to right. The sequence of photographs compare and contrast the flow of aqueous solutions of (i) a Newtonian liquid, (ii) a xanthan gum, and (iii) aqueous solutions of polyacrylamide. (From K. Walters and D.M. Jones, Proc. 10 Int. Congress on Rheology, vol. 1, P.H.T. Uhlherr (Ed.), Australian Society of Rheology, 1988, 103). (b) Two spheres falling along the centerline of a cylinder. Two spheres come closer to each other in a Newtonian fluid with inertia, but move either closer or farther apart in a viscoelastic liquid depending on the initial separation distance. (c) Flow in the four-roll mill-Uebler effect. (i) A schematic diagram of a trapped bubble in the four-roll mill apparatus. Each cylinder rotates at the same angular velocity in the direction of the arrow. (ii) A suspended air bubble in a four-roll mill apparatus for a 1 wt% aqueous solution of polyacrylamide. (From J. Michel, 1973).

1.3 Motivation

Our studies are motivated by polymer processing applications. It is well known that material properties can be manipulated by altering the processing conditions. In general, the properties of polymeric products are very sensitive to the underlying arrangement of the polymer molecules in the product. This arrangement is a direct consequence of the interaction between the dynamics of the polymer and the fluid mechanics of the process. By understanding the underlying fluid mechanics that govern polymer processing, we are able to optimize the design and operating conditions. The onset of flow instabilities in polymer processing often limits the production rates. Therefore, a thorough understanding of the causes of flow instabilities can eventually lead to predicting *a priori* necessary modifications to the process to reach higher throughput in the absence of instabilities. This in turn increases the return on capital investments.

To illustrate the complexity of the flow problems encountered in practical polymer processing applications, let us consider the PVC extrusion shown in Fig. 1-4. From the extruder to the die, the flow is nonisothermal, three-dimensional, and inherently time dependent. This complex problem is analyzed by decomposition into a number of simpler, more tractable subproblems each of which retain a relevant flow characteristic, such as extensional flow or free surface effects. In particular, stagnation flows past submerged objects such as cylinders and spheres are extremely important because of the strong extensional flow near the stagnation point. This extensional flow results in stretching of macromolecules and build-up of large stresses in the wake of the object which in turn may lead to microstructural inhomogeneities and defects in the final product. Several of these geometries have been specified as benchmark problems for viscoelastic calculations including the flow past a cylinder in a channel, a falling sphere in a tube, and the axisymmetric contraction (Brown and McKinley, 1994). Various experimental techniques have been developed over the years to characterize the process flow conditions. The velocity fields are accurately measured by laser Doppler velocimetry (LDV). At MIT, Muller (1986), and McKinley (1991), Quinzani (1991), have used this technique with great success in the study of viscoelastic flow of polyiosbutylene (PIB) solution in axisymmetric and planar contractions, and around a confined cylinder.

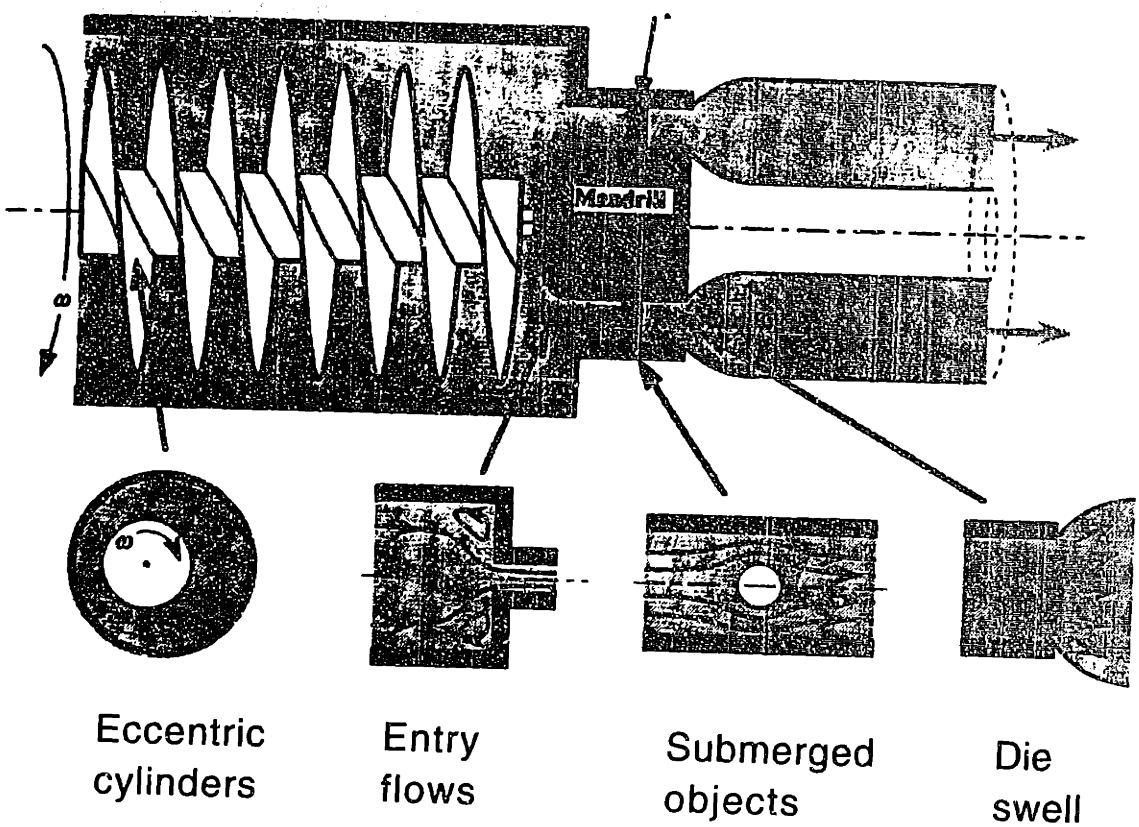

Figure 1-4: Schematic diagram of a commercial PVC extrusion that can be decomposed into a number of simpler subproblems. (McKinley, 1991)

Coupled techniques for spatially resolved measurements of stress, using the flow induced birefringence (FIB), and velocity, using LDV methods have been successfully developed and applied by Quinzani (1991) and Baaijens (1994) for PIB solutions in complex flow geometries. With continuing advances in computer architecture and algorithms, it is possible to perform large-scale numerical modeling that examines subproblems such as the transient start-up of rotational flow (Burdette, 1989; Northey *et al.* , 1990; Szady, 1995), flow past a sphere (Lunsmann *et al.* , 1993), corner singularities (Salamon, 1995), three-dimensional flow (Caola, 1995), transient flow around a linear arrays of cylinders (Sureshkumar *et al.* , 1997), and non-isothermal die-swell (Smith, 1996).

Therefore, it is possible to make quantitative and qualitative comparisons of computations

and experimental measurements. To date, agreement in such comparisons is poor (Quinzani, 1991; Baaijens *et al.* 1994; Becker *et al.* 1994; Byars, 1995). In general, velocity measurements are in good agreement with predictions (Quinzani, 1991; McKinley *et al.* 1993; Becker *et al.* 1994). However, the agreement between the measured and predicted stress fields is disappointing (Quinzani, 1991; Baaijens, 1994; refer to later in this thesis). Numerical modeling of a polymer in a realistic flow situation is a nontrivial task. There are several problems which make the analysis difficult:

First, an accurate constitutive model is needed to describe the behavior of the polymer in a complex flow geometry. Many constitutive equations have been developed over the years and most of them can mimic either qualitatively or quantitatively the response of a viscoelastic fluid in simple, one-dimensional flows (Bird *et al.* , 1987a, b; Larson, 1988), but less satisfactorily in complex two-dimensional or three-dimensional flows.

Second, there is the issue of flow regimes. Experimental work by McKinley *et al.* (1993) and Byars (1995) for flow of a 0.31 wt% PIB/PB/C14 fluid around a confined cylinder indicated that at low flow rates, the flow is steady and two-dimensional. As the flow rate is increased to a critical De, the steady two-dimensional planar flow undergoes a transition and becomes steady, three-dimensional in the wake of the cylinder. Further increases in the flow rate result in increases in the amplitude of the velocity fluctuations until eventually a second transition takes place where the flow becomes three-dimensional and time-periodic at large De.

Third, geometric singularities such as sharp corners can make the computation difficult (Renardy, 1993; Hinch, 1993; Coates, 1992; Salamon, 1995) or ill-posed (Coates, 1992). Local analysis around the geometric singularity reveals that the stress and pressure fields become infinite at a point in the flow domain (Renardy, 1993; Hinch, 1993; Salamon, 1995). These singularities arise either because of an abrupt change in the boundary shape or an abrupt change in a boundary condition.

Mathematical formulations of viscoelastic flow problems generally do not have analytic solutions except under simple flow conditions. Therefore, numerical solution techniques are needed to obtain the solution velocity, pressure, and stress fields. The finite element method (FEM) is naturally the method of choice because of its reliability, accuracy, flexi-

bility and efficiency (Bank, 1981; Babuska and Rheinboldt, 1984; Szabo, 1986). Previous numerical studies have attempted to address all three aspects of the flow described above. Brown *et al.* (1993) and Guenette (1995) have developed robust numerical methods for solving differential constitutive equations; Salamon (1995) has successfully simulated free-surface flow possessing a singularity; and Szady (1995) and Sureshkumar *et al.* (1997) have implemented stable and convergent time-dependent numerical algorithms. The goal of this thesis is to incorporate various viscoelastic constitutive models such as the Giesekus (Bird *et al.* , 1987b), the finitely extensible, nonlinear elastic dumbbell model with Peterlin's approximation (FENE-P) (Bird *et al.* , 1987b), and the FENE dumbbell model of Chilcott and Rallison (CR) (Chilcott *et al.* , 1988) into steady, two-dimensional flow around a linear array of cylinders. Numerical predictions are compared with experimental measurements to select the most adequate constitutive model for describing the complex flow geometry. Newtonian finite element calculations for a linear array of cylinders reveal that when cylinders are closely spaced, the flow is separated between adjacent cylinders; this is not the case for more widely spaced cylinders. In particular, we examine two flow geometries where the half channel height to cylinder radius, $H = H_c/R$, equals 2, and the center-to-center cylinder spacing to cylinder radius ratio, $L = L_c/R$ is 2.5 and 6 corresponding to a closely and widely spaced array, respectively.

Viscoelastic flow instabilities have been observed in a wide range of flow geometries, and comprehensive reviews are given by Petire and Denn (1976) and Larson (1992). In particular, the elastic wake instability for flow past a confined cylinder was well documented by McKinley *et al.* (1993) and Byars (1995), and the flow transition in two-dimensional arrays of cylinders was reported by Chmielewski *et al.* (1993). McKinley *et al.* (1993) showed that the instability in the wake of the cylinder took the form of axially periodic fluctuations in the streamwise velocity for H of 2 and 6. Byars (1995) extended these experiments to include a wider range of H values, determined the dependency of the critical De and wavelength on H at the onset of the flow instability, and examined the structure of the instability near the cylinder. These wake instabilities were caused by strong extensional flow near the stagnation point of the cylinder which in turn can result in large elongational stresses downstream of the cylinder. Chmielewski *et al.* (1993) examined viscoelastic flow around square and hexagonal

arrays of cylinders. The steady flow kinematics in both arrays agreed well with Newtonian finite element calculations. Streak photographs revealed that a flow transition from steady to unsteady took place at a critical De; at the onset of the flow transition, a sudden increase in the pressure drop was observed. However, this flow transition was characterized in neither structure nor time dependence.

In particular, flow around a linear array of cylinders in a rectangular channel is examined in this thesis. Viscoelastic flow in this geometry has not been investigated at all in the Non-Newtonian fluid mechanics community. Yet, in many ways, this geometry is ideally suited for testing the validity of viscoelastic constitutive models for the following reasons: (1) The complex flow has mixed elongational and shear flow behaviors. The shear flow dominating region is in the narrow gap between the cylinder and channel wall, and the elongational flow is developed in the wake of the cylinder. (2) The flow is periodic, and the effects of periodic straining on flow stabilities in these geometries have not been investigated in detail in the literature. (3) The flow geometry is smooth without any geometric singularities; hence, the flow problem can be solved numerically, and comparisons between experimental results and numerical predictions are possible.

Another aspect of the study involves the examination of the effects of neighboring cylinders on flow transitions in this flow geometry. Instabilities such as sharkskin and melt fracture can dramatically distort the surface of an extruded polymer, and can lead to nonuniformities in the final product because of modification in the flow history as a result of the flow instabilities. Therefore, a thorough understanding of the causes of flow instabilities can eventually lead to the ultimate goal of predicting *a priori* necessary modifications to either the fluid's rheology or process design, allowing us to push back the onset of flow instabilities and achieve higher throughput. The critical flow conditions at the onset of viscoelastic flow instabilities, the type and the characteristics of these instabilities need to be first examined in order to understand the causes of viscoelastic flow instabilities in complex flow geometries.

This thesis contains both numerical and experimental investigations of viscoelastic flow in both widely and closely spaced linear arrays of cylinders, modeling a portion of more complex polymer processing operations. LDV is implemented for precise kinematics measurements of steady viscoelastic phenomena. The measured steady two-dimensional streamwise velocity

fields are compared with the numerical predictions, and excellent agreement is reached. At high flow rate, flow transitions are observed in both flow geometries. The LDV system also permits detection and investigation of the structure of the flow instabilities at high Deborah number. Experiments providing details of the onset conditions, and the temporal and spatial characteristics of the instabilities are presented and will be used for future comparison with linear stability calculations provided by Sureshkumar *et al.* (1997). In addition to the streamwise velocity measurements, the drag and lift forces on the cylinder are measured directly using a force transducer.

The aims of this thesis are: (1) to compare the velocity and force measurements with finite element calculations at steady-state; (2) to identify an adequate constitutive model for describing flow behavior in a linear array of cylinders. (3) to investigate the effect of inter-cylinder spacing on the onset conditions of the flow transitions and the structure of the resulting flow instabilities; and (4) to investigate how the drag force on the cylinder change with the changes in flow kinematics.

A literature review is presented in Chapter 2, where detailed discussion of the previous results for Newtonian and viscoelastic flow around spheres and cylinders are discussed. The rest several chapters then deal with computation of viscoelastic flow around arrays of cylinders. The governing equations needed to solve the flow problem are reviewed in Chapter 3. The finite element (FE) formulations used in this thesis are discussed in Chapter 4. FEM results for viscoelastic flow around a linear array of cylinders are presented in Chapter 5. Chapter 6 concerns viscoelastic flow around two-dimensional arrays. This chapter addresses the question of which flow geometry gives rise to the largest molecular extension when the void volume fraction is fixed at 45.5%. Chapter 7 describes the fluid, test geometries, and experimental techniques. Experimental results and comparisons to the steady state finite element calculations are given in chapter 8 for flow around both widely and closely spaced cylinder arrays. In addition to the steady-state results, a sequence of flow transitions in both flow geometries are observed and discussed in detail, along with the drag force behavior as the flow rate increases.

Chapter 2

Literature Review

This thesis is concerned with viscoelastic flow around a periodic array of cylinders mounted centrally in a long planar channel, as shown in Fig. 2-1. The ratio of the channel half-height to the cylinder radius is defined as $\delta = a/b$, and the ratio of the center-to-center cylinder spacing to cylinder radius is defined as $\gamma = l/a$. Viscoelastic flow in this geometry is ideally suited for testing the validity of viscoelastic constitutive models for the following reasons: (1) The complex flow has mixed elongational and shear flow behaviors. (2) The flow is periodic, and the effects of periodic straining on flow stabilities in these geometries have not been investigated in detail in the literature. (3) The flow geometry is smooth without any geometric singularities; hence, comparisons between experimental results and numerical predictions are possible.

A comprehensive review of previous investigations of viscoelastic flow around arrays of cylinders is provided in chapter 5. Therefore, this chapter covers only Newtonian and viscoelastic flow around cylinders and spheres. Relevant analytic and experimental results for Newtonian flow around cylinders and spheres are provided in section 2.1 as a background for a discussion of viscoelastic flows in section 2.2.

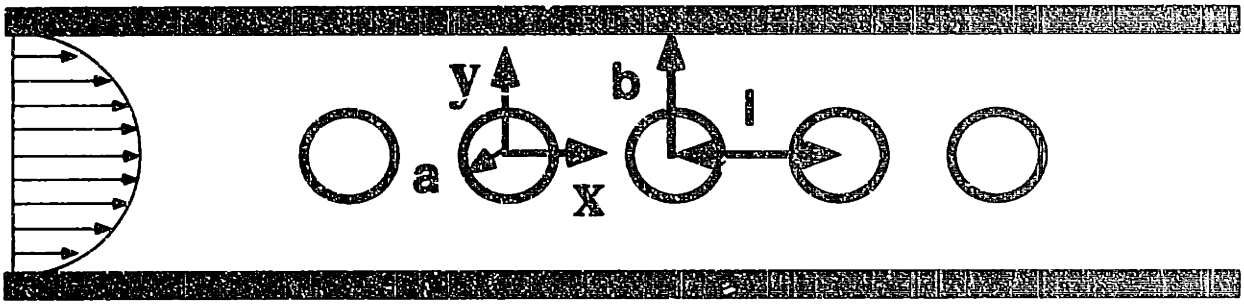

Figure 2-1: Viscoelastic flow around a linear array of cylinders constrained in a planar slit. The centrally mounted cylinder has a radius of a, the channel width is $2b$, and the center-to-center cylinder spacing is l. A local Cartesian coordinate system is defined at the origin of each cylinder.

2.1 Newtonian flow past cylinders and spheres

Unbounded creeping flow of a Newtonian fluid past cylinders and spheres has been investigated by many authors and documented in detail in standard texts (Bird *et al.* , 1960; Batchelor, 1967; Happel and Brenner, 1973). A brief summary of the results are presented for two simple cases: a falling sphere in a viscous fluid, and creeping flow past an infinitely long cylinder.

2.1.1 Creeping flow around a falling sphere

The Stokes' equation of motion for creeping flow ($Re = 0$) has an analytic solution for a solid sphere falling in an unbounded, quiescent fluid of constant viscosity μ. The flow problem is solved by imposing the following boundary conditions: uniform velocity U on the surface of the sphere and zero velocity in the fluid infinitely far from the sphere. The Stokes' equation predicts that the drag force experienced by the sphere is $F_D = 6\pi a\mu U$. There are two forces acting on the sphere: the hydrodynamic drag (F_D) on the sphere and the Buoyancy force (F_B) due to the density difference between the fluid and sphere,

$$F_B = \frac{4}{3}\pi a^3(\rho_s - \rho_l)g \tag{2.1}$$

where ρ_s and ρ_l are the sphere and solution densities, respectively, and g is the gravitational constant. For a falling sphere, the Buoyancy force is given as:

$$F_B = \frac{1}{2}\rho_l U^2 \pi a^2 \tag{2.2}$$

Under steady-state conditions, the Buoyancy force is balanced by the drag force. The drag coefficient, C_D, is defined as:

$$C_D = \frac{F_D}{\frac{1}{2}\rho_l U^2 \pi a^2} \tag{2.3}$$

In the creeping flow limit, the Buoyancy force equals the hydrodynamic drag force, and the drag coefficient reduces to $C_D = 24/Re$, where $Re = 2\rho_l a U/\mu$ is the Reynolds number. Batchelor (1967) applied the singular perturbation technique and obtained a solution to the Navier-Stokes equation at low Re; the resulting drag coefficient is of the form

$$C_D = \frac{24}{Re}[1 + \frac{3}{16}Re + O(Re \ln Re) + \ldots]. \tag{2.4}$$

2.1.2 Newtonian flow around a cylinder

For creeping motion of a Newtonian fluid perpendicular to the axis of a circular cylinder, the boundary conditions of no-slip on the cylinder and finite velocity at infinitely large radius cannot be satisfied simultaneously. This is known as the Stokes' paradox. Unlike the three-dimensional problem of flow past a sphere, there is no solution to Stokes' equation in two-dimensional space for flow around a circular cylinder. In the creeping flow limit, the fluid density is not a parameter. Dimensional analysis suggests that the force per unit length exerted by the fluid on the body, F, can only depend on the viscosity, μ, and the approaching fluid velocity, U. The simplest expression is given by $F/\mu U =$ constant, which is clearly incorrect because of the lack of dependency on the size of the cylinder, a. In the limit of no cylinder, where $a = 0$, the force is non-zero. Lamb (1932) obtained a first order approximation to the drag force by employing the Oseen's equation. The self-consistent solution for the flow field is reached by incorporating inertial effects. The resulting drag

force is expressed as follows,

$$\frac{F}{\mu U} = \frac{4\pi}{\frac{1}{2} - \gamma - \ln \frac{\rho U a}{4\mu}} \tag{2.5}$$

where $\gamma = 0.577$ is Euler's constant. A more rigorous justification of this result is provided by the singular perturbation techniques of Proudman and Pearson (1956); they show that the stream function ψ is of the form

$$\psi(r, \theta) = C \sin\theta(\frac{1}{r} - r + 2r \ln r) \tag{2.6}$$

where r and θ are the radial and angular polar coordinates respectively. Eq. (2.6) satisfies the vanishing motion at the cylinder surface, $r = 1$, and the term $(\sin\theta)$ ensures a uniform velocity at infinity.

Numerical treatment of viscous flow past an isolated cylinder in an infinite medium was first studied by Thom (1933). His approach includes a conformal transformation of the upper half of the physical plane exterior to the cylinder into a semi-infinite rectangular strip to avoid use of irregular mesh points. The solution is obtained by repeatedly improving the initial guess by using Taylor's theorem. Results are presented for $Re = 2\rho U a/\mu = 20$. The computed drag force per unit length, and pressure distribution around the cylinder are in good agreement with measurements (Thom, 1933). A sequence of photographs of streamlines past a cylinder show the gradual development and growth of symmetrical stationary eddies behind the cylinder as Re increases. Kawaguti (1953) applies the finite difference method and examines flow patterns at the critical $Re = 40$. This critical Re is suggested by experimental investigations by Kovasznay (1949). The hot-wire measurements in the wake of the cylinder revealed that above this critical Re, a vortex street begins to form in the wake of the cylinder. Keller *et al.* (1966) examined transient viscous flow past a cylinder; the steady-state solutions were obtained for $Re < 15$ by extrapolating to infinite time. The convergence of the methods was not checked by varying the mesh size and time step. Hamielec *et al.* (1969) solved the steady two-dimensional Navier-Stokes equations using the finite difference approximation by interpolating the stream and vorticity functions. Convergence tests were provided, and the solution proved to be accurate. The estimated drag force on the cylinder agreed exactly

with the theoretical predictions of Keller *et al.* (1966) for $Re \leq 15$, and the agreement with experimental data from Wieselsberger (1922) and Tritton (1959) was excellent.

Flow patterns in the wake of a cylinder were investigated experimentally for Reynolds numbers ranging from 0.1 to 2000 by Taneda (1956). A sequence of photographs revealed the following facts. In the creeping flow limit ($Re = \rho U d/\eta \leq 0.1$, where d is the diameter of the cylinder), the streamlines were perfectly symmetric about the center of the cylinder. Inertial effects become important at $Re \approx 1$, and as a result, the streamlines were shifted downstream. At $Re = 5$, a pair of recirculating vortices, referred to as 'standing eddies', appeared in the wake of the cylinder. The size of the vortices increased with increasing Re, and the flow was stable until Re reached about 45, where the wake flow became asymmetric and unstable. At $Re \geq 60$, two vortices were shed alternately to form a von Karman 'vortex street'.

The creeping motion equations yield bounded solutions when channel walls are introduced at some distance b from the cylinder origin. The Stokes flow solution is sought in terms of the dimensionless aspect ratio defined as the half channel width divided by the cylinder radius, $1/\delta$. Bairstow (1922) applied the method of images to this problem and developed an approximate expression for the stream function ψ for an aspect ratio of $H = 5$. The resistance of the cylinder per unit length is simply given by

$$F = 2.26\pi\mu u_0 \tag{2.7}$$

where u_0 is the free stream velocity in the middle of the channel. Faxen (1946) examined the creeping flow of a confined cylinder and obtained the series expansions for the drag force and pressure drop due to the presence of the cylinder

$$F = \frac{\mu u_0}{A_0} = \frac{\mu u_0}{U_0 - \ln\delta + U_2\delta^2 + U_4\delta^4 + U_6\delta^6 + U_8\delta^8 + \ldots} \tag{2.8}$$

$U_0 = -0.9156892732$

$U_2 = 1.72438440$

and $U_4 = -1.730194$

$U_6 = 2.405644$

$U_8 = -4.59131$

The movement of fluid in the presence of the cylinder causes a difference in pressure.

$$\Delta p = \frac{3\pi\mu}{l} A_0(1 - 0.5\delta^2 + 0.19335134\delta^4 + 0.19427833\delta^6 - 1.003311597\delta^8 + \ldots) \qquad (2.9)$$

where A_0 is defined in eq. (2.8), and Δp is the pressure difference between two points located infinitely far upstream and downstream of the cylinder.

2.1.3 Flow around a two-dimensional array of cylinders

Emersleben (1925) was the first to solve the Navier-Stokes equations for flow parallel to a square array of cylinders. His solution was based on the complex zeta functions, and the approximation is valid when porosity is greater than 0.8.

Tamada and Fujikawa (1957) applied Oseen's equation to steady viscous flow around an infinite row of parallel cylinders. The approximate drag expression is only valid for small Reynolds number ($Re < 0.1$). In the creeping flow limit ($Re \to 0$), the drag per unit length of the cylinder is directly proportional to the product of the viscosity and the undisturbed flow velocity U. Miyagi (1958) extended the analysis of Tamada *et al.* (1958) and obtained a drag force expansion formula in terms of the diameter-distance ratio up to the 14th power. In the limit of $a/b \to 1$, corresponding to a single cylinder in the unbounded flow limit, the drag per unit length converges to

$$F = \frac{15.8\mu U}{(1 - \frac{a}{b})^2} \qquad (2.10)$$

Happel (1959) studied the steady slow motion of fluids in arrays of cylinders to model the flow through fibrous materials. The flow problem was solved for the case of axial and transverse flow relative to the cylinder array by selecting the unit cell as a cylinder surrounded by an envelope of fluid. At the surface of the cylindrical shells, the shear stress was set to

be zero. For flow parallel to the cylinder array, the velocity, u, is of the form

$$u(r) = \frac{1}{4\mu}\frac{dp}{dx}[r^2 - a^2 - 2b^2 \ln\frac{r}{a}] \tag{2.11}$$

where b is the radius of the fluid envelope. The associated boundary conditions are given by

$$u(r = a) = 0 \tag{2.12}$$

$$\frac{du}{dr}(r = b) = 0 \tag{2.13}$$

and the drag force per unit length of the cylinder is given by,

$$F = \frac{4\pi\mu U}{\ln\frac{1}{\alpha} - \frac{3}{2} + 2\alpha - \frac{1}{2}\alpha^2} \tag{2.14}$$

where U is the average velocity of the fluid, and α is the cylinder volume fraction, $\alpha = 1 - \varepsilon$, where ε is the void fraction or porosity. In the case of flow perpendicular to the cylinders, the stream function is expressed as follows,

$$\psi(r,\theta) = \frac{U\sin\theta}{-\ln\alpha + \frac{\alpha^2}{1+\alpha^2}}\{\frac{1}{1+\alpha^2}\frac{1}{r} - \frac{1-\alpha^2}{1+\alpha^2} + 2r\ln r - \frac{\alpha^2}{1+\alpha^2}r^3\} \tag{2.15}$$

The drag force per unit length becomes

$$F = \frac{4\pi\mu U}{-\frac{1}{2}\ln\alpha + \frac{\alpha^2}{2(1+\alpha^2)} - \frac{1}{2}} \tag{2.16}$$

Eqs. (2.14) and (2.16) are accurate for $\varepsilon \geq 0.5$.

Instead of specifying zero shear rate at the boundary (Happel, 1959), Kuwabara (1959) examined the case of the vorticity-free boundary condition at $r = b$, and deduced that the stream function in such a system was modified to

$$\psi(r,\theta) = \frac{u_0\sin\theta}{-\ln\alpha + 2\alpha - \frac{\alpha^2}{2} - \frac{3}{2}}\{(1 - \frac{\alpha}{2})r^{-1} - (1+\alpha)r + 2r\ln r - \frac{\alpha}{2}r^3\} \tag{2.17}$$

In deriving this formula, Kuwabara assumed that the system of cylinders was moving at a

constant velocity u_0 in a stationary fluid. The drag force per unit length was approximated by

$$F = \frac{4\pi\mu u_0}{-\frac{1}{2}\ln\alpha + \alpha - \frac{3}{4} - \frac{\alpha^2}{4} + O(\alpha^4)} \tag{2.18}$$

Velocity fields predicted from eqs. (2.15) and (2.17) differ markedly owning to the difference in the denominators of these expressions, although the predicted stream functions are essentially identical (Kirsch and Fuchs, 1967). Subsequent experiments conducted by Kirsch and Fuchs (1967) were designed to evaluate eqs. (2.15) and (2.17), in search for an accurate description of the velocity field. The experiments were carried out using a 95 wt% glycerol solution, and fluid velocity was calculated by tracing the trajectory of suspended particles. Kisrch *et al.* (1967) only examined the case of flow around a staggered array of cylinders. The flow was essentially inertialess with a corresponding Reynolds number in the range 0.01 to 0.05. Experimental measurements led to the conclusion that eq. (2.17) was more accurate than eq. (2.15), and the pressure drop measurements also confirmed that eq. (2.17) was more accurate than eq. (2.15). Kirsch *et al.* (1967) also used the regular triangular lattice model, and the estimated drag results were comparable with both Happel's and Kuwabara's formulae.

Hasimoto (1959) applied the Fourier series coupled with elliptic functions in the study of viscous fluid flow past a periodic array of cylinders. An expression for the drag per unit length of a cylinder for transverse flow around a square array of cylinders was given by

$$F = \frac{4\pi\mu U}{\ln\frac{b}{a} - c + \pi\frac{a^2}{b^2} + O(\frac{a^4}{b^4})} \tag{2.19}$$

with

$$c = \ln[2\pi\prod_{n=1}^{\infty}(1 - e^{-2n\pi})] + \frac{1}{4} - \frac{\pi}{4} + \frac{\pi}{2}\sum_{n=1}^{\infty}\frac{1}{\sinh^2 n\pi} = 1.3105 + \ldots \tag{2.20}$$

Numerical modeling of viscous flow around an array of cylinders has received a great deal of attention over the years. Griffin and Meisen (1973) revisited Kuwabara's zero vorticity problem and numerically solved the Navier-Stokes equation. Results were obtained for Re in the range of $0.2 - 40$. Neither the drag force nor the velocity fields were compared with the analytic expressions provided by Kuwabara (1959) for the limit of $Re \leq 0.1$.

Gordon (1978) applied the finite difference method to the Navier-Stokes equation and reproduced the stream and vorticity functions predicted by Kuwabara (1959). A more concise treatment was given by Sangani and Acrivos (1982) who used a collocation of cylindrical biharmonics for creeping flow perpendicular to both square and triangular arrays of cylinders. In their studies, the porosity ranged from 0.25 to 0.95. The computed drag on a cylinder as a function of α agreed well with the asymptotic expressions for $\alpha \gg 1$ and $\alpha \ll 1$. For a square array, the authors extend the earlier analysis of Hasimoto (1959), and the drag per unit length was given by

$$F = \frac{4\pi\mu u_0}{\frac{1}{2}\ln\frac{1}{\alpha} - 0.738 + \alpha - 0.887\alpha^2 + 2.038\alpha^3 + O(\alpha^4)} \tag{2.21}$$

for the square array, and by

$$F = \frac{4\pi\mu u_0}{\frac{1}{2}\ln\frac{1}{\alpha} - 0.745 + \alpha - \frac{1}{4}\alpha^2 + O(\alpha^4)} \tag{2.22}$$

for the triangular array. By far the most extensive investigation of flow around two-dimensional cylinder arrays was performed by Drummond and Tahir (1984). They applied the method of singularities to biharmonic equations, and presented rigorous and accurate formulae for several different cylinder arrangements, including flow parallel to square, triangular, hexagonal, and rectangular arrays; and flow normal to square and triangular arrays.

2.2 Viscoelastic flow around cylinders and spheres

Earlier studies of viscoelastic flow past spheres and cylinders attempted to understand the effect of elasticity on the velocity profile and drag force. More recently, combined flow visualization and laser Doppler velocimetry have been used to investigate viscoelastic flow stability in these two geometries.

2.2.1 Viscoelastic creeping flow around spheres

Numerical modeling of creeping flow of a viscoelastic fluid past a sphere predicts drag reduction compared to the Newtonian case. Leslie and Tanner (1961) first studied creeping for an Oldroyd 6-constant model and found a slight downstream shift in the streamline and reduction in the drag force as compared to the Newtonian values. Hassager and Bisgaard (1976) used a Lagrangian finite element method in the study of an Upper Convected Maxwell (UCM) model, and predicted that drag coefficient decreased with De when $\delta = 0.5$. Later studies by Sugeng and Tanner (1986) on the modified Phan-Thien-Tanner (PTT) model also predicted a similar drag reduction for $\delta = 0.5$. Their calculations showed a 40% drag reduction for the shear-thinning PTT model and a 25% reduction for the UCM fluid. Drag reduction (in comparison with the Newtonian results) in a shear-thinning polymer solution can be explained by a decrease in the solution viscosity as the shear rate (or equivalently the flow rate) increases. The effect of elasticity on the drag force cannot be observed when shear thinning is present. In order to isolate the effects of elasticity from viscous shear thinning, Boger fluids of constant viscosity and high elasticity were used in later experimental and numerical investigations.

Chhabra *et al.* (1980) measured the drag coefficient on a sphere falling through a series of polyacrylamide (PAA)/corn-syrup (CS) based elastic Boger fluids; the zero-shear-rate relaxation time ranged from 0.037 s to 0.51 s. The largest sphere radius-to-tube radius ratio was 0.07, minimizing wall effects. In their measurements, the Weissenberg number ranged from 1.66×10^{-4} to 2.02. In the Newtonian limit, $0 \leq We \leq 0.1$, no significant deviations from the Newtonian drag force were observed. As the fluid elasticity increased, $We > 0.1$, the drag coefficient decreased until an asymptotic reduction of 26% was reached for $We \geq 0.7$. Later experiments conducted by Chhabra and Uhlherr (1988) on other PAA/CS Boger fluids also showed drag reductions.

In contrast to the drag reduction observed for corn-syrup based Boger fluids, drag enhancements have been reported for polyisobutylene (PIB)/polybutene (PB) Boger fluids (Tirtaatmadja *et al.* , 1990; Chmielewski *et al.* , 1990; Becker *et al.* , 1993). Tirtaatmadja *et al.* (1990) examined the creeping motion of a sphere in an M1 (PIB/PB) Boger fluid;

experiments showed Newtonian results for $We < 0.1$, and a slight decrease in drag for $We > 0.1$, followed by an increase in drag with respect to the Newtonian values for $We > 0.6$. Chmielewski *et al.* (1990) used both the PAA/CS and PIB/PB Boger fluids in the study of the falling sphere problem. For the PAA/CS solution, a drag reduction similar to that published by Chhabra *et al.* (1980) was noted. For the PIB/PB fluid, the ratio of the measured drag force on the sphere to the Newtonian result, $\chi = F_{D,v}/F_{D,N}$, initially decreases with increasing We until $We > 0.3$. Beyond $We = 0.3$, χ starts to increase, and at $We = 0.7$, a 15% drag enhancement was measured. Chmielewski *et al.* (1990) calculated the extensibility of the polymer chains from intrinsic viscosity measurements. They noted that PAA molecules are more fully extended from the equilibrium state as compared to the PIB molecules. This suggests that in fitting the maximum extensibility, Q_0^2, in the CR model, the PIB solution has a larger Q_0^2 than the PAA/CS solutions. This is consistent with calculations by Lunsmann *et al.* (1993) where the higher values of Q_0^2 led to drag enhancement at higher We.

More recently, Becker *et al.* (1993) investigated a sphere falling along the centerline of a cylindrical tube filled with a 0.31 wt% PIB/PB/C14 Boger fluid. A digital imaging system was used to measure the transient velocity in the wake of the sphere. The ratio of the sphere radius to the tube radius was constant at 0.24, but different sphere densities were used. The transient velocity showed an initial overshoot, followed by a monotonic decrease to a steady value. The drag force coefficient was computed from the sphere settling velocity. Once again, drag force enhancement relative to the Newtonian results was observed at higher We.

2.2.2 Viscoelastic creeping flow around cylinders

Ultamn and Denn (1971) examined viscoelastic flow around a cylinder both experimentally and numerically. The flow problem was solved numerically by linearizing both the equation of motions and the Upper Convected Maxwell model. Numerical results indicated an upstream shift in the streamlines, and the drag force on the cylinder was lower than the Newtonian results. Their experiments on aqueous solutions of carboxymethyl cellulose (CMC) and PAA confirmed the upstream shift of the streamlines.

Dhahir and Walters (1989) studied viscoelastic flow past a cylinder positioned asymmet-

rically in a rectangular channel. Various kind of fluids, including Newtonian, a PAA/CS Boger fluid, and the shear-thinning solutions of PAA/water and Xanthan gum, were used. The aspect ratio was $\delta = 0.6$. The asymmetry in the flow arrangement was amplified by the fluid elasticity; as a result, less fluid passed through the narrow gap. The drag force measurements revealed that for all fluids considered, the drag force on the cylinder decreased as the eccentricity of the cylinder was increased.

McKinley *et al.* (1993) used combined LDV and flow visualization techniques in the study of a 0.31 wt% PIB/PB/C14 fluid around a centrally mounted cylinder with an aspect ratio $\delta = 0.17 - 0.50$. Measurements of the streamwise velocity profile along the centerplane showed that the dimensionless upstream velocity $v_z / \langle v_z \rangle$ does not change with increasing We, but a downstream shift in $v_z / \langle v_z \rangle$ exists in the wake of the cylinder. Further increases in We resulted in a more pronounced downstream shift in $v_z / \langle v_z \rangle$, until a critical We where the flow undergoes a transition from steady 2D to steady 3D. Along the neutral x-direction, the streamwise velocity becomes spatially periodic, and thus the instability has a steady cellular structure. The instability is characterized in terms of its spatial wavelength and onset conditions. Later studies by Byars (1995) considered aspect ratios ranging from $\delta = 0.05$ to 0.86. The critical We and wavelength at the onset of the flow instability depends on δ. Beyond the critical We, the streamwise velocity measurements across the width of the channel showed that v_z was no longer symmetric about the centerplane, with increasing asymmetry in v_z as We increases.

Later experiments by Baaijens *et al.* (1994) measured both the velocity and stress field for a concentrated 5 wt% PIB/PB/C14 fluid flowing past a confined cylinder. The velocity profiles across the channel and along the centerplane agreed well with a single-mode Phan-Thien-Tanner model. Excellent agreement in the stress field upstream of the cylinder was observed, but the agreement was poor downstream.

Chapter 3

Governing equations for viscoelastic flows

The set of governing equations that defines the viscoelastic flow problem is presented in this chapter. For a single component system, there are three fundamental quantities that must be conserved: mass, momentum and energy. We consider isothermal flow with negligible viscous heating. The maximum temperature rise is $0.2°C$ for the viscoelastic flow problems examined experimentally in this thesis. Therefore, the processes under consideration are essentially isothermal, and, as a result, the energy balance equation can be safely neglected. The flow problems are solved by considering only the mass and momentum balances. These conservation equations are written in differential form in section 3.1. The momentum equation requires the specification of a constitutive relation between fluid stress and strain. Section 3.2 describes the development of several constitutive models developed from elastic dumbbell micromechanical models. We consider in detail the Giesekus model, the finitely extensible nonlinear elastic (FENE) dumbbell model with the Peterlin approximation (FENE-P) and the Chilcott and Rallison approximation (CR) models.

3.1 Conservation equations

Mass conservation for an incompressible fluid yields to the continuity equation:

$$\nabla \cdot \boldsymbol{v} = 0 \tag{3.1}$$

where $\boldsymbol{v}$ is the fluid velocity. The momentum balance gives rise to the equation of motion as

$$\rho(\frac{\partial}{\partial t}\boldsymbol{v} + \nabla \cdot \boldsymbol{v}\boldsymbol{v}) = -\nabla p - \nabla \cdot \boldsymbol{\tau} \tag{3.2}$$

where ρ is the fluid density, $\boldsymbol{\tau}$ is the deviatoric stress tensor and p is the thermodynamic pressure. Equation (3.2) ignores external or body forces such as gravity. We assume isothermal flow, which is valid when the characteristic adiabatic temperature rise for the process, $\Delta T_{adiabatic} = \Delta p/\rho C_p$, is small and the energy conservation equation is not needed. For our experiments, the maximum pressure drop, $\Delta p_{max} = 30$ psi, $\rho = 0.88 g/cm^3$, and $C_p \approx 2kJ/kg \cdot K$, leading to a maximum adiabatic temperature rise under steady state conditions of $\Delta T_{adiabatic,max} = 0.12°C$, which is too small a change to be significant. Eq. (3.2) can be simplified by introducing the definition of substantial derivative

$$\frac{D}{Dt} \equiv \frac{\partial}{\partial t} + \boldsymbol{v} \cdot \nabla \tag{3.3}$$

and substituting eq. (3.3) into eq. (3.2):

$$\rho \frac{D}{Dt}\boldsymbol{v} = -\nabla p - \nabla \cdot \boldsymbol{\tau} \tag{3.4}$$

The equation of motion, eq. (3.4), and continuity equation, eq. (3.1), are in dimensional form. These equations are made dimensionless by defining the characteristic length as the cylinder radius, R, the characteristic viscosity as the zero-shear-rate solution viscosity, η_0, and the characteristic time of the flow, $t_c = R/ <v_z>$, where $<v_z>$ is the characteristic mean fluid velocity across the channel. The dimensionless form of the conservation equations

becomes

$$\nabla \cdot \boldsymbol{v} = 0 \tag{3.5}$$

$$Re\frac{D}{Dt}\boldsymbol{v} = -\nabla p - \nabla \cdot \boldsymbol{\tau} \tag{3.6}$$

where the Reynolds number is defined as the ratio of inertia to viscous force, given by

$$Re = \frac{\rho <v_z> R}{\eta_0} \tag{3.7}$$

In eqs. (3.5) and (3.6), η_0 is the zero-shear-rate viscosity, and the pressure is scaled by $\eta_0 <v_z> /R$. For most polymer solutions, $Re \ll 1$ because these fluids are highly viscous, and thus inertia effects are negligible in eq. (3.6). The scope of this thesis is limited to the study of steady-state flows, i.e. the equation of motion is time-independent, and eq. (3.2) reduces to

$$Re\boldsymbol{v} \cdot \nabla \boldsymbol{v} = -\nabla p - \nabla \cdot \boldsymbol{\tau} \tag{3.8}$$

The deviatoric stress $\boldsymbol{\tau}$ in a polymer solution is assumed to be linearly separable into solvent, $\boldsymbol{\tau}_s$ and polymeric, $\boldsymbol{\tau}_p$, contributions as

$$\boldsymbol{\tau} \equiv \boldsymbol{\tau}_s + \boldsymbol{\tau}_p \tag{3.9}$$

The stress $\boldsymbol{\tau}$ and rate-of-strain $\dot{\boldsymbol{\gamma}}$ for a Newtonian fluid are related by the Newton's law of viscosity.

$$\boldsymbol{\tau}_s \equiv -\eta_s \dot{\boldsymbol{\gamma}} \tag{3.10}$$

where η_s is the solvent viscosity, and $\dot{\boldsymbol{\gamma}}$ is the rate-of-strain tensor, written as

$$\dot{\boldsymbol{\gamma}} \equiv \nabla \boldsymbol{v} + (\nabla \boldsymbol{v})^T \tag{3.11}$$

The dimensionless form of eq. (3.8) neglecting the inertia is

$$-\beta \nabla^2 \boldsymbol{v} + \nabla \cdot \boldsymbol{\tau}_p + \nabla p = 0 \tag{3.12}$$

where $\beta \equiv \eta_s/\eta_0$ is the ratio of solvent viscosity to the zero-shear-rate viscosity of the solution. In the limit of $\beta = 1$, $\tau_p = 0$, and eq. (3.12) reduces to the well known momentum conservation of the Navier-Stokes equation for incompressible fluids

$$-\nabla^2 \boldsymbol{v} + \nabla p = 0 \tag{3.13}$$

3.2 Constitutive equations from dumbbell models

There are many ways of obtaining a constitutive model for polymeric materials. One simple approach is to model polymer molecules as dumbbells. A detailed derivation of constitutive equation from dumbbell models is given by Bird *et al.* (1987). In this section, we only outline the salient features of the elastic dumbbell model that are essential in distinguishing the three constitutive equations considered in this thesis.

The dumbbell model assumes that long polymer chains are dissolved in a Newtonian solvent. The multi-bead-rod model (Fig. 3-1(a)) is a Kramers chain. It has universal joints at the bead and models flexible molecules. The multi-bead-spring model (Fig. 3-1(b)) is a Rouse chain. It is just a coarse grained version of Fig. 3-1(a) in which many of the beads and rods have been replaced by "entropic" springs. Both models assume that polymer molecules are point-mass beads and the solvent is a continuum that behaves like a Newtonian liquid. In this thesis, we only concentrate on the development of elastic dumbbell model. The simplest dumbbell model assumes that polymer molecules are two point beads connected by a nonbendable spring as shown in Fig. 3-2. The beads are labeled as "1" and "2", and the "connector vector", $\boldsymbol{Q}$, defines the overall configuration of the polymer molecule. Each bead experiences four kinds of forces: intramolecular ($\boldsymbol{F}^{(c)}$), hydrodynamic ($\boldsymbol{F}^{(h)}$), Brownian ($\boldsymbol{F}^{(b)}$) and external forces ($\boldsymbol{F}^{(e)}$). We neglect the inertia term in the force balance equation, and the equation of motion becomes

$$\boldsymbol{F}^{(c)} + \boldsymbol{F}^{(h)} + \boldsymbol{F}^{(b)} + \boldsymbol{F}^{(e)} = \boldsymbol{0} \tag{3.14}$$

The continuity equation for the configurational distribution function, ψ, is written as (Bird

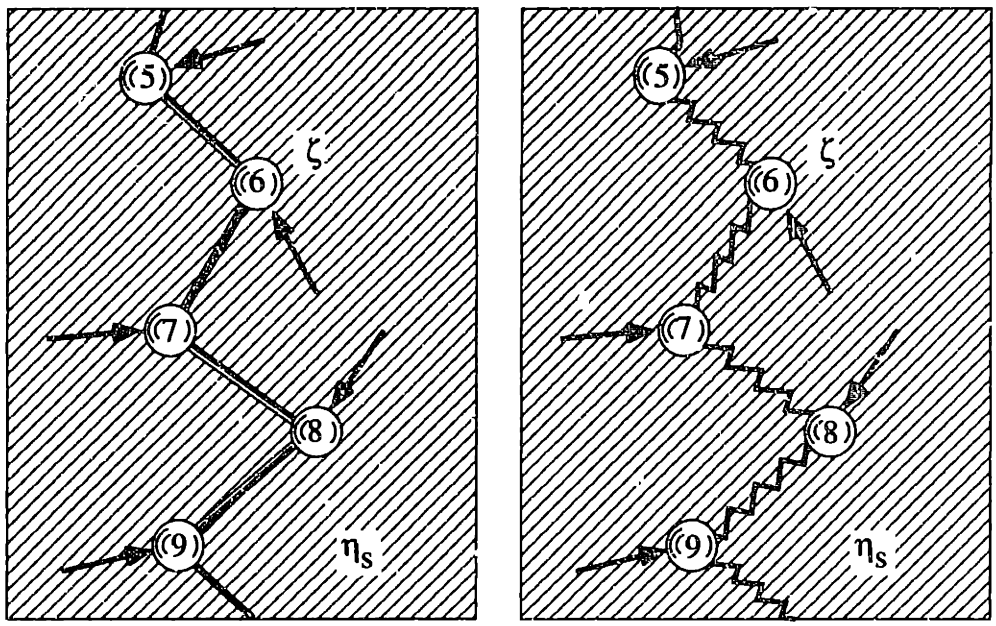

(a) (b)

Figure 3-1: Simple mechanical models for polymer solutions whereby polymer is dissolved in a Newtonian solvent continuum. (a) Multi-bead-rod Kramers chain model, and (b) Multi-bead-spring Rouse chain model.

et al. , 1987)

$$\frac{\partial \psi}{\partial t} = -(\frac{\partial}{\partial \boldsymbol{Q}} \cdot [\![\dot{\boldsymbol{Q}}]\!]\psi) \tag{3.15}$$

where the symbol $\|\cdot\|$ represents the momentum space average, $[\![\dot{\boldsymbol{Q}}]\!]$ is the phase space average of time rate of change of the connector vector $\boldsymbol{Q}$. Assuming that the distribution of configurations is independent of the location of the dumbbells in space, then the configuration-space distribution function Ψ can be factored (Bird *et al.* , 1987)

$$\Psi = n\psi(\boldsymbol{Q}, t) \tag{3.16}$$

where n is number of polymer molecules per unit volume. The distribution function $\psi(\boldsymbol{Q}, t)$ satisfies the normalization condition, that is

$$\int \psi(\boldsymbol{Q}, t) d\boldsymbol{Q} = 1 \tag{3.17}$$

The intramolecular force is represented by a connecting spring whose force $\boldsymbol{F}^{(c)}$ is given in terms of the dumbbell end-to-end vector $\boldsymbol{Q}$ by, $\boldsymbol{F}^{(c)} = H_0 h(Q)\boldsymbol{Q}$, where H_0 is a charac-

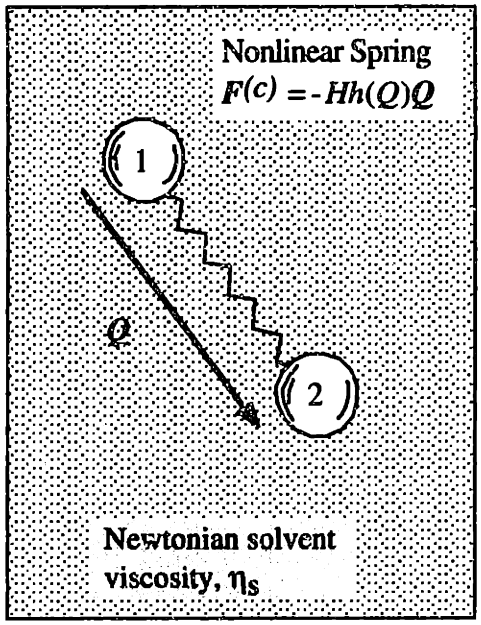

Figure 3-2: A simple elastic dumbbell model.

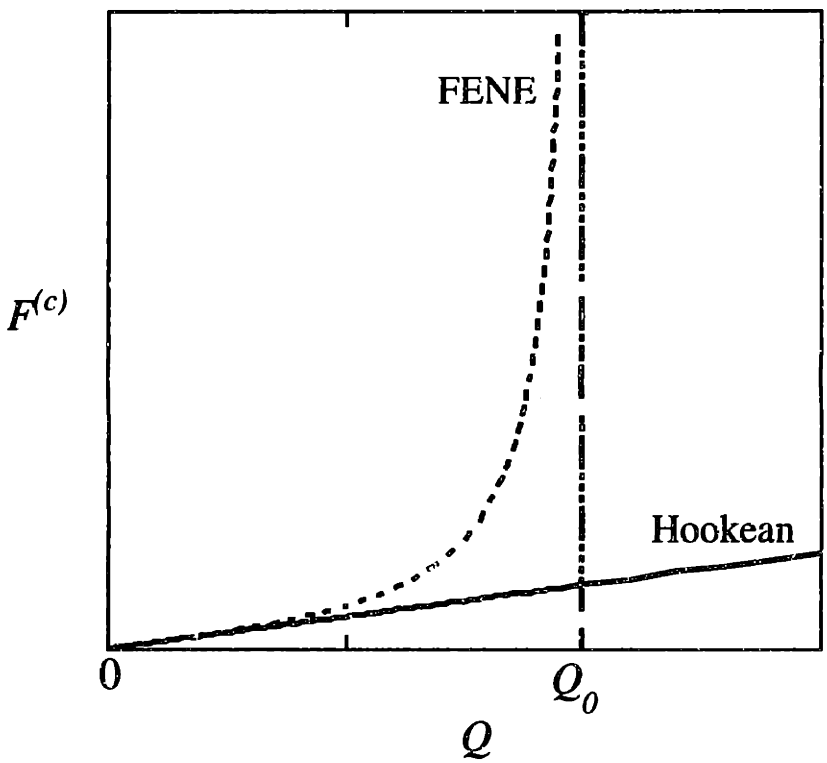

Figure 3-3: Spring modulus, Hookean versus finitely extensible non-linear spring models.

teristic spring constant, and $h(Q)$ is a dimensionless spring modulus which is a function of the separation Q between the two beads. The simplest type of spring is a Hookean spring, which has a constant spring modulus $h(Q) = 1$. For this expression, the intramolecular force is directly proportional to the length of the dumbbell; and, as a result, the macromolecules can be stretched indefinitely as indicated in Fig. 3-3. A more realistic description of the intramolecular force incorporates the finite extensibility of the polymer. A convenient empiricism for the modulus of a finitely extendable nonlinear elastic (FENE) dumbbell is given by the Warner's force law (Bird *et al.* , 1987) as

$$h(Q) = \frac{1}{1 - Q^2/Q_0^2} \tag{3.18}$$

where the maximum dumbbell length is given by Q_0. In the limit $Q_0 \to \infty$, the FENE spring reduces to the Hookean spring. The Giesekus model assumes that the spring is Hookean, whereas the FENE-P and CR models use the Warner expression, eq. (3.18).

Hydrodynamic force, $\boldsymbol{F}^{(h)}$, is the resistance force experienced by each bead as it moves through the solution. A simple expression is given by the modified Stokes' law, $\boldsymbol{F}^{(h)} = -\boldsymbol{\zeta} \cdot (\llbracket \dot{\boldsymbol{r}}_\mu \rrbracket - \boldsymbol{v})$, where $\boldsymbol{\zeta}$ is the friction coefficient tensor, $\llbracket \dot{\boldsymbol{r}}_\mu \rrbracket$ is the phase space average velocity of bead μ, and subscript μ denotes the bead number, $\mu = 1, 2$. The drag force is proportional to the difference between, $\llbracket \dot{\boldsymbol{r}}_\mu \rrbracket$, and mass average velocity of the solution, $\boldsymbol{v}$. In the CR and FENE-P models the drag force $\boldsymbol{F}^{(h)}$ is taken to be colinear with the relative velocity of the bead, $\llbracket \dot{\boldsymbol{r}}_\mu \rrbracket - \boldsymbol{v}$. This restriction is removed in the Giesekus model, with the inverse of the friction tensor written as

$$\boldsymbol{\zeta}^{-1} = \frac{1}{\zeta}(\boldsymbol{\delta} - \alpha \boldsymbol{\tau}_p) \tag{3.19}$$

The coefficient α is the mobility factor (Bird *et al.* , 1987), the dependence of the local resistance on the average conformation of the polymers is expressed through $\boldsymbol{\tau}_p$ (cf Eq. 3.22). In the FENE-P and CR models, which take the drag force on the beads to be isotropic, $\alpha = 0$ in eq. (3.19).

Brownian force, $\boldsymbol{F}^{(b)}$, arises from the thermal fluctuations in the liquid and also con-

tributes to the stress. The true Brownian force is a rapidly and irregularly fluctuating function. However, the average of this fluctuating force is well-defined. For the Giesekus and FENE-P models, $\boldsymbol{F}^{(b)}$ is isotropic with a constant coefficient, kT premultiplying the gradient term (Bird *et al.* , 1987)

$$\boldsymbol{F}^{(b)} = -kT\frac{\partial \ln \psi}{\partial \boldsymbol{r}_\mu} \tag{3.20}$$

whereas for the CR model, $\boldsymbol{F}^{(b)}$ is isotropic with a non-constant coefficient (Herrchen and Öttinger, 1997),

$$\boldsymbol{F}^{(b)} = -\frac{kT}{1-<\frac{Q^2}{Q_0^2}>}\frac{\partial ln\psi}{\partial \boldsymbol{r}_\mu} \tag{3.21}$$

where the symbol $<\cdot>$ denotes a phase space average, k is the Boltzmann constant, and T is the absolute temperature. The above simple expression assumes equilibration in the momentum space, i.e. the influence of the flow field on the velocity distribution is ignored.

External force, $\boldsymbol{F}^{(e)}$ arises from an applied field such as gravity or electrical forces. Here, we neglect the external force.

In order to obtain an expression for the stress tensor, we follow the elementary derivation provided by Kramers (Bird *et al.* , 1987). At an arbitrary plane moving with the fluid velocity $\boldsymbol{v}$, the dumbbells contribute to the stress in the following ways (1) straddled dumbbells give rise to tension and compression because of the momentum transmitted through the connector; (2) the beads themselves may cross the arbitrary plane and bring with them a certain amount of momentum. The resulting polymeric contribution to the stress tensor $\boldsymbol{\tau}_p$ in the dimensional form is related to the molecular configuration $\boldsymbol{QQ}$ by the Kramers equation

$$\boldsymbol{\tau}_p = -nH_0 <h(Q^2)\boldsymbol{QQ}> +nkT\boldsymbol{\delta} \tag{3.22}$$

The molecular extension tensor $\boldsymbol{QQ}$ is non-dimensionalized with respect to the characteristic mean squared 1/3 of equilibrium length of the molecule, $Q_c^2 \equiv kT/H_0$ for the Giesekus and CR models, and $Q_c^2 \equiv (kT/H_0)(b/(b+5))$ for the FENE-P model, so that $tr<\boldsymbol{QQ}>_{eq} \equiv 3$. Here, Q_0 represents the dimensional maximum extensibility and $b \equiv H_0Q_0^2/kT$. For all three constitutive models, the polymeric contribution to the viscosity in the zero-shear-rate limit

is written as $\eta_p = B\lambda nkT$, where the parameter $B = 1$ for the Giesekus and CR models, and $B \equiv b/(b+5)$ for the FENE-P model. The polymeric stress tensor τ_p is non-dimensionalized with respect to the solution viscosity $\eta_0 \equiv \eta_s + \eta_p$ and the characteristic time scale of the flow t_c. The Weissenberg number defined as $We \equiv \lambda/t_c$. A compact dimensionless expression for τ_p is

$$\tau_p = -\frac{1-\beta}{We}[\frac{1}{B}<h(Q^{*2})\boldsymbol{Q}^*\boldsymbol{Q}^*> - \boldsymbol{\delta}] \tag{3.23}$$

For the Giesekus model ($b \to \infty$), τ_p depends only on the second moment of the distribution function, and it can be written exactly in terms of $\boldsymbol{Q}^*\boldsymbol{Q}^*$ as

$$\tau_p = -\frac{1-\beta}{We}\{<\boldsymbol{Q}^*\boldsymbol{Q}^*> - \boldsymbol{\delta}\} \tag{3.24}$$

For the FENE dumbbell models, Peterlin's approximation is introduced to reduce the average of $<h(Q^2)\boldsymbol{Q}^*\boldsymbol{Q}^*>$ by the product of the two averages as

$$<h(Q^{*2})\boldsymbol{Q}^*\boldsymbol{Q}^*>= h(<Q^{*2}>)<\boldsymbol{Q}^*\boldsymbol{Q}^*> + \varepsilon Q_0^2\boldsymbol{\delta} \tag{3.25}$$

An extra isotropic term containing a constant ε is added to ensure that the $<Q^{*2}>$ for the FENE model is identical to that of the FENE-P at equilibrium (Bird *et al.* , 1987). The approximate expression for the polymeric stress tensor

$$\tau_p = -\frac{1-\beta}{We}\frac{1}{B}[Bh(<Q^{*2}>)<\boldsymbol{Q}^*\boldsymbol{Q}^*> - (1-\varepsilon b)\boldsymbol{\delta}] \tag{3.26}$$

In addition to Peterlin's approximation, the CR model includes the dimensionless modulus $h(<Q^{*2}>)$ multiplying the difference $\boldsymbol{Q}^*\boldsymbol{Q}^* - \boldsymbol{\delta}$, so that the final approximation for τ_p for this model is

$$\tau_p = -\frac{1-\beta}{We}[h(<Q^{*2}>)<\boldsymbol{Q}^*\boldsymbol{Q}^*> - \boldsymbol{\delta}] \tag{3.27}$$

Note that the term $\varepsilon Q_0^{*2}\boldsymbol{\delta}$ is not added to the CR equation.

The partial differential equations for the Giesekus, FENE-P and CR constitutive models are first order hyperbolic equations in terms of the stress tensor τ_p for given velocity fields.

The Giesekus model yields an exact closed form evolution equation for τ_p:

$$\tau_p + We\tau_{p(1)} - \frac{\alpha We}{1-\beta}\tau_p \cdot \tau_p = -(1-\beta)\dot{\gamma} \tag{3.28}$$

where the subscript $_{(1)}$ denotes the upper convected derivative,

$$\tau_{p(1)} \equiv \frac{D}{Dt}\tau_p - [(\nabla v)^T \cdot \tau_p + \tau_p \cdot (\nabla v)] \tag{3.29}$$

Incorporation of the Peterlin approximation leads to the evolution equation for the FENE-P model in terms of τ_p as

$$h(<Q^{*2}>)\tau_p + We\tau_{p(1)} = -\frac{Q_0^{*2}}{Q_0^{*2}-3}(1-\beta)\dot{\gamma} \tag{3.30}$$

where Q_0^{*2} is the dimenionless maximum extensibility, and the modulus is written as

$$h(<Q^{*2}>) \equiv \frac{1}{1-\frac{3}{Q_0^{*2}}} - \frac{We}{1-\beta}\frac{1}{Q_0^{*2}} tr\tau_p \tag{3.31}$$

where the term $tr\tau_p \equiv \sum_{i=1}^{3} \tau_{p_i} i$. For the CR model, the evolution equation for τ_p is

$$\tau_p + We\left(\frac{\tau_p}{h(<Q^{*2}>)}\right)_{(1)} = -(1-\beta)\dot{\gamma} \tag{3.32}$$

with

$$h(<Q^{*2}>) \equiv \frac{(1-\beta)Q_0^{*2} - We\, tr\tau_p}{(1-\beta)(Q_0^{*2}-3)} \tag{3.33}$$

The constitutive model parameters for all of the above differential constitutive equations can be obtained by fitting simple viscometric measurements. Quinzani *et al.* (1990) and Byars (1995) characterized the material functions of the PIB/PB/C14 solutions in simple shear flow, and these shear flow properties were used to determine constants in specific non-Newtonian constitutive equations. The best fit for the viscometric properties of the 0.31 wt% PIB/PB/C14 fluids are: $\alpha = 10^{-3}$ for the Giesekus model, $Q_0^* = 15$ for the CR model (Byars, 1995), and $\beta = 0.6$. In this thesis, we performed viscoelastic calculations for constant $\beta = 0.59$, and $\alpha = 0$ (i.e. Oldroyd-B model) to $\alpha = 10^{-2}$ for the Giesekus model,

and $Q_0^{*2} = 10^2$ to $Q_0^* = \infty$ for the CR and FENE-P models.

The most serious defect in fitting model parameters using the three differential models mentioned earlier is none of the models can predict the complex shear thinning behavior in Ψ_1 (Byars, 1995). The fact that single mode constitutive models fail to yield a quantitative fit to the linear viscoelastic data is due to the broad molecular weight distribution of the PIB, as well as the broad distribution of relaxation time scales for even a monodisperse polymer (Bird *et al.* , 1987). To solve this problem, multiple time constants are incorporated into the model by expressing the polymeric contribution to the stress as the sum of stresses arising from each relaxation mode i.e.

$$\boldsymbol{\tau}_p = \sum_{i=1}^{n} \boldsymbol{\tau}_i(t) \tag{3.34}$$

For example, for the multiple Giesekus model, $\boldsymbol{\tau}_i$ is written as

$$\boldsymbol{\tau}_i + \lambda_i \boldsymbol{\tau}_{i(1)} - \alpha_i \frac{\lambda_i}{\eta_i} \boldsymbol{\tau}_i \cdot \boldsymbol{\tau}_i = -\eta_i \dot{\boldsymbol{\gamma}} \tag{3.35}$$

The spectrum of relaxation times and viscosity coefficients $\{\lambda_i, \eta_i\}$ is obtained by fitting the linear viscoelastic measurements using the Levenberg-Marquardt nonlinear regression method (Press *et al.* , 1985). Both Quinzani *et al.* (1990) and Byars (1995) found a quantitative fit of the four mode Upper convected Maxwell (UCM) and Giesekus models to both viscosity and first normal stress coefficient.

Chapter 4

The finite element method

Analytical solutions to the viscoelastic flow problem outlined in chapter 3 can only be found in a few limiting cases. This necessitates the use of numerical methods to solve for the flow kinematics and stress fields. A natural choice is the finite element method. The finite element method (FEM) is a widely used solution technique for solving problems that arise in such diverse fields as fluid dynamics, solid mechanics and computational physics. The FEM belongs to the class of weighted residual methods, where the exactness of the solution of the governing system of differential equations at each point of the domain is replaced with the requirement that the solution satisfies the governing equations in an integrated, or weak, sense over the domain. The ability to treat consistently a variety of boundary conditions and to handle complex geometric shapes demonstrates the flexibility of the FEM. Furthermore, there exists significant mathematical analysis of the FEM for problems that possess a variational form that demonstrates the convergence properties of the method, and places the method on sound mathematical ground, although the FEM has been successfully applied to problems that do not possess a variational form.

This chapter outlines the necessary procedures for solving a viscoelastic fluid flow problem by using the finite element method. Section 4.1 discusses the basic concepts of the finite element method, with the Sturm-Liouville equation in one dimension being used as a model problem. Section 4.2 presents the finite element formulation for the creeping, or Stokes, flow of a Newtonian fluid and illustrates the restrictions placed on the choices for

velocity and pressure spaces imposed by the incompressibility condition. The weak form of the governing equations is summarized at the end of the section. Section 4.3 outlines two methods for solving hyperbolic equations, the Streamline Upwind (SU) and the Streamline Upwinding Petrov-Galerkin (SUPG) methods. Finally, in section 4.4 various methods for treating viscoelastic flow problems are outlined. These include the explicitly elliptic momentum equation (EEME) method (King *et al.* , 1988), and three forms of the elastic-viscous split stress (EVSS) method (Rajagopalan *et al.* , 1990; Brown *et al.* , 1993; Guenette and Fortin, 1995).

4.1 Basic concepts of FEM

The finite element theory for solving systems of partial differential equations (PDE's) is developed on the basis of the well-understood theory for solving a set of ordinary differential equations (ODE's) governed by a second-order elliptic operator (Johnson, 1987; Keunings, 1989). As an example, we will consider the classical Sturm-Liouville problem

$$-\frac{d}{dx}(p(x)\frac{du}{dx}) + q(x)u = f(x), \tag{4.1}$$

where $p(x) > 0$ and $q(x) \geq 0$, with suitable boundary conditions at the endpoints $x = 0$ and $x = \pi$. This equation represents a number of physical processes, such as the temperature distribution along a rod or the displacement of a vibrating string. In particular, if we fix the left-hand end of the string and leave the other end free, this leads to the essential (Dirichlet type) boundary condition at $x = 0$, $u(0) = 0$ and natural (Neumann type) boundary condition at the right-hand end $x = \pi$, $u'(\pi) = 0$.

From a purely mathematical point of view, the above differential equation and associated boundary conditions can be combined into a single equation,

$$Lu = f, \tag{4.2}$$

where L is a linear operator and u is a certain class of functions that can be differentiated

at least twice and satisfies both the differential equation and the boundary conditions. The homogeneous problem $f = 0$ has a trivial solution $u = 0$. To consider the non-homogeneous case, we must place certain restrictions on the space of admissible functions for the inhomogeneous term $f(x)$. We will restrict ourselves to the case where f is square integrable, or has finite energy, as defined by the following norm

$$\|f\|_1^2 \equiv \int_0^\pi ((f(x))^2 + (f'(x))^2)dx < \infty. \tag{4.3}$$

This space of functions which satisfy eq. (4.3) is referred to as H^1 with the superscript indicating the number of derivatives of f. Any piecewise continuous function f in the interval $x = [0, \pi]$ belongs to H^1, but the functions such as Dirac δ-function does not. This space of functions is commonly referred to as L_2.

The solution space u has similar restrictions to those for f. Since the left-side of eq. (4.2) consists of u, u' and u'', the requirement of square-integrability should apply to all three of these terms

$$\|u\|_2^2 \equiv \int_0^\pi [(u''(x))^2 + (u'(x))^2 + (u(x))^2]dx < \infty. \tag{4.4}$$

The solution space $u \in H_B^2$, where the superscript "2" indicates that u satisfies (4.4), i.e., has square integrable second order derivatives, and the subscript "B" indicates that u satisfies the essential boundary conditions at $x = 0$.

For the Sturm-Liouville equation, the continuous dependence of the solution on the data requires that there exists a constant C such that

$$\|u\|_2 \leq C\|f\|_0. \tag{4.5}$$

The analog to eq. (4.5) for an elliptic equation of order $2m$ is

$$\|u\|_{2m} \leq C\|f\|_0, \tag{4.6}$$

where the norm $\|u\|_{2m}$ is defined as

$$\|u\|_2 \equiv \{\int_0^\pi [(u^{2m}(x))^2 + \cdots + (u'(x))^2 + (u(x))^2]dx\}^{1/2}. \tag{4.7}$$

The variational formulation of eq. (4.2) is determined by examining the quadratic functional

$$I(v) = (Lv, v) - 2(f, v). \tag{4.8}$$

The notation (,) represents the inner product of the functions $g(x)$ and $h(x)$ (Strang and Fix, 1973) written as

$$(g, h) = \int_0^\pi g(x)h(x)dx. \tag{4.9}$$

Defined in this fashion, $I(v)$ is minimized at $v = u$ only if the first variation of the functional vanishes. This minimization principle requires that

$$I(u) \leq I(u + \varepsilon v) = I(u) + 2\varepsilon[(Lu, v) - (f, v)] + \varepsilon^2(Lu, v), \tag{4.10}$$

where ε is a small parameter. If the functional I is minimized at u, then the first variation must vanish, i.e.

$$((Lu - f), v) = 0, \tag{4.11}$$

for all choices of the function v. The positive-definiteness of the operator L ensures that the solution u is a true minimum of the functional. Eq. (4.11) is called the *weak*, or *Galerkin form*, of the problem. Here *weak form* refers to the fact that the solution to the differential equation is not necessarily exact at each point, but rather $Lu - f = 0$ is satisfied in the integral sense. Note that eq. (4.11) deals with a stationary point, not necessarily a minimum point, and thus the operator L is no longer required to be positive definite for the weak form. The condition for the vanishing of the first variation corresponds to the Euler equation $Lu = f$. Therefore, the problems of inverting L and minimizing I are equivalent (Strang and Fix, 1973). The two approaches produce the same solution u when the solution is exact. The approach dealing directly with the differential operator L is referred to as the *operational form*, and the second method, which deals with the quadratic functional I, is called the

variational form.

The statement above becomes transparent when L, v and f are real numbers. $I(v) = Lv^2 - 2fv$ is a parabola and

$$\frac{dI}{dv}|_{v=u} = 2(Lu - f) = 0. \tag{4.12}$$

If L is positive ($L > 0$), the parabola attains its minimum at the point u. This can be extended to the case when v and f are n-dimensional vectors, and L is a symmetric positive definite matrix of order $n \times n$

$$I(v) = \sum_{j,k} L_{jk} v_k v_j - 2 \sum_j f_j v_j. \tag{4.13}$$

Since $\boldsymbol{L}$ is symmetric, i.e. $L_{jk} = L_{kj}$, the Euler equation becomes

$$\frac{\partial I}{\partial v_m}|_{v=u} = 2(\sum_k L_{mk} u_k - f_m) = 0, \qquad \forall m = 1, \ldots, n. \tag{4.14}$$

The requirement that $\boldsymbol{L}$ is symmetric positive-definite ensures that $I(v)$ is a paraboloid opening upward with a global minimum at $v = u = \boldsymbol{L}^{-1} f$ (Strang and Fix, 1973).

The quadratic functional to be minimized for the Sturm-Liouville equation is written as

$$I(v) = \int_0^\pi [p(x)(v'(x))^2 + q(x)(v(x))^2 - 2f(x)v(x)]dx. \tag{4.15}$$

Variational theory requires that at the minimum I, the first variation vanishes. The first variation of I is given as

$$\int_0^\pi (pu'v' + quv - fv)dx = \int_0^\pi \underline{[-(pu')' + qu - f]v}dx + p(\pi)u'(\pi)v(\pi). \tag{4.16}$$

The weak form of the Sturm-Liouville equation is also obtained by writing the ODE in terms of eq. (4.11) and integrating by parts. Variational theory requires that the functional space for v that minimizes $I(v)$ is in H_E^1; namely the set of functions that have square integrable first-order derivatives and satisfy the essential boundary condition, i.e. $v(0) = 0$, indicated by the subscript E (Strang and Fix, 1973).

The solution that minimizes the functional I corresponds to the solution of the differential problem. Since u is the solution to the ODE, both the essential and natural conditions are satisfied at the boundary, i.e. $u'(\pi) = 0$. If u is twice differentiable, the underlined integral term is zero for all $v \in H_E^1$ if and only if $-(pu')' + qu = f$ in the interval.

Galerkin's method requires the minimization of the quadratic functional $I(v)$ over a set of functions in the infinite-dimensional space H_E^1. The Ritz method replaces H_E^1 by a finite-dimensional subspace $S \subset H_E^1$ and makes this problem tractable. In the finite element method, a sequence of finite dimensional subspaces S^h is constructed such that $S^h \subset H_E^1$. Here h is related to the characteristic size of the grid associated with the subdivision of the domain Ω into a finite element mesh. The Ritz method obtains a solution u^h by minimizing I over the space S^h, or simply $I(u^h) \leq I(v^h) \quad \forall v^h \in S^h, S^h \subset H_E^1$. The discrete finite element problem becomes finding $u^h \in S^h$ such that

$$((Lu^h - f), v^h) = 0, \tag{4.17}$$

where $R \equiv Lu^h - f$ is the residual equation. In Galerkin's approach, the approximating functions for the solution u^h and those for the weighting functions v^h are chosen to be identical, i.e. $u^h = v^h$. Thus, Galerkin's FEM requires that the residual equation R to be orthogonal to u^h.

The application of the finite element technique requires construction of discrete approximations to the field variables. For the model Sturm-Liouville problem, the computational domain ($x = [0, \pi]$) is divided into N elements with $x_i = i\pi/N$, which may not necessarily equal in size, and the basis functions are chosen to be Lagrangian polynomials. The approximation to the solution $u^h \in S^h$ is the projection of the true solution onto the N basis functions that span S^h, where every member of S^h can be written as a linear combination of ϕ_i^h

$$u^h = \sum_{i=1}^{N} u_i^h \phi_i^h(x). \tag{4.18}$$

The elements ϕ_i^h of the subspace S^h are called the basis functions. The $\{\phi_i^h\}$ constitute a basis for the subspace S^h and lie in H_E^1. The coefficients u_i^h are unknowns determined so as

to minimize I. Galkerin's method ensures that the residual equation is orthogonal to each of the basis functions $\phi_i^h(x)$ as

$$\int_0^\pi (Lu - f)\phi_j^h(x)dx = 0, \quad j = 1, 2, \ldots, N. \tag{4.19}$$

In the finite element method the basis functions $\{\phi_i\}$ are locally defined, in that each ϕ_i is non-zero only in two adjacent elements and zero throughout the rest of the domain. This property for u^h is referred to as having compact support in that at any location in the domain, only a small fraction of the basis functions have non-zero contributions. For example, at node x_i, ϕ_i^h equals one and vanishes at all other nodes. Defined in this way, the coefficient u_i^h coincides with the value of u^h at the node x_i. One particular type of basis is the continuous linear function defined as

$$0 \le x \le x_{i-1}, \quad \phi_i^h = 0 \tag{4.20}$$

$$x_{i-1} \le x \le x_i, \quad \phi_i^h = \frac{x - x_{i-1}}{x_i - x_{i-1}} \tag{4.21}$$

$$x_i \le x \le x_{i+1}, \quad \phi_i^h = \frac{x_{i+1} - x}{x_{i+1} - x_i} \tag{4.22}$$

$$x_{i+1} \le x \le \pi, \quad \phi_i^h = 0. \tag{4.23}$$

The set of basis functions is better understood by mapping each element in the domain into a local isoparametric element defined in a new coordinate system ζ with $-1 \le \zeta \le 1$ as

$$\zeta = 2\left(\frac{x - x_i}{x_{i+1} - x_i}\right) - 1 \tag{4.24}$$

With the above construction, there are two non-zero linear basis function, $\psi^{(1)}$ and $\psi^{(2)}$ within each element that are defined by the equations

$$\psi^{(1)} = \frac{1}{2}(1 - \zeta), \tag{4.25}$$

$$\psi^{(2)} = \frac{1}{2}(1 + \zeta). \tag{4.26}$$

Reconsidering the solutions to the Sturm-Liouville equation, the weak form is written as

$$\int_0^\pi [(-p\frac{du^h}{dx})' + q(x)u^h - f]\phi_j^h(x)dx = 0, \quad j = 1, 2, \ldots, N. \tag{4.27}$$

Substituting the expression for u^h in eq. (4.18) and integrating by parts, leads to

$$\sum_{i=1}^{N} \int_0^\pi u_i^h (p\frac{d\phi_i^h}{dx}\frac{d\phi_j^h}{dx} + q\phi_i^h\phi_j^h)dx = \int_0^\pi f\phi_j^h dx, \quad j = 1, 2, \ldots, N. \tag{4.28}$$

The essential and natural boundary conditions $u(0) = 0, u'(\pi) = 0$ are satisfied automatically. Eq. (4.28) corresponds to a set of N linear algebraic equations with N unknowns given by $\{u_i^h\}$. For the linear basis functions defined in eqs. (4.20-4.23), the matrix arising from the finite element formulation is tridiagonal, symmetric and positive-definite (Strang and Fix, 1973).

4.2 FEM for solving the Stokes problem

Solving the incompressible inertialess flow of a Newtonian fluid using the FEM technique is the basis of solving a viscoelastic flow problem. This is due to the fact that in the limit of $We \to 0$, the flow problem reduces to Stokes flow. For an incompressible steady creeping flow, the governing equations for Stokes flow are summarized as

$$\nabla \cdot \boldsymbol{v} = 0 \qquad \text{in } \Omega, \tag{4.29}$$

$$-\nabla^2 \boldsymbol{v} + \nabla p = 0 \qquad \text{in } \Omega, \tag{4.30}$$

and the homogeneous no-slip boundary condition,

$$\boldsymbol{v} = \boldsymbol{0} \qquad \text{on } \Gamma, \tag{4.31}$$

where Ω denotes the computational domain and Γ is its boundary. The above set of partial differential equations (PDE's) is similar to the two-point boundary-value problem of the

Sturm-Liouville equation examined in section 4.1, in that the momentum equation has an elliptic Laplacian operator.

The Galerkin formulation for the Stokes problem is established by minimizing the total energy $J(\boldsymbol{u})$ defined as

$$J(\boldsymbol{u}) = \int_{\Omega} \boldsymbol{\nabla u} : \boldsymbol{\nabla u} \ d\Omega, \tag{4.32}$$

subject to the incompressibility constraints $(\boldsymbol{\nabla} \cdot \boldsymbol{u}) = 0$ (Carey and Oden, 1983). The variational form of the Stokes problem becomes minimizing J over all components of velocity vector that satisfy the continuity equation.

This problem is a constrained minimization and is best handled by introducing a Lagrange multiplier. This involves taking the original minimization problem and adding to it the constraint term multiplied by the Lagrange multiplier. The variational formulation in terms of a Lagrange multiplier becomes

$$I(\boldsymbol{u}, p) = J(\boldsymbol{u}) + (p, \boldsymbol{\nabla} \cdot \boldsymbol{u}), \tag{4.33}$$

with

$$(p, \boldsymbol{\nabla} \cdot \boldsymbol{u}) \equiv \int_{\Omega} p \boldsymbol{\nabla} \cdot \boldsymbol{u} d\Omega. \tag{4.34}$$

For the Stokes problem, the pressure is the Lagrange multiplier (Carey and Oden, 1983).

A saddle point of the Lagrange multiplier problem eq. (4.33) corresponds to the solution of the Stokes problem. The approximating finite element spaces are $\boldsymbol{V}^h$ and S^h for the velocity and pressure respectively such that the approximated solutions $\boldsymbol{v}^h$ and p^h belong to the finite dimensional spaces, $\boldsymbol{v}^h \in \boldsymbol{V}^h$ and $p^h \in S^h$, respectively. A solution to the flow problem exists, provided that the operator is elliptic and the finite element spaces satisfy a consistency condition (Babuska *et al.* , 1977; Brezzi, 1924; Carey and Oden, 1983). This condition is related to the choice of finite element spaces for solving the Stokes equation. The criterion is

$$\sup_{0 \neq \boldsymbol{v}^h \in \boldsymbol{V}^h} \frac{|\int_{\Omega} q^h \boldsymbol{\nabla} \cdot \boldsymbol{v}^h d\Omega|}{|\boldsymbol{v}^h|} \geq \gamma \|q^h\|, \quad \forall q^h \in S^h \tag{4.35}$$

where the constant $\gamma > 0$ may be chosen independent of h. The above condition is equiva-

lently expressed in the form of

$$|\int_{\Omega} q^h \nabla \cdot \boldsymbol{v}^h d\Omega| \geq \gamma |\boldsymbol{v}^h| \|q^h\|, \quad \forall q^h \in S^h \tag{4.36}$$

The condition (4.35), or equivalently (4.36), is known as the Ladyzhenskaya-Babuska-Brezzi (or LBB) or the *inf-sup* condition (Carey and Oden, 1983; Gunzburger, 1989). The LBB condition is necessary but not sufficient for the existence and uniqueness of the solution to the Stokes flow problem. The choices of polynomials in approximating the velocity and pressure fields must satisfy eq. (4.35) or eq. (4.36). Violation of the LBB condition results in non-uniqueness in the weak solution as well as wiggles in the solution fields. Carey and Oden (1983) proved that the use of biquadratic basis functions for velocity and bilinear approximations for the pressure field satisfies the LBB conditions. With this choice of basis functions, Carey and Oden showed that Galerkin's method has optimal convergence properties, and the errors in the velocity and pressure satisfy

$$\|\boldsymbol{v} - \boldsymbol{v}^h\|_1 \leq Ch^2(\|\boldsymbol{u}\|_3 + \|p\|_2) \tag{4.37}$$

$$\|p - p^h\|_0 \leq Ch^2(\|\boldsymbol{u}\|_3 + \|p\|_2) \tag{4.38}$$

where C is a constant independent of mesh size h.

The weak formulation for the Stokes problem is obtained by applying Galerkin's method. This requires that the residuals for eqs. (4.29) and (4.30) are weighted with appropriate weighting functions associated with variables $\boldsymbol{v}$ and p. Because there are two equations associated with the momentum balance equation and only one equation associated with the incompressibility constraint, also there are two unknowns corresponding to the two components of the velocity vector and one unknown relating to the pressure, it is natural to associate the basis functions for the velocities with the momentum equation and those for the pressure to the incompressibility constraint. It turns out those are the correct choice (Carey and Oden, 1983). The weak form that arises from the application of Galerkin's

method to Stokes flow is given by

$$\int_\Omega (\nabla \cdot \boldsymbol{v}^h)\phi_j^p \; d\Omega = 0, \tag{4.39}$$

and

$$\int_\Omega \{-\nabla \cdot [(\nabla \boldsymbol{v}^h) + (\nabla \boldsymbol{v}^h)^T] + \nabla p^h\} \cdot \boldsymbol{e}_k \phi_j^v \; d\Omega = 0, \tag{4.40}$$

applying integration by parts and the divergence theorem to eq. (4.40) results in

$$\begin{aligned} &\int_\Gamma -\phi_j^v \boldsymbol{n} \cdot [(\nabla \boldsymbol{v}^h) + (\nabla \boldsymbol{v}^h)^T] \cdot \boldsymbol{e}_k \; d\Gamma \\ &+ \int_\Omega \{\nabla \phi_j^v \cdot [(\nabla \boldsymbol{v}^h) + (\nabla \boldsymbol{v}^h)^T] \cdot \boldsymbol{e}_k + \phi_j^v [(\nabla \boldsymbol{v}^h) + (\nabla \boldsymbol{v}^h)^T] : \nabla \boldsymbol{e}_k\} \; d\Omega \\ &+ \int_\Omega \phi_j^v \nabla p^h \cdot \boldsymbol{e}_k \; d\Omega = 0, \qquad k = 1, \; 2 \end{aligned} \tag{4.41}$$

where $\boldsymbol{e}_k$ is the k-th base vector of the coordinate system, $\boldsymbol{n}$ is the outward pointing unit normal on the boundary of the domain, and ϕ_j^v and ϕ_j^p are the basis functions corresponding to the velocity and pressure, respectively. If the boundary integral in eq. (4.41) that arises from the application of the divergence theorem, then this equation is replaced with the essential boundary conditions $\boldsymbol{v}_i^h = \boldsymbol{0}$ on domain Γ, so it does not matter what the integral is.

4.3 Methods for solving hyperbolic equations

In the preceding two sections, we showed that Galerkin's method solves Sturm-Liouville ODE's and Stokes problem and the resulting formulation is equivalent to a variational form. The advective nature of a hyperbolic equation means that information is propagated in a characteristic direction. As an example, let us consider the steady convection of a temperature field T,

$$\boldsymbol{v} \cdot \nabla T = 0, \tag{4.42}$$

where $\boldsymbol{v}$ is the velocity field that advects the temperature T along streamlines. As discussed in section 3.2, the differential constitutive equations are hyperbolic in terms of the stress

tensor τ_p. Therefore, modeling of viscoelastic flow involves solving equations of hyperbolic character. A stable and convergent method for dealing with hyperbolic equations is essential for the success of viscoelastic flow calculations.

Galerkin's FE method is not optimal for solving hyperbolic equations because the weighted residual equations are not subject to variation theory in which the weak form is equivalent to a minimization problem. Thus, the order of convergence $O(h^{k-1})$ for Galerkin's FEM is not optimal for hyperbolic equations as it is for a purely elliptic equations $O(h^k)$, where $k-1$ is the degree of the basis function polynomial (Strang and Fix, 1973). There are a couple of ways to remedy this problem. The Streamline-Upwind (SU) method modifies the purely advective term of the hyperbolic equation by the addition of an extra second-order diffusion term. The Streamline-Upwind Petrov-Galerkin (SUPG) method overcomes the deficiency by modifying the weighting function. In the following two subsections, we discuss each method in more detail.

4.3.1 SU formulation

The SU method is based on the artificial diffusion (AD) method of Brooks and Hughes (1982). In this approach, an elliptic term is added to the original differential equation and Galerkin's method is then applied to solve this modified problem. The small dissipation term is written in the form

$$-\nabla \cdot (\boldsymbol{A} \cdot \nabla \boldsymbol{v}^h) \tag{4.43}$$

where $\boldsymbol{A}$ is the artificial diffusion tensor. First, Brooks and Hughes (1982) assumed that $\boldsymbol{A}$ was isotropic, which gives rise to excessive diffusion in all directions. The nature of hyperbolic equations suggested that the information is passed only along the streamlines of the flow, and consequently $\boldsymbol{A}$ should be anisotropic. The AD method was then modified by Brooks and Hughes (1982), where $\boldsymbol{A}$ was assumed to have the following form:

$$\boldsymbol{A} = \alpha \frac{\boldsymbol{v}\boldsymbol{v}}{|\boldsymbol{v} \cdot \boldsymbol{v}|}, \tag{4.44}$$

where α is a scalar constant and has a magnitude of $O(h)$. This method, known as streamline-upwinding, is more accurate than artificial diffusion method because of the elimination of diffusion across streamlines, although it is still only $O(h)$ accurate.

4.3.2 SUPG method

The SUPG method was first introduced by Brooks and Hughes (1984). It was proved convergent by Johnson *et al.* (1984) for linear hyperbolic equations and was found to be more accurate and stable than the Galerkin method. The distinct feature of the SUPG method is that the weighting function is no longer identical to the basis function. Choices of the weighting functions are chosen to weight upstream points more heavily than downstream points. Brooks and Hughes (1982, 1984) proposed the construction of the weighting function by adding an "upwinding" term taking into account diffusion along streamlines to the standard Galerkin weighting function

$$w^h = \phi^h + h\frac{\boldsymbol{v}^h}{|\boldsymbol{v}^h|} \cdot \boldsymbol{\nabla}\phi^h \tag{4.45}$$

The velocity field in eqn. (4.45) is normalized so that the gradient contribution to the weighting function remains an $O(1)$ quantity. The SUPG method converges to $O(h^{k-1/2})$ for linear first-order hyperbolic equations as long as the dependent variable has square integrable streamwise derivatives (Johnson et al., 1984). As an example, for a linear basis function ϕ^h, the SUPG method improves the accuracy to $O(h^{3/2})$, and is better than either artificial diffusion or streamline-upwinding method whose convergence is $O(h)$.

4.4 Solving viscoelastic constitutive equations

Viscoelastic flow equations are complicated by the fact that the equation set is of mixed mathematical type, with the momentum equation possessing elliptic characteristics and the constitutive equation having hyperbolic characteristic. The mixed finite element method used in this thesis respects the mathematical type of the differential equations. This involves the use of suitable upwinding techniques, either the SU or SUPG method for the

constitutive equation, and Galerkin's method for the momentum and continuity pair. In the following subsections, three finite element formulations for solving the viscoelastic flow problem are presented: the viscous formulation is presented in section 4.4.1, the explicitly elliptic momentum equation (EEME) method is discussed in section 4.4.2, and three variants of the elastic-viscous split stress (EVSS) method are examined in section 4.4.3. These variants are the EVSS method of Rajagopalan *et al.* (1990), the EVSS-G method of Brown *et al.* (1993) and the discrete EVSS (DEVSS) method of Guenette and Fortin (1995).

4.4.1 The viscous formulation

The viscous formulation is based on the Stokes problem and is applicable to constitutive equations with non-vanishing solvent contribution, i.e. $\beta \neq 0$. As an example, let us consider the inertialess flow of an Oldroyd-B fluid. The governing equations for the Oldroyd-B model are

$$\nabla \cdot \boldsymbol{v} = 0, \tag{4.46}$$

$$-\beta \nabla^2 \boldsymbol{v} + \nabla \cdot \boldsymbol{\tau}_p + \nabla p = \boldsymbol{0}, \tag{4.47}$$

$$\boldsymbol{\tau}_p + We[\boldsymbol{v} \cdot \nabla \boldsymbol{\tau}_p - (\nabla \boldsymbol{v})^T \cdot \boldsymbol{\tau}_p - \boldsymbol{\tau}_p \cdot \nabla \boldsymbol{v}] = -(1-\beta)\dot{\boldsymbol{\gamma}}. \tag{4.48}$$

In the viscous formulation, the weak forms of the equations are obtained by applying Galerkin's method to the momentum and continuity equations and the SUPG method to the constitutive equation. The resulting weak forms of the governing equations are

$$\int_\Omega (\nabla \cdot \boldsymbol{v}^h)\phi_j^p \, d\Omega = 0, \tag{4.49}$$

$$\begin{aligned} &-\beta \int_\Gamma \phi_j^v \boldsymbol{n} \cdot [(\nabla \boldsymbol{v}^h) + (\nabla \boldsymbol{v}^h)^T] \cdot \boldsymbol{e}_k \, d\Gamma \\ &+\beta \int_\Omega \{\nabla \phi_j^v \cdot [(\nabla \boldsymbol{v}^h) + (\nabla \boldsymbol{v}^h)^T] \cdot \boldsymbol{e}_k + \phi_j^v [(\nabla \boldsymbol{v}^h) + (\nabla \boldsymbol{v}^h)^T] : \nabla \boldsymbol{e}_k\} \, d\Omega \\ &+\int_\Omega \phi_j^v (\nabla \cdot \boldsymbol{\tau}_p{}^h + \nabla p^h) \cdot \boldsymbol{e}_k \, d\Omega = 0, \qquad k = 1, \ 2 \end{aligned} \tag{4.50}$$

$$\int_\Omega (\boldsymbol{\tau}_p{}^h + We\, \boldsymbol{\tau}_{p(1)}^h + (1-\beta)\dot{\boldsymbol{\gamma}}^h) : \boldsymbol{e}_k \boldsymbol{e}_l (\phi_j^{\tau_p} + h \frac{\boldsymbol{v}^h}{|\boldsymbol{v}^h|} \cdot \nabla \phi_j^{\tau_p}) \, d\Omega = 0, \qquad k, l = 1, \ 2 \tag{4.51}$$

where $\{\phi_j^p\}, \{\phi_j^v\}$ and $\{\phi_j^{\tau_p}\}$ are the basis functions for the pressure, velocity vector, and polymeric stress tensor respectively.

The viscous formulation only converges for β close to unity and small Deborah number (Rajagopalan, 1990; Baranger and Sandri, 1991). Since the term containing β in the equation of motion is elliptic, in the limit of β becoming vanishingly small ($\beta = 0$ in eq. (4.48)), the Oldroyd-B model reduces to the upper convected Maxwell or UCM model), and the ellipticity of the momentum equation is no longer ensured in this limit. The viscous formulation fails to converge for small β and large De where the solution exhibits mesh-sized oscillations in the stress fields. The failure of the viscous formulation led to the development of various splitting methods that ensure the convergence of the numerical method in the limit of small $\beta \rightarrow 0$.

4.4.2 The explicitly elliptic momentum equation (EEME) method

Renardy (1985) introduced a formulation of the momentum equation which ensured the elliptic character of the equation of motion for the UCM model at all Weissenberg number We. Based on this formulation, Renardy (1985) proved the existence and uniqueness of solutions to the UCM equation. A version of this equation, called the "explicitly elliptic momentum equation" (EEME) was developed by King *et al.* (1988) for calculating the two-dimensional viscoelastic flow between eccentric cylinders. The EEME method is derived by taking the divergence of the stress for the steady constitutive equation and substituting it into the steady momentum equation (King *et al.* , 1988). This is best illustrated by considering the governing equations for the UCM fluid

$$\nabla \cdot \boldsymbol{v} = 0, \tag{4.52}$$

$$\nabla \cdot \boldsymbol{\tau} + \nabla p = 0, \tag{4.53}$$

$$\boldsymbol{\tau} + We[\boldsymbol{v} \cdot \nabla \boldsymbol{\tau} - (\nabla \boldsymbol{v})^T \cdot \boldsymbol{\tau} - \boldsymbol{\tau} \cdot \nabla \boldsymbol{v}] = -\dot{\gamma}, \tag{4.54}$$

where $\boldsymbol{\tau}$ is the deviatoric stress tensor.

The divergence of the constitutive equation is given by

$$\nabla \cdot \boldsymbol{\tau} = -We\nabla \cdot [\boldsymbol{v} \cdot \nabla \boldsymbol{\tau} - (\nabla \boldsymbol{v})^T \cdot \boldsymbol{\tau} - \boldsymbol{\tau} \cdot \nabla \boldsymbol{v}] - \nabla \cdot \dot{\boldsymbol{\gamma}}. \tag{4.55}$$

Substituting eq. (4.55) into the momentum equation leads to

$$\nabla \cdot (\boldsymbol{\chi} \cdot \nabla \boldsymbol{v}) + \nabla \boldsymbol{v} \cdot (\nabla \cdot \boldsymbol{\chi}) - \nabla q = 0, \tag{4.56}$$

where $\boldsymbol{\chi}$ is the new stress variable, called the Renardy stress, defined as

$$\boldsymbol{\chi} \equiv -We\boldsymbol{\tau} + \boldsymbol{\delta} \tag{4.57}$$

and q is the new pressure variable, called the substantial pressure, given as

$$q \equiv p + We\boldsymbol{v} \cdot \nabla p, \tag{4.58}$$

and the UCM constitutive equation in terms of the EEME formulation is written as

$$\boldsymbol{\chi} + We\boldsymbol{\chi}_{(1)} - \boldsymbol{\delta} = \mathbf{0}. \tag{4.59}$$

The momentum equation given by eq. (4.56) is an advection-diffusion equation for the velocity $\boldsymbol{v}$. Renardy (1985) proved that when $\boldsymbol{\chi}$ is positive-definite, the equation is elliptic; but when $\boldsymbol{\chi}$ is negative-definite, the equation is hyperbolic. For a steady inertialess flow, King *et al.* (1988) has shown that $\boldsymbol{\chi}$ is always positive-definite and therefore the momentum equation must be elliptic throughout the entire flow domain.

As in the case of the viscous formulation, the momentum and continuity equations are treated with Galerkin's method and the constitutive equation is treated with the SUPG method. The weak form of the governing equations becomes

$$\int_\Omega (\nabla \cdot \boldsymbol{v}^h)\phi_j^q \, d\Omega = 0 \tag{4.60}$$

$$
\begin{aligned}
&- \int_\Gamma \phi_j^v \;\; \boldsymbol{n}\cdot(\boldsymbol{\chi}^h)\cdot\boldsymbol{e}_k \; d\Gamma \\
&- \int_\Omega \{\nabla\phi_j^v\cdot[\boldsymbol{\chi}^h\cdot(\nabla\boldsymbol{v}^h)]\cdot\boldsymbol{e}_k + \phi_j^v[\boldsymbol{\chi}^h\cdot(\nabla\boldsymbol{v}^h)^T]:\nabla\boldsymbol{e}_k\} \; d\Omega \\
&- \int_\Omega \phi_j^v[\nabla\boldsymbol{v}^h\cdot\nabla(\boldsymbol{\chi}^h-\boldsymbol{\delta}) + \nabla q^h]\cdot\boldsymbol{e}_k \; d\Omega = 0, \qquad k=1,\ 2
\end{aligned}
\tag{4.61}
$$

$$
\int_\Omega (\boldsymbol{\chi}^h + We\boldsymbol{\chi}_{(1)}^h - \boldsymbol{\delta}):\boldsymbol{e}_k\boldsymbol{e}_l(\phi_j^\chi + h\frac{\boldsymbol{v}^h}{|\boldsymbol{v}^h|}\cdot\nabla\phi_j^\chi)\; d\Omega = 0, \qquad k,l=1,\ 2 \tag{4.62}
$$

where $\{\phi_j^q\}$, $\{\phi_j^v\}$ and $\{\phi_j^\chi\}$ are the basis functions for the substantial pressure, velocity vector, and Renardy stress tensor respectively.

King *et al.* (1988) showed that the use of biquadratic basis functions for the components of the velocity and stress tensor, and bilinear basis function for pressure yields a stable and convergent finite element scheme. Excellent agreement is reached in comparison with the spectral element calculations of Beris *et al.* (1986) for the eccentric cylinder flow problem. The EEME method is efficient and accurate solution technique for solving viscoelastic flow in the UCM limit ($\beta \to 0$). However, two drawbacks of the EEME formulation tend to limit the application of this method. First, the EEME form of the momentum equation is difficult to derive for many complex constitutive equations, such as the FENE-P and CR models. Second, the inclusion of inertia causes difficulty in resolving the ellipticity of the EEME operator and can in turn cause numerical instabilities in the calculations (Rajagopalan, 1990; Brown *et al.* , 1993).

4.4.3 The elastic viscous split stress (EVSS) methods

The basic concept of a splitting method is to manipulate the momentum equation so that it is elliptic even in the limit $\beta \to 0$. The three splitting methods discussed below are the elastic-viscous split stress (EVSS) formulation originally proposed by Rajagopalan *et al.* (1990), the EVSS-gradient (EVSS-G) method developed by Brown et al. (1993) and the discrete EVSS-G (DEVSS-G) suggested by Guenette and Fortin (1995) and implemented in this thesis.

4.4.3.1 The EVSS method

Rajagopalan *et al.* (1990) developed the EVSS method where an explicitly elliptic operator is introduced into the momentum equation by splitting the extra stress into Newtonian and polymer contributions. The concept of EVSS is illustrated by examining the inertialess flow of a Giesekus fluid which cannot be accommodated with the EEME method. The relevant governing equations are

$$\nabla \cdot \boldsymbol{v} = 0, \tag{4.63}$$

$$-\beta \nabla^2 \boldsymbol{v} + \nabla \cdot \boldsymbol{\tau}_p + \nabla p = \mathbf{0}, \tag{4.64}$$

$$\boldsymbol{\tau}_p + We[\boldsymbol{v} \cdot \nabla \boldsymbol{\tau}_p - (\nabla \boldsymbol{v})^T \cdot \boldsymbol{\tau}_p - \boldsymbol{\tau}_p \cdot \nabla \boldsymbol{v}] - \frac{\alpha\, We}{1-\beta} \boldsymbol{\tau}_p \cdot \boldsymbol{\tau}_p = -(1-\beta)\dot{\boldsymbol{\gamma}}. \tag{4.65}$$

The splitting is accomplished by introducing a new variable, the elastic stress tensor $\boldsymbol{\Sigma}$, defined as

$$\boldsymbol{\Sigma} \equiv \boldsymbol{\tau}_p + (1-\beta)\boldsymbol{\gamma}. \tag{4.66}$$

Substituting eq. (4.66) into the equation of motion yields

$$-\nabla^2 \boldsymbol{v} + \nabla \cdot \boldsymbol{\Sigma} + \nabla p = 0, \tag{4.67}$$

and the constitutive equation now becomes

$$\begin{aligned} &\boldsymbol{\Sigma} + We\boldsymbol{\Sigma}_{(1)} - (1-\beta)We\dot{\boldsymbol{\gamma}}_{(1)} - \frac{\alpha We}{1-\beta}\boldsymbol{\Sigma} \cdot \boldsymbol{\Sigma} \\ &+\alpha We(\boldsymbol{\Sigma} \cdot \dot{\boldsymbol{\gamma}} + \dot{\boldsymbol{\gamma}} \cdot \boldsymbol{\Sigma}) - \alpha We(1-\beta)\dot{\boldsymbol{\gamma}} \cdot \dot{\boldsymbol{\gamma}} = \mathbf{0}. \end{aligned} \tag{4.68}$$

The Laplacian operator $\nabla^2 \boldsymbol{v}$ in eq. (4.67) ensures the ellipticity of the momentum equation in $\boldsymbol{v}$, independent of β. The success of the EVSS/FEM hinges on the treatment of the rate-of-strain tensor $\dot{\boldsymbol{\gamma}} \equiv \nabla \boldsymbol{v} + (\nabla \boldsymbol{v})^T$. The term $\dot{\boldsymbol{\gamma}}_{(1)}$ in eq. (4.68) causes numerical instabilities under transient flow conditions (Northey, 1991). The EVSS method overcomes this problem by interpolating the rate-of-strain tensor onto a bilinear basis function and using a

least-square method to approximate $\dot{\gamma}$

$$\int_\Omega \{\dot{\gamma}^h - [\nabla \boldsymbol{v}^h - (\nabla \boldsymbol{v}^h)^T]\}\phi_j^\gamma d\Omega = 0. \tag{4.69}$$

Similar to the viscous and EEME formulations, Galerkin's method is applied to solve the momentum and continuity equation pair, and the SUPG method is used for the differential constitutive equation. The weak forms for the EVSS/FE formulation for solving for the flow of a Giesekus fluid are

$$\int_\Omega (\nabla \cdot \boldsymbol{v}^h)\phi_j^p \; d\Omega = 0, \tag{4.70}$$

$$\begin{aligned} &- \int_\Gamma \phi_j^v \;\; \boldsymbol{n}\cdot[(\nabla \boldsymbol{v}^h) + (\nabla \boldsymbol{v}^h)^T]\cdot \boldsymbol{e}_k \; d\Gamma \\ &+ \int_\Omega \{\nabla \phi_j^v \cdot [(\nabla \boldsymbol{v}^h) + (\nabla \boldsymbol{v}^h)^T] \cdot \boldsymbol{e}_k + \phi_j^v [(\nabla \boldsymbol{v}^h) + (\nabla \boldsymbol{v}^h)^T] : \nabla \boldsymbol{e}_k\} \; d\Omega \\ &+ \int_\Omega \phi_j^v [\nabla \cdot \boldsymbol{\Sigma}^h + \nabla p^h]\cdot \boldsymbol{e}_k \; d\Omega = 0, \qquad k = 1,\ 2 \end{aligned} \tag{4.71}$$

$$\begin{aligned} &\int_\Omega [\boldsymbol{\Sigma}^h + We\boldsymbol{\Sigma}_{(1)}^h - We(1-\beta)\dot{\boldsymbol{\gamma}}_{(1)}^h] : \boldsymbol{e}_k\boldsymbol{e}_l(\phi_j^\Sigma + h\frac{\boldsymbol{v}^h}{|\boldsymbol{v}^h|}\cdot\nabla\phi_j^\Sigma) \; d\Omega \\ &- \frac{\alpha We}{1-\beta}\int_\Omega [\boldsymbol{\Sigma}^h\cdot\boldsymbol{\Sigma}^h - (1-\beta)(\boldsymbol{\Sigma}^h\cdot\dot{\boldsymbol{\gamma}}^h + \dot{\boldsymbol{\gamma}}^h\cdot\boldsymbol{\Sigma}^h)] : \boldsymbol{e}_k\boldsymbol{e}_l(\phi_j^\Sigma + h\frac{\boldsymbol{v}^h}{|\boldsymbol{v}^h|}\cdot\nabla\phi_j^\Sigma)d\Omega \\ &- \int_\Omega \alpha We(1-\beta)(\dot{\boldsymbol{\gamma}}^h\cdot\dot{\boldsymbol{\gamma}}^h) : \boldsymbol{e}_k\boldsymbol{e}_l(\phi_j^\Sigma + h\frac{\boldsymbol{v}^h}{|\boldsymbol{v}^h|}\cdot\nabla\phi_j^\Sigma)d\Omega = 0, \qquad k,l = 1,\ 2 \end{aligned} \tag{4.72}$$

where $\{\phi_j^p\}, \{\phi_j^v\}, \{\phi_j^\Sigma\}$ and $\{\phi_j^\gamma\}$ are the basis functions for approximating the pressure, the components of the velocity vector, the elastic stress tensor and the rate-of-strain tensor, respectively. Because of the consistency condition for p and $\boldsymbol{v}$ in the limit of Stokes flow (or simply the LBB conditions discussed in section 4.2), the velocity $\boldsymbol{v}$ is approximated by continuous biquadratic basis functions, and the pressure p by bilinear basis function. The elastic stress tensor, $\boldsymbol{\Sigma}$, is interpolated by biquadratic basis function and the rate-of-strain tensor $\dot{\gamma}$ is approximated bilinearly (Rajagopalan, 1990).

The EVSS method yields smoother solutions than either the viscous or EEME formulations and is applicable for all values of β, $0 \leq \beta \leq 1$ (Rajagopalan, 1990). The EVSS/FEM has been tested in various steady-state benchmark problems, such as flow between eccentric cylinders, flow through a corrugated tube and rimming flow, and yielded convergent and

accurate results (King, 1990). The drawback of the EVSS method is the requirement of rewriting the constitutive equation in terms of the elastic stress tensor $\boldsymbol{\Sigma}$. This can be difficult or impossible for some constitutive equations, such as rigid dumbbell models describing rodlike macromolecules (Bird *et al.* , 1987).

4.4.3.2 The EVSS-G method

Although the EVSS method solves the steady-state benchmark problem efficiently (Rajagopalan, 1990), a numerical instability appears in time-dependent planar Couette flow (Brown *et al.* , 1993). Here, the planar Couette geometry refers to the flow where the fluid is placed in between two parallel plates, and the top plate is moved at a constant velocity U and the bottom plate is stationary. The velocity gradient $\dot{\gamma}$ is given as $\dot{\gamma} = U/H$, where H is the gap height. For planar Couette flow of an UCM fluid, analytic solutions of Gorodstov and Leonov (1967) show that the flow is always stable to a small amplitude disturbance. The decay rate of the disturbance is proportional to $-1/De$ with $De = \lambda\dot{\gamma}$. Northey (1991) applied the EVSS/FEM and found that the flow was stable with a decay rate of approximately $-1/De$ for $De < 1$. At higher De, the EVSS/FEM predicted that the flow was unstable, in contrast to the theoretical prediction provided by Gorodstov and Leonov (1967). Analysis of the structure of the disturbance showed that most of the energy of the disturbance was concentrated near the non-moving wall (Brown *et al.* , 1993).

Brown *et al.* , (1993) inferred that the numerical difficulty of the EVSS method arises because of the incompatibility between the velocity gradient $\nabla \boldsymbol{v}$ and the rate-of-strain tensor $\dot{\gamma}$ in the constitutive equation. The incompatibility occurs along the no-slip boundary, where the differential constitutive equation reduces to an algebraic equation. This is illustrated by examining the Giesekus model, eq. (3.28). At the no-slip boundary, where $\boldsymbol{v} = \mathbf{0}$ and hence $\boldsymbol{v} \cdot \nabla \boldsymbol{\tau}_p = \mathbf{0}$, the Giesekus model becomes an algebraic equation in $\boldsymbol{\tau}_p$

$$\boldsymbol{\tau}_p - We[(\nabla \boldsymbol{v})^T \cdot \boldsymbol{\tau}_p + \boldsymbol{\tau}_p \cdot \nabla \boldsymbol{v})] - \frac{\alpha We}{1-\beta}\boldsymbol{\tau}_p \cdot \boldsymbol{\tau}_p = -(1-\beta)\dot{\gamma} \tag{4.73}$$

The EVSS method approximates the velocity $\boldsymbol{v}$ and estimates the velocity gradient tensor $\nabla \boldsymbol{v}$ from $\boldsymbol{v}^h$, and, as a result, the velocity gradient is discontinuous. Brown *et al.* (1993)

concluded that the mesh-sized oscillations near the non-moving wall are caused by the fact that the discontinuous velocity gradient is interpolated on to the continuous rate-of-strain tensor along the zero velocity streamline. The novelty of the method is the suggestion of interpolating the velocity gradient tensor $\nabla \boldsymbol{v}$ instead of the rate-of-strain tensor $\dot{\gamma}$ (Brown *et al.* , 1993). A least-squares approximation to the components of $\nabla \boldsymbol{v}$ is used

$$\int_\Omega \phi_j^g (\boldsymbol{G}^h - \nabla \boldsymbol{v}^h) d\Omega = \boldsymbol{0} \tag{4.74}$$

where $\{\phi_j^g\}$ are the basis for approximating the velocity gradient tensor.

Applying the EVSS-G method to time-dependent planar Couette flow, Brown *et al.* (1993) were able to compute the correct stability behavior for De exceeding 200. As in the case of the EVSS formulation, the EVSS-G method does not alter the weak forms of the continuity and momentum equations, as given in eqs. (4.70) and (4.71), but does modify the weak form of the constitutive equation for the Giesekus model which is changed to

$$\begin{aligned}
\int_\Omega \; & \{\boldsymbol{\Sigma}^h + We[\boldsymbol{\Sigma}^h - (1-\beta)(\boldsymbol{G}^h + (\boldsymbol{G}^h)^T)]_{(1)} \\
& - \frac{\alpha\, We}{1-\beta} \boldsymbol{\Sigma}^h \cdot \boldsymbol{\Sigma}^h + \alpha\, We[(\boldsymbol{G}^h + (\boldsymbol{G}^h)^T) \cdot \boldsymbol{\Sigma}^h + \boldsymbol{\Sigma}^h \cdot (\boldsymbol{G}^h + (\boldsymbol{G}^h)^T)] \\
& - \alpha\, We(1-\beta)[\boldsymbol{G}^h + (\boldsymbol{G}^h)^T] \cdot [\boldsymbol{G}^h + (\boldsymbol{G}^h)^T]\} : \boldsymbol{e}_k \boldsymbol{e}_l \\
& \left(\phi_j^\Sigma + h \frac{\boldsymbol{v}^h}{|\boldsymbol{v}^h|} \cdot \nabla \phi_j^\Sigma\right) d\Omega = 0 \qquad k,\; l = 1,\; 2
\end{aligned} \tag{4.75}$$

where $\{\phi_j^p\}, \{\phi_j^v\}, \{\phi_j^\Sigma\}$ and $\{\phi_j^\gamma\}$ are low-order Lagrangian finite element bases used to approximate the variables, $(p, \boldsymbol{v}, \boldsymbol{\Sigma}, \nabla \boldsymbol{v})$. The approximation spaces are given as $(p^h, \boldsymbol{v}^h, \boldsymbol{\Sigma}^h, \boldsymbol{G}^h)$, where p^h, $\boldsymbol{\Sigma}^h$, and $\boldsymbol{G}^h$ are written in terms of bilinear basis functions and $\boldsymbol{v}^h$ is approximated by biquadratic basis functions.

4.4.3.3 The DEVSS-G method

More recently, Guenette and Fortin (1995) proposed a new splitting technique that ensures the elliptic nature of the momentum equation regardless of the value of β. This method is similar to the EVSS method in that it introduces the rate-of-strain tensor as an additional unknown. The method deviates from the EVSS in that the requirement of splitting the

stress is eliminated. This is accomplished by subtracting the term $(2\alpha - \beta)\dot{\gamma}$ and adding its approximation as the rate-of-strain tensor, where α is a constant, and the momentum equation becomes

$$\nabla p + \nabla \cdot \tau_p - \underbrace{2\alpha\nabla^2 \boldsymbol{v}} + \underbrace{2\alpha\nabla \cdot \dot{\boldsymbol{\varepsilon}}} - \beta\nabla \cdot \dot{\boldsymbol{\varepsilon}} = 0, \tag{4.76}$$

where $\dot{\boldsymbol{\varepsilon}}$ is the continuous approximation to the rate-of-strain tensor $\dot{\gamma}$. Guenette and Fortin (1995) have shown that the optimum value of α is 1/2. In the continuous sense, the underbrace terms in eq. (4.77) cancel each other, and the original momentum equation is recovered. However, the real modification only occurs in the discrete version of the governing equation, where $\dot{\boldsymbol{\varepsilon}}$ is approximated by a continuous bilinear basis function and $\dot{\gamma}$ is computed from the biquadratic approximation of the velocity vector $\boldsymbol{v}$, and hence it is linear and discontinuous.

The DEVSS formulation is preferable to the EVSS method because the elliptic stabilization term is added only to the discrete version of the momentum equation and the constitutive equation is solved directly in terms of the polymeric part of the stress. This is extremely useful for viscoelastic constitutive equations that account for the evolution of microstructure tensors, as in the modeling of liquid crystalline polymers and fiber suspensions.

A contribution of this thesis is to combine the G-term in the EVSS-G formulation with the D-term in the DEVSS method and obtain the so called DEVSS-G method, which ensures the elliptic nature of the momentum equation while allowing the constitutive equation to be solved separately. In the DEVSS-G formulation, the velocity gradient tensor $(\nabla \boldsymbol{v})$ is interpolated instead of the rate-of-strain tensor $(\dot{\gamma})$. The equation of motion in eq.(4.76) reduces to

$$-\nabla^2 \boldsymbol{v} + \nabla \cdot \tau_p + \nabla p + (1 - \beta)\nabla \cdot (\boldsymbol{G} + \boldsymbol{G}^T) = \boldsymbol{0}. \tag{4.77}$$

The weak forms for solving the Giesekus fluid in complex flow geometry by the DEVSS-G method are summarized below. Similar to the EVSS and EVSS-G formulations, the weak forms of the continuity equation is unchanged from eq. (4.70). The weak form of the

momentum equation now is modified to

$$
\begin{aligned}
&-\int_{\Gamma} \phi_j^v \;\; \boldsymbol{n}\cdot[(\nabla \boldsymbol{v}^h) + (\nabla \boldsymbol{v}^h)^T]\cdot \boldsymbol{e}_k \; d\Gamma \\
&+\int_{\Omega} \{\nabla \phi_j^v \cdot [(\nabla \boldsymbol{v}^h) + (\nabla \boldsymbol{v}^h)^T]\cdot \boldsymbol{e}_k + \phi_j^v [(\nabla \boldsymbol{v}^h) + (\nabla \boldsymbol{v}^h)^T] : \nabla \boldsymbol{e}_k\} \, d\Omega \\
&+\int_{\Omega} \phi_j^v \{\nabla \cdot {\boldsymbol{\tau}_p}^h + \nabla p^h + (1-\beta)\nabla \cdot [\boldsymbol{G}^h + (\boldsymbol{G}^h)^T]\}\cdot \boldsymbol{e}_k \, d\Omega = 0, \qquad k = 1,\ 2.
\end{aligned}
\tag{4.78}
$$

The weak form of the constitutive equation for the Giesekus model is identical to the EVSS-G formulation, as given in eq. (4.75). The basis functions used to interpolate the pressure, velocity vector, elastic stress and velocity gradient tensors are identical to those used in the EVSS-G formulations.

The DEVSS-G method has been tested in this thesis (refer to chapters 5 and 6) for viscoelastic flow around arrays of cylinders, and by Szady *et al.* (1995) for the start-up of planar Couette flow and time dependent two-dimensional flow around a closely spaced cylinder array ($L = 2.5, H = 2$). In both cases, the DEVSS-G method yields convergent and accurate results.

Chapter 5

Viscoelastic flow around a periodic, linear array of cylinders

Numerical simulation is used to investigate the flow of polymer solutions around a periodic, linear array of cylinders by using three constitutive equations derived from kinetic theory of dilute polymer solutions: the Giesekus model, the FENE-P model, and the Chilcott-Rallison model. In the Giesekus model, intramolecular forces are described by a Hookean spring, whereas a finitely extensible spring whose modulus is given by the Warner approximation is used in both the FENE-P and Chilcott-Rallison models. Hydrodynamic drag on the beads is taken to be anisotropic for the Giesekus model and isotropic for the other two models. The Chilcott-Rallison and FENE-P models differ subtly in their approximate treatment of the nonlinear force law. The three models exhibit very similar rheological behavior in viscometric flow and steady elongational flow, with the notable exception that the viscosity for the Chilcott-Rallison model is shear-rate independent.

Finite element simulations are performed by using two different formulations: the Elastic-Viscous Split-Stress Gradient (EVSS-G) method and a new variant of this formulation, the Discrete EVSS-G (DEVSS-G) formulation, in which the elliptic stabilization term is added only to the discrete version of the momentum equation, and the constitutive equation is solved directly in terms of the polymer contribution to the stress tensor. Calculations are performed for all models up to a Weissenberg number We where the configuration tensor $\langle \boldsymbol{QQ} \rangle$ loses positive definiteness. However, by locally refining the mesh in the gap region, the positive definiteness of $\langle \boldsymbol{QQ} \rangle$ is recovered. The flow and stress fields predicted by the three constitutive equations are qualitatively similar. A

"birefringent strand" of highly stretched polymer molecules, which appears to emanate from the rear stagnation point in the cylinder, strengthens as We is increased. Not surprisingly, the molecular extension computed for the Giesekus model is considerably larger than that of the two FENE spring models. The drag force on the cylinders differs for the FENE-P and Chilcott-Rallison models, because of the difference in the shear thinning viscosity resulting from the different approximations used in these models.

5.1 A literature survey on viscoelastic flow around cylinders

Viscoelastic flow past a periodic array of cylinders has received considerable attention in the last several years (Georgiou et al., 1991; Khomami et al., 1994; Souvaliotis et al., 1992; 1996; Talwar et al., 1992), because of the variety of engineering applications of polymeric flow in porous media, including enhanced oil recovery and composite and textile coating operations. Experiments on flow through periodic arrays have demonstrated increased flow resistance due to the presence of the polymer (Chmielewski et al., 1990; Skartsis et al., 1992; Vossoughi et al., 1974), which is very similar to that observed for flows through actual porous media (Georgiou et al., 1991; Marshall, 1967). Furthermore, flow through an array of cylinders is a complex problem, involving a mixture of elongational and shear flow behavior. Previous studies on packed beds of cylinders or spheres have emphasized the macroscopic response in terms of pressure drop (flow resistance) across the flow device and the general structure of the flow kinematics. The connections between the configurational changes of the macromolecules and macroscopic flow behavior have not been investigated.

Most previous studies of flow past arrays of cylinders have focused on arrays that are infinite in both the lateral and axial directions, so that channel wall effects are negligible. Neither experimental investigation nor theoretical analysis has been conducted on flow around a periodic, single row of cylinders centrally mounted in a rectangular channel. The closest experimental investigation of viscoelastic flow around such a linear array was conducted by Jones et al. (1989), who considered the flow of shear-thinning polyacrylamide (PAA) and xanthan gum solutions in a channel obstructed by two rows of cylinders placed equidistant from the centerplane of the channel in a staggered arrangement. For the less elastic xanthan gum, the resistance to flow, defined as the ratio of pressure gradient to flow rate, monotonically decreased with flow rate and reached a

plateau at very high flow rates. In contrast, for the highly elastic PAA solutions, the flow resistance initially decreased to a minimum and subsequently gradually increased at high flow rates. Later experiments in this same geometry by Georgiou et al. (1991) again confirmed that flow resistance of the PAA/corn syrup Boger fluids initially decreased with increasing volumetric flow rate and then increased as the flow rate further increased.

Skartsis et al. (1992) studied more complicated, two-dimensional arrangements of confined cylinders, and noted that an increase in pressure drop relative to the Newtonian flow occurred at De = 0.01 when cylinders were placed in either square or staggered two-dimensional arrangements. Here the Deborah number, De, was defined based on the shear-rate-dependent relaxation time of the polymer and the average flow rate across the minimum gap. Because the Reynolds number, Re, was only of order 10^{-12}-10^{-10}, the effects of inertial forces were negligible, and the increased pressure drop was solely caused by the elasticity of the fluid, with the onset of the elastic effect depending on the specific geometric arrangement of the array and the shear-rate-dependent relaxation time of the polymer.

Chmielewski et al. (1992; 1993) examined the effects of viscometric properties on the pressure drop across periodic arrays of cylinders with square or hexagonal pitch and porosity of 70%. For a 0.24% polyisobutylene (PIB) in 92.78% polybutene (PB) and 6.98% kerosene Boger fluid and a 0.25% PIB, 81.05% PB, 18.70% kerosene solution, an increased pressure drop compared to the Newtonian value occurred at De $\approx$ 1 for either array. Here De was based on the superficial velocity, cylinder radius, and zero-shear-rate relaxation time of the polymer. For De $\geq$ 3, the flow resistance became independent of De. Shear-thinning solutions, on the other hand, showed a shift in the onset of elastic effects to higher De $\approx$ 2, and no upper limit in drag for De as high as 8 was observed. Chmielewski et al. also noted downstream pressure fluctuations at some critical De that indicated the presence of a flow instability; streak photographs confirmed the development of unsteady flow patterns. They concluded that the increase in the flow resistance corresponded to progressively increasing amplitude in the time-dependence and asymmetry in the flow fields. The transition from steady to time-dependent flow occurred at De $\approx$ 1.6 for square arrays and at De $\approx$ 0.5 for hexagonal arrays. The kinematics prior to the onset of instability were weakly dependent on De, with slight differences from Stokes flow observed for the velocity profiles along the symmetry lines.

Khomami et al. (1994) applied the spectral finite element method to study the flow of the upper convected Maxwell (UCM) model past square arrays of cylinders with porosity of 45.5% such that the flow is separated between the cylinders. No increase in flow resistance was reported. They attributed the discrepancy between experiments and computations (1992) to the elastic instability observed by Chmielewski et al. (1993). The same test problem was examined by Szady et al. (1995) with the EVSS-G finite element method. Initially, the drag force fell with increasing De, but as De was increased beyond a critical value, a gradual increase in flow resistance was observed.

Viscoelastic flow past a single cylinder in a channel also has received some attention over the years and is relevant to the present study as the spacing between cylinders in the linear array becomes large. Broadbent and Mena (1974) used a linear inductance displacement transducer to measure the drag on a cylinder in a square duct with channel gap to cylinder radius aspect ratio $H_c/R_c = 5$ for an aqueous PAA solution. Their measurements showed a quadratic drag reduction due to increase in flow rate relative to a Newtonian fluid for Re < 0.1. Flow visualization experiments did not show any difference between the viscoelastic and Newtonian flow patterns. Manero and Mena (1981) later used the same experimental configuration but considered various PAA concentrations and H_c/R_c aspect ratios ranging from 5 to 20. The magnitude of elastic contributions to the flow is characterized by the Weissenberg number, $We = \lambda\langle v\rangle/d$, where λ is the zero-shear-rate relaxation time of the polymer, d is the diameter of the cylinder, and $\langle v\rangle$ is the average velocity in the unobstructed channel. They observed a downstream shift of the streamlines for We < 1 and Re < 0.01. As We increased to unity, the streamline displacement disappeared, and for We > 1 the streamlines were shifted upstream. Changes in streamlines were found to be independent of H_c/R_c.

McKinley et al. (1993) used laser Doppler velocimetry to study the elastic instability of PIB Boger fluid flow around a cylinder in a rectangular channel with H_c/R_c aspect ratios between 2.0 and 5.9. Fluid elasticity was characterized by the Weissenberg number defined as $We \equiv \lambda(\dot{\gamma})\langle v\rangle/R_c$, where $\lambda(\dot{\gamma})$ was the shear-rate-dependent relaxation time, R_c was the cylinder radius, and $\langle v\rangle$ was the average flow rate across the channel. The streamwise velocity along the centerplane showed no change with increasing We upstream of the cylinder, whereas the downstream wake extended with increasing We. Beyond a critical We, a flow instability was observed and was characterized as a transition from steady, two-dimensional flow to a three-dimensional,

spatially periodic cellular structure. Baaijens et al. (1994; 1995) carried out the first simultaneous measurements of velocity and birefringence for flow past a cylinder. They used highly concentrated solutions of PIB in tetradecane and an aspect ratio of $H_c/R_c = 2.04$. In the wake of the cylinder, a slight downstream shift of the axial velocity along the centerline was observed for We > 1, where We was defined in terms of the zero-shear-rate relaxation time. They also noted that the flow remained steady and two-dimensional for all We probed (< 9.8). Full field birefringence measurements suggested that large molecular extension was highly localized near the cylinder surface. Pointwise velocity and stress measurements were compared with the predictions of Phan-Thien–Tanner model, and good agreement was found up to We = 2.3. Subsequent experiments by Byars (1995) extended the stability studies on the PIB Boger fluid to include the onset of flow instability for a wide range of gap to cylinder radius ratio, $1.5 \leq H_c/R_c \leq 20$.

Byars (1995) also made full-field birefringence measurements and showed that polymer molecules are highly oriented by the rear stagnation flow and remain oriented over fifteen radii downstream of the cylinder for $H_c/R_c = 2$ at We = 0.54. This highly localized region of stretched and aligned polymer molecules in the rear stagnation region has been referred as a "birefringent strand" (Chilcott et al., 1988). As We is increased, the birefringent strand grows in thickness and extent. Birefringent strands have also been observed in other flows with stagnation points. For example, optical experiments in an opposed jet apparatus reveal a strand of extended polymer molecules that appear as a set of bright birefringent lines around the stagnation point whereas the rest of the fluid appears dark (Muller et al., 1988). This is a direct consequence of the large strains occurring along streamlines that pass close to the stagnation point where polymer molecules have long residence times.

Numerical studies of viscoelastic flow around a cylinder in an unbounded flow have focused on the effects of elasticity on streamline patterns and the drag force. Townsend (1980) used a four constant Oldroyd model and was able to reproduce both the upstream and downstream shifting of streamlines reported by Manero and Mena. He also noted that drag decreased for low Re < 0.1 and increased for Re > 5. Chilcott and Rallison (1988) have considered the creeping flow of the Chilcott-Rallison model around a cylinder in an infinite medium. Contours of constant molecular extension reveal that molecules are highly extended as they approach the upstream stagnation point, in the region of high shear rates along the sides of the cylinder, and in the downstream wake. The drag was found to increase for We > 1 and approach an asymptotic value at high We.

The purpose of this chapter is two fold: First, we want to understand better the interconnections among rheological properties, molecular conformational changes, and the macroscopic behavior of the flow. To do this we perform numerical calculations for three differential constitutive equations with different microstructural bases: the Giesekus model (Bird et al., 1987), the finitely extensible, nonlinear elastic dumbbell model with Peterlin's approximation (FENE-P), and the FENE dumbbell model of Chilcott and Rallison (CR) (1988). All three models treat the macromolecules as dumbbells consisting of two point-mass beads connected by a spring and immersed in a Newtonian solvent. The models differ in that in the Giesekus model, the spring is Hookean and hydrodynamic drag on the beads is anisotropic, whereas in the FENE-P and the Chilcott-Rallison models, a finitely extensible nonlinear elastic spring connector is used and the solvent drag on the beads is assumed isotropic. All three models predict similar behavior in homogeneous, steady-state elongational flow, but different behavior in steady-state shear flow. The Giesekus and FENE-P models predict a shear thinning viscosity, whereas the Chilcott-Rallison model has a constant viscosity. The maximum molecular extension Q_0 in the CR and FENE-P models and anisotropy parameter α in the Giesekus model control the plateau for the elongational viscosity at high strain rates. By proper choice of these parameters, essentially identical elongational viscosities can be obtained for the three models.

The second goal of this study is to examine the effect of the confining channel walls and the effect of center-to-center cylinder spacing on flow kinematics and molecular extension. To do this, we begin by considering viscoelastic flow around a single cylinder in a rectangular channel corresponding to an inter-cylinder spacing of infinity. A linear array of cylinders is then considered in which the inter-cylinder spacing is sufficiently large that the presence of neighboring cylinders does not affect the Newtonian velocity field; in this way we are able to investigate the effects of viscoelasticity on widely spaced cylinder arrays. Finally, we consider closely spaced cylinder arrays where flow is separated between the cylinders. In addition to these two motives, these calculations are useful for comparing with experimental studies of viscoelastic flow around a linear array of cylinders as presented in chapters 7 and 8.

Finite element simulations are performed by using two different formulations: the Elastic-Viscous Split-Stress Gradient (EVSS-G) method (Brown et al., 1993) and a new variant of this formulation, the Discrete EVSS-G, or DEVSS-G (Guénette et al., 1995; Szady et al, 1996), in which the elliptic stabilization term is added only to the discrete version of the momentum equation, and

the constitutive equation is solved directly in terms of the polymeric part of the stress or molecular configuration. The accuracy of the finite element calculation is verified by computing the drag force on a single cylinder in a channel with a Newtonian fluid, and comparing our calculations with Faxens' approximation. Excellent agreement is reached at small values of H_c/R_c, and for large H_c/R_c the computed drag force lies within the error bounds of Faxens' solution.

We begin by briefly discussing the problem formulation and flow geometry. The three dumbbell models are then described along with their rheological predictions in steady simple shear and planar elongational flows. A brief description of the finite element techniques is presented in section 3. In section 4, results for viscoelastic flow around a single cylinder in a rectangular channel are discussed first, followed by results for a linear, periodic array of cylinders with widely and closely spaced geometries. Axial normal stress and molecular extension are used to characterize the macroscopic and microstructural response of the polymer solution. Finally, the drag on the cylinders for each of the three different models is discussed as a function of inter-cylinder spacing.

5.2 Problem formulation

5.2.1 Flow geometry

We consider the steady creeping flow of a viscoelastic liquid past a linear array of cylinders placed along the centerplane of a rectangular channel as shown in Fig. 5-1. The flow is assumed to be two dimensional with the primary flow in the x-direction, and body forces are neglected. The origin of the coordinate system is taken to be at the center of one of the cylinders. The radius of each cylinder is R_c, the channel half-width is H_c, and the center-to-center cylinder spacing is L_c. The configuration of the array is specified by two dimensionless quantities, a cylinder spacing L and a channel gap H, each made dimensionless by the cylinder radius:

$$L \equiv \frac{L_c}{R_c}, \qquad H \equiv \frac{H_c}{R_c} \tag{5.1}$$

In the subsequent analysis we use the cylinder radius R_c as the length scale. We note that in the literature on viscoelastic flow around square arrays of cylinders, half the lateral spacing between cylinders has been used as a length gauge. The corresponding scale here would be the minimum

clearance between cylinder and wall H_c - R_c; for H = 2, which we use here exclusively, the two length scales H_c - R_c and R_c are equivalent. The average x-component of the fluid velocity across the unobstructed channel, $\langle v \rangle$, gives a characteristic velocity; the ratio $\langle v \rangle$ to R_c defines a characteristic strain rate for the flow; and $L_c/\langle v \rangle$ gives a characteristic time, namely the time to traverse a unit cell. The importance of viscoelasticity in flow around the linear, periodic cylinder array is characterized by Deborah and Weissenberg numbers, defined as:

$$\mathrm{De} \equiv \frac{\lambda \langle v \rangle}{L_c}, \qquad \mathrm{We} \equiv \frac{\lambda \langle v \rangle}{R_c} = \mathrm{De}L \tag{5.2}$$

where λ is the zero-shear-rate relaxation time of the polymer solution. Defined in this way, De gives the ratio of the relaxation time of the fluid to the time it takes to traverse the unit cell, and We is a dimensionless shear rate for flow in the narrow gap between the cylinder and the confining wall. Thus, De describes interaction among adjacent cylinders associated with fluid memory, whereas We is related to the nonlinear 'elastic' response of the fluid to the flow. When the cylinders are infinitely far apart, $L \rightarrow \infty$, equivalent to a single cylinder in a channel, there is no interaction between the neighboring cylinders and De = 0 so that the flow is characterized completely by We. In the limit of osculating cylinders, De = We/2.

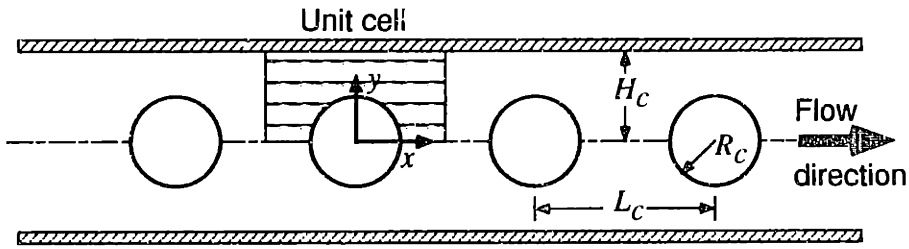

Figure 5-1 Flow past a linear, periodic array of cylinders confined symmetrically between parallel plates. The cylinders each have radius R_c, and the geometry is specified by the cylinder-to-cylinder spacing L_c and the channel half height H_c. The unit cell on which computations are done is shaded.

5.2.2 Governing equations and boundary conditions

The dimensionless stress tensor is written as the sum of contributions from the polymer and solvent as follows

$$\boldsymbol{\tau} = \boldsymbol{\tau}_s + \boldsymbol{\tau}_p = -\beta \dot{\boldsymbol{\gamma}} + \boldsymbol{\tau}_p \tag{5.3}$$

Here the stress tensor has been scaled by a viscous stress $\eta_0 \langle v \rangle / R_c$ based on the zero-shear-rate solution viscosity η_0, so that the dimensionless solvent viscosity in Eq. 5.3 is given by $\beta = \eta_s/\eta_0$. The dimensionless rate-of-strain tensor is denoted by $\dot{\boldsymbol{\gamma}}$.

The governing continuity and momentum equations are written in dimensionless form as

$$(\nabla \cdot v) = 0 \tag{5.4}$$

$$-\beta \nabla^2 v + [\nabla \cdot \tau_p] + \nabla p + \frac{\Delta p}{L} = 0 \tag{5.5}$$

where p denotes the periodic part of the pressure field. The total pressure is the superposition of p, an arbitrary datum pressure p_0, and the non-periodic pressure drop Δp across the computational domain, that is, $p_{total} = p_0 - (\Delta p/L)x + p$. Pressure is scaled in the same way as the stress tensor.

Because of the symmetry in the geometry, it is necessary to solve the flow only in the unit cell shown as the shaded area in Fig. 5-1. There are three types of boundaries in the computational domain. The no slip boundaries are given by the cylinder surface and the channel wall; the periodic boundaries are the two vertical lines; the symmetry line connects the rear and front stagnation points of adjacent cylinders. We fix $H = 2$ and consider variable cylinder spacing. Flow around a single cylinder in a channel corresponds to $L = \infty$; $L = 6$ is used to study cylinders that are placed far apart; and $L = 2.5$ is used to study a closely spaced array where flow is separated between the cylinders. We find it best in computing results for the single cylinder to replace the periodic boundary conditions by specifying the velocity field at $x = -15$ (scaled by R_c) to be that of fully developed, rectilinear flow in a slit and at $x = 15$ to be fully developed. In addition, for the single cylinder viscoelastic calculations we specify values of the normal stress components at $x = -15$ according to the slit flow solution. For We > 1, viscoelastic calculations show that the fully developed channel flow cannot be obtained without extending the computational domain further to $x = \pm 25$. The computed Newtonian solutions for the cases of $x = \pm 25$ and $x = \pm 15$ are identical. For values of L as large as 30, we find that the imposition of periodicity at the inflow and outflow boundaries of the computational domain leads to a 5% discrepancy with results obtained by specifying the inlet and outlet velocity as that corresponding to the creeping Newtonian flow in a channel. The flow is assumed to be inertialess, because in typical experiments the Reynolds number is of order 10^{-3}.

5.2.3 Constitutive equations

The three constitutive equations used in this chapter are all obtained from a kinetic theory treatment of the rheology of dilute polymer solutions in which the macromolecules are modeled

as dumbbells consisting of two point-mass beads connected by a spring and immersed in an incompressible Newtonian solvent with viscosity η_s. Here we summarize the distinguishing features of the Giesekus, FENE-P, and the Chilcott-Rallison models. A more complete treatment of the kinetic theory can be found in Bird, et al. (1987).

In the dumbbell model, the intramolecular force is represented by a connecting spring whose force $\boldsymbol{F}^{(c)}$ is given in terms of the dumbbell end-to-end vector $\boldsymbol{Q}$ by $\boldsymbol{F}^{(c)} = H_0 h(Q)\boldsymbol{Q}$, where H_0 is a characteristic spring constant, and $h(Q)$ is a dimensionless spring modulus which is a function of the separation Q between the two beads. The simplest type of spring is Hookean, with constant spring modulus $h(Q) = 1$. For this spring expression, the intramolecular force is directly proportional to the length of the dumbbell; and, as a result, the macromolecules can be stretched indefinitely as indicated in Fig. 5-2. A more realistic description of the intramolecular force incorporates the finite extensibility of the polymer. A convenient empiricism for the modulus of a finitely extendable nonlinear elastic (FENE) dumbbell is given by the Warner approximation as follows

$$h(Q) = \frac{1}{1 - Q^2/Q_0^2} \tag{5.6}$$

where the maximum dumbbell length is given by Q_0. In the limit $Q_0 \to \infty$, the FENE spring reduces to the Hookean spring. The Giesekus model assumes that the spring is Hookean, whereas the FENE-P and CR models use the Warner expression in Eq. 5.6.

The hydrodynamic drag experienced by a bead in the dumbbell as it moves relative to the solution is given by Stokes' law. In the Giesekus model, the drag force is not assumed to be colinear with the relative velocity between the bead and the solution, so that the inverse of the friction tensor is written as

$$\boldsymbol{\zeta}^{-1} = \frac{1}{\zeta}(\boldsymbol{\delta} - \alpha\boldsymbol{\tau}_p) \tag{5.7}$$

The coefficient α is the mobility factor (Bird et al., 1987), and $\boldsymbol{\tau}_p$ is used to express the dependence of the local resistance on the average conformation of the polymers (cf. Eq. 5.13). The FENE-P and CR models take the drag force on the beads to be isotropic, which corresponds to setting $\alpha = 0$ in Eq. 5.7.

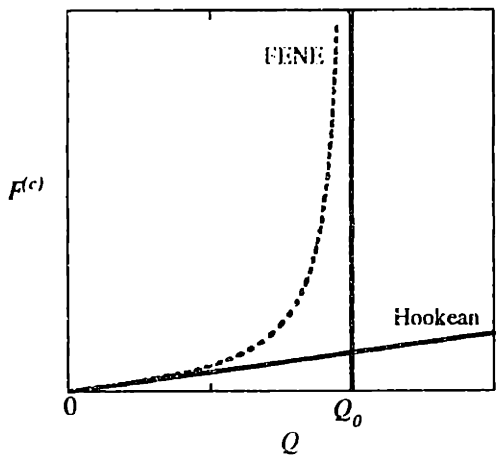

Figure 5-2 Interbead spring force $F^{(c)}$ for Hookean and FENE springs.

The average configuration of the polymer molecules in solution is described by the configuration tensor $\langle \boldsymbol{QQ} \rangle$, where the symbol $\langle \cdot \rangle$ denotes a configuration space average. From this point on, $\boldsymbol{Q}$ is made dimensionless by using the equilibrium length of the dumbbell, $(\langle Q^2 \rangle_{eq})^{1/2}$. For the Giesekus and CR models, $\langle Q^2 \rangle_{eq} = kT/H_0$, and for the FENE-P model $\langle Q^2 \rangle_{eq} = (kT/H_0)(b/(b+5))$. This method of scaling $\boldsymbol{Q}$ means that $\mathrm{tr}\langle \boldsymbol{QQ} \rangle_{eq} = 3$ for all three models. Here the FENE parameter b is related to the ratio of the maximum to equilibrium squared length of the dumbbell, $b \equiv H_0 Q_0^2/kT$. The time rate of change of the distribution function used to compute this average is described by the diffusion equation, whose second moment with respect to $\boldsymbol{Q}$ gives an evolution equation for the configuration tensor. The Giesekus model yieids an exact, closed form evolution equation for $\langle \boldsymbol{QQ} \rangle$. In dimensionless form this is

$$We\langle \boldsymbol{QQ} \rangle_{(1)} + \{\langle \boldsymbol{QQ} \rangle - \boldsymbol{\delta}\} + \alpha\{\langle \boldsymbol{QQ} \rangle - \boldsymbol{\delta}\} \bullet \{\langle \boldsymbol{QQ} \rangle - \boldsymbol{\delta}\} = \boldsymbol{0} \tag{5.8}$$

where the subscript $_{(1)}$ denotes the upper convected derivative. The time constant used in forming the Weissenberg number for each of the models is $\lambda_H \equiv \zeta/(4H_0)$. For the FENE dumbbell models, Peterlin's approximation is introduced by approximating the average of $\langle h(Q^2)\, \boldsymbol{QQ} \rangle$ by the product of the two averages, $h(\langle Q^2 \rangle)$ and $\langle \boldsymbol{QQ} \rangle$, and this leads to the (dimensionless) FENE-P model

$$We\langle \boldsymbol{QQ} \rangle_{(1)} + h(\langle Q^2 \rangle)\langle \boldsymbol{QQ} \rangle + \varepsilon Q_0^2 \boldsymbol{\delta} - \boldsymbol{\delta} = \boldsymbol{0} \tag{5.9}$$

An extra isotropic term containing a constant $\varepsilon = 2/b(b+2)$ is added to ensure that the $\mathrm{tr}\langle \boldsymbol{QQ} \rangle = 3$ at equilibrium (Bird et al., 1987). In addition to Peterlin's approximation, the CR model further

assumes that the dimensionless modulus multiplies both the $\langle \boldsymbol{QQ} \rangle$ and isotropic terms, so that the evolution of $\langle \boldsymbol{QQ} \rangle$ is simply described by

$$We \langle \boldsymbol{QQ} \rangle_{(1)} + h(\langle Q^2 \rangle) \{ \langle \boldsymbol{QQ} \rangle - \boldsymbol{\delta} \} = \boldsymbol{0} \tag{5.10}$$

Note that the ε term need not be added to this equation in order for it to simplify correctly at equilibrium.

The dimensional polymer contribution to the stress tensor $\boldsymbol{\tau}_p$ is related to the molecular configuration by the Kramers equation

$$\boldsymbol{\tau}_p = -\{ nH_0 \langle Q^2 \rangle_{eq} \langle h(Q^2) \boldsymbol{QQ} \rangle + nkT \boldsymbol{\delta} \} \tag{5.11}$$

The polymeric stress tensor $\boldsymbol{\tau}_p$ is non-dimensionalized with respect to $\eta_0 \langle v \rangle / R_c$ where η_0 is the zero-shear-rate solution viscosity and $R_c / \langle v \rangle$ is the characteristic time scale of the flow. The zero-shear-rate solution viscosity is composed of two parts $\eta_0 = \eta_s + \eta_p$. η_S is the Newtonian solvent viscosity. η_p is the polymer contribution to the viscosity and is given by $\eta_p = \lambda_H nkT\, B$. $B = 1$ for the Giesekus and CR models, and $B = b/(b+5)$ for the FENE-P model. The dimensionless polymeric stress $\boldsymbol{\tau}_p$ now becomes

$$\boldsymbol{\tau}_p = -\frac{(1-\beta)}{We} \frac{1}{B} \{ B \langle h(\langle Q^2 \rangle) \boldsymbol{QQ} \rangle - \boldsymbol{\delta} \} \tag{5.12}$$

For the Giesekus model, $\boldsymbol{\tau}_p$ depends only on the second moment of the distribution function, and it can be written exactly in terms of $\langle \boldsymbol{QQ} \rangle$ as

$$\boldsymbol{\tau}_p = -\frac{(1-\beta)}{We} \{ \langle \boldsymbol{QQ} \rangle - \boldsymbol{\delta} \} \tag{5.13}$$

The FENE-P and CR models use the Peterlin approximation for the average $\langle h(Q^2)\, \boldsymbol{QQ} \rangle$. For the FENE-P model this leads to the approximate expression for the stress tensor

$$\boldsymbol{\tau}_p = -\frac{(1-\beta)}{We} \frac{1}{B} \{ Bh(\langle Q^2 \rangle) \langle \boldsymbol{QQ} \rangle - (1 - \varepsilon b) \boldsymbol{\delta} \} \tag{5.14}$$

In the CR model it is further assumed that h multiplies the difference $\langle \boldsymbol{QQ} \rangle - \boldsymbol{\delta}$, so that the final approximate $\boldsymbol{\tau}_p$ for the CR model is

$$\boldsymbol{\tau}_p = -\frac{(1-\beta)}{We} \{ h(\langle Q^2 \rangle)(\langle \boldsymbol{QQ} \rangle - \boldsymbol{\delta}) \} \tag{5.15}$$

5.2.4 Rheological Properties for Giesekus, FENE-P, and Chilcott-Rallison Models

The predictions of the three constitutive equations are presented for viscometric and steady planar elongational flows with $\beta = 0.59$ to simulate the 0.31 wt% PIB Boger fluid that McKinley et al. (1993) used in a single cylinder flow experiment. The parameters α and Q_0 are selected so that identical planar elongational flow properties are predicted by all three models.

Steady Simple Shear Flow

The viscometric properties are shown in Fig. 5-3 as functions of dimensionless shear rate $\lambda\dot{\gamma}$. The most striking differences between the models are that the Chilcott-Rallison model predicts a constant viscosity, whereas both the Giesekus and FENE-P models show shear thinning. Also the Giesekus model predicts a non-zero negative second normal stress coefficient Ψ_2, whereas Ψ_2 vanishes for both the FENE-P and CR models. At high shear rates, η for the two shear thinning models asymptotically approaches the solvent viscosity, or in dimensionless form β. All three models predict shear thinning in the first normal stress coefficient Ψ_1, with the Giesekus model shear thinning the most rapidly, followed by the FENE-P and CR models. The difference in the rate of shear thinning of Ψ_1 is reflected by the high shear rate asymptotic behavior of the models: for $\lambda\dot{\gamma} \gg 1$, $\Psi_1 \propto \dot{\gamma}^{-3/2}$ for the Giesekus model, $\Psi_1 \propto \dot{\gamma}^{-4/3}$ for the FENE-P model, and $\Psi_1 \propto \dot{\gamma}^{-1}$ for the CR model. All the models predict a monotonic increase in the molecular extension $\langle Q^2 \rangle$ with increasing $\dot{\gamma}$. The onset of significant molecular extension appears to occur at $\lambda\dot{\gamma} \approx 1$ for both the Giesekus and CR models, and this onset is delayed by about an order of magnitude in $\lambda\dot{\gamma}$ for the FENE-P model. For the CR and FENE-P models, the maximum extension is bounded by Q_0, whereas the molecular extension continues to increase indefinitely with increasing shear rate for the Giesekus model. Over about three decades in shear rate ($1 < \lambda\dot{\gamma} < 10^3$) the FENE-P model predicts much smaller molecular extension at a given shear rate than the CR model.

Steady planar elongational flow

Close to the symmetry plane, the flow in the wake of a cylinder is approximately planar extension. Although the flow field is not homogeneous in the vicinity of the rear stagnation point, it is interesting to contrast the material properties under simple steady planar extensional flow conditions. For a planar elongational flow, $v_x = \dot{\varepsilon}x$, $v_y = -\dot{\varepsilon}y$, and $v_z = 0$, where $\dot{\varepsilon}$ is the elongation rate,

the planar elongational viscosity is defined as $\bar{\eta}_1 \equiv -(\tau_{xx} - \tau_{yy})/\dot{\epsilon}$. With appropriate choices of Q_0 and α, the three models yield essentially identical curves for $\bar{\eta}_1/4(\eta_0 - \eta_s)$ versus $\lambda\dot{\epsilon}$, as shown in Fig. 5-4. The microstructural behavior of the three models can be compared by plotting $\langle Q^2 \rangle$ versus $\lambda\dot{\epsilon}$. At $\lambda\dot{\epsilon} < 1/2$ identical dumbbell lengths are predicted by all the models, i.e, the nonlinear part of the FENE spring expression is unimportant at low elongation rates. All three models show a rapid rise in the elongational viscosity and the molecular extension at $\lambda\dot{\epsilon} \approx 1/2$. However, at higher $\lambda\dot{\epsilon}$ the average dumbbell extension in the CR and FENE-P models asymptotes to the maximum extensibility ${Q_0}^2$, whereas $\langle Q^2 \rangle$ predicted by the Giesekus model continues to increase approximately linearly. The saturation in $\bar{\eta}_1$ at high elongation rates for the Giesekus model is due to the anisotropic drag experienced by the dumbbell: as the dumbbells become highly extended the drag coefficient on the beads in the principal direction of stretching decreases.

5.3 Computational methods

We employ the Elastic Viscous Split-Stress Gradient (EVSS-G) and Discrete EVSS-G (DEVSS-G) finite element methods appropriate for simulating viscoelastic flows governed by differential constitutive equations. The EVSS-G finite element method has been described in detail in Brown et al. (1993) and the DEVSS-G finite element method is a variation of the Discrete EVSS method of Guénette et al. (1995) that is described by Szady et al. (1996). Thus, we only report the main features of the two methods here. The EVSS-G method is used for the Giesekus and CR models, and the DEVSS-G method is used for the FENE-P and CR models. In order to guarantee the accuracy of our results, non-uniform, locally refined meshes are used to resolve rapid changes in stress and velocity fields.

The flow domain Ω is subdivided into a set of quadrilateral elements $\{\Omega_i\}$ on which the equations of motion are discretized by using classical finite element methods. Low order Lagrangian interpolation functions are used to form approximations for the velocity $\boldsymbol{v}^h(\Omega)$, pressure $p^h(\Omega)$, elastic stress $\boldsymbol{\Sigma}^h(\Omega)$ (or $\boldsymbol{\tau}_p^h(\Omega)$), and velocity gradient $\boldsymbol{G}^h(\Omega)$, The superscript h denotes the dependence of the approximation on the finite element mesh. The individual basis functions are denoted as $\Phi_j^v \subset \boldsymbol{v}^h(\Omega)$, $\Psi_j^v \subset p^h(\Omega)$, $\Psi_j^S \subset \boldsymbol{\Sigma}^h(\Omega)$ (or $\boldsymbol{\tau}_p^h$) and $\Psi_j^G \subset \boldsymbol{G}^h(\Omega)$, where Φ_j represents a biquadratic basis function and Ψ_j denotes a bilinear basis function. All the basis functions are at least piecewise continuous in order for them to have square integrable first derivatives.

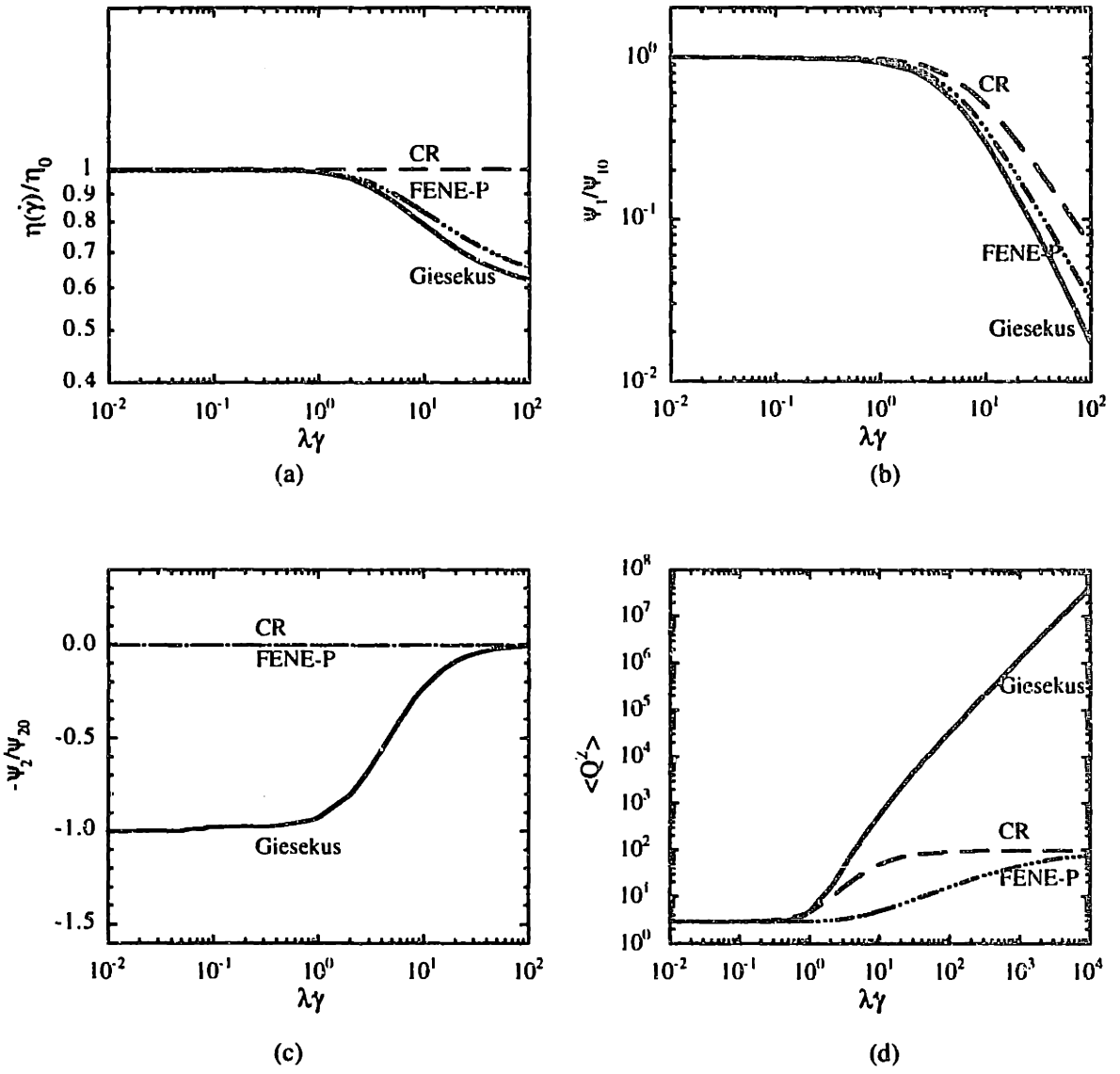

Figure 5-3 Viscometric properties for the Giesekus (———), FENE-P (– · · –), and CR (— —) models with model parameters of $\beta = 0.59$, $\alpha = 10^{-2}$, and $Q_0 = 10$. (a) Viscosity; the dimensionless viscosity for both the Giesekus and FENE-P models approaches 0.59 at infinite shear rate. (b) First normal stress coefficient. (c) Second normal stress coefficient. (d) Average squared molecular extension.

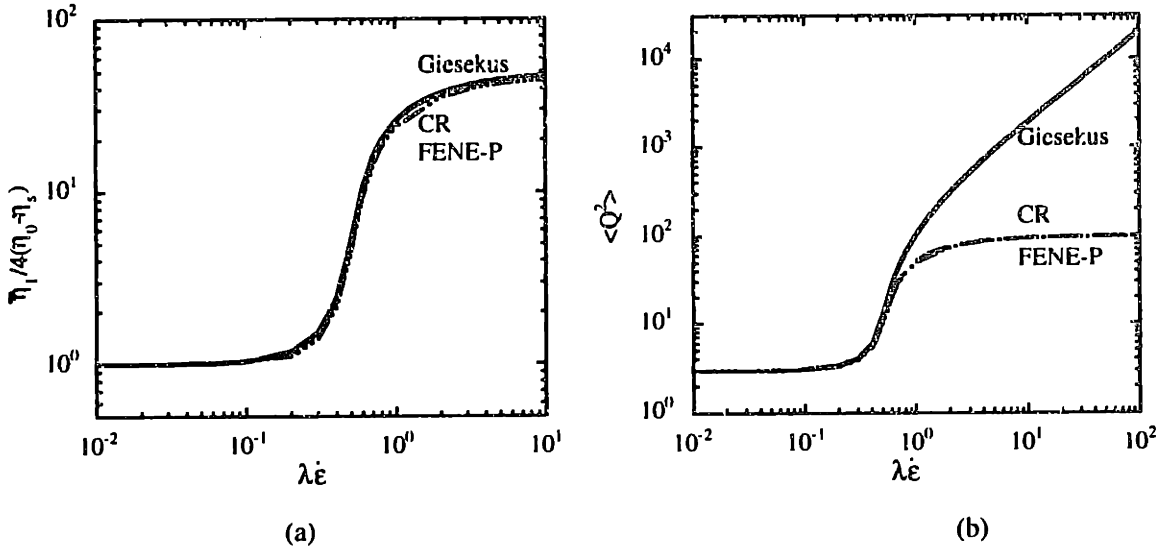

Figure 5-4 Planar elongational flow behavior for the Giesekus (———), FENE-P (– · · –), and CR (— —) models with model parameters of $\beta = 0.59$, $\alpha = 10^{-2}$, and $Q_0 = 10$. (a) Dimensionless elongational viscosity $\bar{\eta}_1$. (b) Mean squared molecular extension as a function of elongation rate $\dot{\varepsilon}$.

In the EVSS-G formulation, the elliptic nature of the momentum equation is ensured by introducing the elastic stress tensor $\Sigma \equiv \tau_p + (1-\beta)\dot{\gamma}$ into the equation of motion. The conservation equations Eqs. 5.4 and 5.5 must be solved along with the constitutive equations Eqs. 5.8-5.14. We use the Streamline Upwind Petrov-Galerkin (SUPG) weighted residual method for solving the hyperbolic constitutive equation, which is written in terms of Σ.

The DEVSS-G method, on the other hand, introduces the elliptic stabilization term only to the discrete version of the momentum equation, and the constitutive equation is solved directly in terms of the polymer contribution to the stress τ_p or molecular configuration $\langle QQ \rangle$. This is achieved by modifying the weak form of the momentum equation, Eq. 5.5, and integrating the stress, the velocity gradient approximation G, and the pressure terms by parts:

$$\int_{\Omega} (\{-p\delta + \dot{\gamma} - \tau_p - (1-\beta)(G+G^{\dagger})\} : \nabla\Phi_i^v \delta_k) d\Omega = 0 \tag{5.16}$$

As in the EVSS-G formulation, the constitutive equation for either stress or molecular configuration is discretized by using the SUPG method.

The set of nonlinear algebraic equations arising from the finite element discretization is solved by a Newton-Raphson scheme coupled with first order continuation in We to allow the calculation to proceed to high We. Simulations are carried out on either a Cray C90 supercomputer or an HP

735 workstation. Each Newton iteration on a typical mesh with 43,462 unknowns, such as M4 shown in Fig. 5-5, takes 13 cpu minutes on the Cray or 250 minutes on the HP. The number of Newton iterations required for a converged solution depends strongly on the step size and the initial guess.

The convergence of the method is based on the L_1 norm, $\sum|\Delta\omega_i| \le 10^{-5}$, where $|\Delta\omega_i| = |\omega_i^{k+1} - \omega_i^k|$, with ω_i^k representing the values of unknowns v^h, p^h, Σ^h, G^h at the kth iteration. The linear system of equations at each Newton iteration is solved by direct LU factorization of the stiffness matrix by using a frontal solver, with the order of element assembly found using a standard bandwidth minimization method (Hood, 1976; 1977).

Local mesh refinement is incorporated in the regions of high stress and velocity gradients and is implemented with an element splitting technique developed by Tsiveriotis and Brown (1993). Refinement from a coarse to a fine grid is achieved by one-to-two element transitions. As an example, we present in Fig. 5-5 a sequence of meshes that were used in calculations of the widely spaced cylinder array with $L = 6$ and $H = 2$.

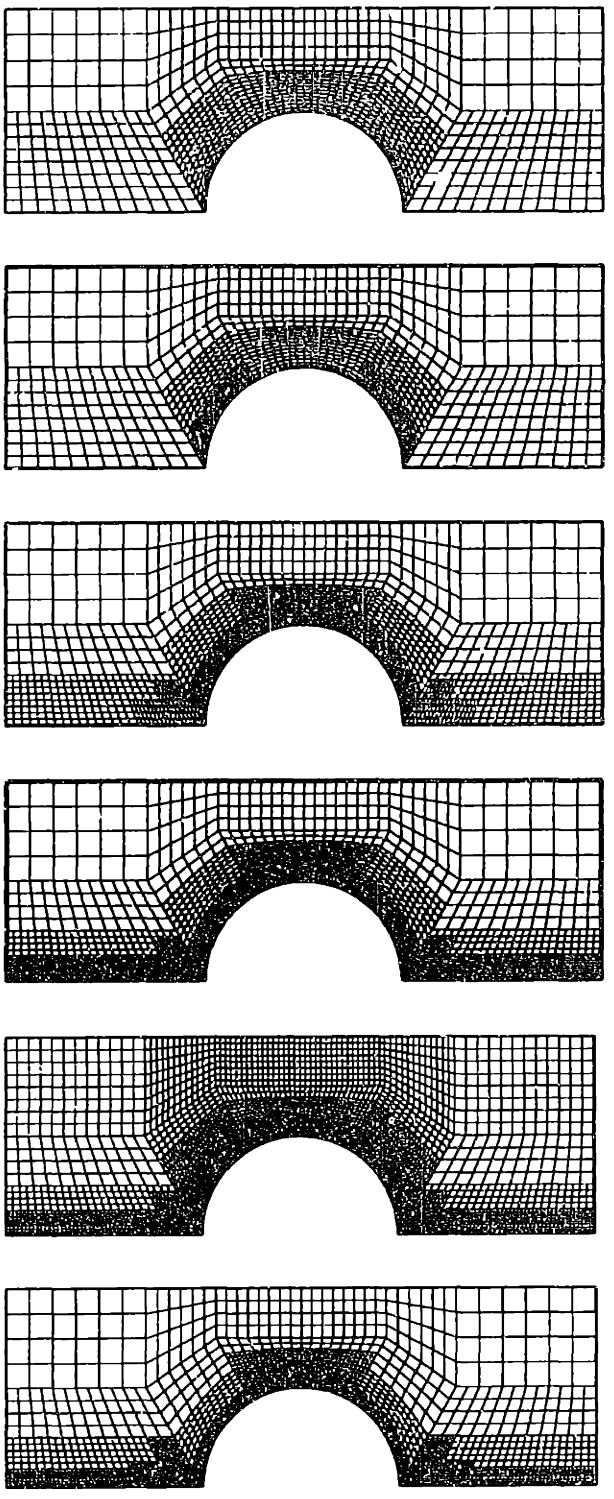

Figure 5-5 Finite element meshes used for calculations of viscoelastic flow around a linear, periodic array of cylinders with $L = 6$, $H = 2$.

5.4 Numerical results

In this section, results for the Giesekus, FENE-P, and CR models are presented in sequence for flow around a single cylinder and for a linear, periodic array of cylinders with both wide and close spacing between the cylinders. It is our observation that the normal stresses and average molecular extension are much more sensitive to changes in We than, for example, the kinematics of the flow, which deviate only moderately from the Newtonian problem. Hence, throughout the results section, we focus on results for normal stress and molecular extension.

5.4.1 Flow around a single cylinder (L = ∞)

Newtonian fluid

The contours of the stream function, and the normal and shear stress components for a Newtonian fluid are shown in Fig. 5-6. The expected symmetry about the plane $x = 0$ is found for the axial velocity v_x and shear stress τ_{xy}, and antisymmetry is observed about $x = 0$ for v_y and τ_{xx}. Fluid is accelerated as it moves toward the gap region at $x = 0$. The presence of the channel wall causes pronounced shearing in the gap region resulting in a maximum and minimum in shear stress on the channel wall and surface of the cylinder, respectively, in the gap region. The maximum and minimum normal stresses τ_{xx} occur at upstream and downstream points on the cylinder surface, respectively. For a Newtonian fluid, continuity requires that $\tau_{xx} = -\tau_{yy}$.

Viscoelastic models

Viscoelastic calculations for flow around a single cylinder with $H = 2$ in a domain $x = [-15, 15]$ converge to We = 1.0; for calculations with larger values of We the computational domain must be extended. As the Weissenberg number is increased, elastic effects result in a progressive modification of the velocity field around the cylinder. The dimensionless centerline velocity shown in Fig. 5-7 demonstrates this effect. The velocity profiles upstream of the cylinder superpose when normalized with the average velocity across the channel, $\langle v \rangle$ and are not affected as We is increased to unity.

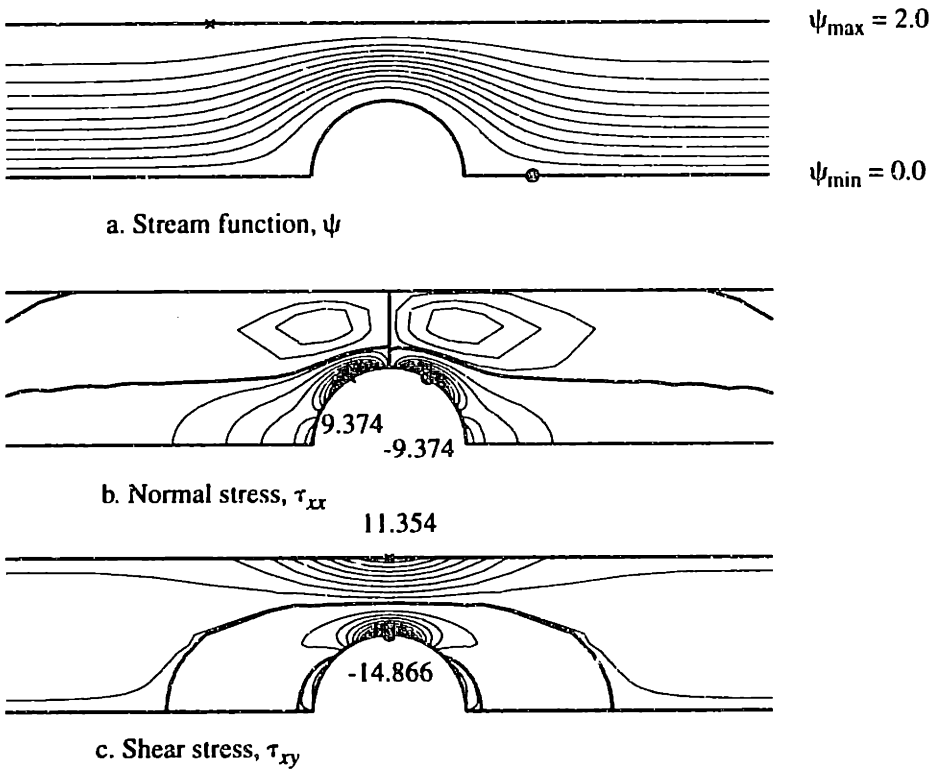

Figure 5-6 Solution fields for Newtonian flow around a single cylinder in a channel with gap $H = 2$. (a) Ten equally spaced contours are shown for the streamlines. Twenty equally spaced contours between the minimum and maximum values are shown for (b) the normal stress τ_{xx} and (c) the shear stress τ_{xy}. The region shown is for $x \in [-5, 5]$ and $y \in [0, 2]$. In each plot the maximum and minimum locations are denoted by × and ⊜, respectively.

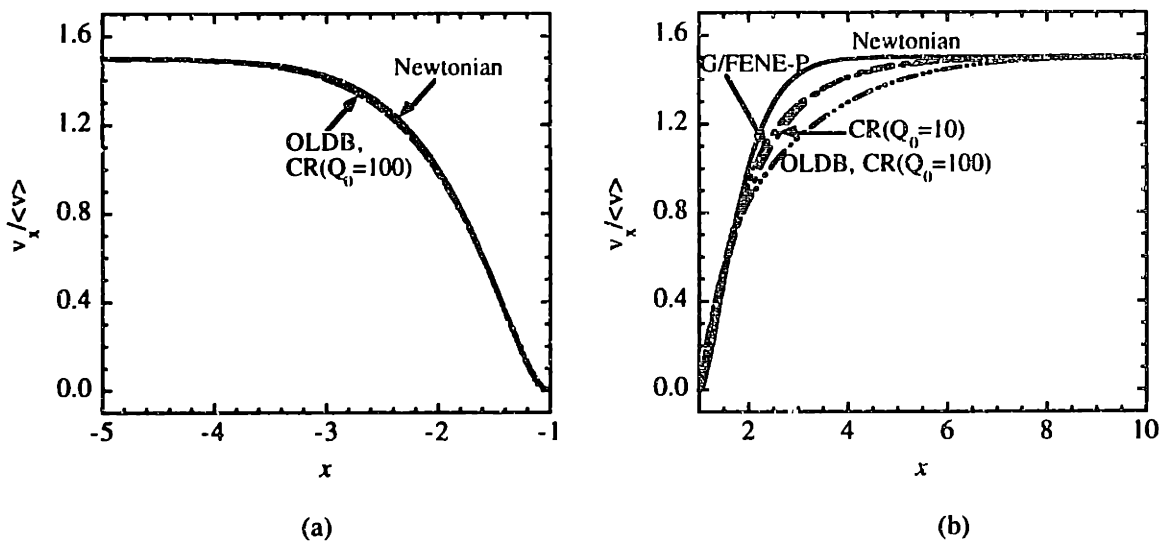

Figure 5-7 Axial velocity v_x along the symmetry line for flow around a single cylinder in a channel with $H = 2$ (a) upstream and (b) downstream of the cylinder. Results are for We = 1.0.

Very close to the rear stagnation point $x \leq 1.5$, the velocity profiles for the three viscoelastic models superpose, and all show a slight increase in strain rate compared to Newtonian flow in this region. For $x \geq 1.5$ the polymer solutions exhibit a pronounced downstream shift in the velocity relative to Stokes flow. Similar changes in the velocity field are observed in the experiments of McKinley *et al.* (1993). As a result of this downstream shifting at We = 1.0, the viscoelastic models predict that the velocity of the fluid moving away from the cylinder recovers more slowly to its ultimate value $v_x = 1.5$. It is interesting that the degree of downstream shift for $x > 1.5$ appears to correlate with a shear-rate-dependent time constant defined by $\lambda(\dot{\gamma}) \equiv \Psi_1(\dot{\gamma})/2\eta(\dot{\gamma})$. The Newtonian fluid has a time constant of zero. If we ignore the shear thinning in viscosity, which is less than a factor of two for the value of β used here, then at fixed $\dot{\gamma}$, the relaxation times of the models varies like Ψ_1. If increasing memory (λ) causes the downstream shift, then we should see the sequence Newtonian, Giesekus, FENE-P, CR according to the relative Ψ_1 in Fig. 5-3. This is followed in Fig. 5-7, though the Giesekus and FENE-P models almost superpose. (Note that η is somewhat higher for FENE-P than Giesekus, however). To explore this trend further we performed calculations for the CR model with $Q_0 = 100$ and for the Oldroyd-B model (CR as $Q_0 \to \infty$). Since Ψ_1 increases with Q_0 at fixed $\dot{\gamma}$, we expect an ever greater downstream shift for these models, as is born out in Fig. 5-7.

As indicated in Fig. 5-8, the axial stress, τ_{pxx}, predicted by all three models is qualitatively similar. The CR model predicts the highest negative tensile stress, followed by the Giesekus and FENE-P as would be expected from the Ψ_1 results in Fig. 5-3. Far upstream and downstream of the cylinder, the flow is approximately Newtonian ($\tau_{pxx} \approx 0$ and $\langle Q^2 \rangle \approx 3$).

There are four regions where polymer molecules are highly extended. Polymers first become deformed in the compressive region ($\tau_{pxx} > 0$) upstream of the cylinder, where the flow is nearly planar elongation with a negative elongation rate in the x-direction. Close to the front stagnation point, the flow is slow enough that the macromolecules have sufficient residence time to become highly stretched. The second and third regions of large extension are found adjacent to the surfaces of the cylinder and channel. The no slip boundary condition on these solid surfaces leads to large shear rates and stresses, and the maximum $\langle Q^2 \rangle$ and minimum τ_{pxx} are on the surface of the cylinder where the shear rate is a maximum. Away from the solid surfaces, the shear rate drops and $\langle Q^2 \rangle$ decreases. Finally, in the wake of the cylinder, large molecular extension is observed along the stagnation streamline where polymer molecules that are stretched by the planar elonga-

tional flow near the rear stagnation point are advected far downstream thereby forming a "birefringent strand" before relaxing back to equilibrium. At both the front and rear stagnation points, all components of ∇v and v vanish, and polymer molecules are at equilibrium ($\langle Q^2 \rangle = 3$).

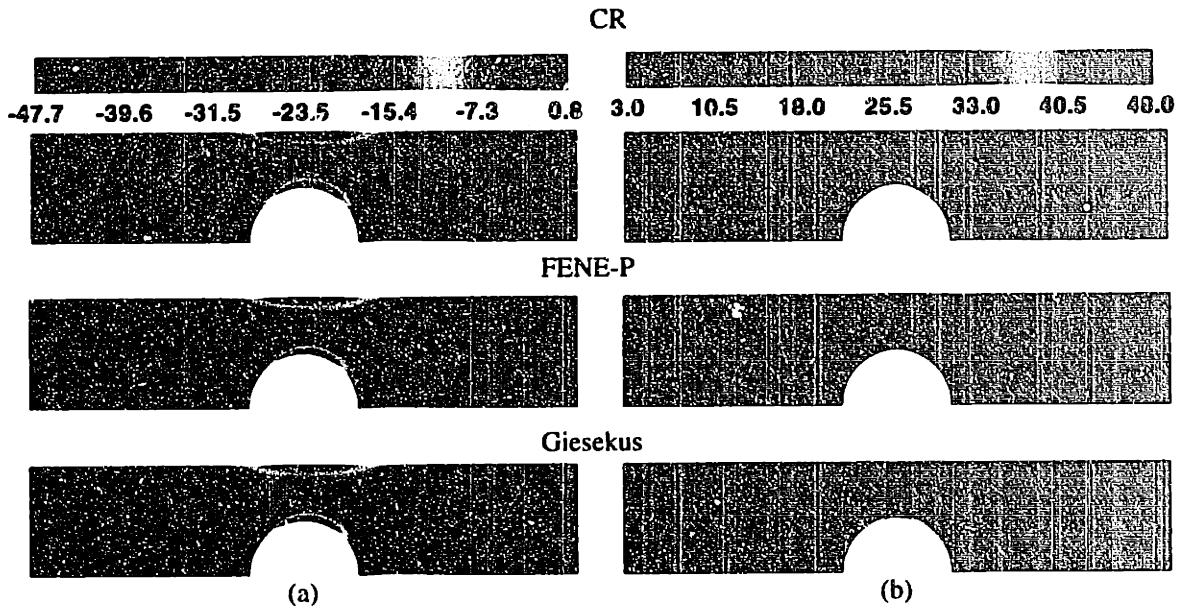

Figure 5-8 Comparisons of (a) axial normal stress τ_{pxx} and (b) average molecular extension for flow around a single cylinder ($H = 2$) at We = 0.5 for the Chilcott-Rallison, FENE-P, and Giesekus models.

All three constitutive models predict that the birefringent strand in the wake extends about five radii downstream of the cylinder for We = 1.0. This is significantly different from recent experimental findings by Byars (1995) where large extension remains over fifteen radii at We = 0.54. However, qualitative agreement in the response of $\langle Q^2 \rangle$ is predicted here. As We increases, the birefringent strand grows in thickness, downstream extent, and intensity, as shown in Fig. 5-9. Extending the computational domain further has no effect on the region of highly extended polymers in the wake. Moreover, the predicted stress fields are in qualitative agreement with the flow induced birefringence measurements on shear thinning, concentrated PIB/C14 solution flow around a cylinder (Baaijens *et al.*, 1995). The measured stresses in these experiments became fully developed within six radii for $H = 2$ and We up to 8.0.

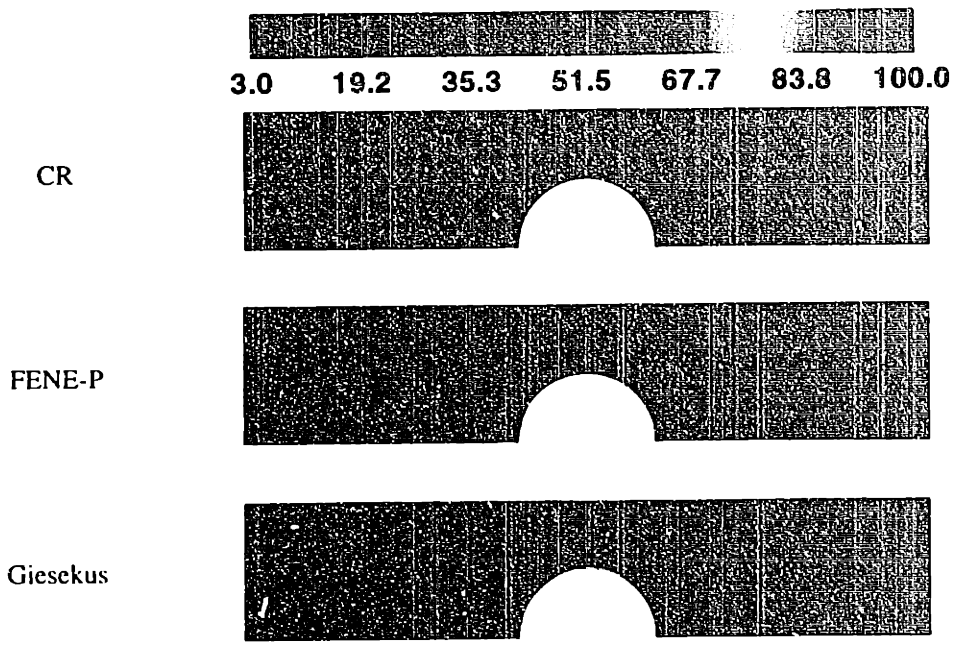

Figure 5-9 Comparison of the average molecular extension at We =1.0 for viscoelastic flow around a single cylinder with $H = 2$.

5.4.2 Cylinders spaced far apart (L = 6.0)

Newtonian fluid

When the cylinders are placed far apart, with $L \geq 6$, the velocity across the periodic plane midway between the cylinders approaches 95% of the undisturbed fully developed channel flow. As shown in Fig. 5-10, the maximum and minimum normal and shear stresses τ_{xx} and τ_{xy} are comparable to that for a single cylinder. Thus, the presence of neighboring cylinders does not affect appreciably the Stokes flow kinematics.

The contribution per cylinder Δp_c of the cylinders to the pressure drop shows the influence of neighboring cylinders more sensitively than the kinematics. Although there are only subtle changes in the velocity field in going from the single cylinder ($L = \infty$) to the periodic array ($L = 6$), Δp_c decreases from 181.64 to 52.83. This sensitivity of Δp_c to the presence of other cylinders is consistent with the observation in section 2.2 that a very large value of L (> 30) is necessary to

compute a drag force on the cylinder that is identical to that on a single cylinder in an infinite channel.

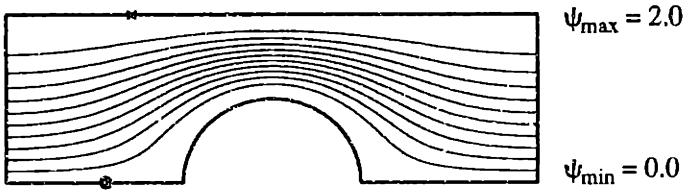

a. Stream function, ψ

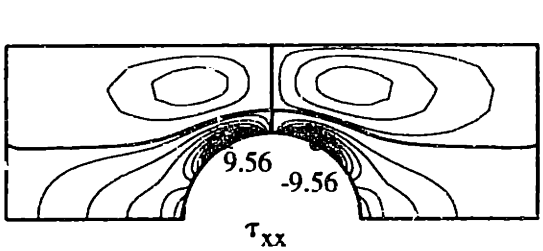

b. Normal stress, τ_{xx}

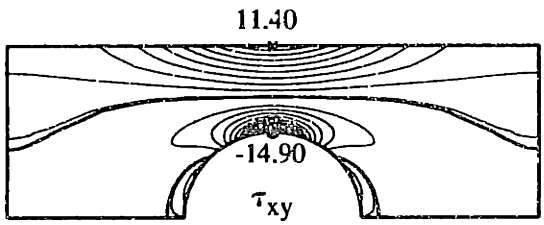

c. Shear stress, τ_{xy}

Figure 5-10 Solution fields for Newtonian fluid flow around a periodic array of cylinders with $L = 6$ and $H = 2$. (a) Ten equally spaced streamlines; Twenty equally spaced contours between the minimum and maximum values are shown. (b) and (c) are the components of the extra stress τ_{xx} and τ_{xy}.

CR model

Calculations for the CR model can be performed for We ≤ 1.0 with mesh M4 before the configuration tensor loses positive definiteness. Although a more refined mesh such as M6 allows the calculations to continue to We ≈ 1.2 without the loss of positive definiteness of the $\langle \underline{Q}\underline{Q} \rangle$ tensor, the violation of the positive definiteness of $\langle \underline{Q}\underline{Q} \rangle$ for the CR model does not prevent the continuation of the calculation to a higher We. Moreover, the loss of positive definiteness in $\langle \underline{Q}\underline{Q} \rangle$ does not compromise the quality of the overall solution. The regions where $\langle Q^2 \rangle < 0$ are highly localized near the front and rear stagnation points as well as midway between the cylinder and wall where the mesh is inadequately refined. Fig. 5-11 is a plot of $\langle Q^2 \rangle$ across a few elements in mesh M4. Upon refining the mesh in the gap between the cylinder and the channel wall, the positive definiteness of the $\langle \underline{Q}\underline{Q} \rangle$ tensor is regained. In addition, the region of negative $\langle Q^2 \rangle$ in the coarser mesh becomes a region of approximately equilibrium dumbbell length in the more refined mesh. One important observation in comparing the results between the two meshes is that global solution fields for molecular extension and stresses are unchanged. Thus, the local, aphysical dumbbell

length is solely due to the corresponding inadequate local mesh refinement in regions where the dumbbells are near their equilibrium configuration, and this problem only occurs close to the two stagnation points and in the gap between the cylinder and the channel wall.

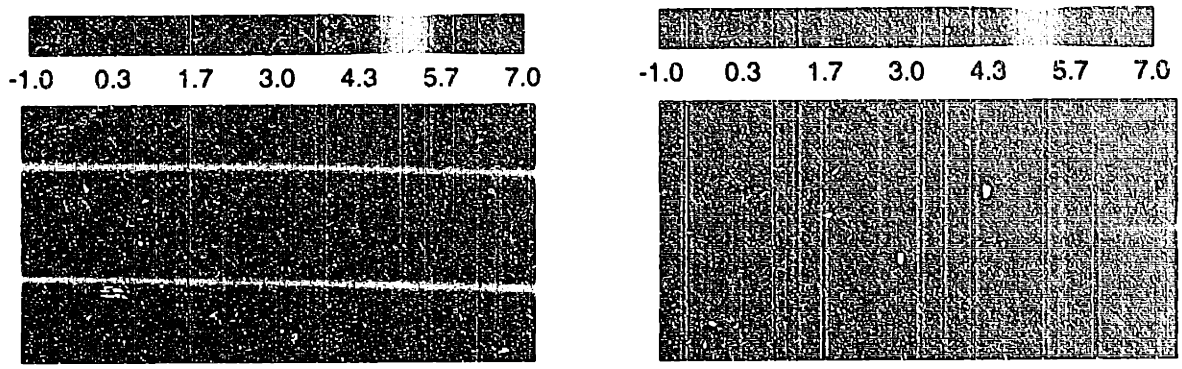

a. M4 b. M5

Figure 5-11 Molecular extension characterized by $\langle Q^2 \rangle$ across a couple of elements midway between the cylinder and wall for mesh M4 and the more refined mesh M5. The region shown is $x \in [0, 0.2]$ and $y \in [1.45, 1.55]$.

The effect of increasing We on the velocity field is shown in Fig. 5-12. As observed for the isolated cylinder in Fig. 5-7, the axial velocity on the centerline immediately next to the downstream stagnation point increases with increasing We, and further away from the cylinder ($x > 1.5$) the axial velocity is shifted downstream and thus decreases relative to the Newtonian solution. The interesting result of the proximity of the cylinders on the velocity field is that this downstream shift which originates behind the rear stagnation point is convected increasingly further downstream as We is increased, so that the velocity upstream of the following cylinder also shows a decrease relative to Stokes flow. In fact for the range of We shown in Fig. 5-12, the centerline axial velocity never recovers to the fully developed slit flow value, so that a cross sectional plot of v_x along the periodic boundary at $x = 3$ shows a local minimum on the centerline.

Stress and molecular extension fields for the CR model at We = 0.7 are shown in Fig. 5-13. At this value of Weissenberg number, the interaction between the polymer and flow field is confined to relatively thin layers adjacent to the solid surfaces in the narrowest part of the gap and in the wake just behind the cylinder. The figure shows clearly that in most of the flow domain, $\tau_p \approx 0$, and the polymer molecules are in their equilibrium configuration, $\langle Q^2 \rangle \approx 3$. However, at the two solid boundaries, the molecules are extended to as much as 40 percent of ${Q_0}^2$ with resulting large increases in the magnitude of τ_{pxx}.

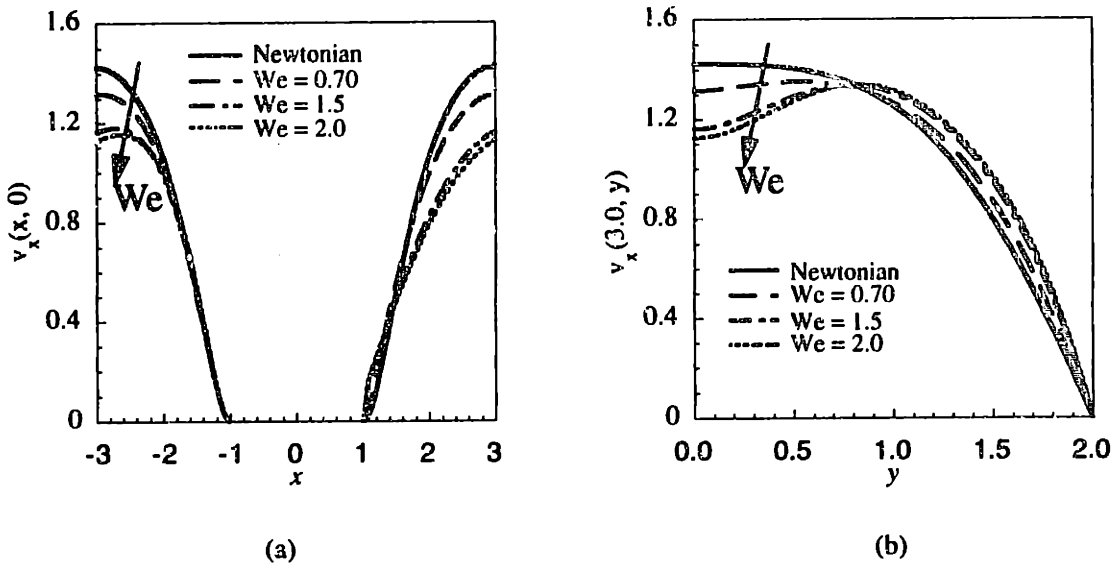

Figure 5-12 Evolution of v_x for the CR model with $Q_0 = 10$ (a) along the symmetry line $y = 0$; (b) v_x across the periodic boundary $x = 3.0$.

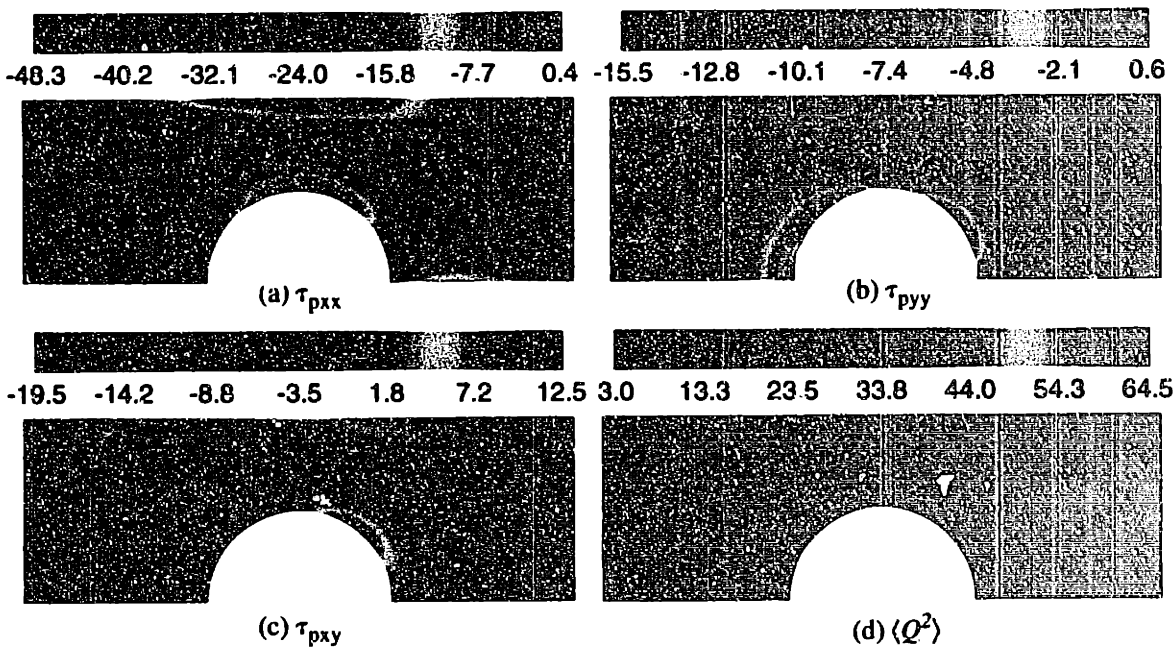

Figure 5-13 Contours of the (a) axial normal stress τ_{pxx}, (b) normal stress τ_{pyy} (c) shear stress τ_{pxy}, and (d) molecular extension $\langle Q^2 \rangle$ for the CR model with $Q_0 = 10$, $\beta = 0.59$ at We = 0.7.

As We increases, the maximum value of $\langle Q^2 \rangle$ increases, and the location of this maximum remains close to the cylinder surface where the shear rate is highest. For We < 1, molecular extension in the wake is noticeably smaller than that of the maximum, but with further increases in We, the region of large molecular extension in the wake intensifies and becomes wider. As noted from

comparing the contours of $\langle Q^2 \rangle$ in Fig. 5-13c and Fig. 5-14b, the importance of memory on polymer stretching becomes significant with increasing We. At We = 2.0, the strong extensional flow ($\dot{\varepsilon} > 0$) in the wake of the cylinder stretches polymers to about $0.65{Q_0}^2$, and this large extension is convected to the upstream of the next cylinder. The compressive flow ($\dot{\varepsilon} < 0$) just upstream of the cylinder also stretches the polymer, but in the y-direction, i.e., perpendicular to the alignment of the polymer approaching from the previous cylinder. The result is that $\langle Q^2 \rangle$ passes through a minimum value of nearly 3 just prior to the compressive flow region. Since $\langle Q^2 \rangle$ is also 3 at the stagnation points, the upstream region of highly stretched molecules is confined to a thin layer upstream of the cylinder. Resolution of this thin layer is difficult computationally, as is capturing the somewhat thicker transition from equilibrium to highly stretched molecules in the downstream region. The maximum $\langle Q^2 \rangle$ is greater in a periodic array of cylinders than that for a single cylinder at any We. In particular, for the CR model at We = 2.0, the maximum $\langle Q^2 \rangle$ decreases from 81 in a periodic array with $L = 6$ (De = 0.33) to 74 for an isolated cylinder with ($L = \infty$, De = 0), and the location of the maximum remains on the cylinder surface near $x = 0$.

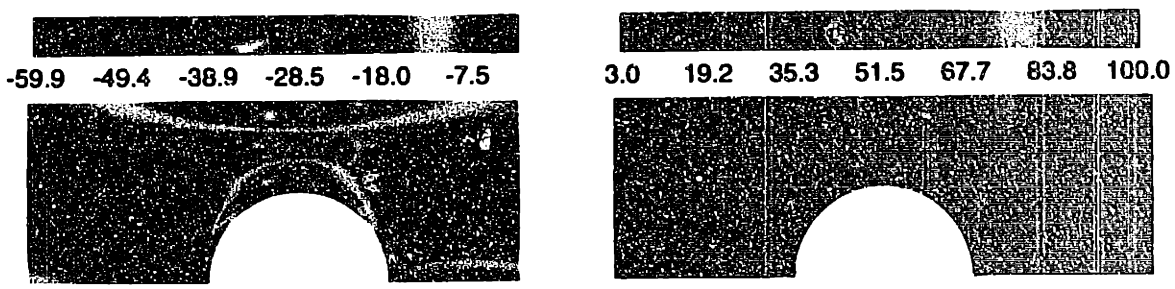

Figure 5-14 Contours of the (a) axial normal stress τ_{pxx} and (b) molecular extension $\langle Q^2 \rangle$ for the CR model with Q_0 = 10 and β = 0.59 at We = 2.0 for a periodic cylinder array with $L = 6$ and $H = 2$.

To examine the details of the molecular stretching and the form of the birefringent strand in the wake region, $\langle Q^2 \rangle$ is plotted along several streamlines close to the symmetry plane in Fig. 5-15. These streamlines are identified by the y-coordinate, y_{-3}, through which they pass at the left periodic boundary of the computational domain, x = -3. The values of y_{-3} range from 0.001 to 0.05. At low We = 0.7, the most significant molecular extension occurs in the narrow gap, with the maximum $\langle Q^2 \rangle$ occurring very near $x = 0$. Much smaller local maxima occur along the streamline closest to the centerline near both the fore and aft stagnation points. The local maximum in the upstream region occurs closer to the cylinder (x = - 1.2) than the corresponding maximum in the

downstream region (x = 1.6). When We is increased to 2.0, although the maximum $\langle Q^2 \rangle$ remains in the gap, the amounts of molecular extension in the wake and in front of the cylinder are comparable to the maximum. In addition as We is increased, it is clear that the region of extended molecules behind the cylinder is stretched axially, whereas the corresponding region upstream is compressed. The variation of $\langle Q^2 \rangle$ in the cross-stream direction for a fixed x-location is illustrated by the plot of $\langle Q^2 \rangle$ as a function of y for x = 1.1, 1.5, 2.0, and 2.5. At each of these locations, it appears that $\langle Q^2 \rangle$ decreases most rapidly with increasing y at the centerline. Moreover $\langle Q^2 \rangle$ passes through a minimum very near to its equilibrium value mid-way across the gap for each of these cross-sections.

The effect of molecular extensibility (Q_0) on molecular stretching and stress is investigated by considering the CR model with various maximum molecular lengths Q_0 at a fixed We = 2.0. Fig. 5-16 shows contours of $\langle Q^2 \rangle$ for Q_0 = 5 and 15 at We = 2.0. Although varying Q_0 produces no significant changes in the flow field, the fractional extension of the molecules is drastically affected. Notice that the maximum $\langle Q^2 \rangle$ increases with increasing Q_0, but the fraction of maximum extensibility $\langle Q^2 \rangle / Q_0^2$ drops from 94% to 90% to 80% as Q_0 is increased from 5 to 10 to 15.

FENE-P model

The solution fields for the FENE-P model were computed with the same parameters as for the CR model, in order to assess the effect of the different approximations made in these two models for the stress tensor and evolution equation for $\langle \boldsymbol{QQ} \rangle$. The strong shearing flow in the region between the channel wall and the cylinder surface gives rise to large negative normal stresses and significant polymer extension, as shown in Fig. 5-17. Comparing this figure with Fig. 5-14 and similar results at other We shows that, although qualitatively the FENE-P and CR models predict very similar τ_{pxx} contours, the FENE-P model predicts smaller negative normal stress τ_{pxx} and molecular extension at all We. The difference in the extremum of τ_{pxx} is consistent with the ordering of the first normal stress coefficient for these two models. Furthermore, the thickness of the layer of large extension in the gap is smaller than for the CR model, presumably because shear thinning in the FENE-P model concentrates the shearing closer to the solid surface. The fact that the birefringent strand in the wake is also thinner for the FENE-P model suggests that the localization produced by shear thinning in the gap is convected downstream into the wake region.

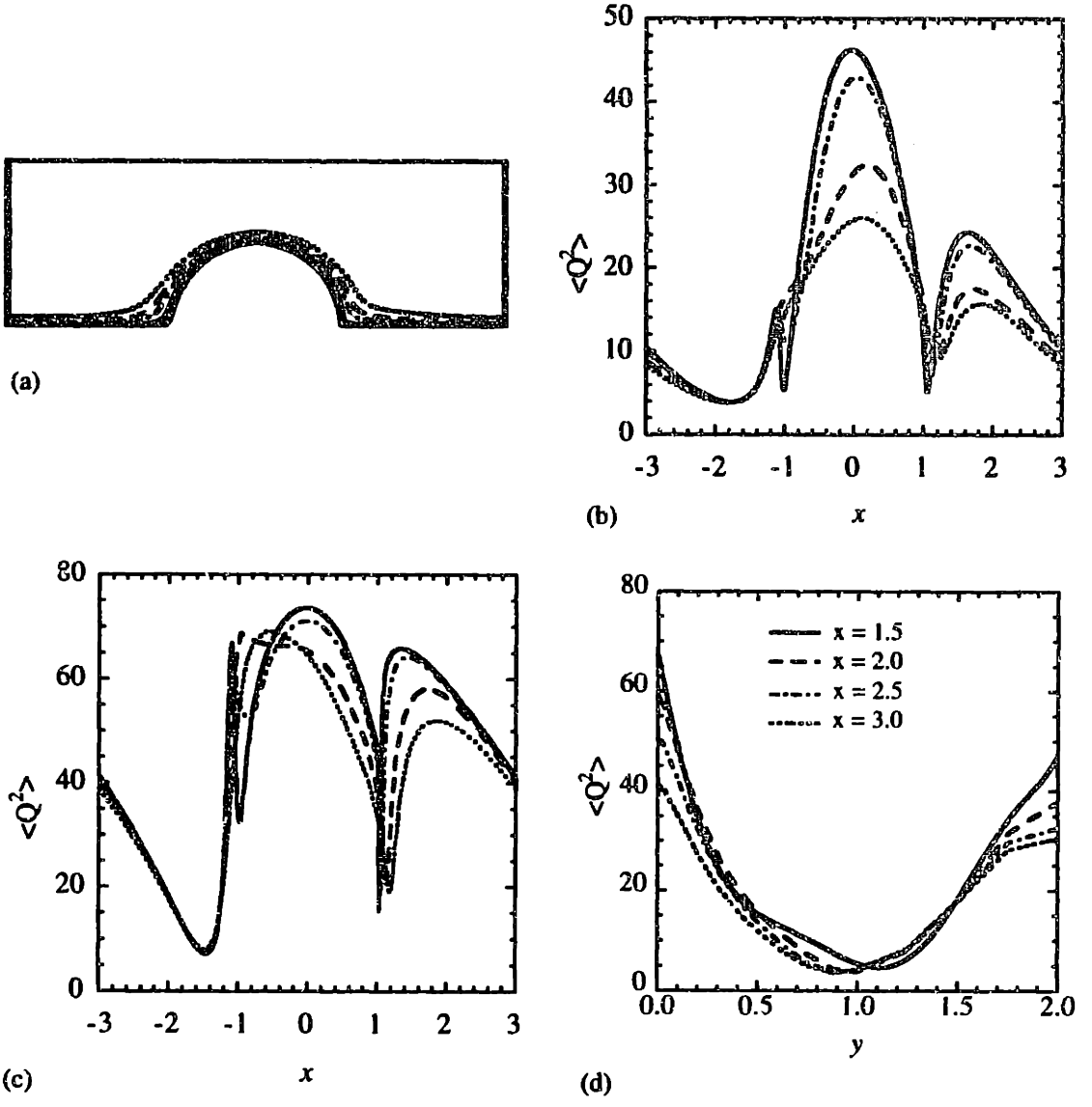

Figure 5-15 Molecular extension along several streamlines close to the symmetry plane for the CR model with Q_0 = 10 and β = 0.59. The streamlines are shown in (a) and are identified by their y-location (y_{-3}) at the left edge of the computational domain, x = -3: $y_{-3} = 10^{-3}$ (———), $y_{-3} = 5 \times 10^{-3}$ (— · · —), $y_{-3} = 2.5 \times 10^{-2}$ (— —), and $y_{-3} = 5 \times 10^{-2}$ (- - - - -). $\langle Q^2 \rangle$ for (b) We = 0.7 and (c) We = 2.0. (d) $\langle Q^2 \rangle$ across the channel at several locations downstream from the cylinder for We = 2.0.

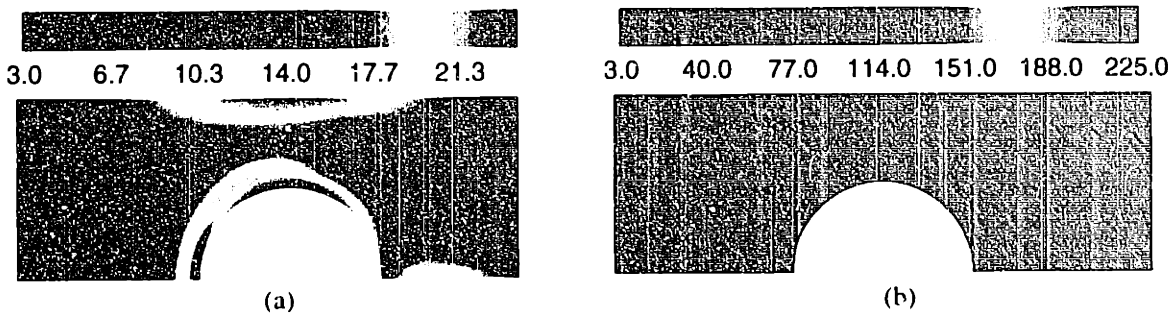

Figure 5-16 The effect of Q_0 on molecular extension for the CR model with fixed $\beta = 0.59$ and We = 2.0. (a) and (b) correspond to $\langle Q^2 \rangle$ for $Q_0 = 5$ and 15, respectively. The maximum value on the color scale corresponds to a fully extended dumbbell in each figure.

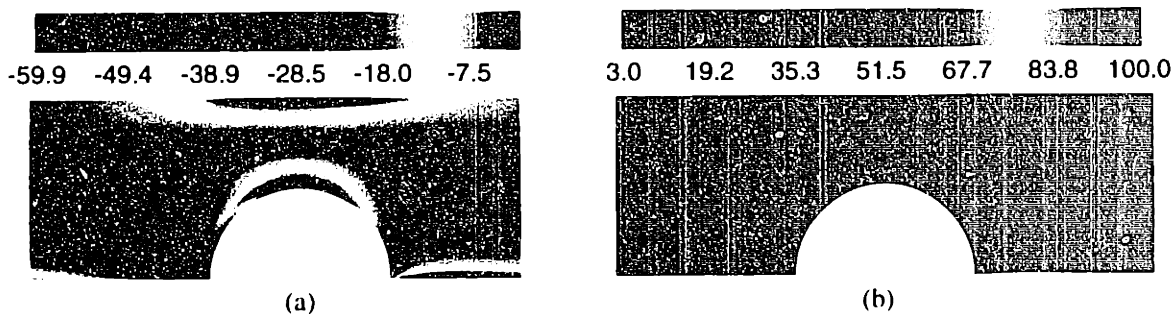

Figure 5-17 Contours of the (a) axial normal stress $\tau_{p,xx}$ and (b) molecular extension $\langle Q^2 \rangle$ for the FENE-P model with $Q_0 = 10$ and $\beta = 0.59$ at We = 2.0 for a periodic cylinder array with $L = 6$ and $H = 2$.

Giesekus model

The evolution of molecular extension $\langle Q^2 \rangle$ and normal stress $\tau_{p,xx}$ predicted for the Giesekus model are given in Fig. 5-18. Although the dumbbells in this model can be stretched out indefinitely, due to the Hookean nature of the intramolecular force, we set the maximum value of the displayed contours for $\langle Q^2 \rangle$ to $1/\alpha$ in order to facilitate comparison with the CR and FENE-P models. Qualitatively, all three models predict similar stress fields, though the CR model predicts the highest normal stress $|\tau_{p,xx}|$ at a given We. The ordering in the magnitude of $\tau_{p,xx}$ is consistent with the ordering of the first normal stress coefficient, for which the Giesekus model shear thins the most quickly, followed by the FENE-P and CR models. Similar to the behavior of $\tau_{p,xx}$, qualitative agreement in $\langle Q^2 \rangle$ is observed among the three models. At We = 0.7, all three models predict that the maximum $\langle Q^2 \rangle$ occurs in the gap region, and that a thin region of highly extended polymer molecules is formed downstream of the rear stagnation point. However, the dumbbells are much more highly extended for the Giesekus model than for the CR and FENE-P models, with

the least extension being predicted by the FENE-P model. This is consistent with the steady homogenous shear flow results (cf. Fig. 5-3d) that show $\langle Q^2 \rangle_{\text{FENE-P}} < \langle Q^2 \rangle_{\text{CR}} < \langle Q^2 \rangle_{\text{G}}$ at a given shear rate.

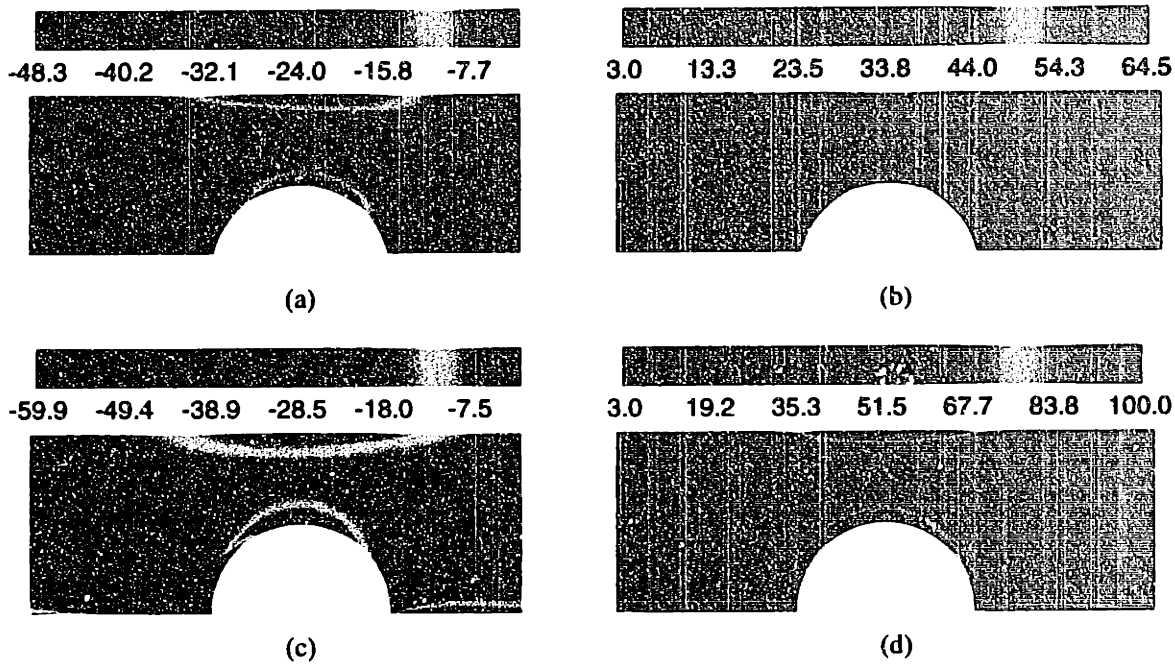

Figure 5-18 Contours of the (a and c) axial normal stress τ_{pxx} and (b and d) molecular extension $\langle Q^2 \rangle$ for the Giesekus model with $\alpha = 10^{-2}$ and $\beta = 0.59$ at We = 0.7 (a and b) and 2.0 (c and d) for a periodic cylinder array with $L = 6$ and $H = 2$.

At We = 2.0 the stress fields are also qualitatively similar for all models, with the largest $|\tau_{pxx}|$ predicted by the CR model. However, at this value of We the Giesekus model predicts that the minimum (largest tensile) value of τ_{pxx} is shifted to the wake region, whereas both the CR and FENE-P models predict that the minimum τ_{pxx} remains in the highest shear rate region. The Giesekus model also predicts a much thinner region (in the y-direction) of τ_{pxx} in the wake than either the CR or FENE-P models. The evolution of the microstructure predicted by the models also is qualitatively similar when fields of $\langle Q^2 \rangle$ are viewed on the same scale in Fig. 5-18. The effect of the periodicity of the cylinders is clearly visible for all three models, since polymer molecules are extended far from their equilibrium state throughout the flow domain. The region of large $\langle Q^2 \rangle$ starts slightly downstream from the rear stagnation point and extends all the way to the upstream of the next cylinder where the compressive flow forces $\langle Q^2 \rangle$ to 3 before the polymer stretches in the y-direction. As the elongational flow in the wake becomes more intense with increasing We, the Giesekus model predicts that the maximum $\langle Q^2 \rangle$ moves to the wake region. In

addition, the maximum $\langle Q^2 \rangle$ predicted by the Giesekus model for a given value of We is significantly higher than that for the FENE dumbbell models, because there is no upper bound on the dumbbell length for a Hookean spring. The maximum value of $\langle Q^2 \rangle$ predicted for the Giesekus model is far beyond the maximum value of ${Q_0}^2$ allowed by the FENE-P and CR models. Although the maximum value of $\langle Q^2 \rangle$ along the centerline is substantially higher for the Giesekus model than for the CR or FENE-P models, the length of the region of extended molecules in the wake of the cylinder is comparable for the three models. It is interesting that although the Giesekus model predicts unreasonable values for molecular extension, the velocity and stress fields are quite similar to those of the two finitely extensible models.

5.4.3 Cylinders spaced close together (L = 2.5)

Newtonian fluid

The most striking change in the flow field as the spacing between the cylinders is reduced from 6 to 2.5 is the development of a recirculation region connecting the rear and front stagnation points on adjacent cylinders; this is illustrated in Fig. 5-19. The extra pressure drop per cylinder, Δp, in the linear, periodic array is decreased from 52.83 for widely spaced arrays ($L = 6$) to 38.82 for $L = 2.5$. Although the flow fields of widely and closely spaced cylinder arrays differ significantly, the extreme values of the axial normal stress τ_{xx} and shear stress τ_{xy} are essentially the same.

CR model

As in the flow around widely spaced cylinder arrays, calculations can be continued to a maximum We $\approx$ 0.95 before the tensor $\langle \boldsymbol{QQ} \rangle$ loses positive definiteness for a mesh similar to M4. The regions where $\langle Q^2 \rangle < 0$ are localized in the central zone of the gap between the cylinder and channel and very close to the front and rear stagnation points, where large stress and velocity gradients are found. Halving the mesh size throughout the computational domain allows the calculations to be continued to We $\approx$ 1.0 without the loss of positive definiteness of $\langle \boldsymbol{QQ} \rangle$. However, the cost of mesh refinement is substantial for such a small increase in We: the computation time increases by a factor of 8.5 and the computer memory requirements increase four-fold. We find that although refining the mesh in the central region of the flow alleviates the loss of positive definiteness in

$\langle QQ \rangle$, the improvements in results do not justify the additional computational costs: $\langle QQ \rangle$ in the region with increased mesh refinement is near equilibrium, and elsewhere the quality of the solution is unchanged. Hence we present results below for the unrefined mesh (similar to M4) for high We.

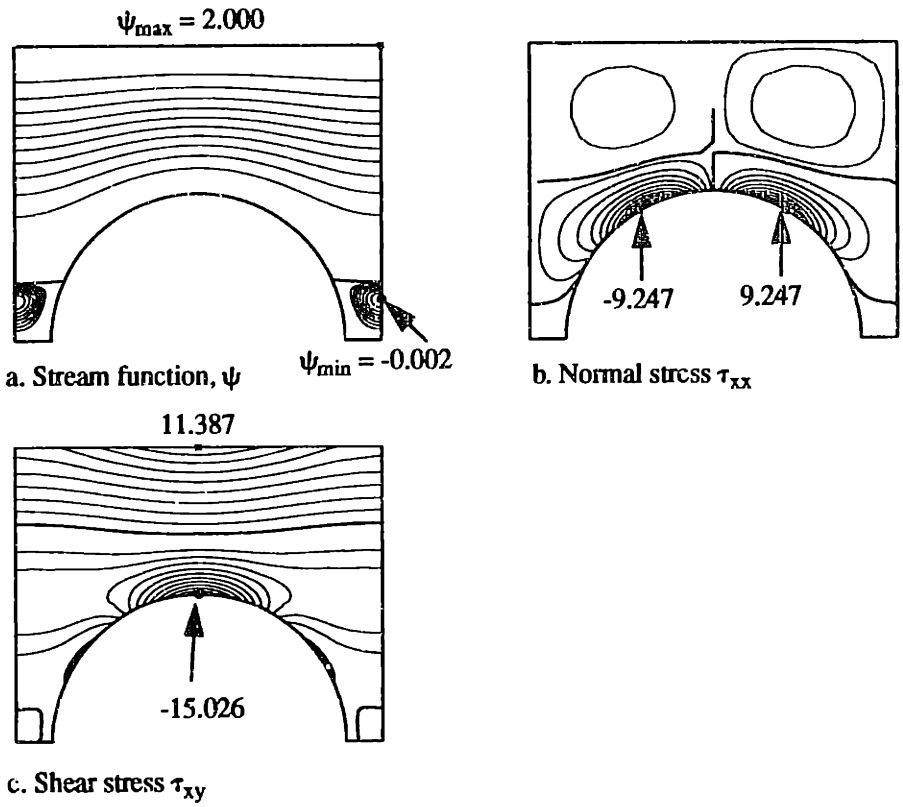

Figure 5-19 Creeping flow of a Newtonian fluid around a linear, periodic array of cylinders with spacing $L = 2.5$ and $H = 2$. (a) Stream function. The zero streamfunction is the darker curve; there are 10 equally spaced contours from 0 to the maximum and 5 equally spaced contours from the minimum to 0. (b) Normal stress τ_{xx}. (c) Shear stress τ_{xy}. For the stress contours there are 20 equally spaced contour lines between the minimum and maximum values marked on the plots.

As the Weissenberg number increases, the size of the flow recirculation region decreases as the boundary between the wake and bulk flow moves closer to the symmetry line. Similar behavior has been observed in calculations for flow around a periodic, square array of cylinders (Szady *et al.*, 1995). No doubt shrinkage of the recirculation region is driven by forces similar to those that produce increasing die swell with We (Salamon *et al.*, 1995), i.e., the relaxation of normal stresses and molecular extension in the flow direction after the fluid passes out of the high shear rate region between the cylinder and wall into the region where the no-slip cylinder surface is replaced by the moving fluid surface of the separated region as well as the strong extensional flow

that exists at the separation point where fluid is accelerated away from the cylinder. The strength of the flow recirculation, characterized by the minimum value of the stream function ψ_{min} scaled by $\langle v \rangle H_c$, monotonically increases with We as shown in Fig. 5-20. Within the flow separation region, the fluid velocity and velocity gradient are small, $\psi_{min} \sim O(10^{-3}\psi_{max})$, so that the stresses τ_{pij} and molecular extension are near equilibrium in the recirculation. This can be seen in Fig. 5-21, where contours of the stresses are shown for the CR model with We = 0.5. The largest tensile stresses remain at the solid boundaries in the gap between the cylinder and channel wall where the flow is shear dominated. In contrast to the flow with large cylinder spacing $L \geq 6$, the polymer molecules along the centerline of the geometry are essentially at equilibrium because of the recirculation. The stagnation points where the recirculation region attaches to the cylinder do not appear to produce much molecular extension. Molecules do not appear to relax substantially as they travel along streamlines near the boundary of the separated flow; and, as a result, there is a region of high molecular extension away from the cylinder surface and slightly upstream from x = 0.

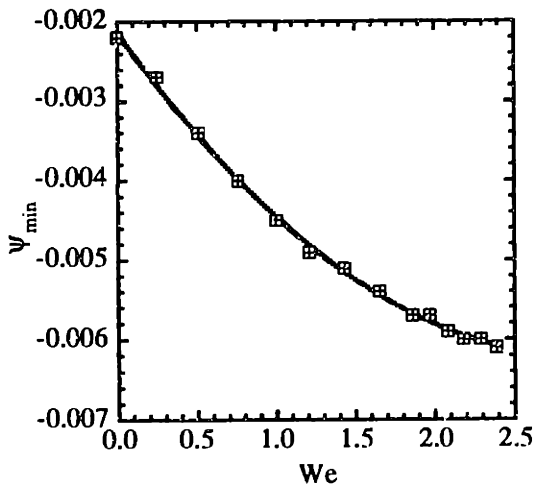

Figure 5-20 Strength of the flow recirculation, characterized by ψ_{min}, in an array with L = 2.5 and H = 2 for the CR model with Q_0 = 10 and β = 0.59. The value ψ_{max} = 2.0, so that the average velocity across the channel is unity.

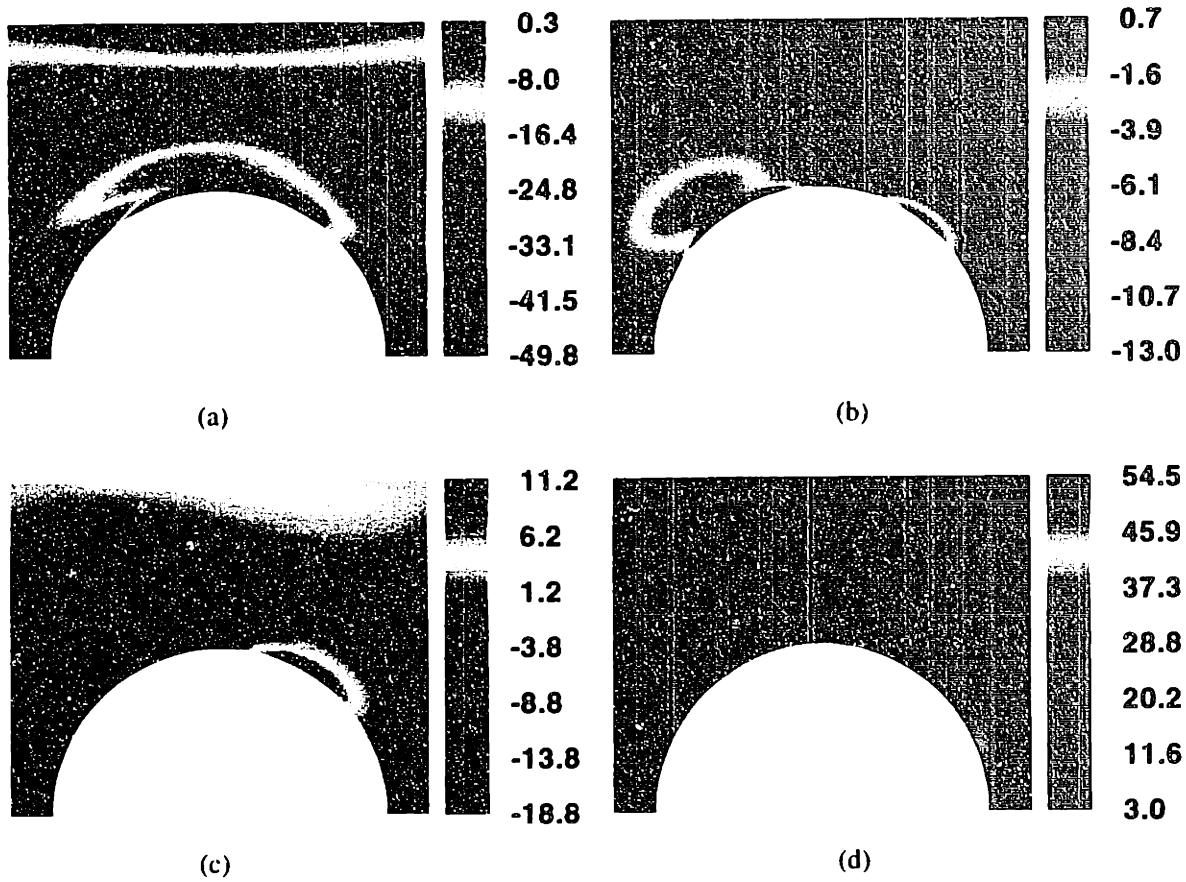

Figure 5-21 Contours of the (a) normal stress $\tau_{p,xx}$, (b) normal stress $\tau_{p,yy}$, (c) shear stress $\tau_{p,xy}$, and (d) average molecular extension $\langle Q^2 \rangle$ for flow around closely spaced cylinder arrays ($L = 2.5$, $H = 2$). Results are for the CR model with $Q_0 = 10$ and $\beta = 0.59$ at We = 0.5.

The effect of cylinder spacing on molecular extension is presented in Fig. 5-22 by the evolution of $\langle Q^2 \rangle$ for We = 1.0 along the two streamlines that pass through $y_0 = 1.1$ and 1.25 at $x = 0$. The closer cylinder spacing $L = 2.5$ gives rise to the largest molecular extension, followed by $L = 6$, and the least extension is given by the single cylinder flow. The effect of decreasing L (increasing De) on the molecular extension is most apparent on the streamline farthest away from the cylinder. On the cylinder surface, residence times are infinite, so that the local extension depends only on the local shear rate, which we have noted does not change dramatically as the geometry is varied at fixed We. For a confined, single cylinder flow, $\langle Q^2 \rangle$ monotonically increases from the equilibrium value far upstream to a maximum at $x = 0$, and relaxes to a local minimum at $x \approx 1.0$ near the rear stagnation point. Subsequently, $\langle Q^2 \rangle$ goes through a second, local maximum in the wake of the cylinder, which is caused by the extensional flow in that region, and slowly relaxes to equilibrium downstream of the cylinder. However, for widely spaced, linear, periodic arrays, $\langle Q^2 \rangle$

passes through a minimum upstream of the cylinder, followed by an increase in $\langle Q^2 \rangle$ to a maximum value at $x \approx 0$, and then by subsequent secondary local minima and maxima in the downstream stagnation flow and elongational flow region. However when the inter-cylinder spacing is decreased to the point that there is a recirculation region, only a single minimum and single maximum are seen along the streamline. This elimination of one of the pairs of extrema is directly associated with the removal of the interaction of the two stagnation points, each of which produced a local minimum in $\langle Q^2 \rangle$, on the rear of one cylinder and the front of the following cylinder. Eliminating one of the minima also results in larger total molecular extension, as well as an upstream shift of both extrema.

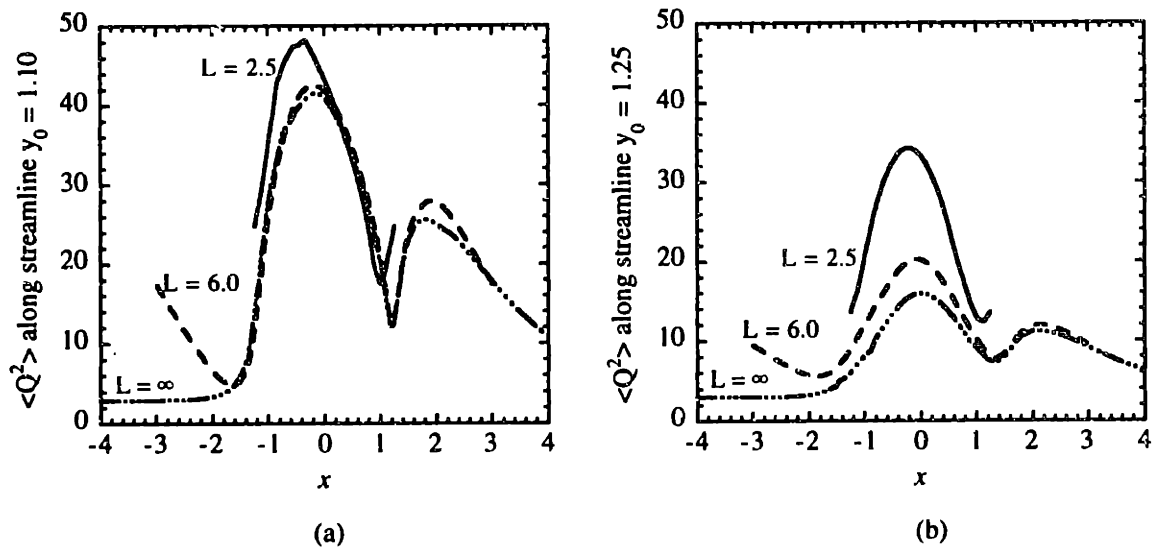

Figure 5-22 Comparison of $\langle Q^2 \rangle$ along selected streamlines for the CR model with $Q_0 = 10$ and $\beta = 0.59$ at We = 1.0 for cylinder spacings of $L = 2.5$ (———), $L = 6.0$ (— —), and $L = \infty$ (— · · —). In all cases, $H = 2.0$. At $x = 0.0$, the streamlines pass through (a) $y = 1.10$ and (b) $y = 1.25$.

The average molecular extension $\langle Q^2 \rangle$ for the CR model at We = 2.0 is shown in Fig. 5-23; the upper limit of the displayed contours corresponds to the maximum allowable value Q_0^2. For all values of We considered, $\langle Q^2 \rangle$ remains largest in the gap close to the cylinder surface and is convected downstream of the cylinder in the layer of fluid adjacent to the recirculation region. The most interesting feature of this field is the appearance of a local maximum in molecular extension, which is nearly as large as the global maximum that occurs on the cylinder surface, in an island about $0.1R_c$ away from the cylinder surface and upstream of the minimum gap. This local maximum is evidently a result of a combination of the high shear rates that exist near the cylinder and the high (positive) elongation rates that occur in the converging region of the flow. There also is a

layer of highly stretched molecules all along the surface of the confining slit. The layers of stretched molecules on the two solid surfaces are separated by a horizontal layer of nearly equilibrium shaped molecules.

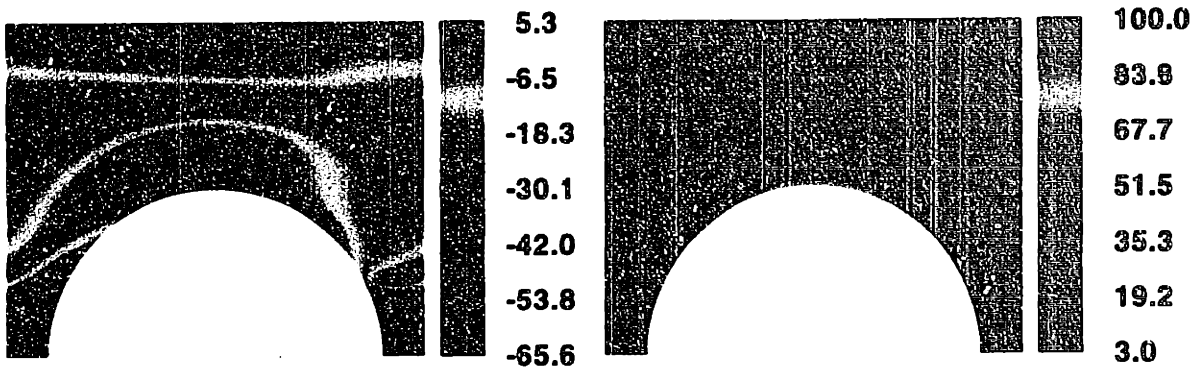

Figure 5-23 Contours of the (a) normal stress τ_{pxx} and (b) average molecular extension $\langle Q^2 \rangle$ for flow around closely spaced cylinder arrays ($L = 2.5$, $H = 2$). Results are for the CR model with $Q_0 = 10$ and $\beta = 0.59$ at We = 2.0.

FENE-P model

The evolution of $\langle Q^2 \rangle$ for the FENE-P model is shown in Fig. 5-24 for We = 0.5 and 2.0 and for $Q_0 = 10$ as used for calculations with the CR model. The tensor $\langle QQ \rangle$ loses positive definiteness at We $\approx$ 1.0, but calculations proceed to higher values of We. The molecular extension predicted with the FENE-P model is very similar to the results for the CR model: the largest molecular extension remains in the maximum shear rate region for all values of We, and a local maximum is observed slightly away from the cylinder and upstream of the narrowest part of the gap. As was the case for widely spaced cylinders ($L = 6.0$), the FENE-P model predicts smaller maximum value of $\langle Q^2 \rangle$ than the CR model for any We. The extent of the region of highly extended polymer molecules along the cylinder surface is also smaller than for the CR model. This difference confirms that shearing contributes to significant molecular extension in this flow. As shown in Fig. 5-3 and Fig. 5-4, shearing produces noticeable differences in molecular stretching between the CR and FENE-P models, whereas planar elongation does not, at least for steady state flow.

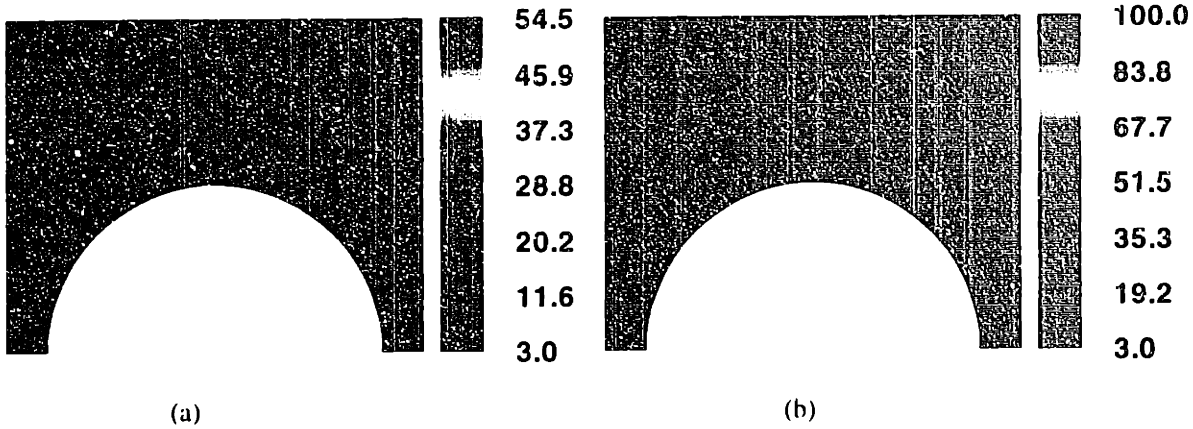

Figure 5-24 Dependence of $\langle Q^2 \rangle$ on We for the FENE-P model with $Q_0 = 10$ and $\beta = 0.59$. (a) We = 0.5; (b) We = 2.0.

Giesekus model

As indicated by Fig. 5-25, the response of the molecular extension predicted by the Giesekus model is qualitatively similar to those of the CR and FENE-P models. However, at large We, the lack of finite extensibility in this model becomes very noticeable; at We = 2.0 there are large regions in Fig. 5-25b that show extensions greater than the value of Q_0^2 needed for equivalent rheological properties in the CR and FENE-P models.

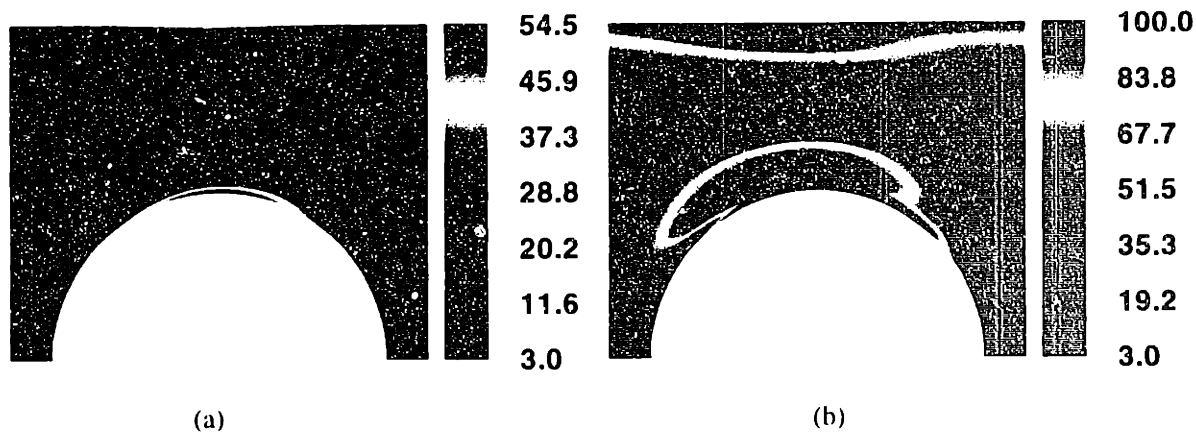

Figure 5-25 Dependence of $\langle Q^2 \rangle$ on We for the Giesekus model with $\alpha = 10^{-2}$ and $\beta = 0.59$. (a) We = 0.5; (b) We = 2.0.

5.4.4 Drag force on the cylinders

The macroscopic response of all three models is examined by computing the drag force on a cylinder. The drag force $\boldsymbol{F}_D$ on a cylinder is computed by integrating the total stress over the surface of the cylinder, S. In dimensionless form the force per unit length of cylinder is given by

$$\boldsymbol{F}_D = -\int_S (\boldsymbol{\delta}_r \cdot \{p\boldsymbol{\delta} + \boldsymbol{\tau}\}) dS = -\int_S (\boldsymbol{\delta}_r \cdot \{p\boldsymbol{\delta} + \boldsymbol{\tau}_p - \beta\dot{\boldsymbol{\gamma}}\}) dS \tag{5.17}$$

where $\boldsymbol{\delta}_r$ is the unit vector in the radial direction. The force $\boldsymbol{F}_D$ is made dimensionless by $\eta_0\langle v\rangle$, consistent with the scaling used for stress and pressure.

Single cylinder

The drag force on an isolated cylinder induced by creeping flow of a Newtonian fluid does not exist due to the Stokes paradox (Happel et al., 1973). The Stokes paradox is avoided by bounding the free stream flow by introducing rectangular channel walls at a distance H from the center of the cylinder. Faxens (1946) applied the method of images and obtained a series expansion for the drag force on the cylinder up to terms of order H^{-8}.

Comparison of the computed drag force for Stokes flow around a single cylinder in a channel with Faxens' analytical results (Faxens, 1946) provides a convenient test of the accuracy of the finite element calculations presented here. The finite element calculation are compared with Faxens' approximate series solution in Table 5.1. The terms in parentheses for several value of H denote the magnitude of the last term computed in an eight term Faxens' perturbation solution and indicate the error in Faxens' series. For small values of H^{-1}, Faxens' solution is accurate and excellent agreement is found with the FEM calculations. Discrepancies appear at high values of H^{-1}, but the FEM results lie within the error bounds of Faxens' solution.

Drag force calculations for viscoelastic fluids are reported in terms of a drag enhancement χ, defined as the ratio of the drag on the cylinder for a viscoelastic fluid F_D divided by the corresponding drag for a Newtonian fluid, $F_{D,N}$:

$$\chi \equiv \frac{F_D}{F_{D,N}} \tag{5.18}$$

The values of F_D and $F_{D,N}$ in Eq. 5.18 are evaluated for the same average velocity through the channel and with the viscosity of the Newtonian fluid equal to the zero-shear-rate viscosity of the viscoelastic fluid.

Table 5.1: Drag force per unit length of cylinder for Stokes flow past a single cylinder in a channel. H is the dimensionless channel half-gap, and the drag force is made dimensionless with the product of viscosity and average velocity, $\eta_0\langle v\rangle$.

H	Faxens Approximate Result	Finite Element in/out-flow bcs	Finite Element periodic bcs
2.0	138.48 (14.63)[a]	132.34	125.44
4.0	31.943 (0.0030)	31.942	30.744
6.0	20.148 (0.0001)	20.147	19.768
8.0	15.713	15.713	15.512
10.0	13.359	13.360	13.253
20.0	9.0321	9.0322	9.0074
30.0	7.5737	7.5737	7.5737

a. Magnitude of last computed term in eight term perturbation solution

As shown in Fig. 5-26, both the Giesekus and FENE-P models predict that the drag force on the cylinder monotonically decreases with increasing We, whereas the drag enhancement for the CR model shows a minimum at We ≈ 0.6 for both large and small values of Q_0^2 ($Q_0^2 \rightarrow \infty$ corresponds to the Oldroyd-B model). The fact that all three models predict identical elongational response but differ in viscometric behavior, suggests that the shearing aspect of this flow is critical in determining the drag force on a single, confined cylinder with H = 2. It is possible that for larger H, elongational behavior plays a more important role in the drag. Including inertia in the simulations has no effect on the drag for Reynolds numbers up to 0.1. Figure 5-26 also shows that the confining slit is sufficiently long that end effects are unimportant. This is seen by comparing the Giesekus results obtained with a computational domain extending over x = [-25, 25] with those obtained for x = [-15, 15]. The latter domain is used in all other calculations in this figure.

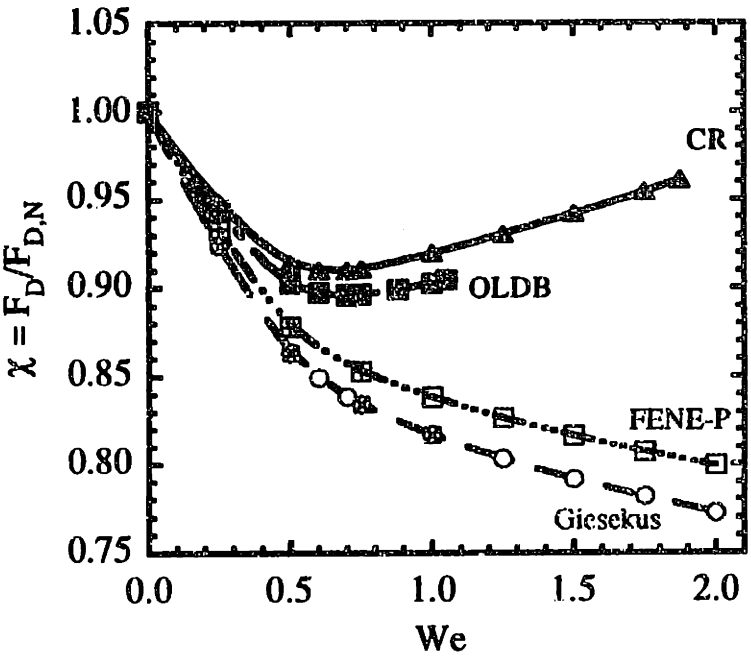

Figure 5-26 Evolution of the viscoelastic drag enhancement χ with We for viscoelastic flow around a confined, single cylinder with $H = 2$. Model parameters are chosen as $\beta = 0.59$ and $1/\alpha = Q_0^2 = 100$. The Oldroyd-B (OLDB) model corresponds to $Q_0^2 = \infty$. The points marked by an "×" on the Giesekus and "+"on the FENE-P curves were obtained on a computational domain of $x = [-25, 25]$. All other results are for a domain [-15, 15].

The viscoelastic drag enhancement for the confined single cylinder problem also was reported by Barakos and Mitsoulis (1995), who used a four-mode K-BKZ model to simulate the flow of a 5 wt% PIB/C14 solution around a cylinder. These authors report a value for χ greater than unity for $We \leq 0.1$, which monotonically decreased with increasing We. This is counter-intuitive, because at very small We ($\approx 10^{-3}$), one expects the flow to be approximately Newtonian, so that by definition $\chi = 1.0$.

Widely spaced cylinder array (L = 6)

As for the single cylinder geometry, we use the drag force calculation for the linear, periodic array to test the accuracy of the finite element method. This is done by comparing the computed drag force on the cylinder as the mesh around the cylinder is progressively refined. As indicated in Fig. 5-5, depending on the level of mesh refinement, the number of unknowns ranges from 10,784 to 67,495. The dimensionless drag force for a Newtonian fluid is plotted in Fig. 5-27 as a function of the characteristic mesh size h_D, defined as the root-mean-square area of the elements adjacent to the cylinder surface. The best fit polynomial to the results shows approximately quadratic convergence with decreasing element size. If the transition in element size is not smooth or if the ele-

ments are highly deformed from squares around the cylinder, the resulting drag force does not vary perfectly quadratically with h_D.

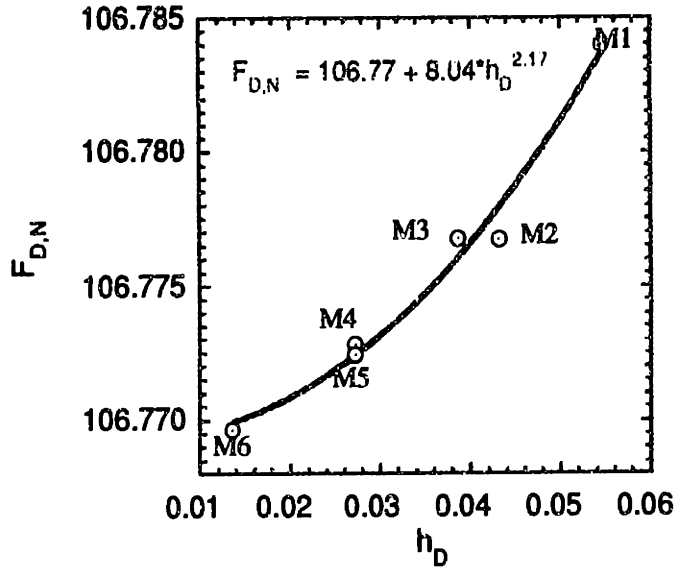

Figure 5-27 Convergence of the dimensionless Newtonian drag force $F_{D,N}$ on a cylinder in a linear, periodic array with $L = 6$ and $H = 2$ with decreasing mesh size h_D. The computed $F_{D,N}$ per unit length is made dimensionless with $\eta_0\langle v\rangle$. The best fit polynomial to the numerical data is also shown.

The convergence of the finite element calculations for viscoelastic models is demonstrated in Table 2, which displays the computed dimensionless drag on a cylinder for the Oldroyd-B model (CR and FENE-P for $Q_0 \to \infty$, Giesekus for $\alpha \to 0$) for a series of We and for different levels of mesh refinement. Clearly, the dimensionless drag converges with mesh refinement, even for We above the value at which $\langle \boldsymbol{QQ} \rangle$ loses positive definiteness. For example, with mesh M4, the positive definiteness of the $\langle \boldsymbol{QQ} \rangle$ tensor is lost between We = 0.82 and 1.01; however, the computed drag for We = 1.01 is not significantly different (less than 0.3%) from that obtained with a more refined mesh M6, for which $\langle \boldsymbol{QQ} \rangle$ remains positive definite past We = 1.01.

The neighboring cylinders in the linear array partially shield a given cylinder from the flow, so that the Newtonian drag force experienced by a cylinder decreases from 132.34 for the single cylinder ($L = \infty$) to 106.77 for $L = 6$. The drag enhancements predicted for various viscoelastic models in the widely spaced linear periodic array are compared in Fig. 5-28. For the three nonlinear models, $\langle \boldsymbol{QQ} \rangle$ loses positive definiteness at We ≈ 1.2 for the mesh M4 used here. The non-shear thinning CR and Oldroyd-B models predict that the drag force passes through a minimum at We ≈ 0.8. Since this occurs substantially below 1.2, the drag recovery observed at high We is not an arti-

fact of inadequate mesh refinement. The accuracy of the drag results for We ≥ 1.2 is uncertain, however, unless a more refined mesh is considered. The shear thinning FENE-P and Giesekus models predict a qualitatively different response from the constant viscosity models, in that both show a monotonically decreasing drag enhancement with increasing We. Thus, the effect of shear thinning on the drag enhancement is similar to that for the flow around a single confined cylinder.

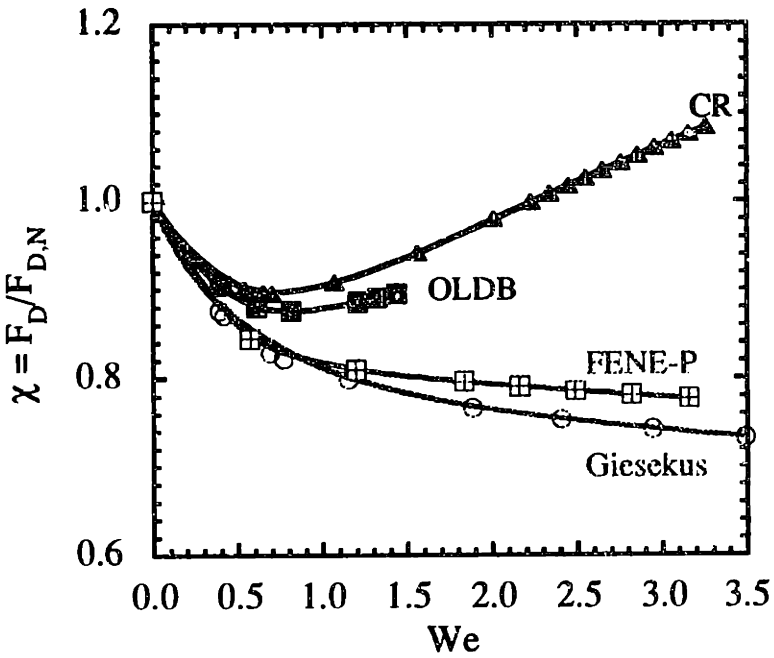

Figure 5-28 Comparison of viscoelastic drag enhancement χ for different viscoelastic constitutive equations for flow in a widely spaced array of cylinders ($L = 6, H = 2$). The model parameters are $\beta = 0.59$ and $Q_0^2 = 1/\alpha = 100$. Results are obtained with mesh M4.

The depth of the minimum in χ increases with increasing molecular extensibility, as shown in Fig. 5-29a for the CR model with values of Q_0 ranging from 5 to ∞. The location in We of the minimum depends very weakly on Q_0, increasing from about We = 0.7 at $Q_0 = 5$ to We = 0.8 for the Oldroyd-B limit ($Q_0 \rightarrow \infty$). It is interesting that the Giesekus model shows the opposite trend. Since α^{-1} in the Giesekus model plays a role similar to Q_0^2 in the Chilcott-Rallison model, it is unexpected, based on Fig. 5-29a, that the minimum in χ would decrease for increasing α as seen in Fig. 5-29b. Moreover, the minimum disappears altogether for α between 10^{-3} and 10^{-2}. The behavior of χ for the Giesekus model is understood in terms of the effect of α on the shear thinning behavior of the model. A fluid with a greater α shear thins more rapidly than a fluid with a smaller α; therefore, the drag force on the cylinder is lower than for a Newtonian flow with the same zero-shear-rate viscosity, and the difference increases as We increases.

Table 5.2: Convergence of dimensionless drag force on a cylinder for the Oldroyd-B model with $\beta = 0.59$ flowing around a linear, periodic array of cylinders with $L = 6$ and $H = 2$. The dashed entries indicate that the calculations can not be continued to higher We with the given mesh.

We	M1	M2	M3	M4	M6
0.00	106.7840	106.7767	106.7768	106.7724	106.7680
0.41	94.7049	96.5578	96.7208	96.6454	96.6570
0.61	(94.0540)[a]	94.5655	94.2418	94.0541	94.0849
0.82	(93.5736)	(93.5263)	(93.8330)	93.5325	93.5916
1.01	---------	(93.8898)	(94.2643)	(93.9065)	94.0476
1.21	---------	(94.5690)	(94.9476)	(94.5916)	(94.7201)
1.32	---------	---------	----------	(95.0681)	(95.3156)
1.44	---------	----------	---------	(95.6133)	----------

a. Numbers in parentheses indicate results for which $\langle QQ \rangle$ is not positive definite.

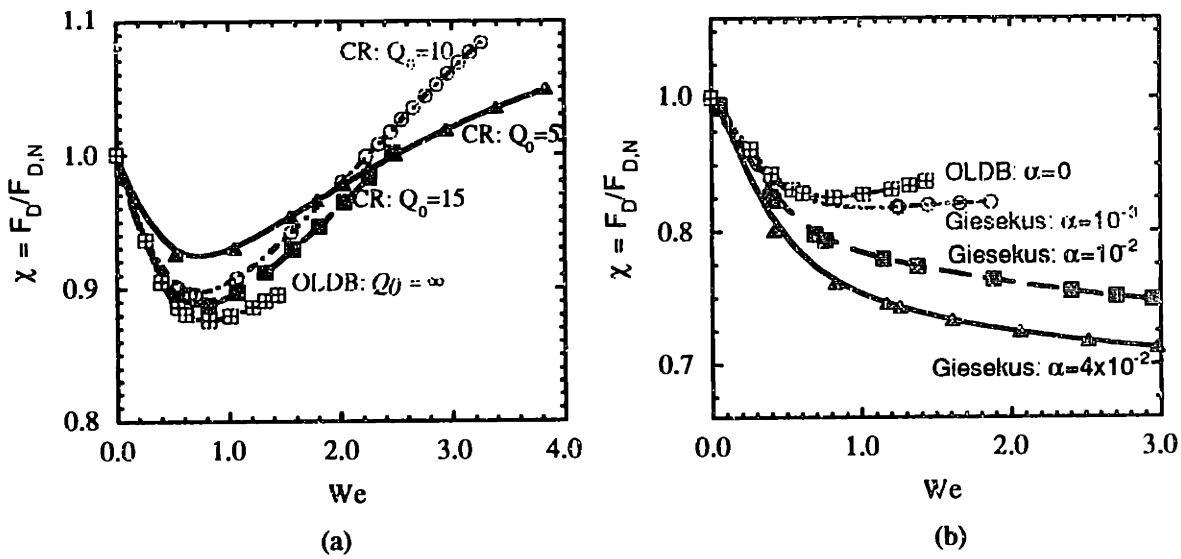

Figure 5-29 Dependence of the viscoelastic drag enhancement χ on molecular extensibility for the Chilcott-Rallison and Giesekus models in flow around a periodic array of cylinders ($L = 6$, $H = 2$). (a) CR model with fixed $\beta = 0.59$ but variable Q_0; (b) Giesekus model with fixed $\beta = 0.59$ and variable α.

Closely spaced cylinder arrays (L = 2.5)

Bringing the cylinders close enough together to produce a separated flow between adjacent cylinders results in a dramatic drop in the drag. For a Newtonian fluid, the dimensionless drag decreases from 106.77 for $L = 6$ to 66.24 for $L = 2.5$. The influence of viscoelasticity on this reduced drag is shown in terms of χ in Fig. 5-30. We incorporate results from three meshes in this

figure. The solution labeled 'full problem' was obtained by solving the flow problem in a unit cell that includes the entire cylinder and slit, that is, no symmetry condition is used. In addition, two meshes very similar to M4 and M6 around the cylinder are employed. For $Q_0 = 10$, the CR model predicts a minimum drag force at De ≈ 0.2. The shear thinning FENE-P and Giesekus models exhibit a monotonically decreasing drag enhancement. The effect of increasing Q_0 or decreasing α on the drag is also shown in Fig. 5-30. Again, the Oldroyd-B and CR models predict that χ reaches a minimum at some critical We, whereas the FENE-P and Giesekus models predict that χ decreases monotonically.

The drag force on the cylinder is decomposed in Fig. 5-31 into form drag, which arises from the total normal stress acting on the cylinder, and friction drag, which arises from the shear stress acting on the surface. All of the models predict the existence of a minimum in form drag as a function of We. The constant viscosity models show that form drag increases extremely rapidly with We beyond the minimum, whereas, a much more gradual increase in the form drag is predicted by the shear thinning models. The friction drag has a maximum for the Oldroyd-B and Chilcott-Rallison models at De ≈ 0.8, but decreases monotonically with We for the Giesekus and FENE-P models. The scales for the form drag and friction drag are different in this figure; and clearly the form drag dominates at any We. Thus, for all three models, the drag force shows an initial decrease with increasing We. For the constant viscosity models, the drastic increase in the form drag at large We overshadows the small decrease in the friction drag, thereby leading to the observed minimum in the total drag. However, for the shear thinning models the rapid decrease in the friction drag dominates the gradual increase in form drag, and as a result the drag force decreases monotonically.

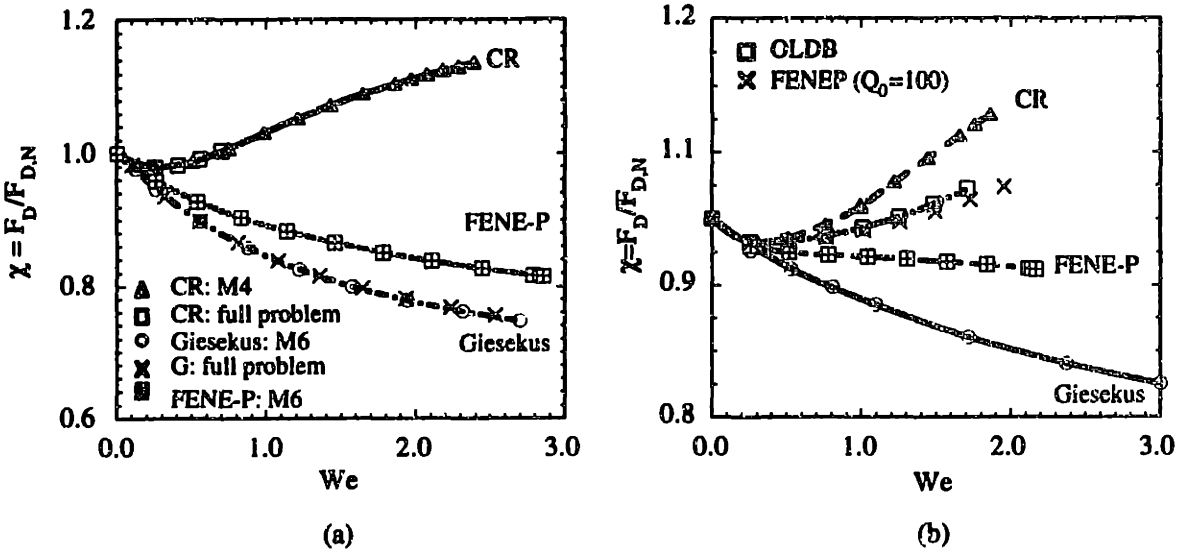

Figure 5-30 Comparison of the viscoelastic drag enhancement x for the Chilcott-Rallison, FENE-P, and Giesekus models for two degrees of molecular extensibility: (a) $Q_0^2 = 1/\alpha = 100$; (b) $Q_0^2 = 1/\alpha = 400$. In all cases $L = 2.5$, $H = 2$, and $\beta = 0.59$.

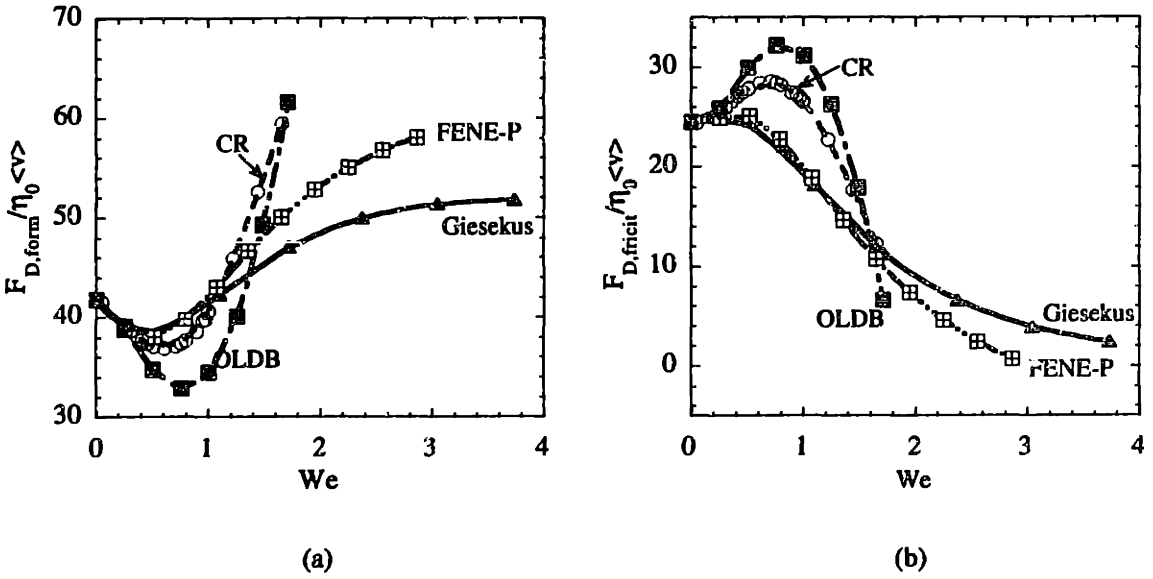

Figure 5-31 (a) Dimensionless form drag and (b) friction drag force on a cylinder in a linear, periodic array with $L = 2.5$, $H = 2$, $\beta = 0.59$, and $Q_0^2 = 1/\alpha = 400$.

5.5 Summary on viscoelastic flow around a linear array of cylinders

Numerical simulation is used to investigate the flow of polymer solutions around a linear, periodic array of cylinders for three constitutive equations based on the elastic dumbbell model: the Giesekus, FENE-P, and Chilcott-Rallison models. The FENE-P and Chilcott-Rallison models share a common underlying physical model which has a maximum length Q_0; the Giesekus model, though infinitely extensible, closely mimics the elongational flow properties of the other two models. Perhaps the most surprising result of this study is that, even though the fore and rear stagnation points and the converging and diverging regions around the cylinder suggest the importance of elongational flow in this problem, the results are clearly dominated by the shear flow behavior of the models. This is seen in at least three ways: First, the normal stress contours for τ_{pxx} for the cylinder spacings considered are very similar; moreover, the slight variation from model to model in the magnitude of τ_{pxx} follows the relative values of Ψ_1 in steady shear flow. Second, the contours of molecular extension also are similar (apart from the very large elongations possible for the Giesekus model), and the ordering of $\langle Q^2 \rangle_{max}$ is consistent with the response of $\langle Q^2 \rangle$ in simple shear flow. Third, the viscoelastic drag enhancement χ is very sensitive to shear thinning in the viscosity. This is seen in the dramatic difference in χ between the Chilcott-Rallison and FENE-P models. The constant viscosity that results from the approximation used in deriving the Chilcott-Rallison model appears to be responsible for the fact that χ shows a minimum with increasing We, whereas the FENE-P model does not. This surprising result serves as a warning that subtle differences in approximations used in deriving constitutive equations from molecular theory can produce large effects in the fluid mechanics of the resulting models.

We might suspect that the dominance of shear flow behavior in the calculations presented here is due to the high degree of confinement by the slit, whose half-height is only twice the cylinder radius. Thus as H is increased, elongational flow properties of the models will become increasingly important. I have performed calculations with mesh M4 for a gap of $H = 4$ with all of these models, and I obtain very similar trends. This suggest that H must be quite large for the effects of the walls to be negligible.

The effects of inter-cylinder spacing L are also interesting. As L is decreased from 6 to 2.5, flow separation appears even for the Newtonian fluid. I have not done enough calculations to determine the impact of viscoelasticity on the critical L for the appearance of the flow separation, but the results which show the decrease in recirculation zone thickness with increasing We strongly suggest that viscoelasticity would inhibit separation. This effect would cause the critical value of L for flow separation for a viscoelastic fluid to be somewhat smaller than that for the Newtonian fluid.

Decreasing the inter-cylinder spacing also alters the stretching mechanism for the molecules. For large spacing L, the maximum molecular extension $\langle Q^2 \rangle$ occurs adjacent to the cylinder surface closest to the channel wall, except for the Giesekus model at large We for which the maximum extension shifts into the rear birefringent strand. In this latter situation, the predicted molecular extension would be aphysical for the equivalent finitely extensible counterparts. There appears to be little cumulative effect of the elongational flows near the front and back of the cylinders. This is because the molecular elongation produced by the stretching flow behind one cylinder is destroyed by the compressive flow in front of the succeeding cylinder. That is, the molecules do not rotate in a stretched state to align with the new direction of stretching at the front of a cylinder so that they can be further stretched; rather they are first stretched in the main flow direction and compressed in the transverse direction in the downstream region, but as the upstream region of the next cylinder is approached they are compressed in the axial direction to nearly equilibrium size before being stretched transversely.

When the cylinders are moved close enough to each other that the flow is separated between adjacent cylinders, the interaction between the cylinders is much more effective in increasing molecular extension than is the case for larger L. The reason for this is that the molecules are able to rotate into the principal direction of stretching as they move from one cylinder to the next. As a result large molecular extensions associated with the converging region of the flow are seen upstream of the narrowest part of the gap and away from the cylinder surface.

Chapter 6

Viscoelastic flow around a 2D Array of Cylinders

In this chapter, we extend the previous numerical studies on viscoelastic flow around a linear array of cylinders (Chapter 5), to include both square and staggered cylinder arrays all with a porosity of 45.5%. Here, we attempt to determine which array arrangement gives rise to the most molecular extension, and how does the flow kinematics and pressure drop depend on the geometry. We will also examine the role of inertia and the effect of varying solvent fraction on flow kinematics and molecular extension. We find that the largest molecular extension is achieved when polymer solutions are introduced into a linear periodic array of cylinders, followed by the square arrays, and the least extension is found in the staggered array of cylinders. Similar trends are observed in the pressure drop and drag force on the cylinder.

Results on inertialess viscoelastic flow of Giesekus and Chilcott-Rallison (CR) models around a linear, periodic array of cylinders are first presented. Viscoelastic flow around a square array of cylinders is then discussed. The effects of changing solvent contribution and inclusion of inertia are considered for the square arrays. Flow kinematics, normal stress and molecular extension are used to characterize the macroscopic and microstructural response of the polymer solution. Finally, the drag enhancement as a function of We for both the Giesekus and CR models is presented.

6.1 Flow geometry and dimensionless numbers

We use the same nomenclature as in chapter 5. Figure 6-1 is a sketch of all three geometries. The configuration of the cylinder array is uniquely specified by L and H:

$$L \equiv \frac{L_c}{R}, \qquad H \equiv \frac{H_c}{R} \tag{6.1}$$

In conjunction with the spatial arrangement of the cylinder, we use the cylinder radius R as the length scale. The average x-component of the fluid velocity across the periodic boundary, $\langle v \rangle$, gives a characteristic velocity; the ratio $\langle v \rangle$ to R defines a characteristic strain rate for the flow. The importance of viscoelasticity in the flow is characterized by the Weissenberg number, defined as:

$$We \equiv \frac{\lambda \langle v \rangle}{R} \tag{6.2}$$

where λ is the zero-shear-rate relaxation time of the polymer solution.

In this following sections, results for the inertialess flow of Giesekus, FENE-P and CR model fluids around a linear periodic array of cylinders are discussed. It is our observation that the kinematics of the flow, the normal stresses, and average molecular extension change with increasing We.

6.2 Flow around a linear periodic array of cylinders (L = 2.4, H = 1.2)

6.2.1 Newtonian fluid

When the cylinders are arranged very close to each other, the flow is separated as the slow recirculation zone connects the rear and front stagnation points on adjacent cylinders. This separating flow is weak, because both the velocity and velocity gradient are nearly zero, leading to low stresses in this region.When the channel wall is moved closer to the cylinder, from H = 2.0 to 1.2, the strength of the shearing in the gap region is increased. Although the locations of maximum and minimum stresses remain on the surface of the cylinder, the magnitude is increased by a factor of ten. The extremes of τ_{xx} are changed from ± 9.131 for the wider channel gap of $H = 2.0$ to

± 70.20 for $H = 1.2$, and τ_{xy} is increased from 11.366 for $H = 2.0$ to 179.22 for $H = 1.2$. For the same change in H, the minimum value of τ_{xy} decreases from -15.035 to -189.77. The extra pressure drop per cylinder, Δp (the pressure drop beyond that found for an empty channel) rises sharply from 39.139 for $H = 2.0$ to 1395.8 for $H = 1.2$.

In Fig. 6-2, we present a sequence of meshes that were used in calculations of all three geometries. Three meshes M1 to M3 are used for the linear and square arrays of cylinders, and M4 and M5 are the coarse and most refined meshes that were used for staggered array calculations. A typical mesh M2 with 38,944 unknowns takes 2 cpu minutes per iteration on a Cray C90.

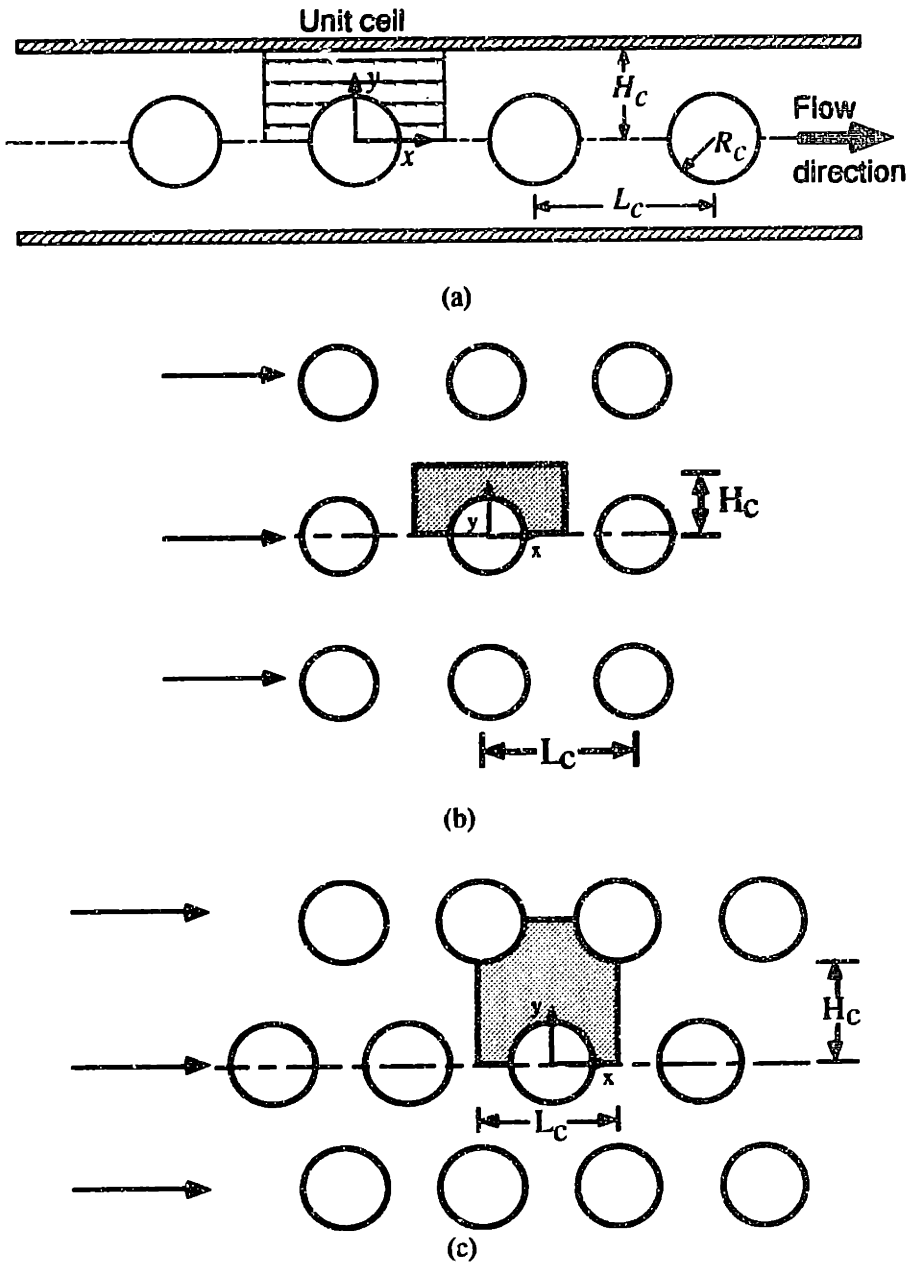

Figure 6-1 Flow past (a) a linear periodic array of cylinders confined symmetrically between parallel plates; (b) a square array of cylinders; and (c) a staggered array of cylinders. The cylinders each have radius R, and the geometry is specified by the horizontal cylinder-to-cylinder spacing L_c and the vertical spacing H_c. The unit cell on which computations are done is shaded.

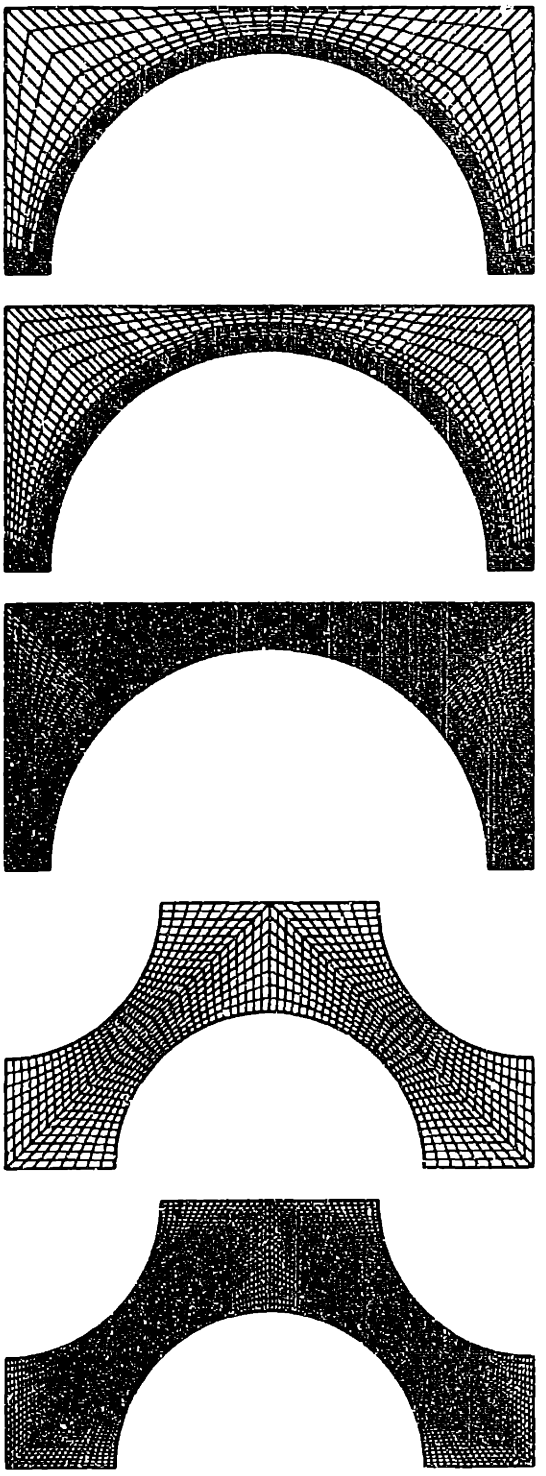

Figure 6-2 Finite element meshes used for calculations of viscoelastic flow around various flow geometries. Meshes M1, M2 and M3 are used for flow around a linear periodic or square array of cylinders with $L = 2.4$ and $H = 1.2$, and meshes M4 and M5 are used for flow around staggered array of cylinders.

6.2.2 Viscoelastic models

Calculations for the Giesekus model with $\alpha = 0.01$ and $\beta = 0.59$ can be performed for $We \leq 0.52$ with mesh M2 before the configuration tensor loses positive definiteness.The violation of the positive definiteness of $\langle QQ \rangle$ for the Giesekus model does not prevent the continuation of the calculation to a higher We. The loss of positive definiteness in $\langle QQ \rangle$ does not compromise the quality of the overall solution, and similar conclusions have been reached for FEM calculations in widely (L = 6) and closely (L = 2.5) spaced linear periodic arrays of cylinders with H = 2 (see chapter 5).

The effect of increasing We on the axial velocity v_x is shown in Fig. 6-3. Along the centerline (y = 0.0), v_x is symmetric about the periodic boundary x = 1.2. The strength of the flow recirculation, characterized by the minimum v_x, increases with increasing We. Across sectional plot of v_x along the periodic boundary (x = 1.2) clearly indicates that the recirculating zone $v_x \leq 0$ occupies 1/4 of the radius. The presence of a flow recirculation zone in the region where $0 \leq y \leq 0.25$ suggests that the flow is weak, since both the velocity and velocity gradients are close to zero (Fig. 6-3(b)), and polymer molecules are essentially at the equilibrium state ($\langle Q^2 \rangle \approx 3$) (see Fig. 6-3(c)). Outside of the flow recirculation zone, increasing y results in increasing velocity and velocity gradients, until the center of the flow geometry ($y \approx 0.5$) is reached, where a local maximum in $\langle Q^2 \rangle$ is observed. Further increase in y effectively decreases the molecular extension, consistent with the continuous decrease in the slope of the streamwise velocity across the width of the channel, until $y \approx 0.9$, close to the rear stagnation point, where the shear-rate is essentially zero, as indicated in Fig. 6-3(b) where $\partial v_x/\partial y \approx 0$, and $\langle Q^2 \rangle$ reaches a local minimum. The largest velocity gradient ($\partial v_x/\partial y$) is on the channel wall (y = 1.2) for all We because of the shear dominated flow in the narrow slit. As a result, polymer molecules are highly extended, reaching a true maximum in $\langle Q^2 \rangle$ in this region.

For the CR model with $\beta = 0.59$ and $Q_0 = 10$, the positive definiteness of the $\langle QQ \rangle$ tensor is lost at $We \geq 0.35$. When the minimum gap distance between the channel wall and the cylinder is decreased from $H = 2.0$ to $H = 1.2$, while the center-to-center cylinder spacing is kept constant at $L = 2.4$, the global maximum molecular extension, $\langle Q^2 \rangle_{max}$, occurring at the cylinder surface in the minimum gap between the cylinder surface and channel wall, is increased from 27.58 to 78.56 at We = 0.3.

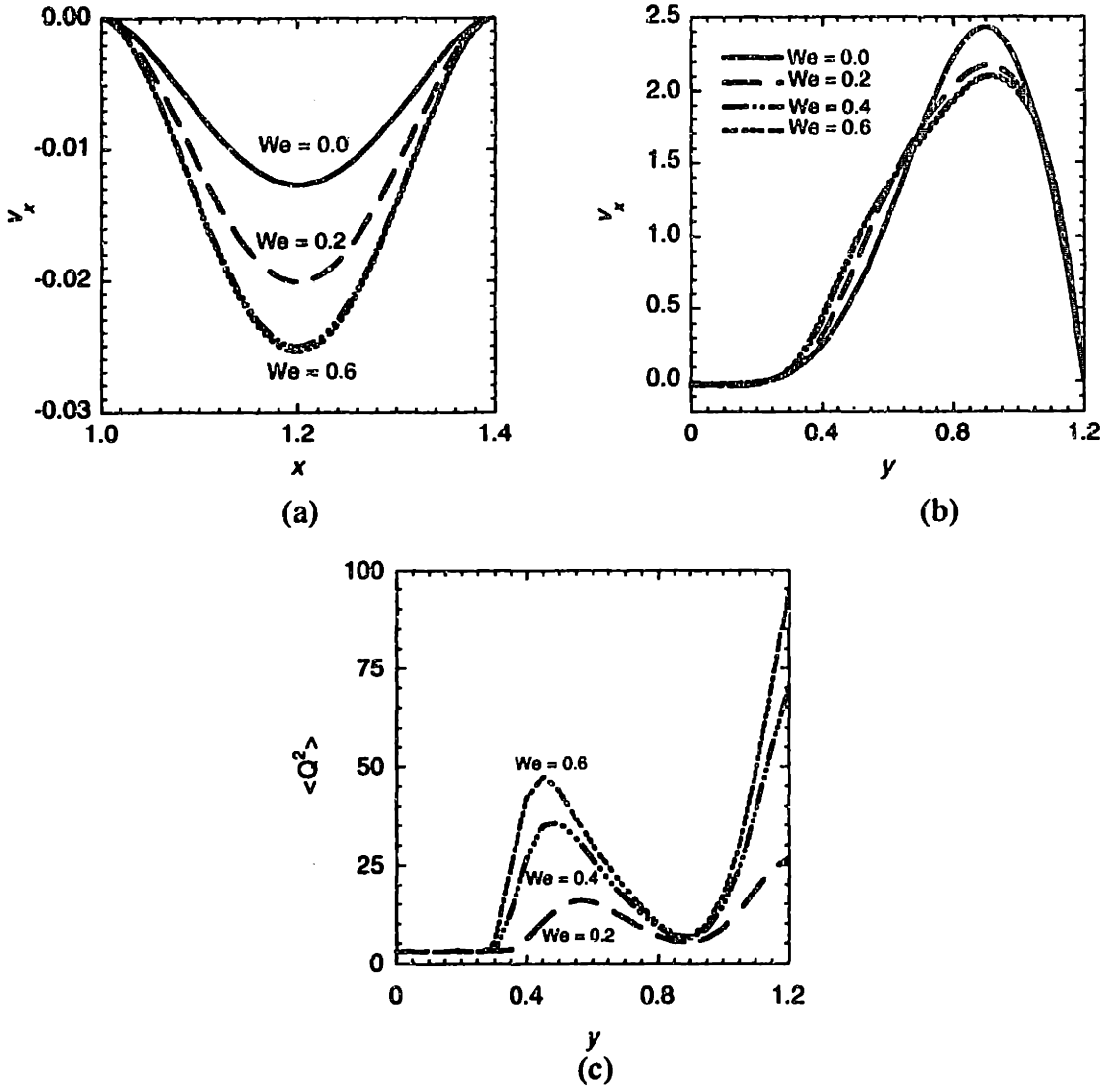

Figure 6-3 Evolution of axial velocity v_x (a) along the centerline line (x = 1.0 and x = 1.4 correspond to the rear and front stagnation points respectively; (b) across the periodic boundary at x = 1.2, for flow around a linear periodic array of cylinders in a channel with $H = 1.2$; (c) $\langle Q^2 \rangle$ across the periodic boundary for the Giesekus model with $\alpha = 10^{-2}$ and $\beta = 0.59$.

6.3 Flow around a square array of cylinders (L = 2.4, H = 1.2)

6.3.1 Newtonian fluid

When cylinders are positioned in both the x and y directions to form a square array, the maximum and minimum normal stress τ_{xx} is halved to ±35.394 from ±70.204 for a linear periodic

array. As with the linear periodic array of cylinders, the minimum τ_{xx} remains on the cylinder surface, whereas the maximum τ_{xx} is shifted from the channel wall to the upstream. The extremes of τ_{xy} are lowered from 179.224 to 1.304 and increased from -189.772 to -96.949, though the locations of the extremes for τ_{xy} are not shifted. The size of the flow recirculation zone is enlarged by about 50% in going from linear to square arrays, and the strength of the recirculating flow $-\psi_{min}$ is increased from 0.021 to 0.031. The most noticeable change in the flow kinematics is the shift in maximum v_x from the middle of the narrow gap to the symmetry plane. Thus, the Stokes flow kinematics is modified appreciably due to the absence of channel wall.

The contribution per cylinder to the pressure drop shows the influence of array arrangement more sensitively than the flow kinematics. Δp_c is decreased from 1395.8 for a linear array to 358.09 for a square array.

6.3.2 Inertialess flow of viscoelastic fluid with $\beta = 0.59$

Calculations for the Giesekus model with $\alpha = 0.01$ can be continued to a maximum We ≈ 0.40 with mesh M1 before the positive definiteness of the configuration tensor is lost. More refined meshes such as M2 and M3 allow calculations to continue to We ≈ 0.54 and We ≈ 0.69 without the loss of the positive definiteness of $\langle QQ \rangle$. The regions where $\langle Q^2 \rangle < 0$ are localized in the central zone of the gap between the cylinder and the boundary between the flow recirculation and bulk flow, where large stress and velocity gradients have been previously observed.

The effect of increasing We on v_x along the centerline (y = 0.0) is very similar to the case of linear periodic arrays, with the exception that the magnitude of v_x is smaller. As shown in Fig. 6-4, across the periodic boundary, small shifts in v_x with increasing We are noted. The most significant change due to fluid elasticity is demonstrated by the molecular extension $\langle Q^2 \rangle$. In contrast to the linear arrays, the maximum $\langle Q^2 \rangle$ is shifted from y = 1.2 to y $\approx$ 0.6 because the channel wall is now replaced by the symmetry boundary at y = 1.2. The effective shear rate $(\partial v_x / \partial y)$ is decreased from the global maximum at y = 1.2 for a linear array, to zero corresponding to the symmetry boundary condition. Thus, the elimination of narrow walls lowers the shear rate and molecular extension, and the maximum $\langle Q^2 \rangle$ across the periodic boundary is lowered by a factor of two compared with the case of a linear array discussed in section 6.2.

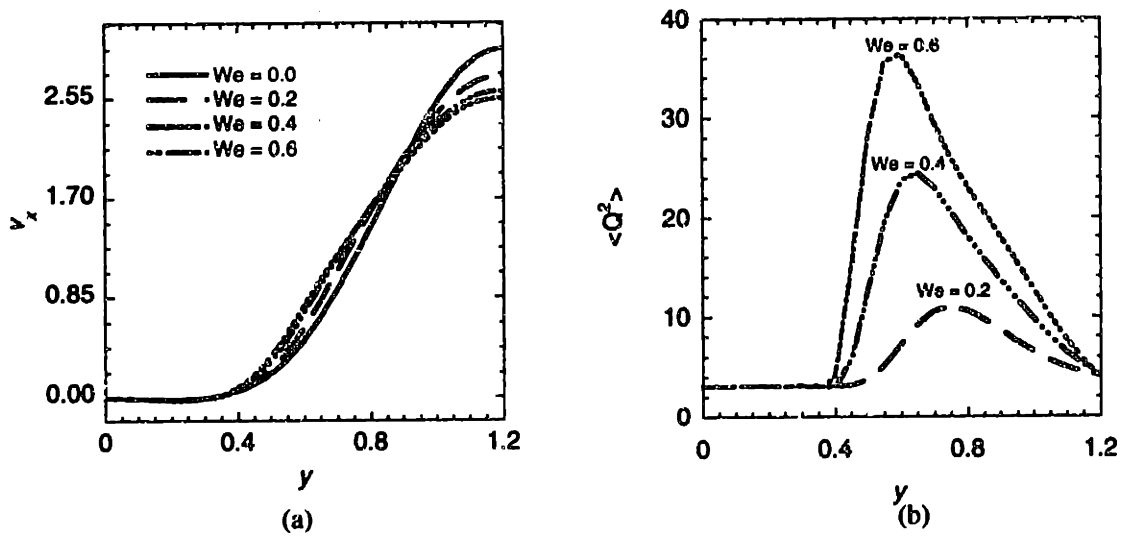

Figure 6-4 (a) Axial velocity v_x across the periodic boundary at x = 1.2; (b) $\langle Q^2 \rangle$ across the periodic boundary. Results are for flow around a square array of cylinders with $L = 2.4$ and $H = 1.2$ of a Giesekus fluid with $\alpha = 10^{-2}$ and $\beta = 0.59$.

The evolution of average molecular extension $\langle Q^2 \rangle$ for the Giesekus model at We = 0.2 and 0.5 is shown in Fig. 6-5; the upper limit of the displayed contours corresponds to $1/\alpha = 100$. There are two regions where polymer molecules are highly extended. One region is very close to the cylinder surface and the other is slightly displaced to the upstream of the cylinder. For all values of We considered, the global $\langle Q^2 \rangle_{max}$ remains in the gap close to the cylinder surface and is connected downstream of the cylinder in the layer of fluid adjacent to the recirculation region. This large extension convects downstream of the cylinder forming a region of uniformly extended polymer chains outside of the flow recirculation region. The most striking similarity between these of $\langle Q^2 \rangle$ contours and those for the closely spaced linear periodic array is the appearance of this second large molecular extension, where the local maximum (which occurs in an island about 0.1R away from the cylinder surface and upstream of the minimum gap) is nearly as large as the global maximum that occurs on the cylinder surface. This local maximum is evidently a result of the combination of the high shear rates that exist near the cylinder and the high (positive) elongation rates that occur in the converging region of the flow. However, the presence of a symmetry plane due to the existence of upper cylinders decreases the shear rate and results in the elimination of the third possible region of highly stretched molecules along the surface of the confining slit.

Figure 6-5 also illustrates the importance of the elongational flow in the wake of the cylinder by exhibiting the development of the normal stress τ_{pxx}. We arbitrarily set the minimum value of τ_{pxx} to be plotted to -100 to make the evolution of wake more apparent. The region of negative stress in the gap becomes wider with increasing We. Outside of the boundary between the wake and bulk flow, changes in τ_{pxx} are abrupt and the gradient in τ_{pxx} increases with increasing We. Thus, the extensional flow in the wake of the cylinder becomes increasingly important with increasing We. Similar phenomena have also been observed for both the CR and FENE-P model calculations as in the case of a linear array of cylinders discussed in chapter 5.

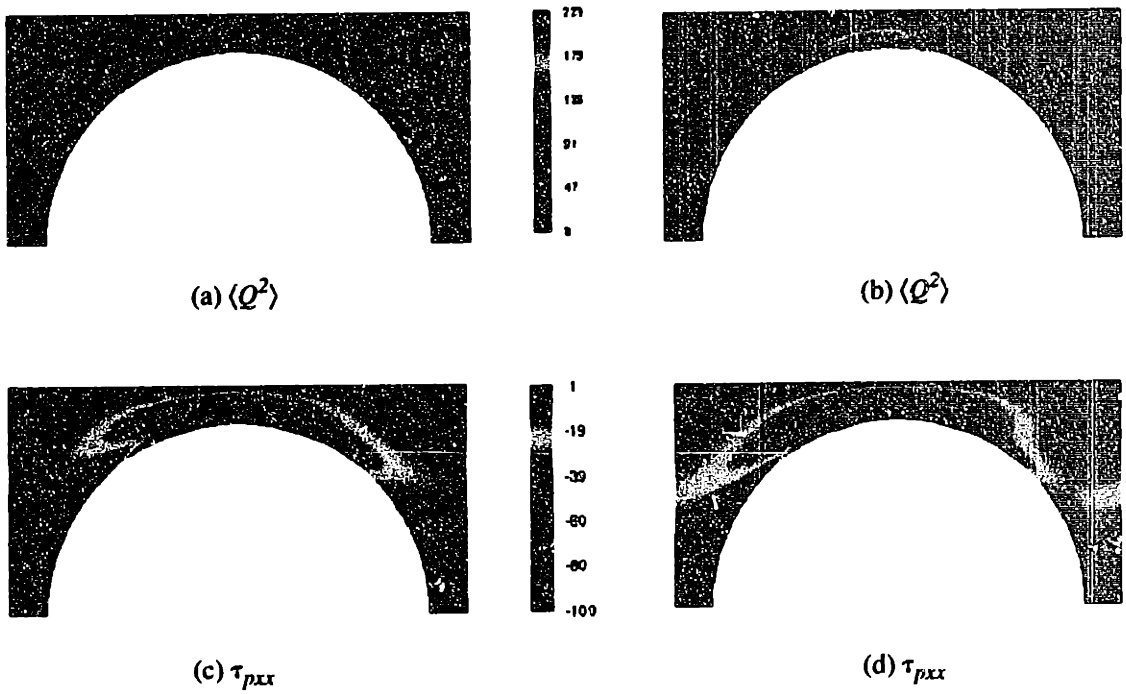

Figure 6-5 Dependence of $\langle Q^2 \rangle$ on We for the Giesekus model with $\alpha = 10^{-2}$ and $\beta = 0.59$. (a) We = 0.2; (b) We = 0.5, flow around a square array of cylinders with $L = 2.4$ and $H = 2$. Importance of wake extensional flow on axial normal stress τ_{pxx} for the Giesekus model for (c) We = 0.2 and (d) We = 0.5.

For the finitely extensible dumbbell models, calculations can be performed up to We ≈ 0.35 for the CR model and We ≈ 0.38 for the FENE-P model with mesh M1 before the positive definiteness of the configuration tensor is lost. For the two FENE models, a more refined mesh such as M2 allows the calculations to reach We ≈ 0.52 and We ≈ 0.58, respectively, without the loss of positive definiteness of the $\langle QQ \rangle$ tensor. All three constitutive equations, the Giesekus, CR and FENE-P models, predict very similar stresses. Similarities in the stress field have also been

reported in the study of viscoelastic fluid around a linear periodic array of cylinders (in Chapter 5). This is not surprising because all three models predict very similar planar elongational flow behavior. At a fixed We, the Giesekus model predicts the largest $|\tau_{pxx}|$, followed by the CR model and the least is given by the FENE-P model. The ordering in the extreme value of τ_{pxx} is consistent with the response of the first normal stress coefficient, Ψ_1, in steady simple shear flow (see chapter 5). Thus, as in the case of a periodic, linear array of cylinders, the importance of the shear flow behavior of the models is also observed in viscoelastic flow around a square array of cylinders. Similar to the case of a linear array of cylinders (see chapter 5), the contours of molecular extension also are qualitatively similar (apart from the very large elongations possible for the Giesekus model). All three models predict that the largest molecular extension remains in the highest shear rate region, reconfirming the importance of shear flow in flow around cylinders in any kind of arrangement. At any We, the ordering of $\langle Q^2 \rangle_{max}$ is consistent with the response of $\langle Q^2 \rangle$ in simple shear flow, with the FENE-P model predicting the smallest $\langle Q^2 \rangle_{max}$, followed by the CR and Giesekus models.

6.3.3 Inertialess flow of viscoelastic fluid with $\beta = 0.1$

The effect of changing β on molecular extension for the CR model is examined in Fig. 6-6. Decreasing β from 0.59 to 0.1 effectively lowers the contribution of the solvent. At We = 0.5, the size of the flow recirculation is decreased by 43% as the boundary between the bulk flow and recirculation zone moves closer to the symmetry plane. The strength of flow separation $-\psi_{min}$ is increased slightly from 0.0076 at $\beta = 0.59$ to 0.0079. Significant changes in the molecular extension with decreasing β are also noted. Although the overall shape of $\langle Q^2 \rangle$ contours remains unchanged, $\langle Q^2 \rangle_{max}$ is smaller for smaller β (see Figs. 6-6(b) and (d)). Similar changes in flow behavior and $\langle Q^2 \rangle$ fields are also noted for both the Giesekus and FENE-P models, once again confirming the results in a linear array of cylinders presented in chapter 5.

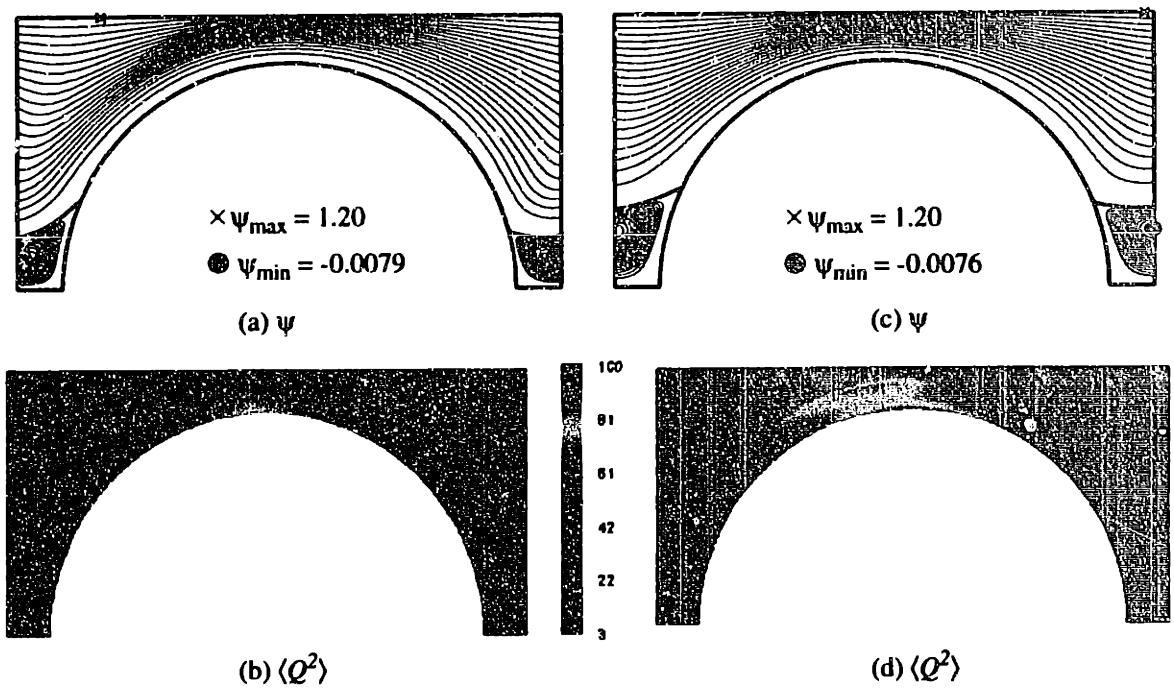

Figure 6-6 Effects of β on stream function (ψ), and molecular extension ($\langle Q^2 \rangle$) for the CR model with $Q_0 = 10$ at We = 0.5 for a square array of cylinders with $L = 2.4$ and $H = 1.2$. (a)-(b) β = 0.1 and (c)-(d) β = 0.59.

6.3.4 Flow with inertia

For a Newtonian fluid, inclusion of inertia modifies both the flow kinematics and pressure drop across the cylinder. Both the size and strength of the flow recirculation are increased with increasing Reynolds number as the boundary between the wake and bulk flow moves farther away from the centerline. For Re < 1, the pressure drop across the unit cell is fairly insensitive to Re; however, a significant increase in Δp_c due to fluid inertia begins to occur at Re ≈ 4.

For a viscoelastic fluid, the effect of inertia is examined by keeping We constant while varying Re, where Re is defined in terms of the zero-shear-rate viscosity and cylinder radius $\mathrm{Re} = \rho \langle v \rangle R_c / \eta_0$. Using this definition, the viscoelastic models predict that inertia has very little effect on flow kinematics for Re < 1; and the maximum molecular extension, $\langle Q^2 \rangle_{max}$, decreases with increasing Re for Re < 1. For Re > 1, the flow and periodic pressure fields are modified significantly, leading to a noticeable increase in the maximum molecular extension with Re. As shown in Fig. 6-7, the size of the flow recirculation is significantly enhanced because of incorpo-

ration of inertia, and the pressure generated in the minimum gap region is tripled as Re increased from 1.0 to 17.0. As Re further increases, $\langle Q^2 \rangle_{max}$ increases gradually.

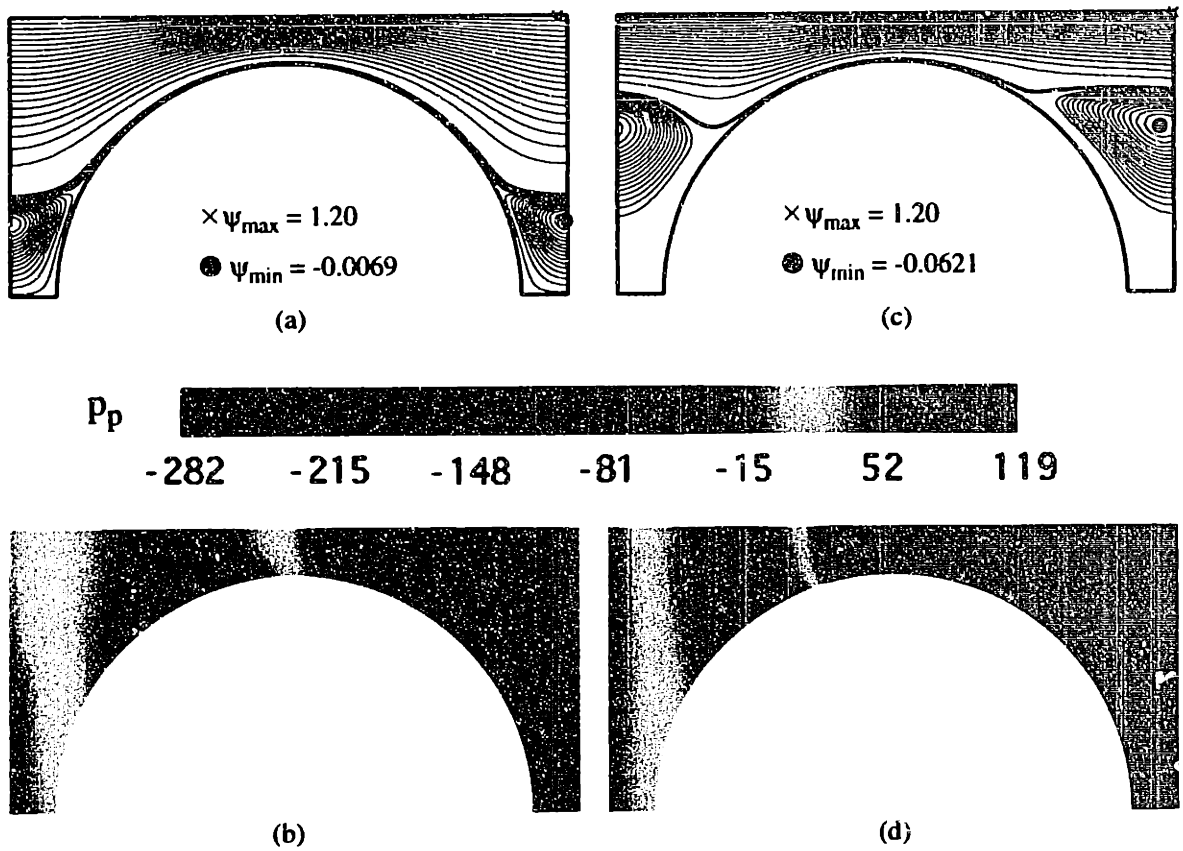

Figure 6-7 Effects of inertia on flow and pressure fields for a Giesekus model ($\alpha = 10^{-2}$, $\beta = 0.59$) flow around a square array of cylinders; comparisons are made at fixed De = 0.5. The streamfunction, ψ, and periodic pressure, p_p contours shown in (a)-(b) correspond to Re = 1.0, and (c)-(d) are for Re = 17.0.

6.4 Flow around a staggered array of cylinders (L = 2.4, H = 2.4)

We examine the case where alternating layers of cylinders are displaced to form a staggered array of cylinders. Here, we consider L = H = 2.4 in order to keep porosity constant at 45.5%.

6.4.1 Newtonian flow

Across the periodic plane (x = 1.2), the v_x is the same as in the case of the linear periodic arrays when y is normalized with the gap width. Thus, the no slip cylinder wall is equivalent to the channel wall. As in the square arrays, the flow is separated in between adjacent cylinders. The stress fields are significantly modified from the square array case. However, much of this is due to the difference in scaling we use between the square and staggered arrays, although the scaling used seems to give rise similar streamwise velocity profiles across the periodic plane. The extreme normal stress τ_{xx} is halved from ±35.394 for square arrays to ±17.884 for staggered arrays, the minimum τ_{xy} is shifted by a factor of six from -96.949 for square arrays to -15.546, while the maximum τ_{xy} is increased from 1.304 for square arrays to 15.402 for the staggered arrays.

Although there are only small changes in the velocity field in going from the square array to the staggered cylinder arrangements, the dimensionless, Δp_c is significantly decreased from 358.09 to 93.780. The large difference is due to the scaling in the mean fluid velocity, consistent with the aforementioned large differences in the components of stress field.

6.4.2 Viscoelastic flow

Viscoelastic calculations for the Giesekus model can be carried out to a maximum We ≈ 0.33 with mesh M4 before the positive definiteness of the configuration tensor is lost. Quadrupling the number of elements in M4 allows the calculations to continue to We ≈ 0.58 without the loss of the positive definiteness of the $\langle \boldsymbol{QQ} \rangle$. The regions where $\langle Q^2 \rangle < 0$ are localized to the boundary between the flow recirculation zone and the bulk flow, which has the large stress gradient as indicated in Fig. 6-8(b), thus inadequately refined meshes.

For a viscoelastic fluid, slight shifts in v_x with We are noted across the periodic boundary. Rescaling of y to the vertical gap width reduces v_x to the same form as in the linear periodic arrays. Changes in flow kinematics are small in comparison with stress and molecular extension fields. The most significant changes for an increasing We are observed in the molecular extension and normal stress fields. Fig. 6-8 is a contour plot of $\langle Q^2 \rangle$ and τ_{pxx} for the Giesekus model at We = 0.5. The overall degree of molecular extension is smaller than in the square arrangement because the effective minimum gap distances between the neighboring cylinders are increased

while keeping the porosity constant. The maximum molecular extension $\langle Q^2 \rangle_{max}$ is shifted from the cylinder surface in the square arrays to the side of the cylinder at the minimum gap region.

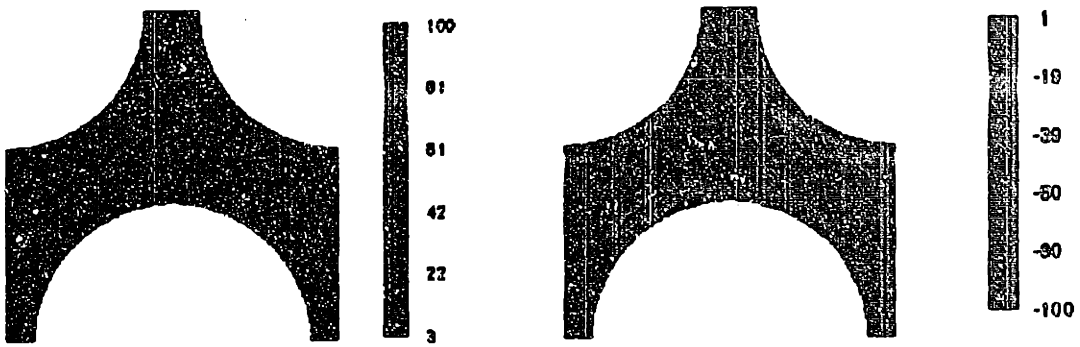

(a) $\langle Q^2 \rangle$ (b) τ_{pxx}

Figure 6-8 Contours of the (a) average molecular extension, $\langle Q^2 \rangle$, and (b) polymeric normal stress, τ_{pxx}, for viscoelastic flow around a staggered array of cylinders ($L = H = 2.4$). Results are for the Giesekus model with $\alpha = 10^{-2}$ and $\beta = 0.59$ at We = 0.5.

6.5 Flow around a staggered array of cylinders (L = 3.4, H = 1.7)

We consider the case where horizontal spacing L is lengthened and vertical spacing H is shortened so that $L = 2H = 3.4$ to keep the porosity constant at 45.5%.

6.5.1 Newtonian flow

At a fixed porosity of 45.5%, lengthening the lateral spacing L eliminates the flow separation zone that connects the two neighboring cylinders. The axial velocity across the periodic plane at x = 1.7 is very similar to the case of a widely spaced linear periodic array of cylinders, with the exception that v_x does not yet approach fully developed channel flow. The components of stress τ_{xx} and τ_{xy} are modified when L and H are changed. As shown in Fig. 6-9, compared to the previous staggered arrays in section 6.4, stress gradients close to the cylinder surface are steeper. This is consistent with the limiting behavior for $L/H = \infty$ where the staggered array reduces to a square array of cylinders.

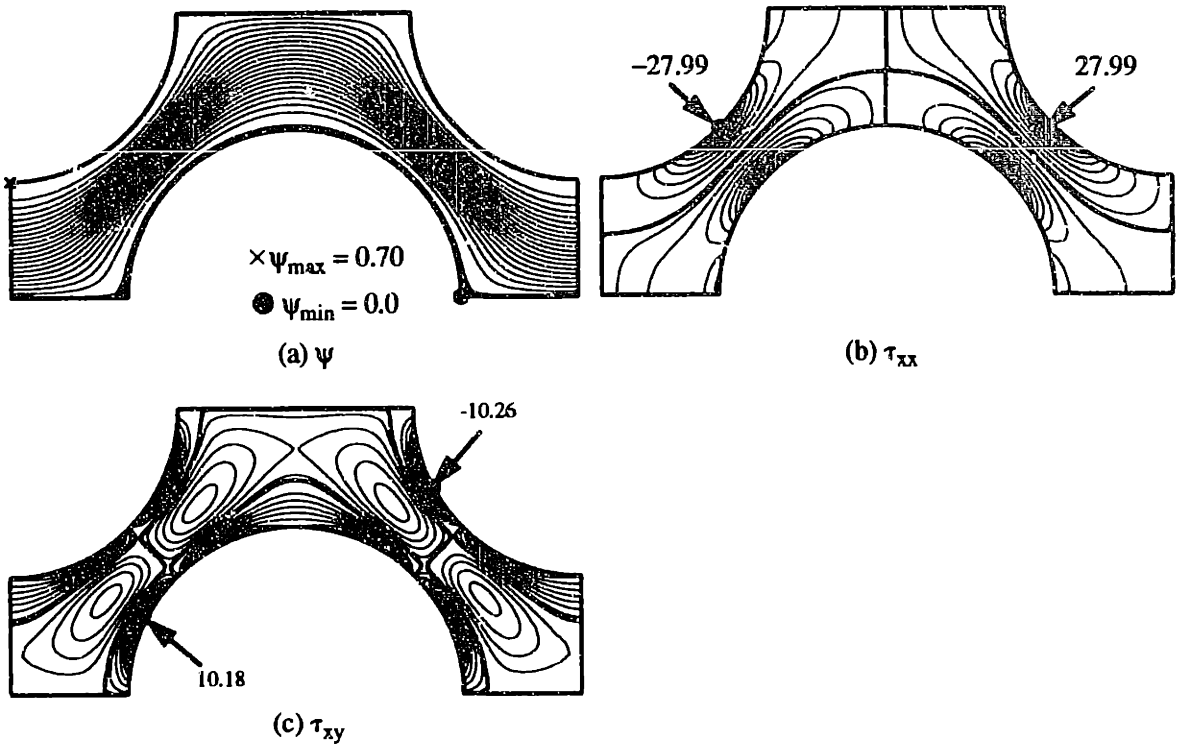

Figure 6-9 Solution fields for Newtonian fluid flow around a staggered array of cylinders with L = 3.4, H = 1.7. Twenty equally spaced contours between the minimum and maximum values are shown. (a) Streamfunction, ψ; (b) and (c) are components of the extra stress τ_{xx} and τ_{xy}.

The doubling in the extreme τ_{xx} is consistent with the increased pressure drop Δp_c per cylinder. Δp_c is increased from 93.780 for the staggered arrangement where $L = H$ to 172.43. The strong dependence of Δp_c on array arrangement suggests that the highest pressure drop is achieved by placing cylinders in a channel, the second largest Δp_c is found in square arrays, and the lowest Δp_c is achieved in the staggered arrays in which the larger the horizontal spacing, the higher the pressure drop.

6.5.2 Viscoelastic flow

Calculations for the Giesekus model can be continued to a maximum We ≈ 0.35 with mesh similar to M4 before the positive definiteness of the configuration tensor is lost. Quadrupling the number of elements in M4 allows the calculations to continue to We ≈ 0.40 without the loss of the positive definiteness of $\langle QQ \rangle$. As shown in Fig. 6-10, the regions of large molecular extension are highly localized in the narrow strip along the side of the cylinder as well as in the wake of the cyl-

inder where strong extensional flow develops. As in the linear, square and staggered arrays presented in section 6.2 to 6.4, the maximum molecular extension remains in the minimum gap. This indicates that shear flow dominates in all these flow geometries.

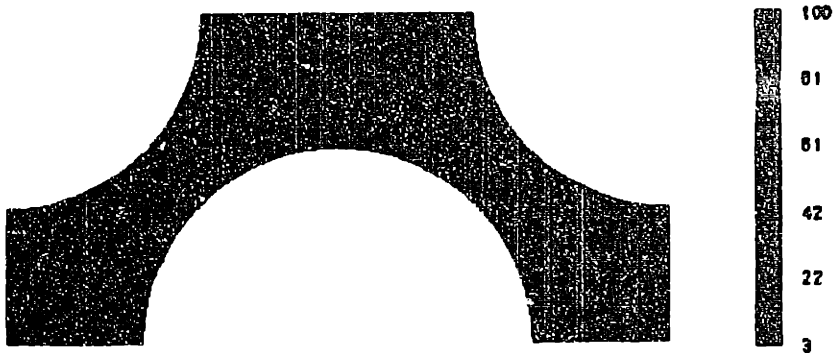

Figure 6-10 Contours of the average molecular extension $\langle Q^2 \rangle$ for flow around a staggered array of cylinders ($L = 2H = 3.4$). Results are for the Giesekus model with $\alpha = 10^{-2}$ and $\beta = 0.59$ at We = 0.5.

The strong dependency of pressure drop per cylinder on array arrangement raises the question: at a fixed porosity, how does the degree of molecular extension depend on the geometric arrangement of the cylinders? Here, we characterize the degree of molecular extension in a given flow geometry by $\langle Q^2 \rangle_{max}$. Fig. 6-11 clearly indicate that at any given We the ordering in $\langle Q^2 \rangle_{max}$ for all three constitutive equations, is consistent with the ordering in the pressure drop. Furthermore, the Giesekus model predicts the largest $\langle Q^2 \rangle_{max}$, followed by the CR model. The least molecular extension is given by the FENE-P model. This ordering is consistent with the response of $\langle Q^2 \rangle$ in simple shear flow.

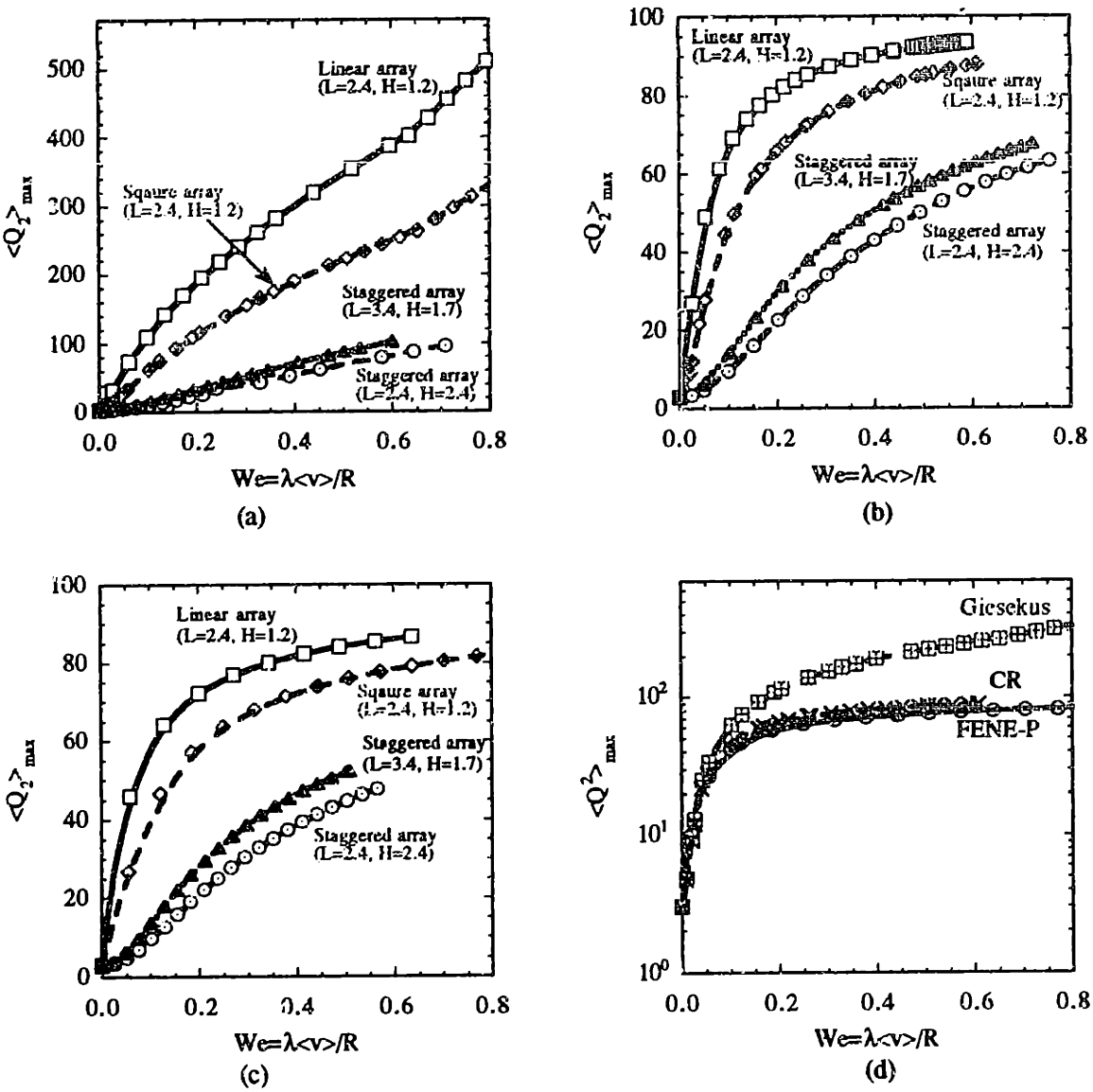

Figure 6-11 Maximum molecular extension, $\langle Q^2 \rangle_{max}$ for the (a) CR, (b) Giesekus, and (c) FENE-P models with model parameters of $\beta = 0.59$ and $1/\alpha = Q_0^2 = 100$, flowing around various cylinder arrays with a porosity of 45.5%. (d) compares the degree of molecular extension predicted by all three models in a square array of cylinders.

6.6 Drag force on the cylinder

6.6.1 Newtonian Fluid

The drag force on the cylinder in four different array arrangements is given in Table 6.1. Clearly, the drag force converges with mesh refinement. A cylinder experiences the most flow

resistance when it is placed in a line that is confined in a channel. Drag force can be reduced by rearranging the cylinders to form a square array. Further drag reduction can be achieved by staggering the cylinders, and at a fixed porosity, increasing spacing that is normal to the flow direction further decreases the drag force.

Table 6.1: Convergence of the dimensionless Newtonian drag force per unit length of cylinder $F_{D,N}$ on a cylinder in different cylinder arrangements with a fixed porosity of 45.5%. The drag force is made dimensionless with the product of viscosity and average velocity, $\eta_0\langle v\rangle$.

Array arrangement	Course mesh	Intermediate mesh	Refined mesh
linear (L = 2.4, H = 1.2)	1169.663	1169.588	1169.588
square (L = 2.4, H = 1.2)	395.205	395.150	395.139
staggered (L = H = 2.4)	103.940	105.034	105.208
staggered (L = 2H = 3.4)	149.112	155.369	157.032

6.6.2 Effect of array arrangements

The importance of the array geometry on pressure drop and the drag for a Newtonian flow have suggested that the linear array gives rise to the largest pumping cost, followed by the square and staggered arrays. Figure 6-12 shows that the Giesekus model predicts that the drag force enhancement, $\chi = F_D/F_{D,N}$, also depends strongly on array arrangement. The largest change in χ is given by the linear periodic arrays, and the ordering is consistent with the response of the pressure drop as expected. As in the case of viscoelastic flow around a linear periodic array of cylinders, shear thinning seems to play a significant role in determining the drag response when the porosity is fixed at 45.5%. Both the Giesekus and FENE-P models predict shear thinning behavior and both predict that drag enhancement monotonically decreases with We, whereas the drag enhancement for the constant viscosity CR model shows a minimum. The sensitivity of drag enhancement to array arrangement is identical for the shear thinning Giesekus and FENE-P models. The constant viscosity CR model, on the other hand, shows the same kind of dependence on flow geometry in χ as the shear thinning models of Giesekus and FENE-P for low We prior to the recovery in the drag force. At higher We, the dependence of χ on flow geometry is altered. We suspect that the dominance of shear flow behavior in the calculations presented here is due to the high degree of confinement by the slit for a porosity of 45.5%. It is possible that the elongational flow

properties of the models will become increasingly important when the porosity is increased. We have performed calculations with mesh M4 for a porosity of 55% with all of these models, and we obtain very similar trends for the shear thinning Giesekus model. This suggests that porosity must be quite large for the effects of the walls to be negligible.

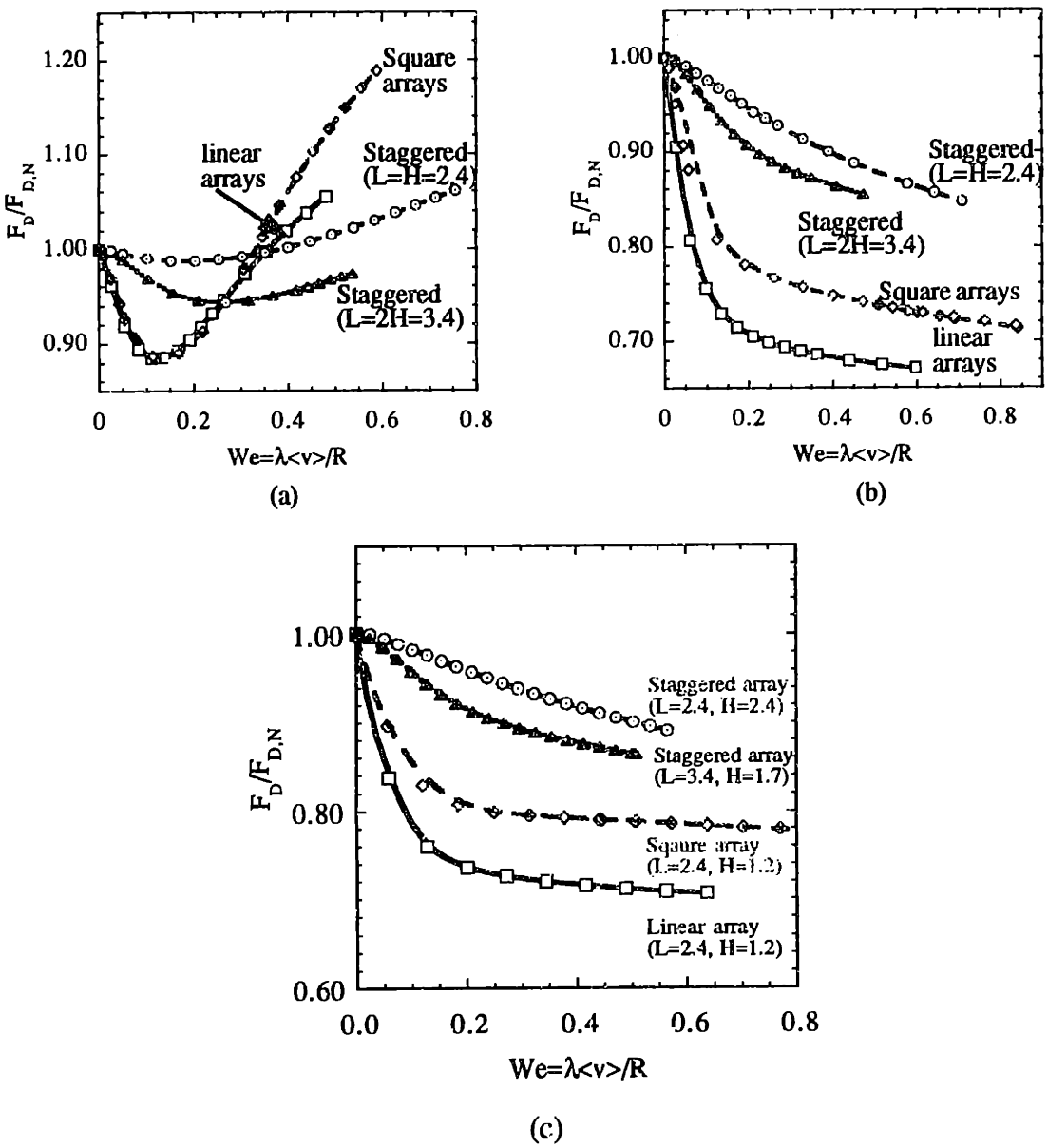

Figure 6-12 Effects of array arrangement on the viscoelastic drag enhancement χ with We for (a) CR model and (b) Giesekus model fluids flow around these geometries. Model parameters are chosen as $\beta = 0.59$ and $1/\alpha = Q_0^2 = 100$.

6.6.3 Effects of model parameters

The effects of changing β and the maximum extensibility Q_0 for the CR model or the degree of anisotropic mobility factor α for the Giesekus model on the drag is only examined for viscoelastic flow around a square array of cylinders. As shown in Fig. 6-13, for $Q_0^2 = 1/\alpha = 100$, the largest change in drag force enhancement is found for smaller β values. For both large and small β values, both the Giesekus and FENE-P models predict that the drag force on the cylinder monotonically decreases with increasing We, whereas the drag enhancement for the CR model shows a minimum at We ≈ 0.15 for β = 0.59 and We ≈ 0.2 for β = 0.1. The unexpected differences between the drag force on the cylinders for the FENE-P and Chilcott-Rallison models has also been reported for viscoelastic flow around a single, confined cylinder and linear periodic array of cylinders with variable L and $H = 2$. Since all three models predict identical elongational response but different viscometric behavior, we conclude that the shearing aspect of this flow is critical in determining the drag force in both linear periodic square array of cylinders.

The depth of the minimum in x increases with increasing molecular extensibility, as shown in Fig. 6-13c for the CR model with values of Q_0 ranging from 5 to ∞. The location in We of the minimum is shifted from about We = 0.1 at $Q_0 = 5$ to We = 0.2 for the Oldroyd-B limit ($Q_0 \rightarrow \infty$). The Giesekus model, on the other hand, shows the opposite trend.

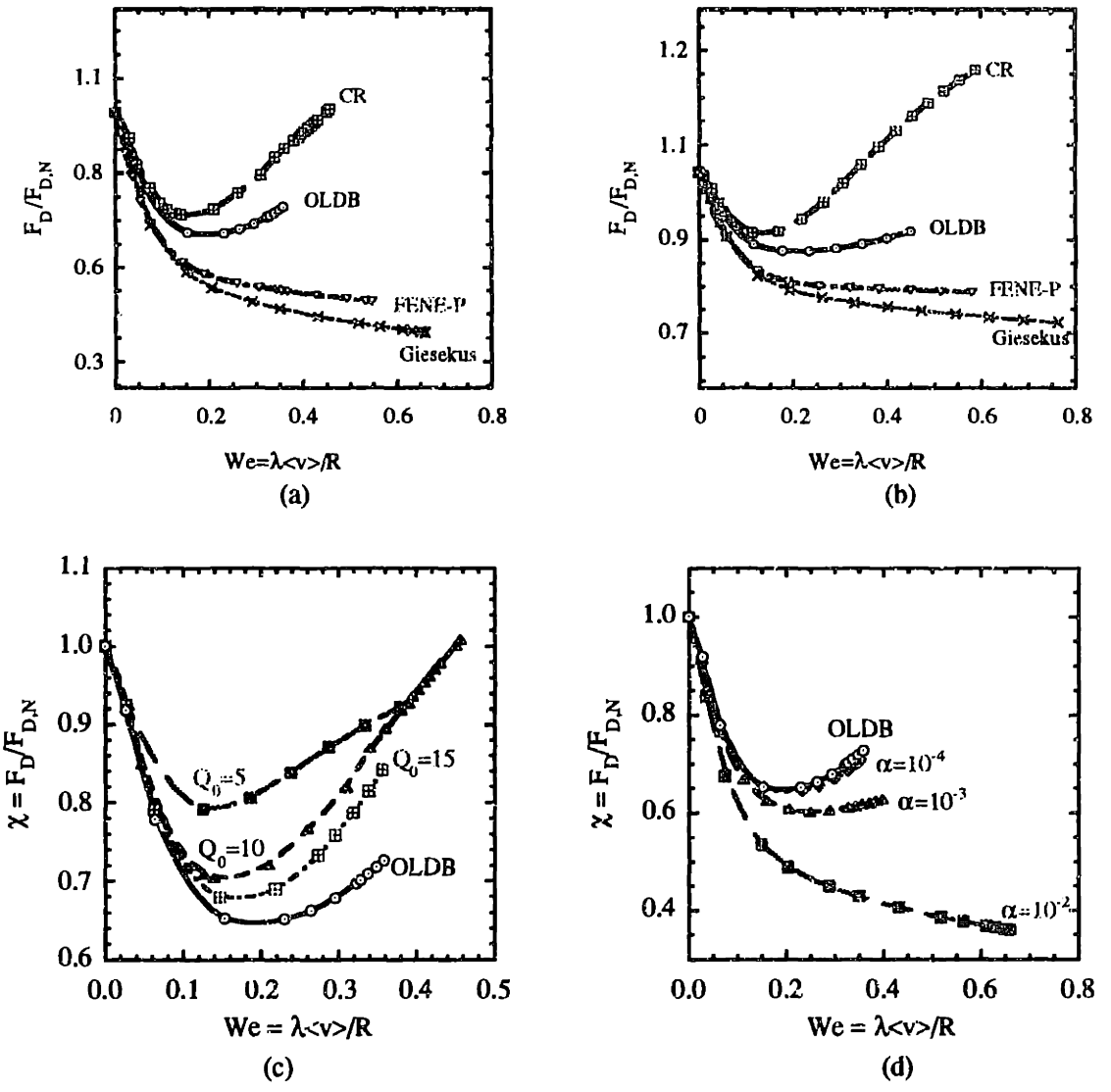

Figure 6-13 Effects of model parameters on the drag enhancement χ for viscoelastic flow around a square array of cylinders with $L = 2.4$ and $H = 1.2$ (a) $\beta = 0.1$ and (b) $\beta = 0.59$, and $1/\alpha = Q_0^2 = 100$. Dependence of the viscoelastic drag enhancement χ on molecular extensibility for the Chilcott-Rallison and Giesekus models in flow around square array of cylinders. (c) CR model with fixed $\beta = 0.1$ but variable Q_0; (d) Giesekus model with fixed $\beta = 0.1$ and variable α.

6.6.4 Effect of inertia

The effect of taking into account fluid inertia is examined only in the square array of cylinders. For a Newtonian fluid, the onset of a significant increase in the drag force occurs at $Re_{crit} \approx 5$. Introduction of a dilute polymer solution reduces the value to $Re_{crit} \approx 1$ as shown in Fig. 6-14. All three constitutive models predict that inertia enhances flow resistances, and as a result, the drag on the cylinder increases with increasing Re when We is fixed. The critical Re for all three

models is O(1), which suggests that cylinder radius and zero-shear-rate viscosity are appropriate characteristic quantities with which to characterize the inertial effects in viscoelastic flow studies.

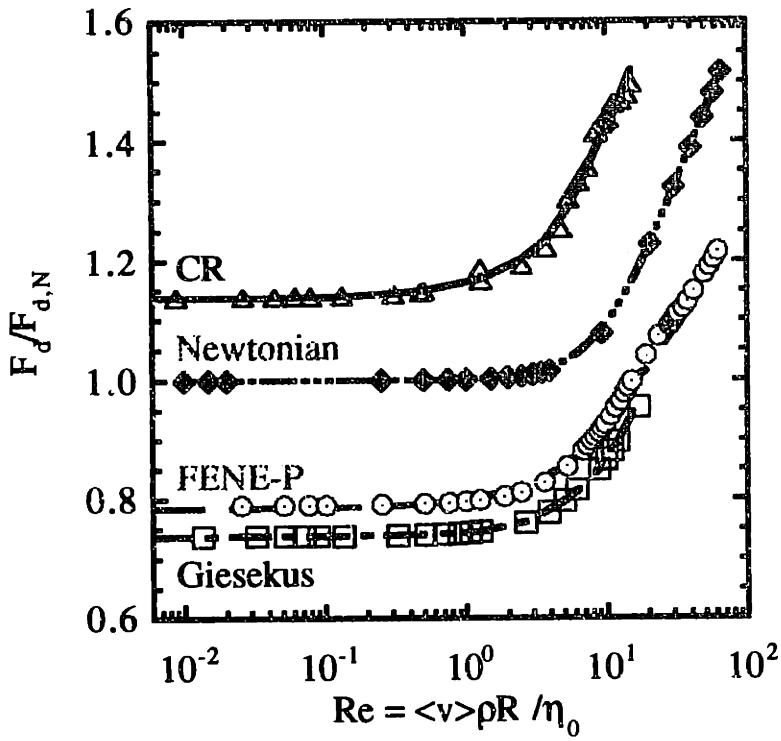

Figure 6-14 Effect of inertia on the drag force per unit length of cylinder for Newtonian and viscoelastic fluid (Giesekus, FENE-P and CR models) flow around a square array of cylinders with $L = 2.4$ and $H = 1.2$ and model parameters $\beta = 0.59$ and $1/\alpha = Q_0^2 = 100$.

As shown in Fig. 6-7, inertia tends to enhance flow recirculations, which seems to suggest that the flow is somewhat weakened when inertia is included for Re > 1. Within the flow recirculation zone, pressure is increased slightly with Re, but the most significant rise in pressure is found in the minimum gap region where the shear rate is highest. Fig. 6-15 shows that the contribution of form drag to total drag is approximately constant for Re < 0.1, and decreases quickly, reaching a minimum at Re ≈ O(10) for all three constitutive models. The pressure field remains unchanged for Re < 0.1 and the extreme values of p_p increases for Re > 0.1, leading to a greater pressure buildup outside of the flow recirculation region. Although the contribution of the pressure to the total drag force actually decreases with Re, the pressure drop due to the presence of neighboring cylinders, $\Delta p_p = p_{p,max} - p_{p,min}$ continues to increase as inertia becomes increasingly important.

The increase in Δp_p is needed to overcome additional frictional forces arising from inertia, and as a result the drag force experienced by the cylinder increases with increasing Re.

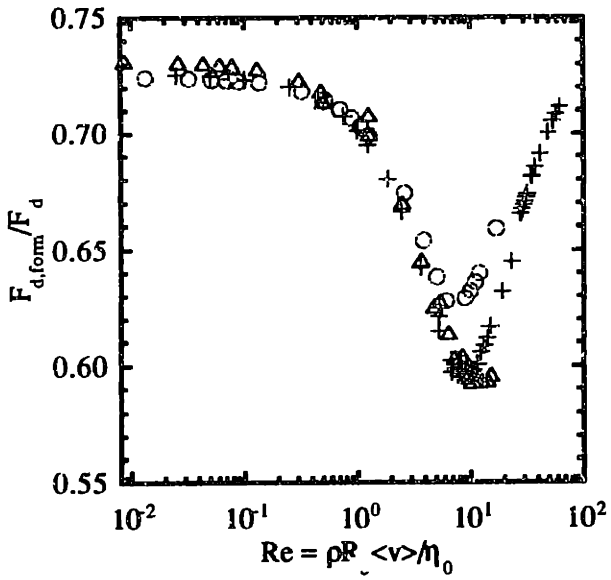

Figure 6-15 Contribution of pressure to drag force in terms of fraction of form drag, for viscoelastic flow around a square array of cylinders. Different symbols denotes different constitutive models: "○" for Giesekus model, "+" for FENE-P model and "△" for the CR model. Model parameters are $\beta = 0.59$ and $1/\alpha = Q_0^2 = 100$ at fixed We = 0.5.

6.7 Summary on flow around arrays of cylinders

Numerical simulation is used to investigate the flow of polymer solutions around linear, square and staggered periodic arrays of cylinders with a constant porosity of 45.5%. The most interesting result of this study is that, the pressure drop per cylinder depends strongly on array arrangement, and as does the maximum molecular extension. For the three types of arrays, the ordering in $\langle Q^2 \rangle_{max}$ is consistent with the ordering in the pressure drop, Δp. The linear arrays have the most efficient array arrangement for stretching out polymer chains, followed by the square arrays; the least extension is found in the staggered arrays. Even though the fore and rear stagnation points and the converging and diverging regions around the cylinder suggest the importance of elongational flow in this problem, the solution fields clearly illustrate that the shear flow dominates in all three flow geometries. This is seen in at least two ways: First, the contours of molecular extension show that the largest extension remains in the highest shear rate region for all three array arrangements. Secondly, the viscoelastic drag enhancement χ is very sensitive to shear thin-

ning in the viscosity. This is seen in the dramatic difference in χ between the Chilcott-Rallison and FENE-P models.

The constant viscosity that results from the approximation used in deriving the Chilcott-Rallison model appears to be responsible for the fact that χ shows a minimum with increasing We, whereas the FENE-P model does not. This is consistent with the previous numerical studies in linear periodic arrays of cylinders. For the Giesekus model, intramolecular forces are described by a Hookean spring, whereas a finitely extensible spring whose modulus is given by the Warner approximation is used in both the FENE-P and Chilcott-Rallison models. Hydrodynamic drag on the beads is taken to be anisotropic for the Giesekus model and isotropic for the other two models. The Chilcott-Rallison and FENE-P models differ subtly in their approximate treatment of the nonlinear force law. Thus, regardless of the array arrangements, subtle differences in approximations used in deriving constitutive equations from molecular theory can produce large effects in the fluid mechanics of the resulting models.

In the staggered arrays, the effects of horizontal intercylinder spacing L are also surprising. As L is increased from 2.4 to 3.4 at fixed porosity of 45.5%, flow separation disappears even for a Newtonian fluid. As the separation distance in the flow direction is increased, the Newtonian drag force on the cylinder doubles, the pressure drop per cylinder also doubles, and $\langle Q^2 \rangle_{max}$ increases.

In the square arrays, viscoelastic calculations have shown the decrease in recirculation zone thickness with increasing We, and this strongly suggest that viscoelasticity would inhibit separation. Decreasing β from 0.59 to 0.1 reduces the size of the flow recirculation zone and decreases $\langle Q^2 \rangle_{max}$, though the overall shape of $\langle Q^2 \rangle$ field is unchanged. Decreasing β also lowers the drag force enhancement. Increasing the maximum extensibility Q_0 for the CR model or the degree of anisotropic mobility α for the Giesekus model further reduces the drag force on the cylinder at a given We. Inclusion of fluid inertia shifts the critical Reynolds number for significant increase in the drag force to a lower value.

Chapter 7

Experimental methods

Another important contribution of this thesis is the comparison of predictions using standard viscoelastic constitutive equations with experimental data for 0.31 wt% PIB/PB/C14 solution flowing around a linear array of cylinders. Fluid characterization is presented in section 7.1. The fluid used in the experiments was characterized in both simple shear and elongational flow geometries. The flow geometry design is described in section 7.2. The use of laser Doppler velocimetry (LDV) for pointwise velocity measurements and a strain gauge for force measurements on a cylinder are discussed in sections 7.3 and 7.4, respectively.

7.1 Fluid characterization

7.1.1 Rheological Methods

The fluid used in this thesis is the MIT PIB Boger fluid, consisting of 0.31 wt% high molecular weight polyisobutylene (PIB) (Exxon Vistanex L-120, MW $\approx 1.8 \times 10^6$ g/mol) dissolved in a Newtonian solvent of 4.83 wt% tetradecane (C14) and 94.86 wt% polybutene (PB) (Amoco H100, $MW \approx 900$ g/mol). The MIT fluid was first formulated by Muller (1986) and is a member of a class of polymer solutions now known as "Boger fluid" (Boger 1977, 1978) which were designed to have a constant viscosity over a large range of shear rates and to be highly elastic. The particular solution used for this study was prepared by Byars (1995) in the study of viscoelastic wake instabilities in the flow around a cylinder in a channel.

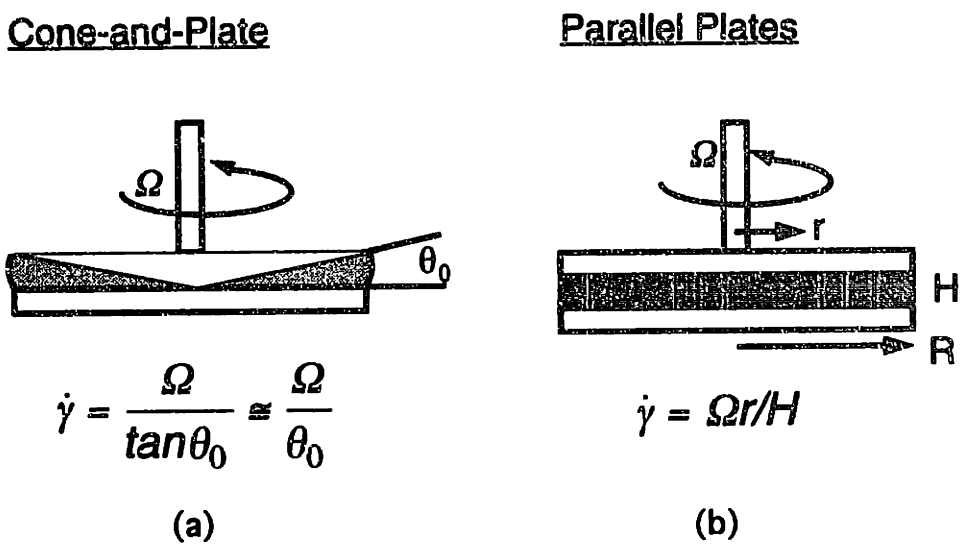

Figure 7-1: Schematic diagrams for (a) cone-and-plate and (b) parallel-plate flow geometries.

The fluid was prepared by first dissolving PIB in C14 and then mixing the PIB/C14 with PB. Quinzani *et al.* (1990) first thoroughly characterized the PIB/PB/C14 fluids of different composition by varying the relative amount of the three components. McKinley *et al.* (1993) used a similar 0.31 wt% PIB/PB/C14 fluid for examining the flow around a cylinder confined in a channel. Later experiments by Byars (1995) were conducted by preparing a new batch of fluid with the same recipe. Both McKinley *et al.* (1993) and Byars (1995) noted that the fluid underwent mechanical degradation after being pumped through the experimental apparatus. In this work, the viscosity ($\eta(\dot{\gamma})$) and the first normal stress coefficient ($\Psi_1(\dot{\gamma})$) of the original and present degraded fluids were measured. Although both η and Ψ_1 were essentially unchanged, the plateau in the apparent Trouton ratio for strain rate, $\dot{\epsilon} \geq 10\ s^{-1}$ of the degraded fluid was decreased by a factor of three from that of the original fluid.

7.1.1.1 Simple shear flow

Cone-and-plate Viscometer

Cone-and-plate flow is one of the most common viscometric flows used for obtaining rheolog-

ical material functions. A homogeneous shear flow is generated in the narrow gap between a plate and an inverted cone. The flow is purely azimuthal with no recirculating secondary flow in the limit of creeping flow and small cone angles. Under these conditions the shear-rate-dependent material functions, (η, Ψ_1) are uniform throughout the gap; Fig. 7-1(a) illustrates a cone-and-plate rheometer. For a very small cone angle $\theta_0 \ll 1$, the uniform shear rate throughout the flow domain is approximated by $\dot{\gamma} = \Omega/\theta_0$, where Ω is the cone rotation rate. The total torque $\mathcal{T}$ and normal force $\mathcal{F}$ exerted by the fluid on the lower plate for creeping flow are related to the material functions η and Ψ_1 by

$$\eta(\dot{\gamma}) = \frac{3\mathcal{T}\theta_0}{2\pi R^3 \Omega} \tag{7.1}$$

$$\Psi_1(\dot{\gamma}) = \frac{2\mathcal{F}\theta_0^2}{\pi R^2 \Omega^2} \tag{7.2}$$

Care is needed in interpreting any results obtained in a cone-and-plate rheometers because of the possible onset of flow instabilities at large shear rates. Experimental measurements in cone-and-plate viscometers have indicated the presence of viscoelastic flow instabilities at high rotation rates and large cone angles. Kocherov *et al.* (1973) first presented flow visualization evidence of flow instability for polyethylene melts in a disc-type extruder containing a cone-and-plate fixture at the exit. Their photographs clearly demonstrated that the fluid pathlines were not concentric circles but of a non-axisymmetric spiral form. The extent of this secondary flow depended on the rotation rate and cone angle. More recently, McKinley *et al.* (1991b, 1995) and Byars (1995) reported a similar type of flow instability with the 0.31 wt% Boger fluid. Byars (1995) considered cone angles between $4 - 15°$ and found that as the cone angle was decreased, the shear rate increased for a given rotation rate, and the flow was stabilized. He noted that the flow was steady at any rotation rate up to the maximum obtainable Deborah number, $De_0 = \lambda_0 \Omega \simeq 8.31$, and $Re = \rho \Omega R^2/\eta \simeq 0.42$ for a cone angle of 4°. Neither the total torque nor the normal force exerted on the fixture exhibited time-dependent variation up to the maximum shear rates. The spatial and temporal evolution of the secondary flow at larger cone angles was quantified by analyzing the recorded gray-scale video-image of the flow. Because of the lack of a characteristic length scale in this flow

geometry, the instability took the form of a self-similar logarithmic spiral as shown in Fig. 7-2. The sequence of the flow images shows that the recirculation moves inward with time, and fills the entire region between the cone and plate. As the cone angle was increased, the critical Deborah number $De_{0,crit}$ for the onset of flow instability increased and its wavenumber decreased. All of the observations indicated that the flow undergoes a transition even under creeping flow $Re < 0.5$ and small cone angle conditions $\theta \leq 15°(0.26\,\text{rad})$.

The linear stability analysis of Öztekin *et al.* (1994) using the OLDB model predicted the critical De and wavenumber, but failed to predict the restabilization. Calculations for the CR model and the single-mode Giesekus model showed restabilization for small cone angles because of shear thinning in the first normal stress coefficient. Because the shear rate is uniform throughout the entire gap, the instability filled the entire gap. Numerical results of Öztekin *et al.* (1994) confirmed the experimental findings of Byars (1995) in that as the cone angle decreases, the shear rate increases for a given rotation rate, which leads to stabilization of the flow for small angles. Good quantitative agreement at the critical conditions was obtained for a four-mode Giesekus model.

Parallel-plate Viscometer

The parallel-plate system is another widely used flow geometry in shear flow rheological characterization. Fluid samples are placed in between the two coaxial parallel disks as shown in Fig. 7-1(b). Although the flow is purely azimuthal, the flow field is inhomogeneous. Thus, the material functions such as $\eta(\dot{\gamma})$, and $\Psi_1(\dot{\gamma})$ are not constant throughout the flow domain. The measurements of the torque $\mathcal{T}$ and normal force $\mathcal{F}$ exerted by the fluid on the upper plate are again used to compute the shear-rate-dependent material functions. The shear rate is not uniform, and the shear rate at edge defines the characteristic shear rate of the flow,

$$\dot{\gamma}_R = \frac{\Omega R}{H} \tag{7.3}$$

The shear-rate-dependent viscosity and first normal stress coefficient are

$$\eta(\dot{\gamma}_R) = \frac{\mathcal{T}}{2\pi R^3 \dot{\gamma}_R}\left[3 + \frac{d\ln(\mathcal{T}/2\pi R^3)}{d\ln\dot{\gamma}_R}\right] \tag{7.4}$$

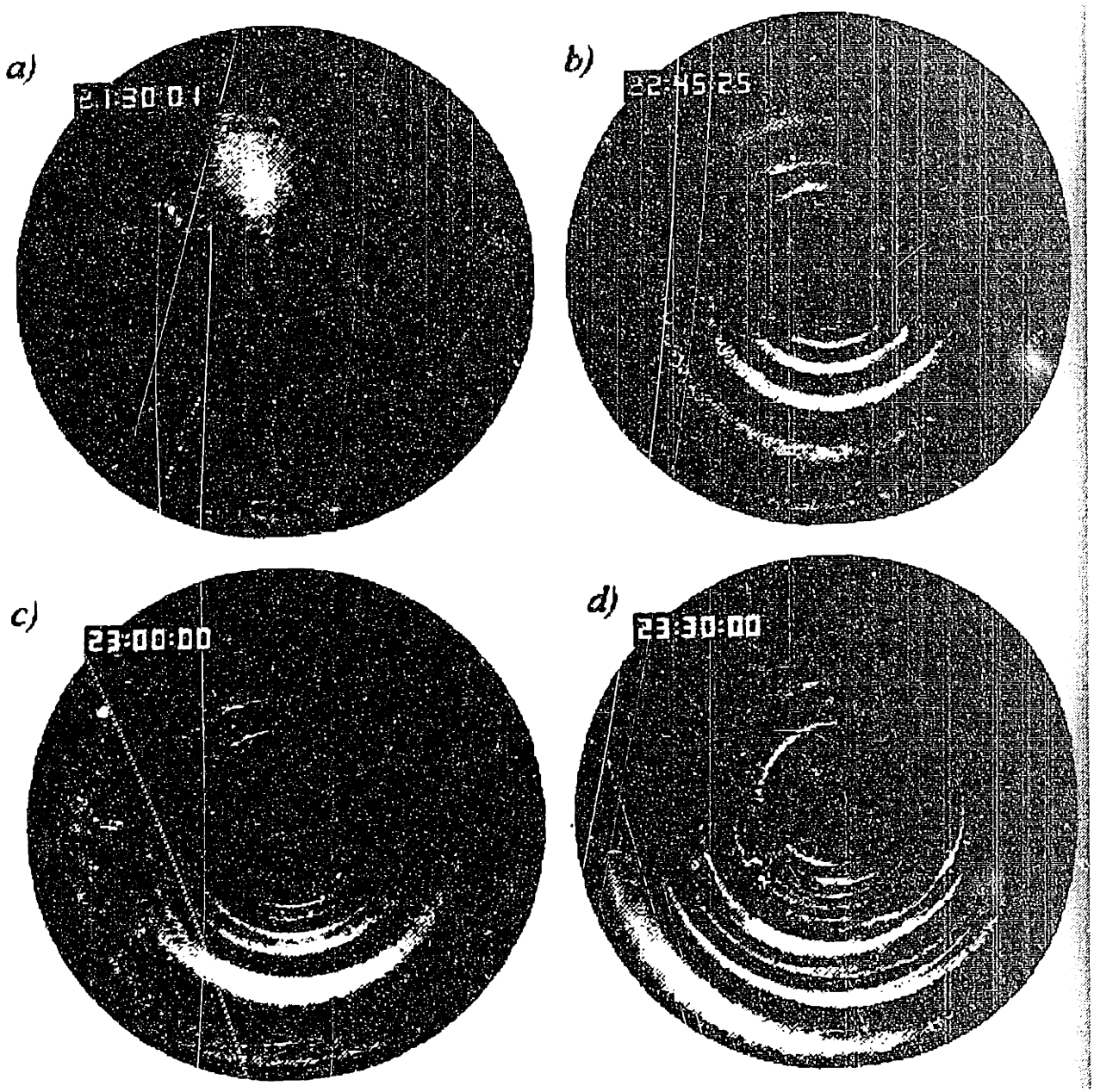

Figure 7-2: Onset and growth of the purely elastic instability observed in the 0.31 wt% PIB fluids in a cone-and-plate geometry with $\theta_0 = 10°$. The direction of rotation of the upper conical fixture is counterclockwise. (a) flow appears stable shortly after the Deborah number is increased from the supercritical value $De_0 = 5.28$ at time (t=21:00:00) (min:sec:frame); (b) 75 seconds later the secondary flow becomes visible; (c) inward traveling non-axisymmetric flow consisting of a single logarithmic spiral vortex; (d) ultimate fully nonlinear state. (Photographed by Byars, 1995.)

$$\Psi_1(\dot{\gamma}_R) = \frac{1}{\dot{\gamma}_R^2}\{\mathcal{F}/\pi R^2[2 + \frac{d\ln(\mathcal{F}/\pi R^2)}{d\ln\dot{\gamma}_R} + \frac{d\pi_{zz}(0)}{d\ln\dot{\gamma}_R}]\} \tag{7.5}$$

where $\pi_{zz}(0)$ is the normal pressure measured on disk at the center. The basic assumptions for interpreting experimental data are that the flow is always steady and purely azimuthal for all rotation rate.

Similar to the case of cone-and-plate flow, purely elastic instabilities can be present in the parallel plate flow at creeping flow conditions. Jackson *et al.* (1984) observed a purely elastic instability in the torsional flow of a polyacrylamide Boger fluid. The instability corresponded to an increase in the apparent viscosity and first normal stress coefficient as both the torque and normal forces showed a steady increase over a period of 20 minutes. More recent experiments conducted by McKinley *et al.* (1991b, 1995) and Byars (1995) using the 0.31 wt% PIB solution indicated the development of secondary flow. The series of gray-scale video images shown in Fig. 7-3 depict the evolution of flow at a fixed aspect ratio of $R/H = 20$. When the Deborah number is increased above the critical value, the stable base flow (a) becomes a single, azimuthal-mode, spatially periodic spiral (b-d), and at even higher De_0, the flow is in the ultimate fully nonlinear state with many modes present (e-f). The wavelength of the cells scales with the separation distance between the two plates. Flow visualization indicated that the spiral vortices travel outwards at a constant velocity across the disk but are confined to an annular region. The critical $De_{0,crit}$ required for the onset of the elastic instability increases as the separation distance between the plates is enlarged. The wavelength and wavespeed are scaled with the gap distance H and the rotation rate. At the onset of the rotational flow instability, the wavelength increases as the gap is enlarged, but the dimensionless wavenumber scales with the gap H and remains almost constant.

As for the cone-and-plate geometry, the linear stability analysis of Öztekin and Brown (1993) utilizing the OLDB model yielded good agreement for the wavespeed, wavelength, and azimuthal structure, but the instability existed for all radii greater than a critical value that depended on the Deborah number. Calculations with the CR model predicted an outer radius beyond which the flow was restabilized due to shear-thinning of the first normal stress coefficient (Öztekin and Brown, 1993). In the parallel-plate geometry, the shear rate increases linearly with increasing radius, but the shear-rate dependent relaxation time de-

creases. Therefore, at larger radius, the flow restabilizes, due to the lower effective Deborah number.

7.1.1.2 Shearfree flow

The study of polymer solutions in extensional flow fields has attracted significant attention in recent years. This is due to the fact that extensional flow is very important in industrial applications such as coatings and extrusion. Many techniques have been developed to generate extensional data. The homogeneous stretching methods illustrated in Figs. 7-4 (a) and (b) have been extensively used to measure material functions for uniaxial elongational flows of polymer melts. Both methods provide direct means of obtaining elongational flow and rate of stretching properties from the force and instantaneous cross-sectional area of the sample measurements. Other techniques include the fiber spinning system shown in Fig. 7-4 (c), the contraction flow (d), and the opposed-jet apparatus (e) considered in this study.

Sridhar *et al.* (1991) applied a filament stretching technique (Fig. 7-4 (a)) for measuring the extensional viscosity of 0.185 wt% PIB/PB/kerosene solutions. The liquid sample was held between two coaxial discs that move apart at a rate that increases exponentially with time. The filament length increases exponentially with time, and the resulting flow is approximately uniaxial extension at constant stretch rate. Later measurements by Tirtaatmadja *et al.* (1993) expanded the study to include three ideal elastic solutions, the model fluid M1 (0.24 wt% PIB/PB/kerosene), a 0.31 wt% PIB/PB/C14 MIT Boger fluid, and a shear-thinning model fluid A1 (2 wt% PIB/Decalin). The transient Trouton ratio, T_R, for all three fluids showed an initial linear viscoelastic region where T_R rises to 3, independent of extensional rate, followed by a dramatic increase in T_R to values in excess to 10^3. Steady state elongational stress measurements were attained only when $\dot{\varepsilon} = 2 - 3\,s^{-1}$ for a 0.31 wt% PIB/PB/C14 solution. Later experiments conducted by Spiegelberg *et al.* (1996) confirmed that solutions containing high molecular weight PIB exhibit significant strain-hardening for Hencky strain, ε, greater than two. The two solutions used in the experiments were 0.31 wt% PIB/PB/C14 and 0.30 wt% PIB/PB Boger fluids. The transient extensional viscosity increased by three orders of magnitude for both fluids, similar to the measurements by

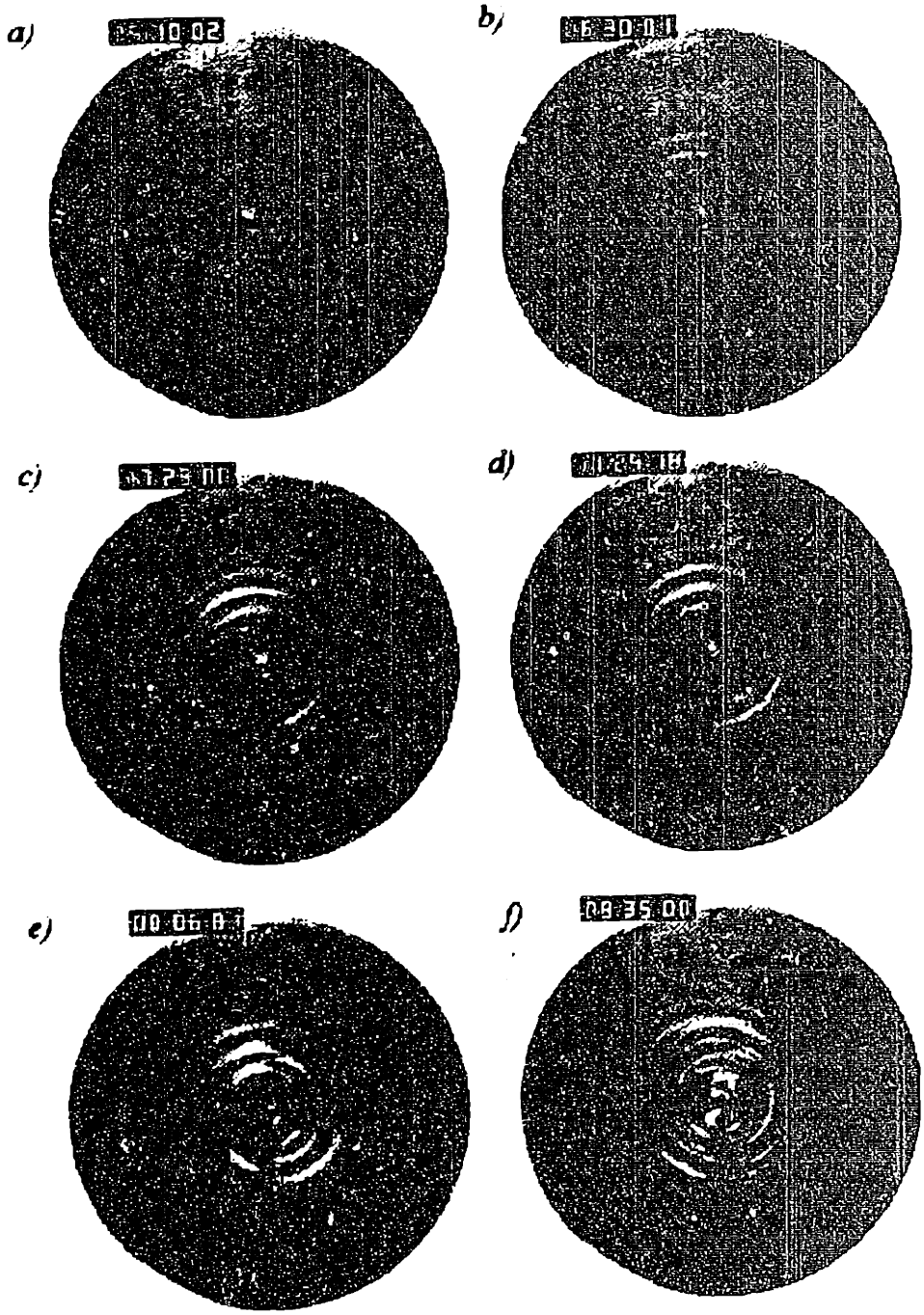

Figure 7-3: Onset and growth of the purely elastic instability observed in the flow of 0.31 wt% PIB fluids in a coaxial parallel disk with $R/H = 20$. (a) flow appears stable shortly after the Deborah number is increased from the supercritical value $De_0 = 5.99$ at time (t=5:00:00) (min:sec:frame); (b) after induction time of 90 seconds, the spatial structure of the secondary flow becomes visible; (c-d) outward traveling non-axisymmetric secondary flow consisting of a single spiral vortex; (e) nonlinear mode interaction; (f) ultimate fully nonlinear state. (Photographed by Byars, 1995).

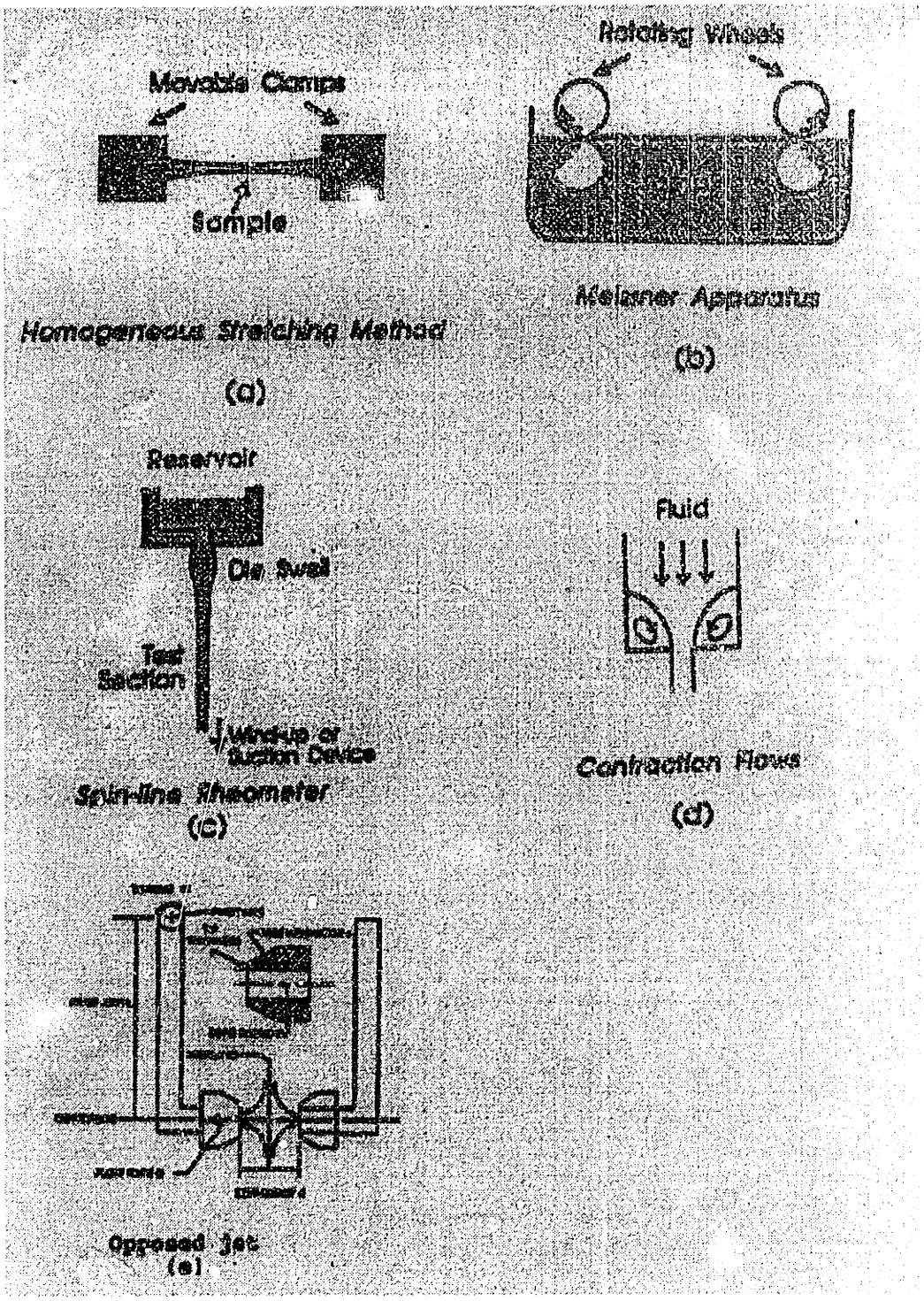

Figure 7-4: Schematic diagrams of the most commonly used extensional flow arrangements. (a) Approximately homogeneous stretching method; (b) Meissner apparatus; (c) spin-line rheometer; (d) contraction flows; (e) opposed jet rheometer (Armstrong and McKinley, 1995).

Tirtaatmadja *et al.* (1993). Video imaging of the flow near the stationary endplate showed that an instability arises when the Hencky strain greater than 4.5. Steady-state values of the extensional viscosity were not achieved in those experiments.

The purpose of the opposed jet rheometer (Rheometrics, RFX rheometer) described in this subsection is to measure the extensional viscosity of a polymer solution. The Rheometrics RFX opposed jet device is used to characterizing the elongation behavior of the fluid used in this thesis. The device is commercially available and designed for investigations of moderately viscous fluids. It has the flexibility of measuring liquids with viscosities ranging from 10 to $10^3\, Pa \cdot s$, and apparent extensional viscosities ranging from 3×10^{-2} to $10^3\, Pa \cdot s$.

The operating principles of the RFX rheometer are outlined here and a more detailed description can be found in the user's manual (1995). Two jets, facing each other across an adjustable gap are immersed in a beaker of the test sample, shown in Fig. 7-5(a). One jet is attached on to a movable arm while the second jet is held stationary. A torque transducer is mounted to the stationary arm. When liquid is drawn into the jets, the strain rate is approximately constant across the gap between them, provided the gap between nozzles is less than 2-3 times their diameter.

An extensional flow field is created in between the two nozzles as the fluid is drawn into both nozzles. A coordinate system is defined in Fig. 7-5(a), and a sketch of the flow field is given in Fig. 7-5(b). A stagnation point is created at the center of the geometry, with the flow approximately in uniaxial extension along the axis of the jets. The fluid accelerates as it moves away from the geometric center. A stretching deformation occurs in the x direction and a compression in the y and z directions. The velocity field around the stagnation point is $\boldsymbol{v} = (\dot{\epsilon}x, -\dot{\epsilon}y/2, -\dot{\epsilon}z/2)$, where $\dot{\epsilon}$ is the extension rate.

Both the inside diameter of the nozzles and the nozzle-to-nozzle separation distance are used to compute the apparent elongational viscosity $\overline{\eta}$. The force at the face of each nozzle is determined by dividing the torque (M) on the moment arm by its length (L). The apparent normal stress difference τ_N at the face of each nozzle is obtained by dividing the force by

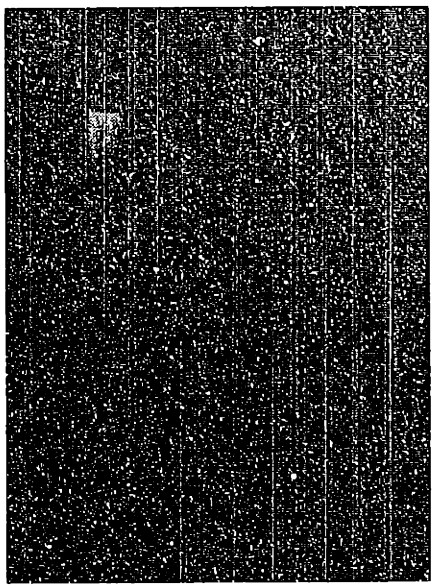

(a)

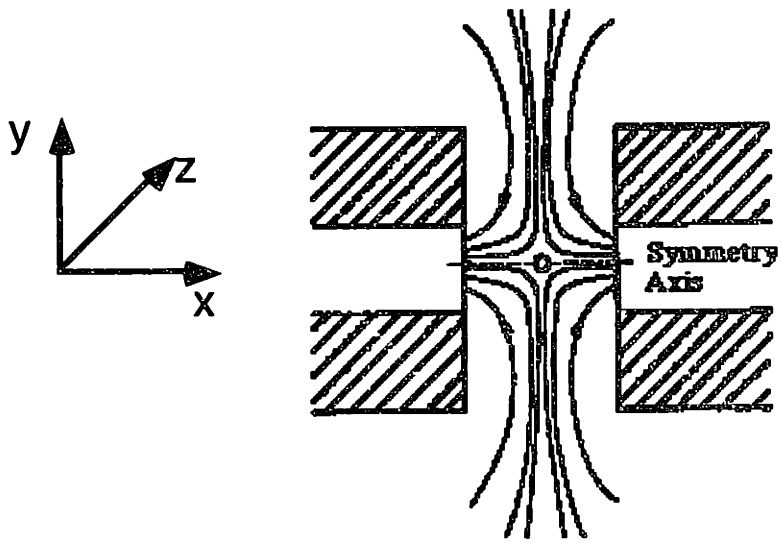

(b)

Figure 7-5: Opposed jet rheometer. (a) a photograph of the RFX rheometer (Rheometrics) used in characterizing the elongational behavior of the 0.31 wt% PIB/PB/C14 fluids and (b) a sketch of the flow field (Armstrong and McKinley, 1995).

the area of the nozzle's bore πR^2, where R is the radius of the nozzle bore:

$$\tau_N = \frac{M}{\pi R^2 L} \tag{7.6}$$

The apparent strain rate ($\dot{\varepsilon}$) is derived by dividing the mean fluid velocity by the half separation distance between the nozzles:

$$\dot{\varepsilon} = \frac{2Q}{\pi R^2 d} \tag{7.7}$$

Here d is the separation distance and Q is the volumetric flow rate through each nozzle. The apparent extensional viscosity is then the quotient of the stress and strain rate

$$\overline{\eta} = \frac{\tau_N}{\dot{\varepsilon}} \tag{7.8}$$

7.1.2 Fluid Rheology

The viscometric properties of the 0.31 wt% PIB/PB/C14 fluid have been measured with a Rheometrics RMS-800. In this subsection, simple rheological measurements for both original PIB/PB/C14 fluid, prior to being introduced into the flow cell, and the present solution labeled as 'degraded solution' are presented.

For the 0.31 wt% PIB/PB/C14 fluid, Quinzani *et al.* (1990) reported that a_T depends on temperature according to an Arrhenius expression as

$$a_T = \exp\left[\, 7362 \times \left(\frac{1}{T} - \frac{1}{298.15}\right)\right] \tag{7.9}$$

Mechanical degradation of polymer molecules after viscoelastic fluids flow past complex geometries has been widely observed (Müller *et al.* , 1988; Chmielewski *et al.* , 1991; Skartsis *et al.* , 1992). McKinley (1991) reported polymer degradation of the 0.31 wt% PIB/PB/C14 fluid after flowing past a cylinder in a rectangular channel. The degradation was characterized by the decreased molecular weight of the polyisobutylene when it was measured with a GPC column. The current test fluid, which was used for the experiments in this study, has

a zero-shear-rate viscosity $\eta_0 = 12.4\ Pa \cdot s$, that is 8% lower than the original PIB/PB/C14 solution ($\eta_0 = 13.45\ Pa \cdot s$). The viscosities of the original fluids, prior to being introduced into any flow cell, and degraded solutions used in this work remain nearly constant over four decades of shear rate, as shown in Fig. 7-6(a).

The first normal stress coefficient for both solutions exhibits complex shear thinning behavior at high shear rates. The steady viscometric measurements reveal that Ψ_1 for the present solution is noticeablely lower as compared to the original fluid for shear rates of $10s^{-1} < \dot{\gamma} < 60\ s^{-1}$. Comparing the two solutions, changes in Ψ_1 for small shear rate $\dot{\gamma} \leq 1.0\ s^{-1}$ are not measurable because of the resolution of the normal force transducer; at very large shear rates where $\dot{\gamma} \geq 100\ s^{-1}$, Ψ_1 becomes identical for the two fluids. This indicates that the shift in the longest relaxation time of the material is unclear, the intermediate relaxation time of the fluid is slightly lowered, while the shortest relaxation time of the polymer chains remain essentially unchanged. To resolve the uncertainties in the behavior of Ψ_1 in the low shear-rate limit, dynamic viscometric measurements are carried out and the results are presented in Fig. 7-6(b).

The zero-shear-rate first normal stress coefficient, Ψ_{10} is not measurable in the Rheometric RMS 800 because the normal force transducer is not sensitive enough. Small amplitude oscillatory shear flow measurements (Fig. 7-6(b)) are used to infer $\Psi_{10} \equiv \lim_{\omega \to 0}(2\eta''/\omega) = 2.52\ Pa \cdot s^2$, and once again confirm the value of zero-shear-rate viscosity η_0. These zero-shear-rate values lead to $\beta = \eta_s/\eta_0 = 0.67$ and $\lambda_0 \equiv \Psi_{10}/2(\eta_0 - \eta_s) = 0.3\ s$ for both the original and current fluids. No detectable changes in the complex viscosity $\eta'(\omega)$ and $\eta''(\omega)$ are observed in the linear viscoelastic shear rate region of small strain.

Later experiments in an opposed jet rheometer show that the onset of the significant increase in the apparent Trouton ratio for the degraded fluid is shifted to a higher strain rate as compared to the original fluid as shown in Fig. 7-7. This contradicts the fact that a change in λ_0 arising from the viscometric flow in the low shear-rate limit where $\dot{\gamma} \to 0$ should be exactly the same as in the case of homogeneous extensional flow where $\dot{\epsilon} \to 0$ (Bird *et al.* , 1987). The apparent discrepancy is caused by (1) the opposed jet rheometer is not a good device for approximating uniaxial extensional flow; (2) the steady-state first normal stress coefficient in viscometric flow measurements for $\dot{\gamma}$ ranging from $0.2\ s^{-1}$ to

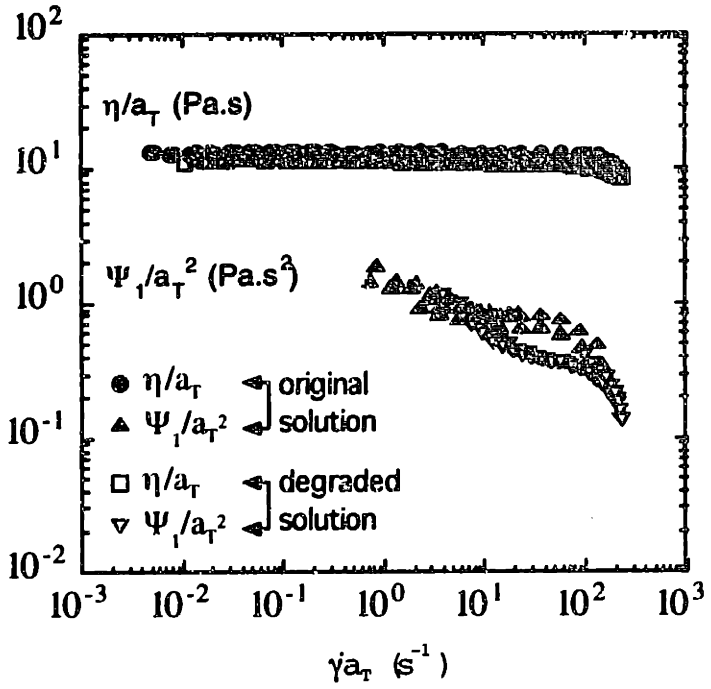

(a)

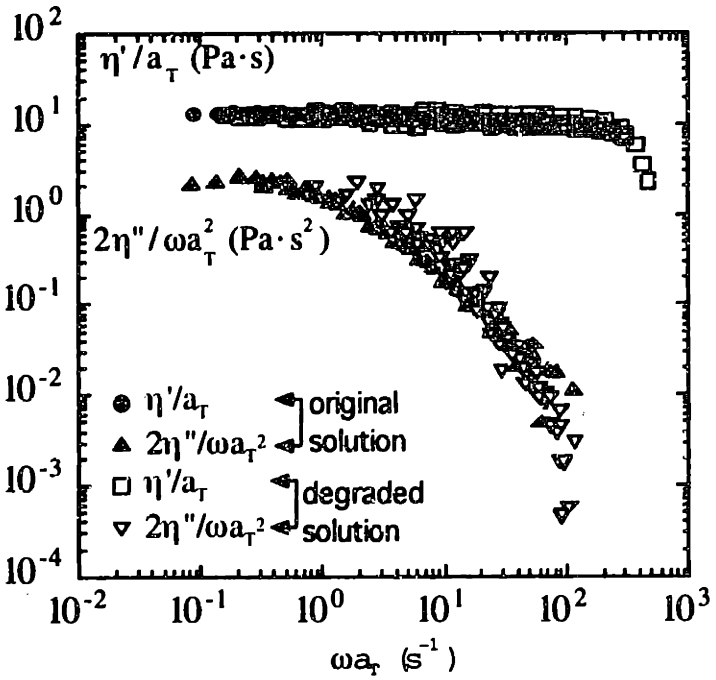

(b)

Figure 7-6: (a) Viscosity $\eta(\dot{\gamma})$ and first normal stress coefficient $\Psi_1(\dot{\gamma})$ under steady-state conditions. (b) Dynamic viscosity $\eta'(\omega)$ and $2\eta''(\omega)/\omega$ for small amplitude oscillatory shear flow. Solid symbols of '•' and '▲' represent measurements for the original 0.31 wt% PIB/PB/C14 fluid, prior to being introduced into any flow cell, and the symbols '□' and '▽' denote results for the degraded fluid used in this work.

1.0 s^{-1} are not obtained because of the sensitivity of the torque transducer. Therefore, apparently elongation flow properties can be used to detect any degradation arising from the breakage of the polymer chains. This is consistent with the fact that polymer degradation can have marked effects on the extensionally dominated flow behavior of macromolecules (Jones *et al.* , 1989).

The elongational flow properties have been measured in an opposed jet apparatus (Rheometrics RFX). Although polymer degradation decreases the first normal stress coefficient by a factor of 2 for $20s^{-1} \leq \dot{\gamma} \leq 50s^{-1}$, more pronounced changes are noted in apparent uniaxial elongation viscosity as shown in Fig. 7-7. For this reason, we use the apparent Trouton ratio to compare current ("degraded 2"), "degraded 1" and "original" solutions. The solid circle denotes the original solution. "Degraded 1" is the fluid after the single cylinder experiments performed by Byars (1995), and it is the initial fluid for our 'linear array' experiments. "Degraded 2" is the same fluid after the present experiments. No further degradation is measured after flow around a single cylinder. For the degraded fluid, the Trouton ratio increases beyond a critical strain rate of $\dot{\varepsilon} \approx 1.0s^{-1}$ and plateaus at $T_R = 22$, whereas for the original non-degraded fluid, the increase occurs at $\dot{\varepsilon} \approx 0.2s^{-1}$ and plateaus at $T_R = 60$. This indicates that the longest relaxation time, λ, changes by a factor of five, while only a smaller shift in the intermediate relaxation time of the fluid is observed from the first normal stress coefficient measurements in Fig. 7-6 (a). The measured apparent Trouton ratio from the opposed jet rheometer is thirty times lower than that measured by the filament stretching (Tirtaatmadja and Sridhar, 1993) at $\dot{\varepsilon} = 2s^{-1}$. For the M1 fluid, Tirtaatmadja and Sridhar (1993) also noted that the steady extensional viscosity is greater than the apparent viscosity obtained from other methods for the M1 project. They proposed that the difference was due to the fact that other measurements were limited to small strains. Although Spiegelberg *et al.* (1996) were not able to obtain the steady-state extensional viscosity, the transient Trouton ratio can be quantitatively described by the CR model with Q_0 ranging from 40 to 55, leading to an expected apparent elongational viscosity fifteen times greater for the CR model than the measured steady-state T_R from an opposed jet rheometer at $\dot{\varepsilon} = 2\ s^{-1}$.

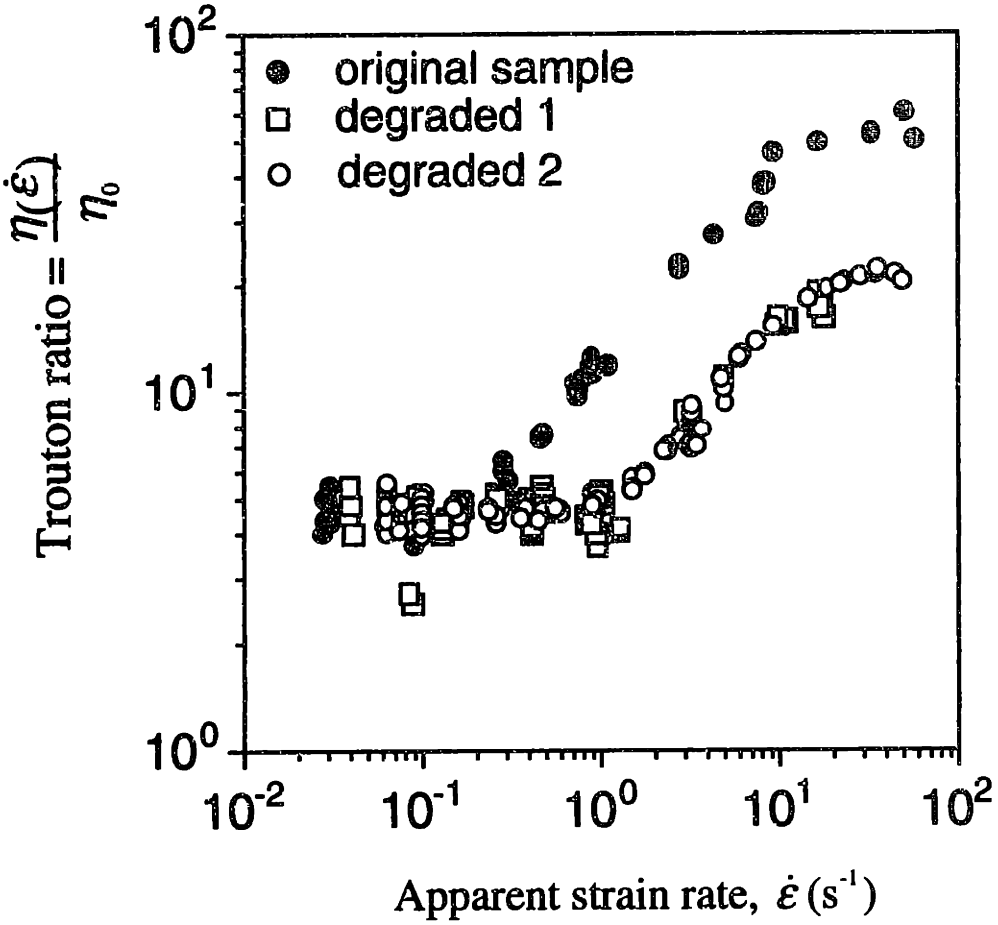

Figure 7-7: Apparent Trouton ratio for 0.31 wt% PIB/PB/C14 solutions from an opposed jet rheometer. The symbol '•' denotes measurements for the "original" sample, and '□' and 'o' represent data collected for the "degraded 1" fluid after flow past single cylinder experiments performed by Byars (1995), and "degraded 2" fluid is the "degraded 1" solution after being used in the present work.

7.2 Flow Geometry

The experimental test geometry consists of a series of smooth circular cylinders of radius R mounted centrally in a long planar channel of height $2H_c$. A schematic diagram of the flow geometry is given in Fig. 7-8. A local coordinate system is defined for each cylinder such that the origin is located at the center of the cylinder, halfway across the channel. The z-axis lies along the main flow direction, the x-axis lies along the length of the cylinder, and the y-axis is normal to the channel walls. The geometric configuration of the array is specified by two dimensions, the center-to-center cylinder spacing L and the channel half gap width H, each made dimensionless by the cylinder radius as

$$L = \frac{L_c}{R} \tag{7.10}$$

$$H = \frac{H_c}{R} \tag{7.11}$$

We consider two cylinder arrangements in detail: closely spaced and widely separated arrays of cylinders for a fixed $H = 2$. For a closely spaced cylinder array, for which we take $L = 2.5$, there is flow separation between two adjacent cylinders for a Newtonian fluid. For widely spaced cylinder arrays, $L = 6.0$, the velocity profile across the periodic plane midway between the two adjacent cylinders approaches 92% of the undisturbed fully developed channel flow for a Newtonian fluid. For $L = 6.0$, the presence of neighboring cylinders has essentially no effect on the Newtonian flow field around a given cylinder.

The flow cell is constructed from 1/2" plexiglass, matching the refractive index of the PIB/PB/C14 fluid ($n_f = 1.49$). The internal length, height, and width of the rectangular channel are $l = 279.4$ mm, $2H_c = 6.35$ mm, and $w = 63.5$ mm. The aspect ratio of the channel cross-section is $w/2H_c = 10$, and is designed to minimize edge effects and ensure that the flow in the vicinity of the mid-length of each cylinder is two-dimensional. An axial velocity profile at typical flow rates $We = \lambda(\dot{\gamma}) < v_z > /R = 1.2$ measured by LDV at $z = -21R$ upstream of the first cylinder is shown in Fig. 7-9 The almost uniform velocity extends over 90% of the length of the cylinder confirming that the three-dimensional edge effects are confined to the 10% of the flow outside this region. All the axial velocity

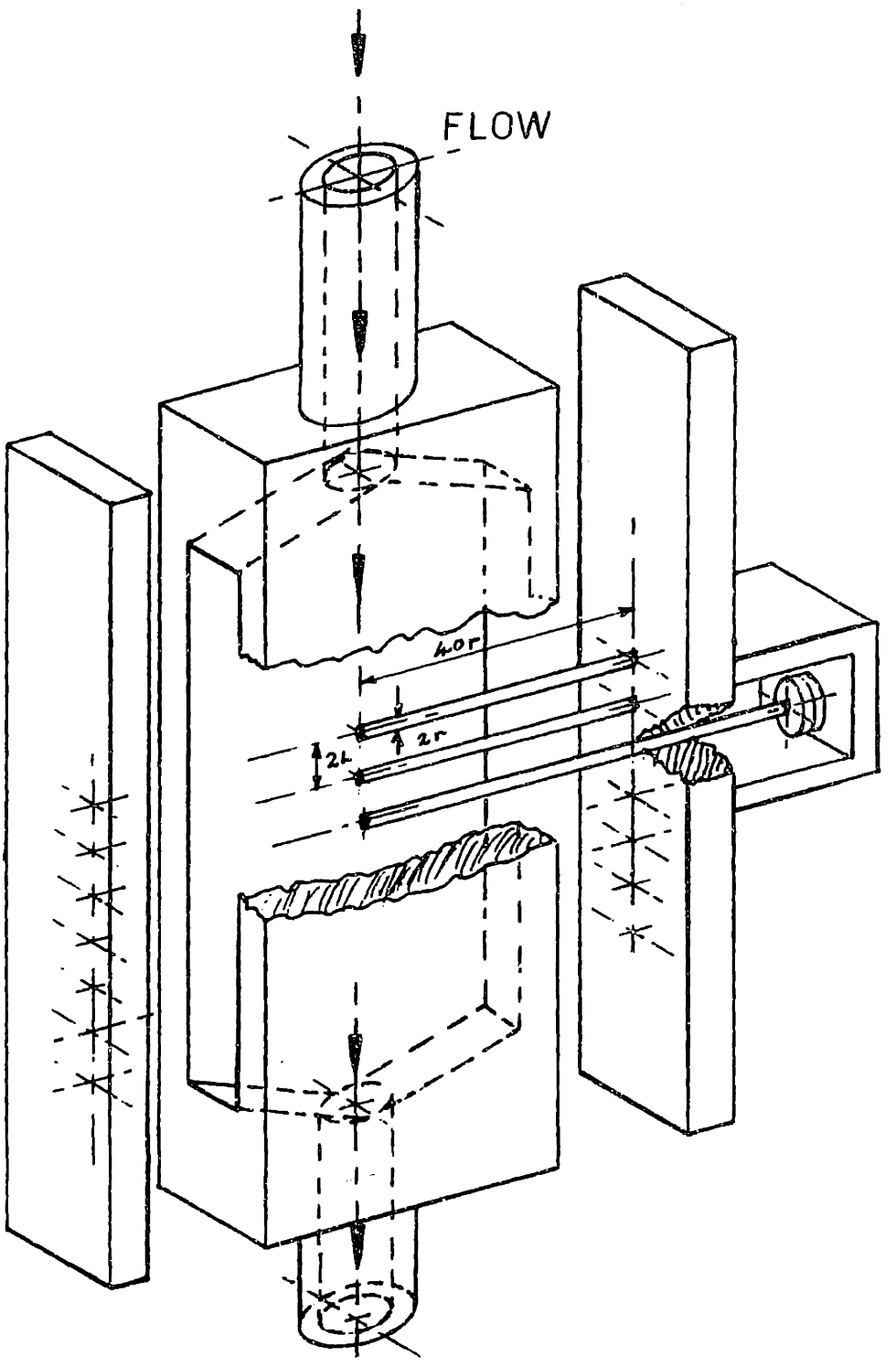

Figure 7-8: Design of flow geometry for investigating viscoelastic flow around a linear array of cylinders.

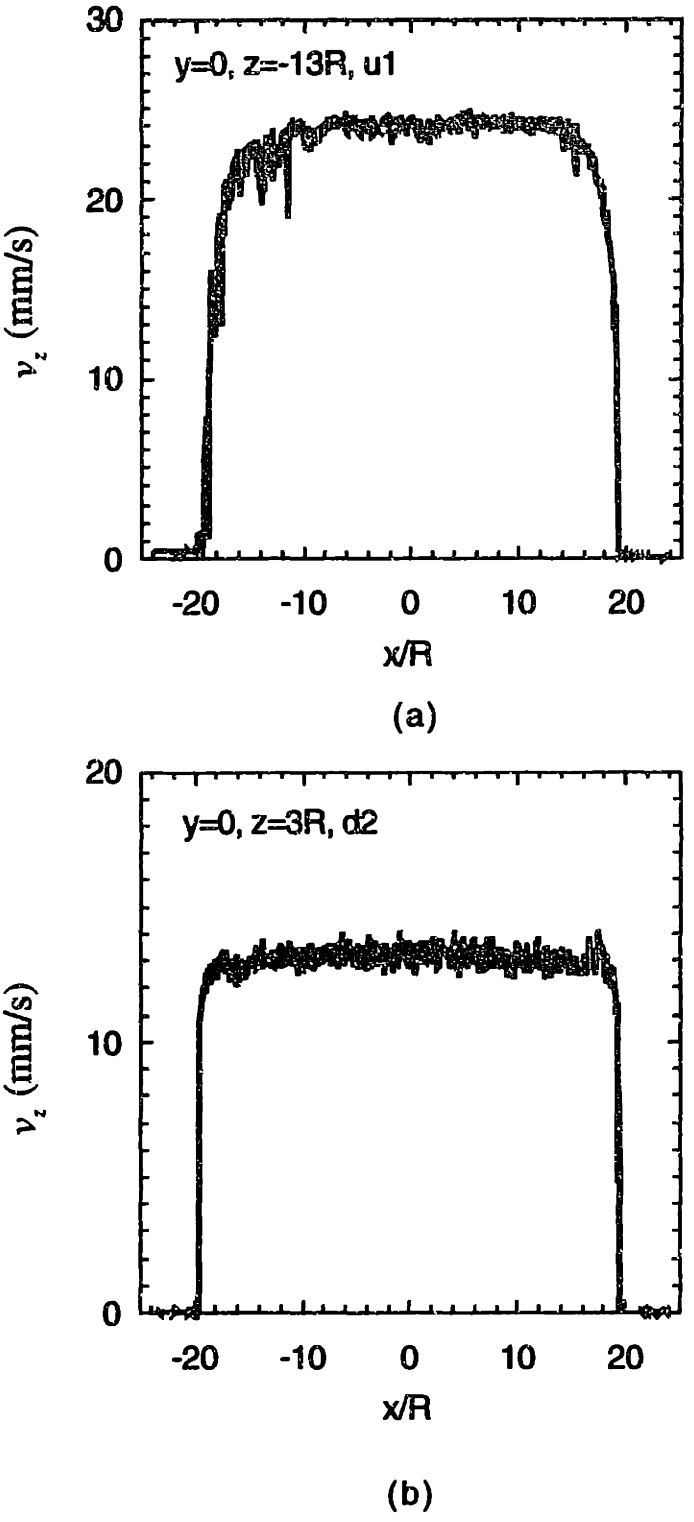

Figure 7-9: Streamwise velocity scan along the length of the cylinder (a) at $z = -21R$ upstream of the first cylinder at $We(\dot{\gamma}) = 1.2$ and (b) at the center of the periodic boundary between the second and third cylinders at $We(\dot{\gamma}) = 1.1$ prior to flow transition. The side walls are located at $x/R = \pm 20$.

measurements reported here are restricted to the center region $-12R \leq x \leq 12R$. The ratio of the entrance length to channel height is 14:1 to ensure that flow becomes fully developed prior to reaching the cylinder array, and a large exit region is used to allow the fluid to relax.

Ten equally spaced cylinders are mounted in the channel. The circular cylinders are made of stainless steel rods that are held rigidly in place along the centerline of the channel by recessed holes in the side walls of the flow cell. It is well-known that the viscoelasticity of the fluid tends to amplify slight asymmetries in this flow geometry (Georgiou *et al.* , 1991; Boger, 1993) and care is taken to ensure that these mounting holes are centered to within $\triangle y = \pm 0.025$ mm, so that the dimensionless eccentricity $\triangle y/2H_c$ associated with the cylinder mounting is no more than 0.5% of the channel height.

A schematic diagram of the flow loop is presented in Fig. 7-10. The test fluid is stored in a holding tank, and it is forced through the flow cell by pressurizing the holding tank. After passing through the flow cell, it is recycled back to the tank via a positive displacement pump. All tubing is made from PVC in order to withstand the solvent tetradecane C14. The amount of Boger fluid in the flow loop is approximately 60 gallons, and the volumetric flow rate at the maximum circulation speed is approximately 2 gallons/minute. The maximum flow rate is about $127 mm^3/s$. The highest zero-shear-rate Weissenberg number We_0, $We_0 = \lambda_0 <v_z> /R$, achievable in this arrangement is $We_0 \approx 20$.

It has been noted during the course of the experiments that the drag force measurements are very sensitive to the inlet pressure. Therefore, the tank pressure is carefully regulated to ± 0.025 psi by a pressure controller from Cole-Parmer (Model E-68502-10). By controlling the pressure to the setpoint, the reproducibility and accuracy of the experiments are ensured. The flow rate can be regulated by varying the setpoint of the pressure controller or adjusting the valves of the system. The Moyno positive displacement pump (Moyno, Model 2L8) provides a gentle means of recycling the fluid with minimum polymer degradation.

The volumetric flow rate Q through the channel is used to define an average velocity, $<v_z> \equiv Q/2H_c w$, and the ratio $<v_z> /R$ gives a characteristic shear rate $\dot{\gamma}$. The time to traverse the distance between successive cylinders, $L_c/ <v_z>$ defines a characteristic residence time of the polymer. Since the first normal stress coefficient decreases with shear

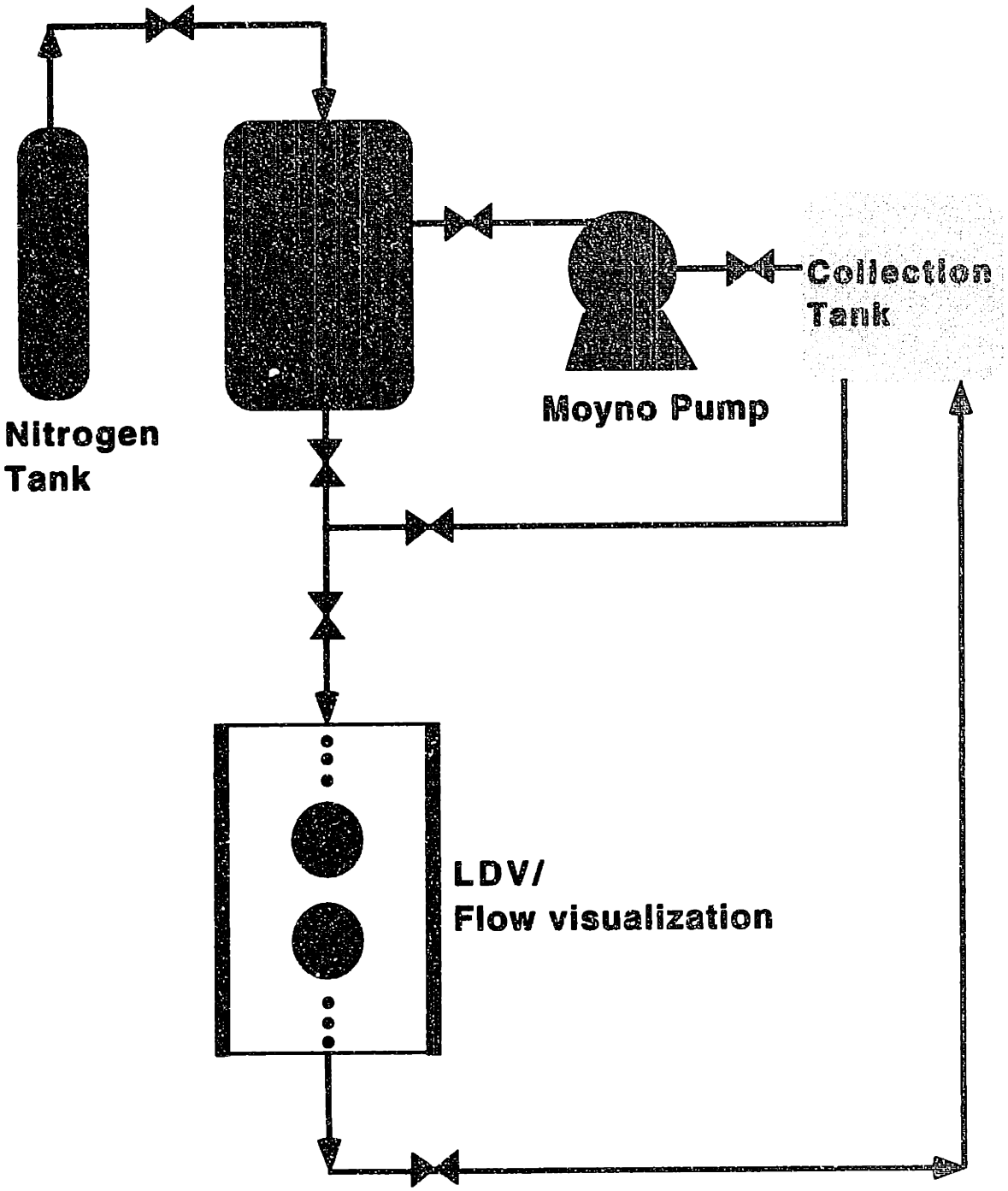

Figure 7-10: Schematic diagram of the experimental system.

rate, it is reasonable to define the shear-rate-dependent relaxation time as:

$$\lambda(\dot{\gamma}) \equiv \frac{\Psi_1(\dot{\gamma})}{2(\eta(\dot{\gamma}) - \eta_s)} \tag{7.12}$$

The importance of fluid viscoelasticity in periodic arrays of cylinders is characterized by the Weissenberg and Deborah numbers, defined as:

$$We \equiv \frac{\lambda(\dot{\gamma}) <v_z>}{R} \tag{7.13}$$

and

$$De \equiv \frac{\lambda(\dot{\gamma}) <v_z>}{L_c} \tag{7.14}$$

Defined in this way, De describes interaction among adjacent cylinders due to fluid memory, whereas We is related to the nonlinear response of the polymer to the kinematics of the flow. As $De \rightarrow 0$ for arbitrary We, we recover the flow for a single cylinder in a channel. The importance of inertia is given by the well known Reynolds number

$$Re = \frac{\rho <v_z> R}{\eta_0} \tag{7.15}$$

For the highly viscous polymer solution, the Reynolds number in all the experiments is less than 0.1. These definitions are given in chapters 5 and 6, and re-introduced in chapter 8.

7.3 Laser Doppler Velocimetry

The Laser Doppler velocimetry (LDV) technique is used to investigate the steady, two-dimensional axial velocity, as well as to characterize the flow transitions in the linear array of cylinders. Steady 2-D pointwise velocity measurements are compared in Chapter 8 to the FEM calculations (Chapter 5).

Laser Doppler velocimetry is a noninvasive means of measuring fluid velocity. The principle of LDV is well documented in Drain (1980) and Durst *et al.* (1981). McKinley (1991) provided a very detailed description of the implementation of laser Doppler velocity used

in this work. Velocities are measured by detecting and analyzing the Doppler shift at the intersection of two coherent, in-phase laser beams induced by scattering particles. When a moving particle passes through the intersection point, it scatters light in all directions. The velocity of the particle is then proportional to the frequency shift of this scattered light.

A simple fringe model (Fig. 7-11) illustrates the concept of LDV. When the laser beams intersect, a diffraction pattern is established with the interference of the wavefronts creating parallel bright and dark fringes. These fringes are parallel to the bisector of the two laser beams. A particle moving with the fluid through these interference fringes will scatter light in all directions. The inverse of the shift frequency of the scattered light can be thought of as the time taken by the particle to travel from one bright fringe to the next. The detected shift frequency, f_s, is related only to the component of the particle's velocity normal to the fringes. For a fringe spacing, d_f, and velocity normal to the fringes, the frequency of the scattered light is related to the fluid velocity, v, by

$$v = \frac{d_f}{f_s^{-1}} \tag{7.16}$$

The fringe spacing can be easily computed as, $d_f = \lambda/2\sin\alpha$, where λ is the wavelength of the incident beam and α is the half-angle between the incident beams. In our system, α equals to 11.8°. The particle velocity is given by

$$v = \frac{\lambda f_s}{2\sin\alpha} = C \cdot f_s \tag{7.17}$$

All LDV measurements are carried out using a two-color laser Doppler velocimetry system (TSI 9100-12). The monochromatic blue and green laser beams from a 4 Watts Argon-ion laser (Lexel, Model 95-4) used in the experiments have wavelengths of 488 nm and 514.5 nm, respectively. The dual-beam back scattering system provides an accurate and fast means of measuring the streamwise (v_z) and neutral (v_x) components of the velocity. Each beam is split into two beams in a beam splitter, then focused or crossed at a point in the flow geometry that defines the measuring volume. The optics are arranged in such a way so that all four beams are focused at a single point, and each pair of beams independently measures one of

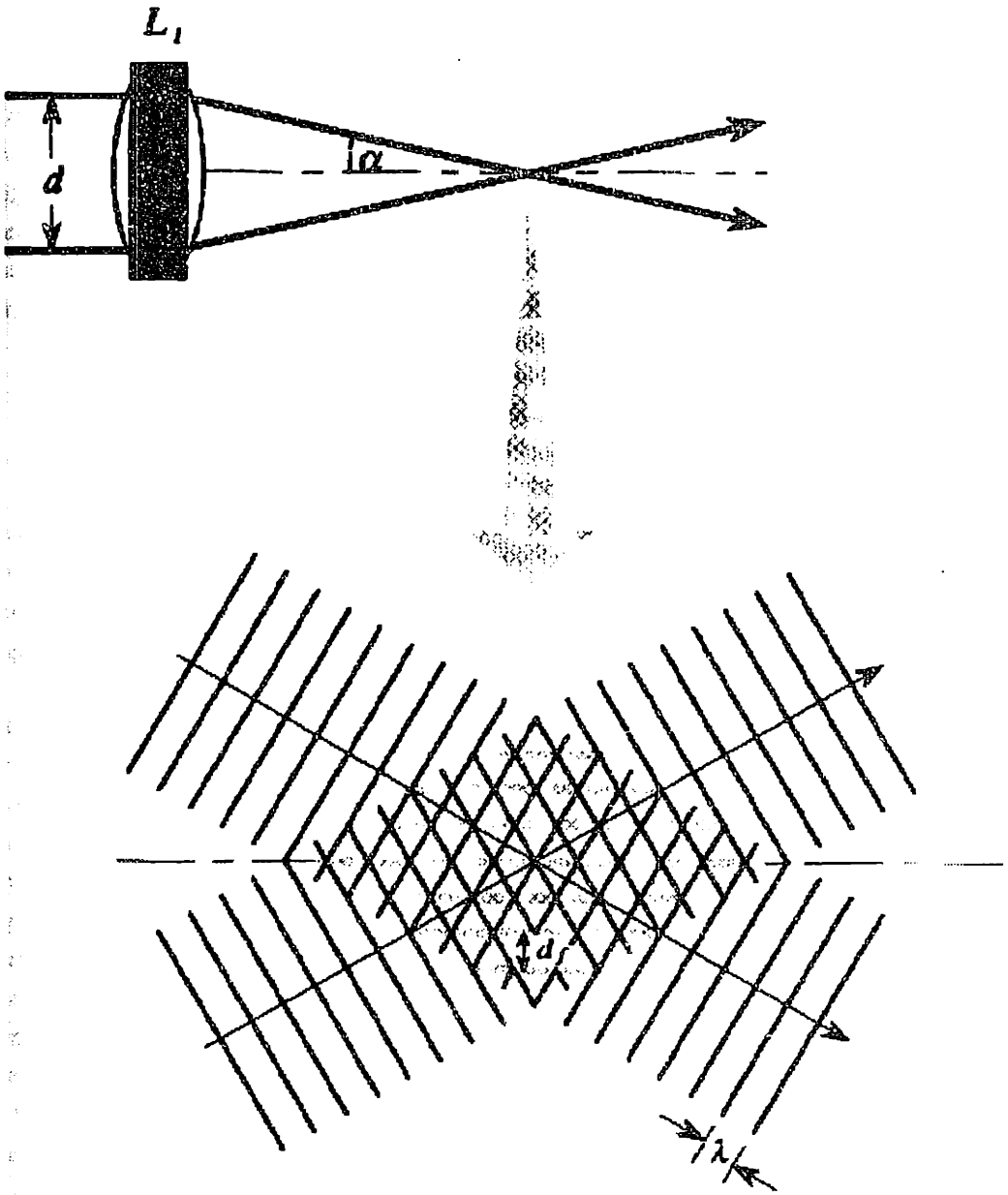

Figure 7-11: Geometric arrangement for a typical 'dual-beam' laser Doppler velocimeter and its interpretation in terms of the 'fringe model' (McKinley, 1991).

the two perpendicular components of velocity. The measuring volume from the intersection of all four beams forms an ellipsoid with dimensions of approximately $20 \times 20 \times 80\ \mu m$. Since the minimum gap between the cylinder and channel wall is 6.35 mm, over 300 distinct possible data points lie across the width of the channel, with the velocity in each measuring volume being essentially pointwise.

In the LDV system used in this study the scattered light is collected along the same optical train as the incident light. This backscatter arrangement allows for movement of the measuring volume by relative translation of only the optical components. In addition, this arrangement reduces the constraints on the type and orientation of flow geometries which can be studied and makes the optics independent of the flow system. The entire optical train is mounted on a computer-controlled, three-dimensional translating table (TSI, Model 9500) which allows pointwise velocity measurements to be made at any point within the flow cell without realigning the flow geometry. The scattered light is collected by a photomultiplier and analyzed by a dual-channel, fast Fourier transform spectrum analyzer (Nicolet, Model 660B).

For pointwise velocity measurements, the "Doppler burst" caused by a particle or particles passing through the measuring volume is computed by averaging 50 to 100 frequency spectra. The range of the steady velocity measurements that can be obtained in the present system is 0.04 - 400 cm/s with an accuracy of $\pm 1\%$ of full scale. Axial velocity scans along the length of the cylinder are recorded by using frequency trackers (DISA, Model 55N20/21) as the measuring volume is translated through the flow cell; the time-dependent velocity measurements are in the range of 0.1 - 100 cm/s with an accuracy of $\pm 2\%$ of full scale. The trackers lock onto the Doppler frequency and follow its evolution in time. The longest tracking time is 400 seconds; this is a serious limitation in resolving the time period of the three-dimensional flow instability in both widely spaced and closely spaced linear cylinder arrays.

7.4 Direct drag force measurement

Stress in the fluid cannot be measured directly. It must be computed from other measurable parameters such as strain or birefringence. There are methods for measuring strain based on various mechanical, optical, acoustical, pneumatic, and electrical phenomena (Beckwidth *et al.* , 1993; Dally and Riley, 1978).

Several optical methods are used for stress measurements. Flow induced birefringence (FIB) is probably one of the most widely used experimental techniques for pointwise stress measurements in the viscoelastic community (Quinzani *et al.* , 1991; Byars, 1995; Baaijens *et al.* , 1994). The method is made possible by the presence of optical anisotropy in the solution (Quinzani, 1991). Anisotropy can be produced by the partial orientation of macromolecules under applied hydrodynamic force. When polarized light passes through the fluid, flow birefringence (difference in refractive index in and perpendicular to the chain orientation directions), Δn. Birefringence arises observed, arising from the anisotropic polarizability of the molecules due to an applied stress. The significance of Δn lies in the fact that birefringence and stress are interrelated by the stress-optical rule. The limitations of the FIB system are: (1) The flow induced birefringence technique is only applicable to a two-dimensional flow system (Quinzani, 1991; Baaijens, 1994). (2) Combined LDV and FIB measurements cannot be on-line, but the current setup allows LDV and drag force measurements to be carried out simultaneously. (3) The linear stress-optical rule is applicable to both dilute and concentrated polymer solutions, but it is expected that the linear relation will break down when the velocity gradient is sufficiently large, i.e. where the polymer molecules are close to full extension. (4) The fluid must be clean to minimize scattering by particles in the fluid. In-line filters must be installed to remove dust and dirt particles (Quinzani, 1991). In addition, glass with a small stress-optical coefficient is required to improve the resolution of the FIB system. The measurements are sensitive and accurate, but the technique is costly.

Another type of strain measurement device is based on the sensitivity of the electrical characteristics of a material to applied strain (Perry and Lissner, 1962; Beckwidth *et al.* , 1993). Capacitance and inductance strain gauges have been developed, but the mounting difficulties, complex circuit requirements and sensitivity to vibration keep them from being

a common device for strain measurements. The most easily and reproducibly measured electrical change is the variation of electrical resistance with applied load. Strain gauges explore the dependence of electrical resistance with strain, and are by far the most widely used strain measurements technique today (Omega Encyclopedia, 1996; Beckwidth *et al.* , 1993). In particular, it is the basis of our experimental setup for measuring the drag force on the cylinder. In the following subsections, we limit our discussion to strain gauges. In section 7.4.1, we first present the fundamentals of strain gauge operation in force measurements, followed by a discussion of the features of the current force transducer (FT) in section 7.4.2, and in section 7.4.3, the mounting of the FT for direct drag force measurements is described.

7.4.1 Fundamentals of strain gauges

Thomson (1856) demonstrated that the resistance of copper and iron wires change when they are subject to mechanical strain. He used a Wheatstone bridge circuit with a galvanometer as an indicator and found that changes in resistance were linearly related to the applied force. The first wire resistance strain gauge was made by Eaton (1931). The theory of operation of the metallic resistance strain gauge is relatively simple (Beckwidth *et al.* , 1993). When a length of wire is mechanically stretched, the electrical resistance changes as the wire is deformed. A simple equation that relates the electrical resistance and physical properties of the material is given as

$$R_R = \frac{\rho L}{A_c} = \frac{\rho_R L}{CD^2} \tag{7.18}$$

where R_R is the resistance (Ω), ρ_R is resistivity ($\Omega \cdot m$), L is the conductor length, A_c is the cross-sectional area, and C is a geometric constant that relates A_c and the characteristic cross-sectional length scale D. If the wire is circular, then $C = \pi/4$ and D is the diameter of the wire. If the conductor is strained axially in tension or compression, the resistance R_R is changed as the wire is either stretched or compressed because of the applied force.

The relationship between stress and strain is one of the most fundamental concepts in the area of solid mechanics. In the linear elastic range, the applied force and strain are related by Hooke's law:

$$\sigma = E\varepsilon \tag{7.19}$$

where E is the elastic modulus of the specimen, and σ and ϵ are the stress and infinitesimal strain, respectively. Thus, the stress exerted on the material can be computed from the measured strain.

For most experimental work, the measured strain is typically less than 0.005 (Omega Encyclopedia, 1996), ensuring that under normal operating conditions stress and strain are related by Hooke's law, so that eq. (7.19) is valid. The most commonly used strain gauge employs a wire with a resistance of 120 Ω, and the percentage change in its resistance is less than 0.5% (or 0.6 ohms) under a typical operation conditions. This small change in resistance can be detected by the use of a Wheatstone bridge circuit (Fig. 7-12). If the resistance element is intimately attached to a strained member in such a way that the element will also be strained, then the measured change in resistance can be calibrated with strain. A bonded resistance strain gauge is the most widely used strain measurement tool for current experimental stress analysis (Beckwidth *et al.* , 1993). It consists of a grid of very fine wires (or thin metallic foil), bonded to a thin insulating backing carrier matrix as shown in Fig. 7-13. The grid is typically made with printed circuit technology using conductive alloys that are strain sensitive. The grid configuration is employed because of higher resistance while maintaining short length. The backing matrix serves as an electrical insulator between the grid and specimen. The grid conformation also provides a large surface area for the conductor in order to ensure low shear stress in the adhesive and carrier matrix when the specimen is strained. The large surface area allows good heat transfer between grid and specimen.

Typically, the carrier matrix is mounted on the test specimen with an adhesive. Two wires coming out of the solder tabs, are connected to the Wheatstone bridge, where the resistance change is measured. The grid material is carefully chosen so that its electrical resistance varies linearly with applied strain. When the specimen is deformed, the strain on its surface is transmitted to the grid material by the adhesive and carrier system. The strain in the specimen is computed from the change in the electrical resistance of the grid material.

The name "bonded resistance strain gauge" refers to both nonmetallic or metallic gauges. Both types operate on the same basic principle. A gauge made from a semiconductor material tend to have a much higher sensitivity to strain than a metallic gauge, but the cost is higher.

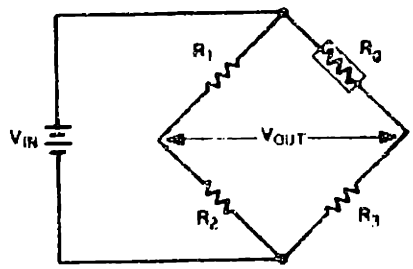

Figure 7-12: Wheatstone bridge circuit.

A strain gauge is characterized by the type of material, its physical dimensions, in terms of the gauge length and gauge pattern, the desired gauge resistance and the gauge factor. The gauge factor F is defined as:

$$F = \frac{dR_R/R_R}{dL/L} = 1 - 2\frac{dD/D}{dL/L} + \frac{d\rho_R/\rho_R}{dL/L} \tag{7.20}$$

The above equation can be simplified by defining the following parameters; $\varepsilon_L = \frac{dL}{L} =$ lateral strain, $\varepsilon_a = \frac{dD}{D} =$ axial strain, and $\gamma = -\frac{\varepsilon_a}{\varepsilon_L} = \frac{dD/D}{dL/L} =$ Poisson's ratio. Equation (7.20) thus reduces to

$$F = 1 + 2\gamma + \frac{d\rho_R/\rho_R}{\varepsilon_L} \tag{7.21}$$

If the resistivity, ρ_R, remains constant with strain ($d\rho_R = 0$), the gauge factor, F, is linearly related to Poisson's ratio, and, in the elastic range where the Poisson's ratio is 0.3, the gauge factor is thus $F = 1 + 2(0.3) = 1.6$ (Crandall *et al.* , 1978). The gauge factor for a metallic gauges is essentially constant in the normal range of strains, and its value is determined experimentally for a given material. Table 7.1 lists the gauge factor for various metals (Beckwidth *et al.* , 1993). As expected, for most metallic materials except nickel, the gauge factor is positive and around 2. The reported gauge factor is usually greater than the expected value of 1.6 because of the dependence of resistance on strain, but the ratio of $d\rho_R/\rho_R\varepsilon_L$ remains essentially constant. The negative gauge factor for Ni indicates that if the

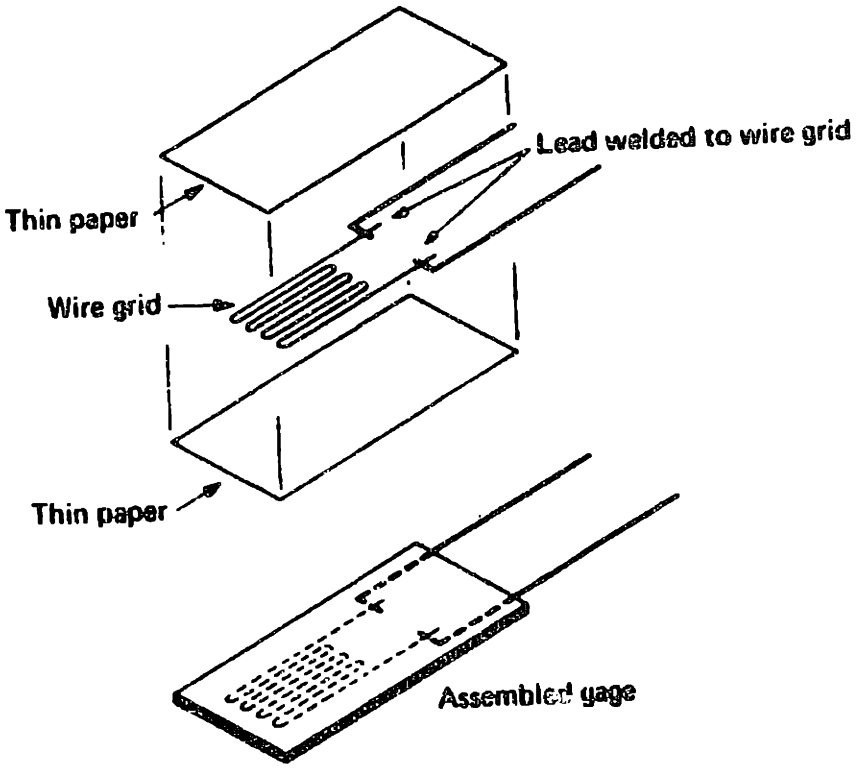

(a)

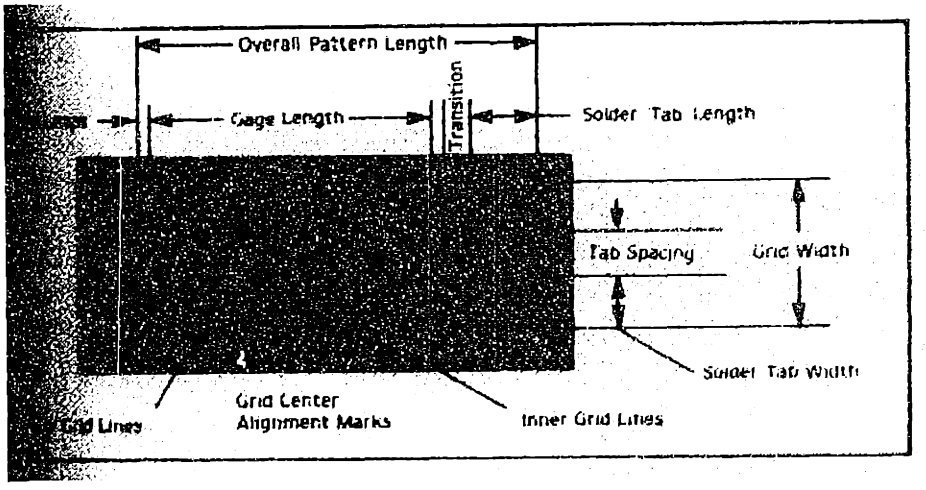

(b)

Figure 7-13: (a) construction of bonded-wire-type strain gauge (Crandall *et al.* , 1978); (b) strain gauge nomenclature (Omega encyclopedia, 1996).

Grid material	Composition	Approx. Gauge factor, F
Nichrome V*	80% Ni; 20% Cr	2.0
Constantan*; Copel*	45% Ni; 55% Cu	2.0
Isoelastic*	36% Ni; 8% Cr; 0.5% Mo; Fe remainder	3.5
Karma*	74% Ni, 20% Cr; 3% Al, 3% Fe	2.4
Manganin*	4% Ni; 12% Mn; 84% Cu	0.47
Platinum-Iridium	95% Pt; 5% Ir	5.1
Monel*	67% Ni; 33% Cu	1.9
Nickel	-	-12
Platinum	-	4.8
* Trade names.		

Table 7.1: Representative gauge factor for various grid materials.

element is strained axially, causing an increase in length, the resistance actually is reduced.

Rearranging eq. (7.20) yields a formula relating strain and resistance change:

$$\varepsilon_L = F\frac{dR_R}{R_R} \tag{7.22}$$

For most engineering materials, strain is a small number, commonly on the order of 10^{-6}, allowing the differential in eq. (7.22) to be replaced by an incremental resistance change,

$$\varepsilon_L = F\frac{\triangle R_R}{R_R} \tag{7.23}$$

In practice, vendors supply the gauge factor and gauge resistance, obviating the necessary for calibration.

Commercially, strain gauges come in all sizes and shapes. The gauge resistance typically ranges from $30 - 3,000\,\Omega$, with $120\,\Omega$ and $350\,\Omega$ being the most commonly used. Gauge length ranges from 0.008-4.0 inc' ·s. Because of the required sensitivity to resistance change under applied strain, the Wheatstone bridge, depicted in Fig. 7-12, is the most frequently used circuit for strain measurements.

There are a few factors that need to be considered for reliable strain gauge measurements (Perry *et al.* , 1962; Beckwidth *et al.* , 1993):

(1) Temperature sensitivity is one of the most worrisome factors in the resistance of strain gauges. The resistivity of all strain sensitive materials vary with temperature. In many applications, temperature sensitivity arises from: (i) thermally induced strain. The thermal expansion coefficients between the gauge and the grid support are different, and gauge resistance changes due to thermally induced strain, which is different from the load strain. (ii) the change in resistivity ρ_R with temperature. Temperature compensation can be provided by processing the strain sensitive alloy so that its thermal resistance characteristics compensate the effects of mismatch in thermal expansion coefficients and resistivities between the gauge and grid support (Beckwidth *et al.* , 1993). This technique is only effective in a limited temperature range because of the nonlinear response of both the thermal expansion coefficient and resistivity. The force transducer employed here has linear temperature compensation over the temperature range from 10 to $40°C$. This allows sufficient accuracy since the maximum temperature variation in the course of these experiments is only $\pm 2°C$ from $22°C$.

(2) The carrier matrix and the adhesive must work together to faithfully transmit the strain experienced by the specimen to ensure instantaneous, accurate and consistent force readings.

(3) Cleanliness and smoothness of the mounting area are absolute requirements to ensure consistently satisfactory results.

(4) Protection of the gauge from a harsh ambient environment is necessary during gauge installations and operations.

7.4.2 Force transducer

The current force/torque transducer (F/T), the Nano, is manufactured by Assurance Technologies in North Carolina (Model, FT 3513). The Nano is currently the smallest six-axis force/torque transducer in the world. The Nano sensor is the size of a dime and weighs about 9.4 grams. The petite size allows the FT to fit nicely into restricted spaces. The sensor has the capability of measuring all three components of force and torque simultaneously. Fig. 7-14 is a sketch of the three-beam transducer. Strain-sensitive semiconductor strain gauges

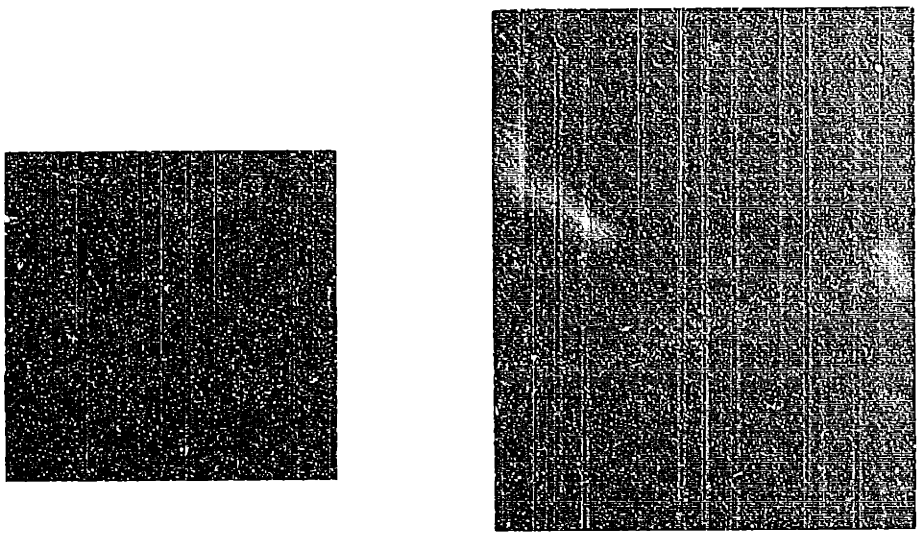

(a) (b)

Figure 7-14: (a) Overall features of the Nano force transducer; (b) schematic drawing of internal configuration of the Nano F/T (Photographs from Assurance Technologies Inc.).

are mounted onto all three beams. As discussed in section 7.5.1, the resistance of the gauge changes as a function of applied load according to

$$\triangle R_R = F R_{R0} \varepsilon \tag{7.24}$$

where $\triangle R_R$ is the change in the resistance of the strain gauge and R_{R0} is the resistance of the unstrained strain gauge. The change in resistance $\triangle R_R$ is calculated using a Wheatstone bridge as discussed in section 7.4. The analog strain gauge signals are discretized by an A/D (Analog to digital) board. The digitized strain values are read into a PC. The maximum sampling rate for a serial I/O (input/output) arrangement is 750 Hz. Since the frequency of the flow instability in a linear array of cylinders is on the order of 100 seconds, as determined from pointwise velocity measurements discussed in chapter 8, and longest relaxation time of the material is 0.3 seconds, a sampling rate of 10 Hz is sufficient to avoid aliasing effects. The accuracy of the drag and lift force measurements for the F/T transducer is $\pm 0.02\ N$ (see Table 7.2). The force and torque readings are stored in the computer for later analysis. For the present study, only the force measurements are relevant.

When the Nano is in operation, the strain gauges generate heat, possibly causing drifts of

	$F_x, F_y(N)$	$F_z(N)$	$T_x, T_y, T_z \pm N \cdot mm$
Sensing ranges	12.5	22.5	0.125
Resolution	0.013	0.025	0.063
Overload protection	350	650	2,500

Table 7.2: Specification for the Nano F/T transducer (Assurance Technologies Inc.)

bias and gain. These temperature induced drifts can change the force readings. The current Nano has built-in temperature compensation that proves to be effective when the operating temperature is within the range of 10 to 40°C, and the changes in temperature occur slowly without an externally by imposed temperature gradient (the compensation is not accurate for a sudden change in working environment). The bias drift can be eliminated by performing a sensor bias prior to applied load. Furthermore, the strain gauges are connected to a Wheatstone bridge circuit that has temperature compensation built into it: a thermistor within the gauge measures the operating temperature, and the controller compensates the gain and bias shifts linearly. vendor tests have indicated that the gain shift error can be corrected to 0.05%/°F full scale and thus be virtually eliminated.

Because flow is confined within a channel, neither the force nor the flow are uniform over the entire length of the cylinder. If the fluid were Newtonian, these nonuniformities could be compensated for using the average velocity across the channel to define the mean fluid velocity, because the components of stress tensor are linearly related to the rate-of-strain tensor. This is clearly demonstrated in the force measurements presented in chapter 8 where the drag force on the cylinder follows Newtonian behavior for $We \leq 0.4$.

7.4.3 Mounting of Nano transducer for drag force measurements

The Nano F/T transducer has a tool adapter which allows it to be directly attached to the strain element. The mechanical layout of the Nano transducer and all interface plates is shown in Fig. 7-15. The mounting adapter is used to bolt rigidly the transducer to a fixture.

One of the objectives of this thesis is to measure the drag force on the cylinder, which is the integral of all differential forces exerted by the fluid along the entire length of the

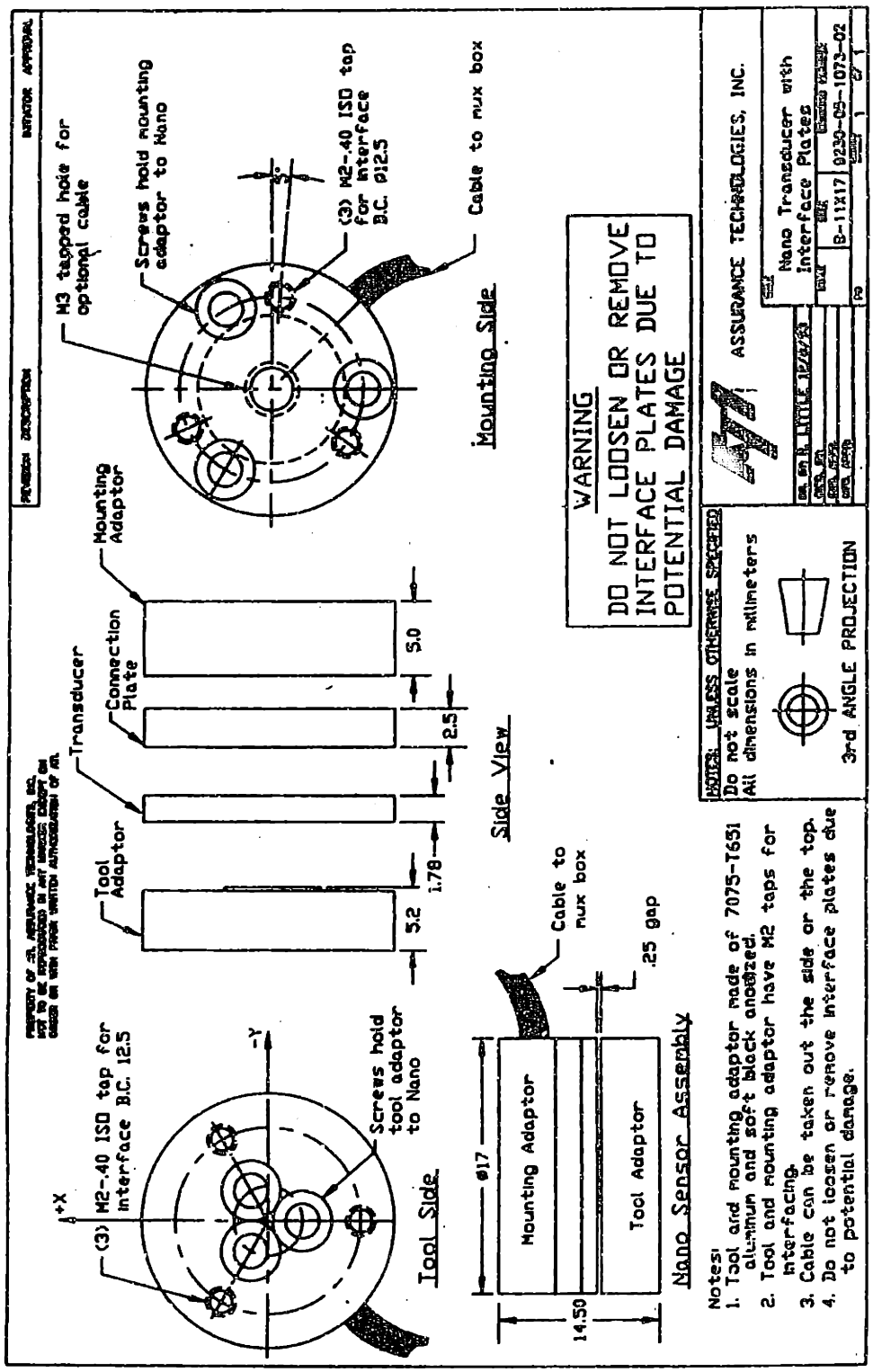

Assurance Technologies, Inc.

Figure 7-15: Mechanical layout for the Nano F/T transducer (Assurance Technologies Inc.). 5in

cylinder, i.e.

$$F_D = \int_0^b w(x)dx, \tag{7.25}$$

where $w(x)$ is the load density, shown in Fig. 7-16 and b is the length of the rod. Since approximately 90% of the flow is uniform along the length of the cylinder, the resulting load is essentially uniform, $w(x)$ = constant, except at the two end points. The layout of the Nano transducer suggests a Cantilever design whereby the Nano F/T sensor is mounted at the end of the cylinder and the other end is free to rotate. Because the measured force is independent of the location of the applied force, calibration of the Nano is achieved by hanging standard weight at any location along the rod.

A Cantilever design tends to cause deflection of the beam in the neutral direction under applied load. For viscoelastic flow around a linear array of cylinders, the flow is two-dimensional, and the fluid applies approximately uniform load along the length of the cylinder. The maximum deflection, δ, under a uniformly distributed load of intensity w per unit length is obtained from a force balance (Crandall *et al.* , 1978) as

$$\delta = \frac{wb^4}{8EI} \tag{7.26}$$

where b is the length of the rod that experiences the uniform load, and EI is the bending modulus of the stainless steel rod. For the current design, the maximum deflection of the beam $\delta_{max} = 10^{-7}m = 0.1\mu m$ when the fluid was assumed to be Newtonian, at the maximum flow rate. Since each rod has a length of 63.5 mm, $\delta_{max}/l = 1.6 \times 10^{-6}$, thus the bending of the end due to introduction of the viscoelastic fluid is essentially un-detectable. Since the clearance between the free end of the cylinder and the channel wall is 0.0254 mm, and the diameter of the cylinder is 3.175 mm, the large aspect ratio of 3.175 : 0.0254 = 125 means that the flow there is approximately flow through a narrow slit. The resulting shear force exerted on the cylinder end face in the streamwise direction is given by (Bird *et al.* , 1960)

$$F_{slit} = (\frac{\Delta p}{z})Bw_s l_s \tag{7.27}$$

where $\Delta p/z$ is the pressure drop across the seventh cylinder, B is the half width of the

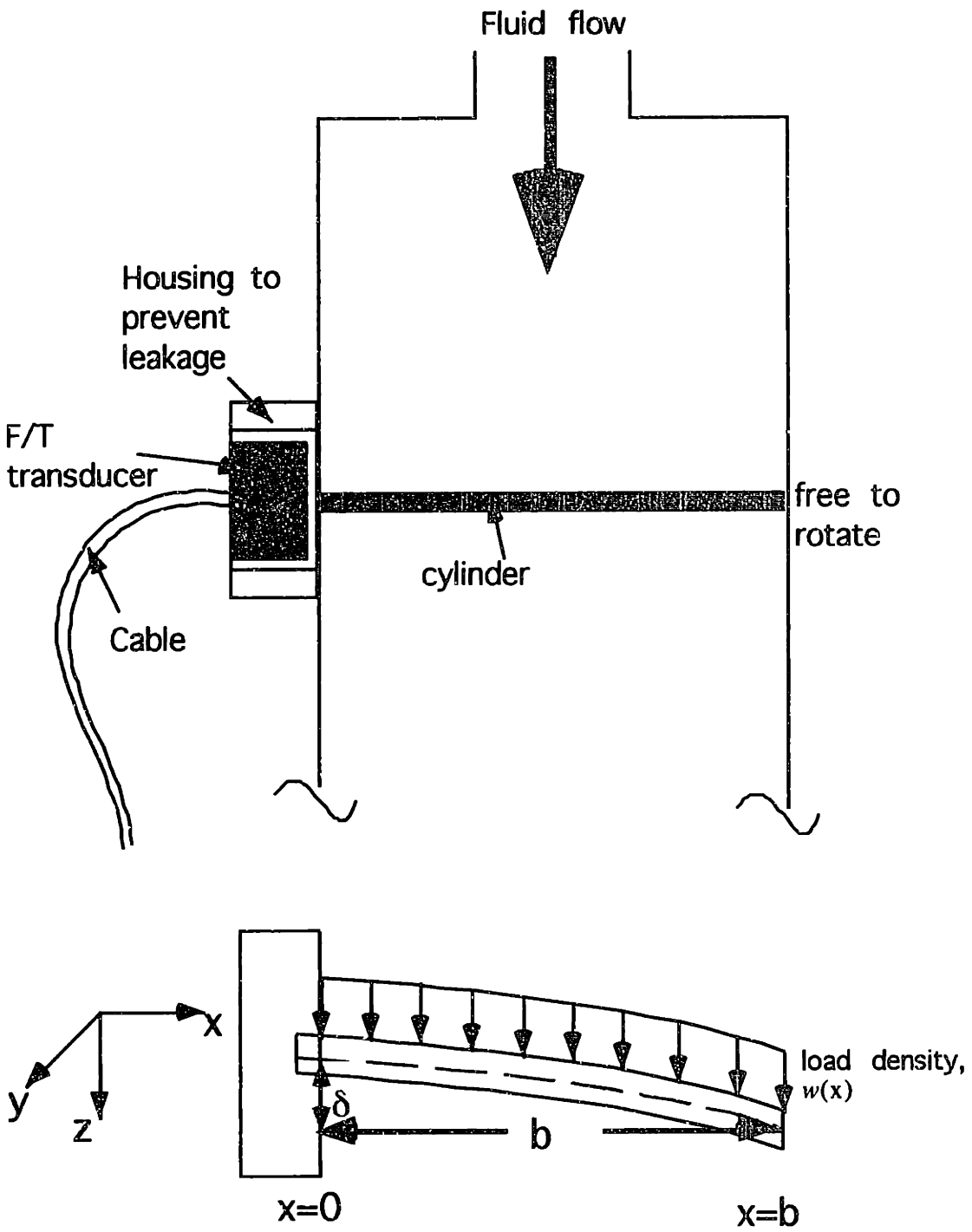

Figure 7-16: Cantilever design for mounting of the cylinder to the Nano F/T transducer for drag force measurements on the cylinder.

clearance, w_s and l_s are the depth and length of the slit, respectively. The maximum allowable pressure drop across the width of the channel is 30 psi, resulting in an expected force due to the slit of $1.8 \times 10^{-4} N$, significantly smaller than the resolution of the transducer. Therefore, the measured force is solely due to the differential forces along the entire length of the cylinder.

The diameter of each cylinder is 3.175 mm and the width of the channel is only 6.35 mm, but the diameter of the tool side for the Nano transducer is 17 mm. This suggests that some kind of adapting plate is needed to connect the end of the cylinder to the Nano. In addition, the sensor has to be protected from the harsh tetradecane solvent environment, so sealing the unit to prevent the leakage of polymer fluids is essential in ensuring a reliable force reading. The sensor can be protected from the PIB/PB/C14 solution by placing viton o-rings around the shaft of the rod at the interface between the cylinder and side channel. However, viton rubber is an elastic material that can absorb part of the applied load slowly. Hence, the response of the force transducer is no longer instantaneous, but delayed by the presence of o-ring. To avoid this problem, a new design is given in Fig. 7-17. A recess is formed at the end of the side channel. A small o-ring is intimately attached to the cylinder and a larger o-ring is positioned adjacent to the smaller one in the recess to achieve a seal. Prevention of fluid leakage and instantaneous force measurement are achieved by tightening a metal collar which compresses the two o-rings with a side screw. Another significant feature of the present design is the placement of the attachment unit outside the channel. This is extremely important in ensuring an undisturbed flow field at all times, especially in the case of closely spaced cylinder arrays where the center-to-center cylinder spacing is only $2.5R$.

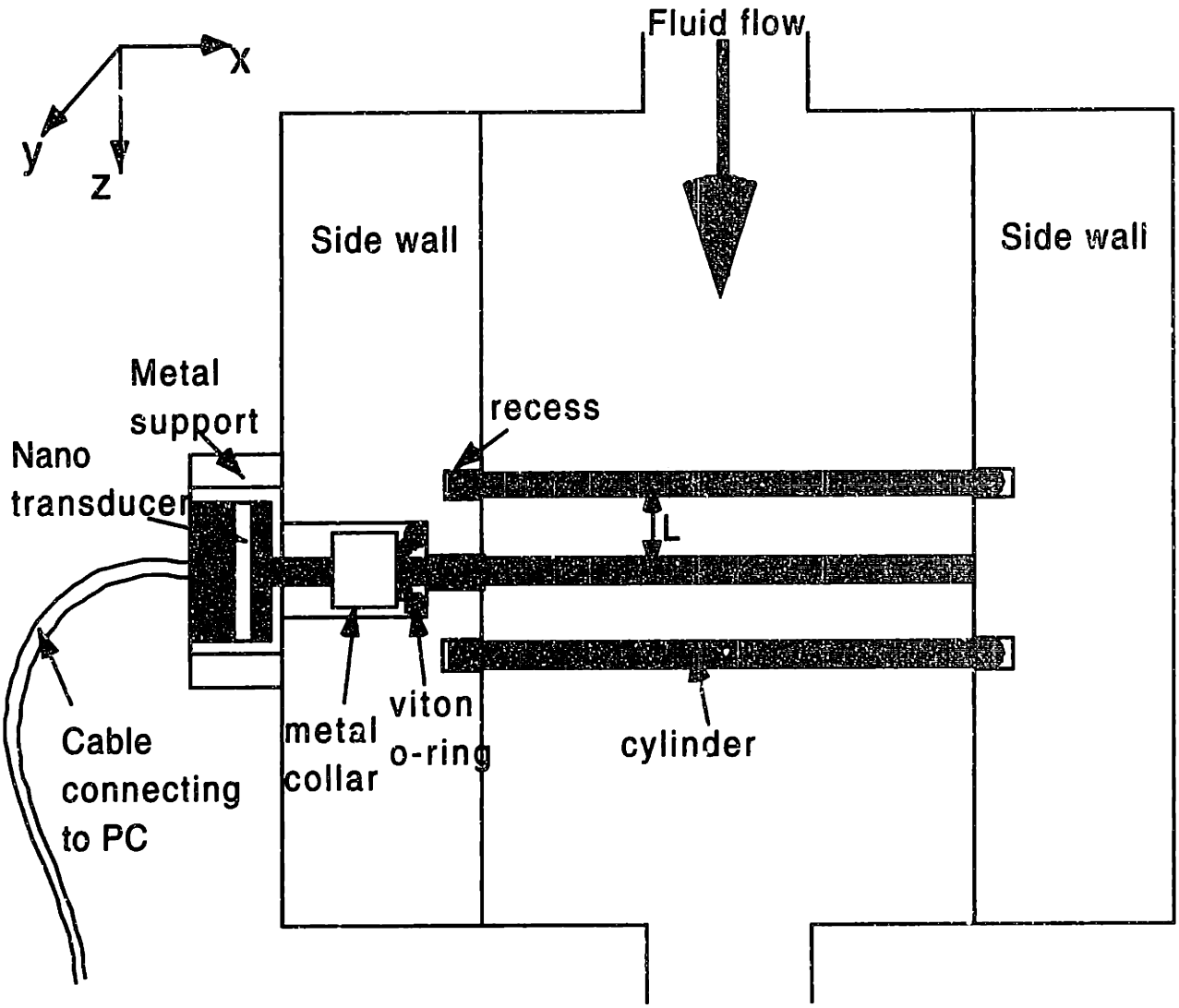

Figure 7-17: Cantilever mounting of the Nano F/T at the end of the cylinder for drag force measurements in a linear array of cylinders.

Chapter 8

Experimental investigation of viscoelastic flow around a linear array of cylinders

In this chapter, we report measurements of viscoelastic flow around a linear array of cylinders for aspect ratios of $H = 2$, and $L = 2.5$ and 6. Equally spaced cylinders of radius R were mounted centrally in a planar channel of half width H_c, as shown in Fig. 8-1. The flow geometries are uniquely specified by the ratio of the channel half-width to the cylinder radius, defined as $H = H_c/R$, and the ratio of the center-to-center cylinder spacing to the cylinder radius, given by $L = L_c/R$. Far upstream and downstream of the cylinder arrays, the flow is fully developed plane Poiseuille flow.

The literature review presented in section 5.1 showed that numerous experimental investigations have been carried out for both a single cylinder and a two-dimensional array of cylinders, but no studies on a linear array of cylinder have been done. The aim of this chapter is to document, in detail, viscoelastic effects on the steady-state flow kinematics, and to investigate the flow stability in a linear array of cylinders as L is decreased from 6 to 2.5, where flow separation appears. In addition, the drag force on the seventh cylinder is measured and compared with the two-dimensional steady-state numerical predictions. Changes in the drag force behavior can be used to identify the onset of flow instability.

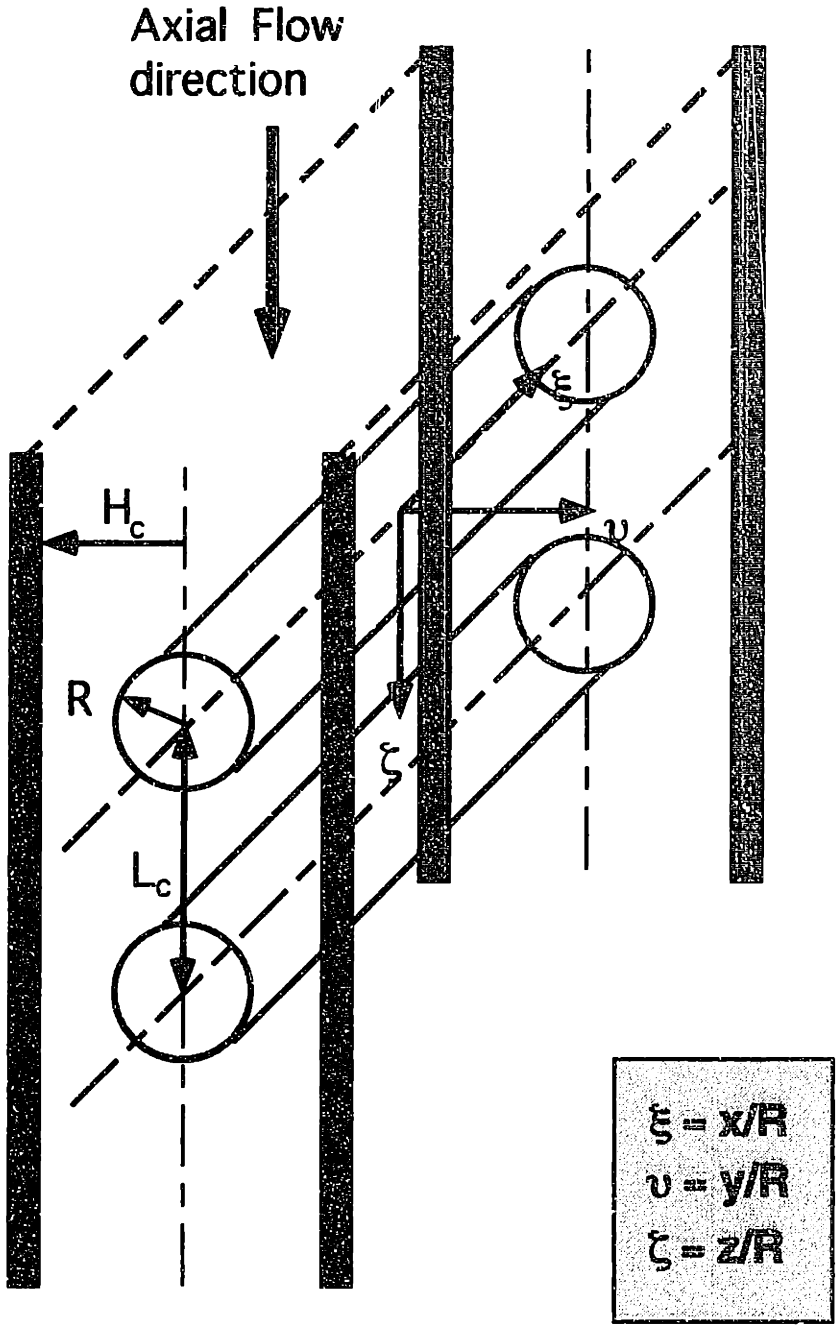

Figure 8-1: Viscoelastic flow around a linear array of cylinders. A cylinder of radius R is centrally mounted in a rectangular channel with a width of $2H_c$. A local Cartesian coordinate system is defined with its origin at the center of each cylinder. The z-axis is the streamwise flow direction, the y-axis is the transverse direction, and the x-axis is along the length of the cylinder.

8.1 Flow in a rectangular channel

A local Cartesian coordinate system $\{x, y, z\}$ is defined in Figure 8-1 with the center of each cylinder being the origin 0. The z-axis is aligned along the flow direction, the y-axis is in the transverse direction, and the x-axis is in the neutral direction along the length of the cylinder. The characteristic length scale is the cylinder radius R. The coordinates are nondimensionalized with respect to R, and defined as $\xi \equiv x/R, \nu \equiv y/R$ and $\zeta \equiv z/R$ respectively. Flow geometry design specifications are discussed in chapter 7.2. In particular, we consider two flow arrangements where H is fixed and equal to two, and L is from 6 or 2.5. Careful measurements of the cylinder diameter and center-to-center cylinder spacing with a micrometer show that the cylinder radius is $R = 1.5875 \pm 0.013\, mm$, half-channel width is $H_c = 3.175 \pm 0.013\, mm$, and the cylinder spacing is $L = 9.525 \pm 0.025\, mm$, yielding $H = 2.0 \pm 0.01$ and $L = 6.0 \pm 0.002$. Because of the machine precision, cylinders are centered to within $\Delta y = \pm 0.025 mm$, and the dimensionless eccentricity $\Delta y/2H_c$ associated with the cylinder mounting is no more than 0.5%.

The flow geometry is designed to have a ratio of the length of the cylinder (Δx) to the channel width $2H_c$, $\Lambda \equiv \Delta x/2H_c = 10$, so that the flow is approximately uniform in the neutral x-direction with the exception of the vicinity of the end-walls (Quinzani, 1991; McKinley, 1991). Figure 8-2 presents the streamwise velocity measurements along the length of the cylinder fifteen radii upstream of the first cylinder ($z = 0$ corresponds to the center of the first cylinder) in a widely spaced cylinder array at $We = 0.49$ and $We = 0.66$. The streamwise velocity rises rapidly from zero at either end of the wall, to an approximately constant value across 80% of the domain from $-16 \leq \zeta \leq 16$. In a periodic array of cylinders, the flow is two-dimensional across 90% of the length of the cylinder at the center of the periodic boundary. The streamwise velocity, shown in Fig. 8-3, increases rapidly to a constant value at $x = \pm 18R$. The maximum difference, shown in Figs. 8-2 and 8-3, is $0.13\, mm/s$, within the accuracy of the LDV measurements. The average velocity across the channel is defined as $<v_z> = Q/2\Delta x H_c$, and the characteristic time scale of the flow is given as $T = R/ <v_z>$. The Reynolds number (Re) and Weissenberg number (We) are defined by equations (7.14) and (7.13), respectively.

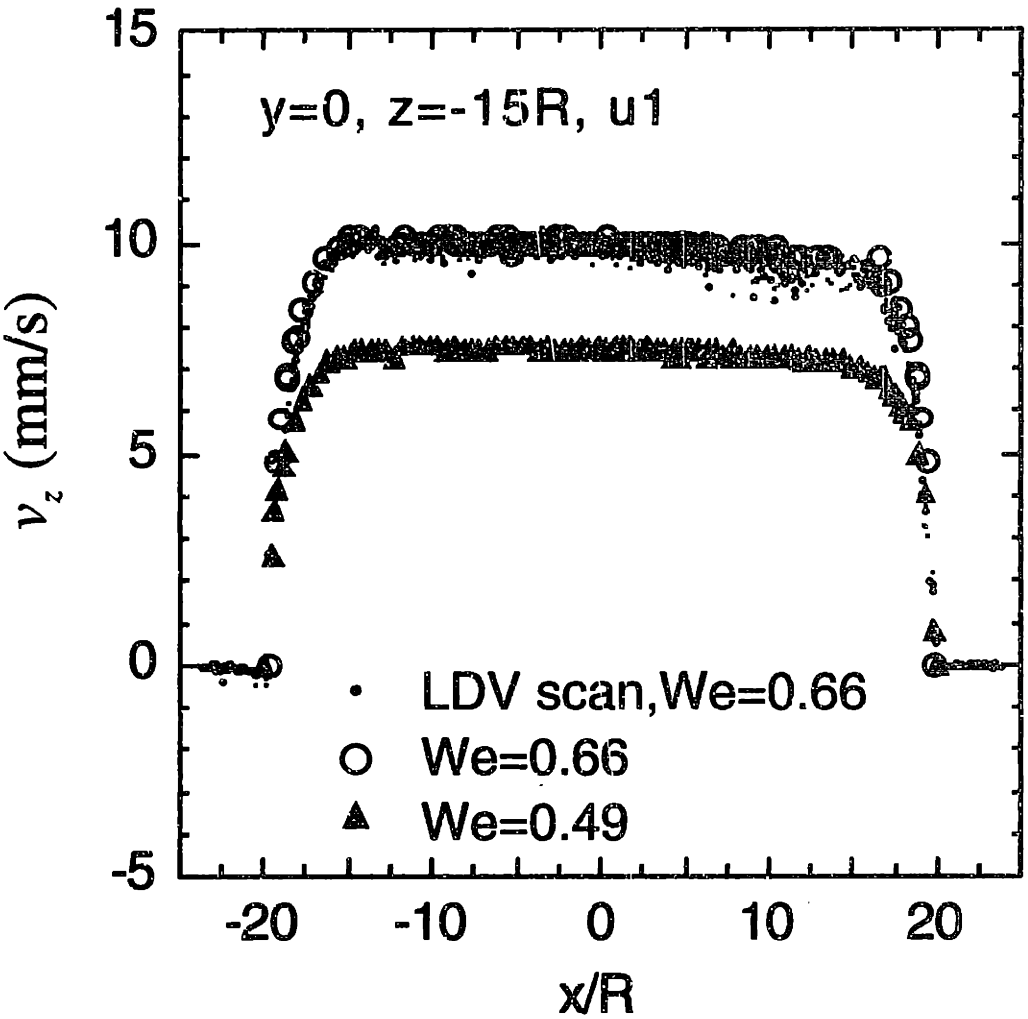

Figure 8-2: Streamwise velocity $v_z(x, 0, -15R)$ measured along the neutral x-direction fifteen radii upstream of the first cylinder. The symbol '•' represents the tracker LDV scan from $x = -25R$ to $x = 25R$, the symbol 'o' corresponds to the pointwise Nicolet LDV measurements at $We = 0.66$, and the symbol '▲' represents the pointwise streamwise velocity taken at $We = 0.49$.

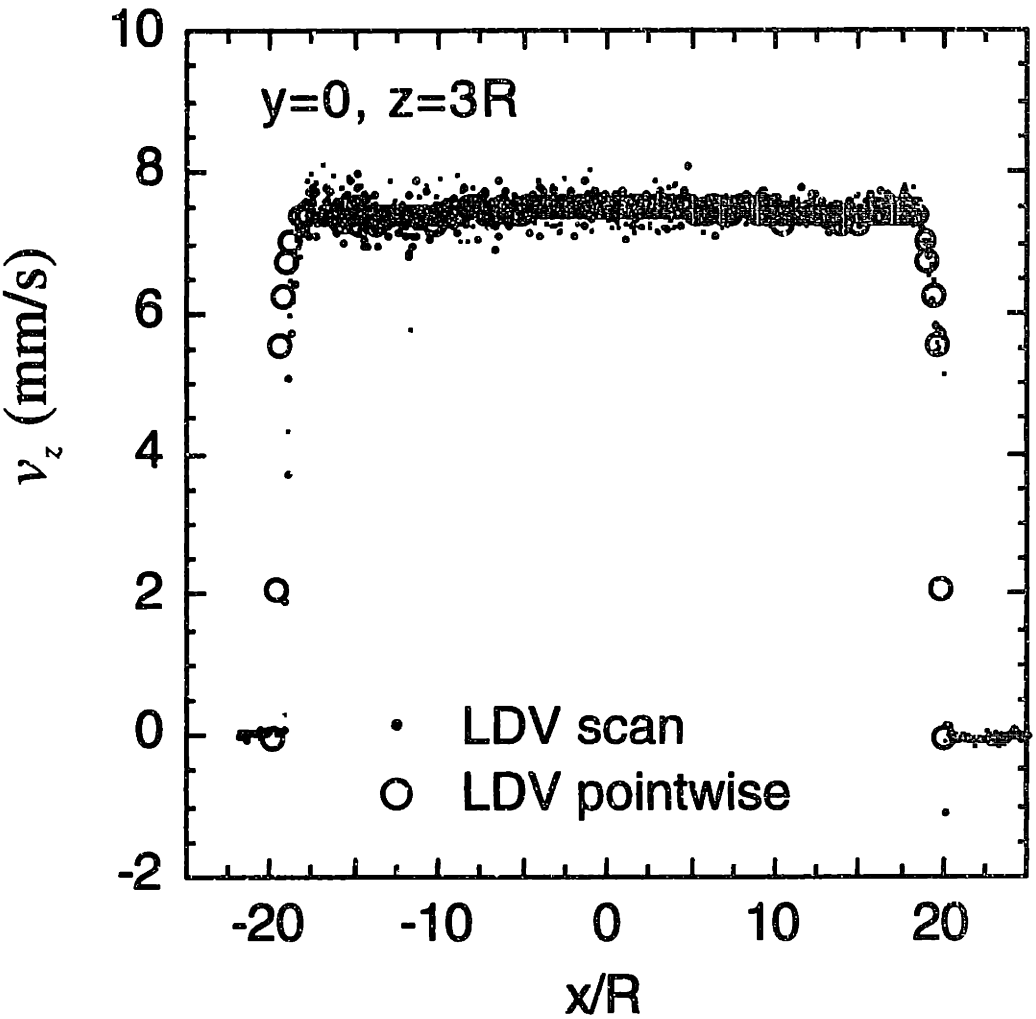

Figure 8-3: Streamwise velocity $v_z(x, 0, 3R)$ along the length of the cylinder at the center of the periodic boundary $\zeta = 3$ downstream of the fifth cylinder at $We = 0.66$. The symbol '$\bullet$' represents the tracker LDV scan from $x = -25R$ to $x = 25R$, with the side walls are located at $x = \pm 20R$, and the symbol 'o' corresponds to the pointwise Nicolet LDV measurements at $We = 0.66$.

Far upstream and downstream of the cylinder arrays, the flow is fully-developed, plane Poiseuille flow with a parabolic velocity profile of the form

$$\frac{v_z}{<v_z>} = \frac{3}{2}[1 - (\frac{\nu}{H})^2] \tag{8.1}$$

The streamwise velocity measured fifteen radii upstream of the first cylinder at either side of the channel ($x = 0$ corresponds to the center of the channel) is parabolic in y as shown in Fig. 8-4.

8.2 Creeping flow in widely spaced cylinder arrays, $L = 6, H = 2$

In this section, LDV measurements are used to characterize the viscoelastic flow in a widely spaced cylinder array. The steady, two-dimensional, streamwise velocity measurements are compared with the finite element calculations reported in chapter 5. Because of the machining precision limitations in mounting of the cylinders, the linear array is off-centered by approximately 0.5% of the channel width, and this slight asymmetry in the flow geometry is amplified as a profound asymmetry in the streamwise velocity profile. At first, results on steady flow in widely spaced cylinder arrays are presented. There was excellent agreement between numerical predictions and experimental measurements of v_z. In addition to the steady flow results, the flow undergoes a transition at a critical Weissenberg number. Details of the onset conditions are provided, and further information about the temporal and spatial extent of the instability is also discussed in this section.

8.2.1 Steady flow in a widely spaced cylinder array, $L = 6, H = 2$

Here, we first examine numerically the effects of off-centering on flow kinematics. As discussed in chapter 7, dimensionless eccentricity associated with the cylinder mounting is no more than 0.5% of the channel width. The basic assumption for solving the flow problem is that the cylinders are uniformly off-centered by 0.5% of the channel width. We then present

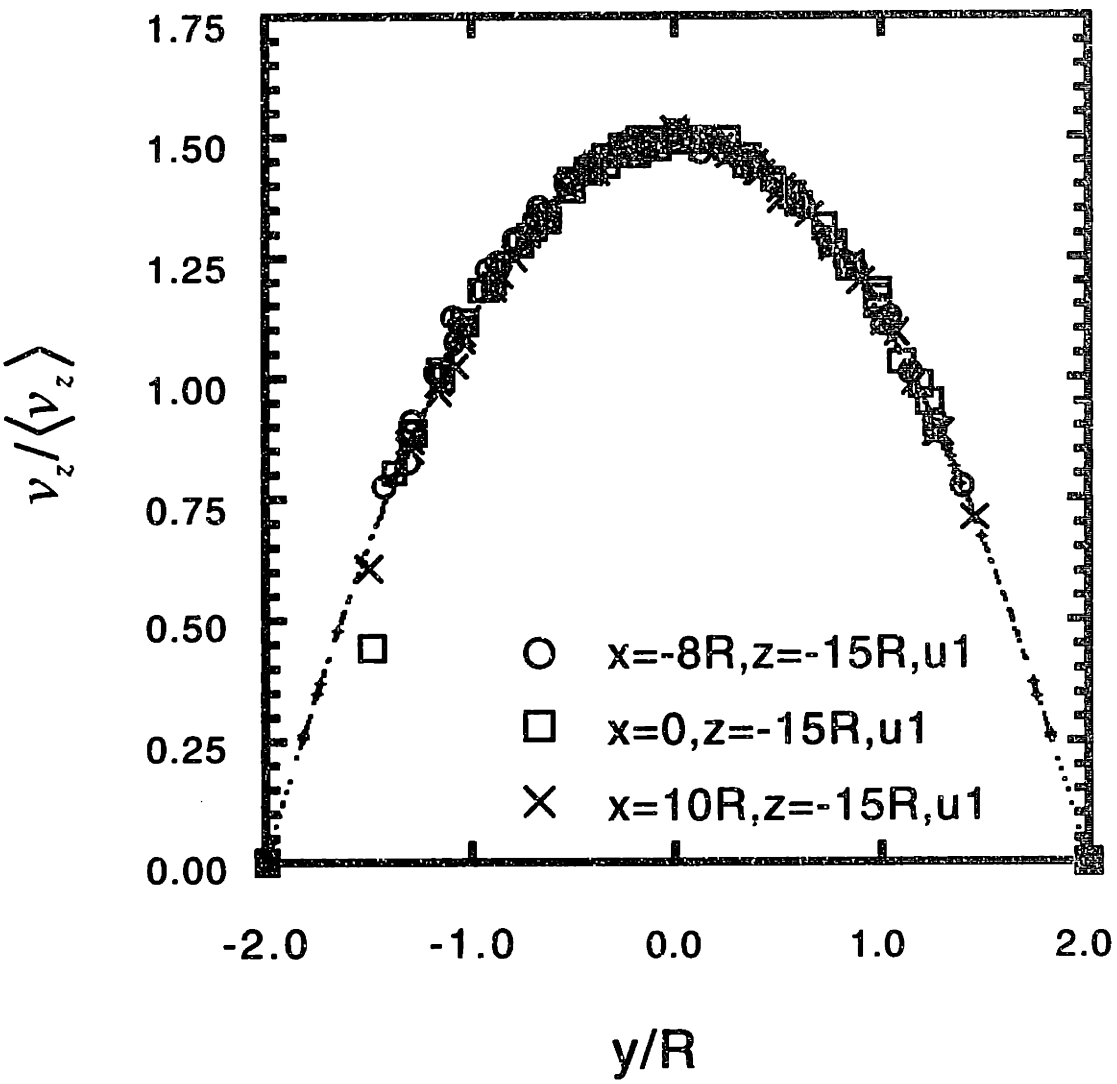

Figure 8-4: Parabolic fully developed channel flow $v_z(0, y, -15R)$ fifteen radii upstream of the first cylinder. The dimensionless streamwise velocity $v_z(y)/ < v_z >$ in the transverse direction is represented by the symbol 'o' at $x = -8R$, the symbol '□' at the channel center, $x = 0$, and the symbol '×' at $x = 10R$ at $We = 0.78$. The solid line is the predicted solution for fully developed channel flow.

pointwise velocity measurements and compare them with the predictions.

8.2.1.1 Effects of off-centering on flow kinematics from FEM calculations

It is well known that viscoelasticity tends to amplify slight asymmetries in any flow geometry (McKinley, 1991). Figure 8-5 presents the FEM calculations for an OLDB model with $\beta = 0.59$ at $We = 0.5$ with 0.5% off-centering with wider gap distance in the positive y-direction. The off-centering is assumed to be uniformly for all cylinders in the array. The evolution of the streamwise velocity, v_z, across the channel at different ζ positions indicates that a greater fraction of the fluid flows through the wider gap ($y > 0$) than the narrow one for all values of ζ. When cylinders are 0.5% off-centered, geometric arguments imply that 50.5% of the fluid flows through the wider gap. Newtonian calculations reported in Table 8.1 demonstrate that over 51% of the fluid actually passes through the wider gap ($y > 0$), and this fraction depends on the streamwise position. Also, the volume fraction of fluid flowing through the wider gap is independent of the Weissenberg number, although increases in We result in an increase in the asymmetry of the streamwise velocity profile. Very close to the cylinder rear stagnation point ($\zeta = 1$ in the dimensionless form), the asymmetry in $v_z / \langle v_z \rangle$ is much more pronounced than elsewhere in the channel. Downstream, at $\zeta = 2$, the degree of asymmetry in v_z decreases until it reaches the periodic boundary ($\zeta = 3$) where the asymmetry in v_z essentially disappears.

The effect of off-centering on the streamwise velocity is examined by scanning v_z in the flow direction. At fixed $\nu = \pm 1$ ($\nu = 0$ corresponds to the center of the channel or the symmetry plane), v_z is plotted as a function of ζ. The solid line in Fig. 8-6 represents the perfectly centered case, and the dotted line corresponds to 0.5% off-centering. Fluid moves faster in the wider gap region than the narrow region, but the difference in v_z is less than 2% of the mean fluid velocity.

8.2.1.2 Effects of elasticity on flow past the cylinder

Figure 8-7 gives the streamwise velocity profiles along the symmetry plane for a steady two-dimensional flow prior to any flow transition. The solid lines correspond to the two-

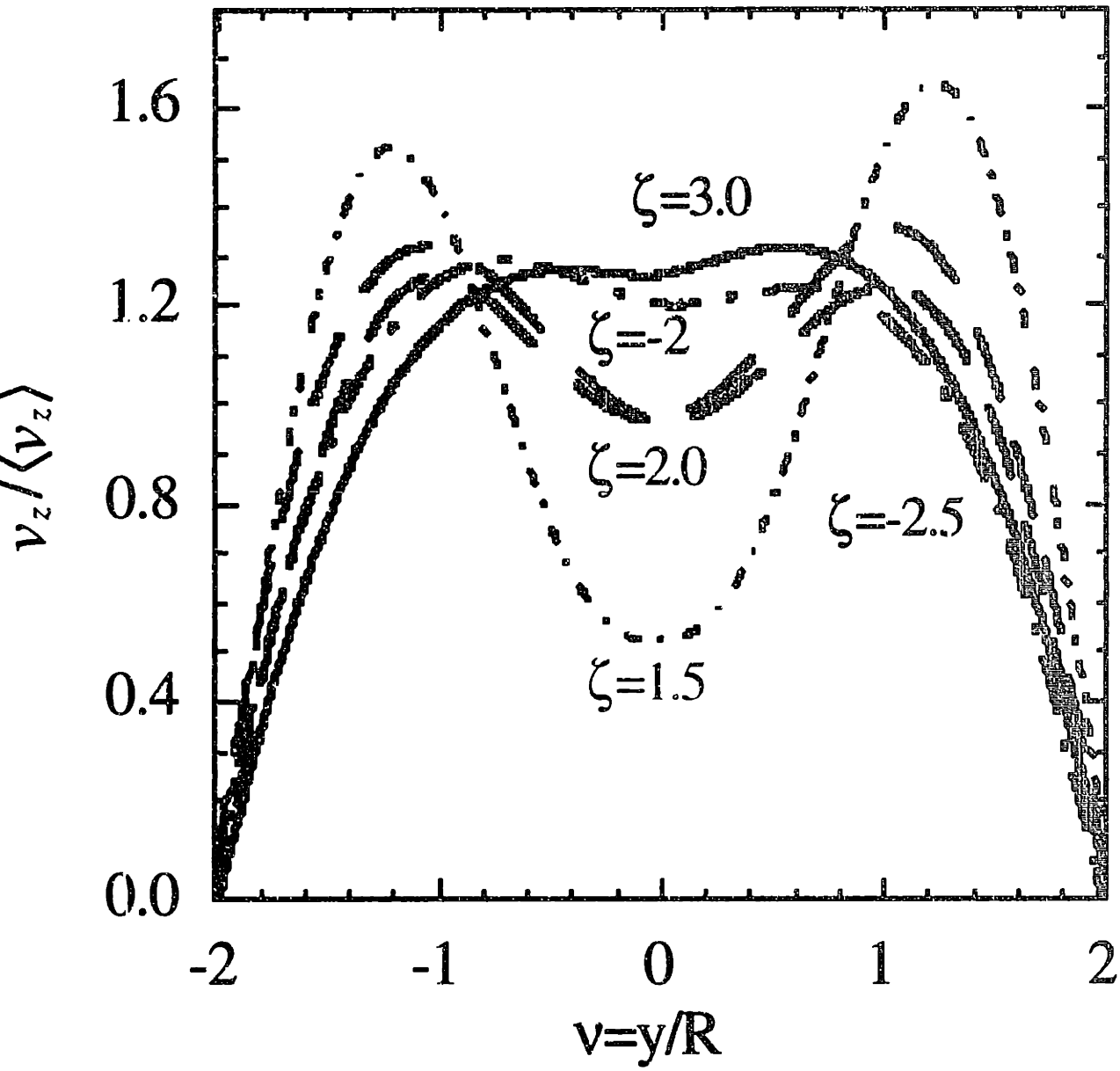

Figure 8-5: Transverse velocity profiles of the dimensionless axial velocity $v_z / \langle v_z \rangle$ for an OLDB model with $\beta = 0.59$, 0.5% off-centering in the positive y direction at $We = 0.5$.

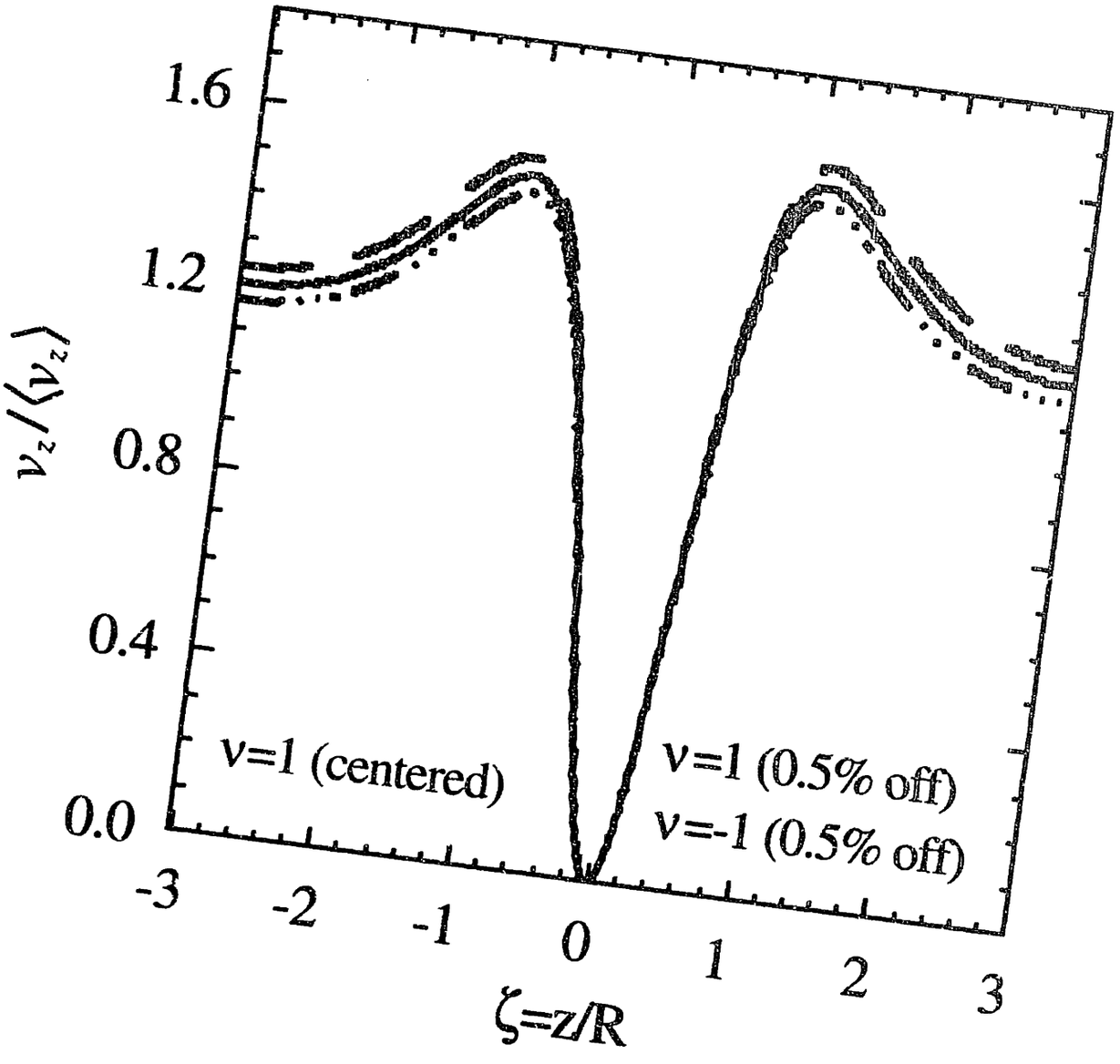

Figure 8-6: Effects of off-centering on the streamwise velocity scan in the streamwise direction at $\nu = \pm 1$. The straight line is the centered case, and the dotted lines are for the 0.5% off-centering in the positive direction at $We = 0.5$. The fluid moves faster at $\nu = 1$ than $\nu = -1$ at all ζ positions.

$\zeta = z/R$	$Q_{y>0}/Q$ ($We = 0$)	$Q_{y>0}/Q$ ($We = 0.25$)	$Q_{y>0}/Q$ ($We = 0.50$)	$Q_{y>0}/Q$ ($We = 0.80$)
-3.0	0.510	0.510	0.510	0.511
-2.5	0.511	0.510	0.510	0.511
-2.0	0.512	0.512	0.512	0.512
-1.0	0.515	0.515	0.515	0.515
0.0	0.517	0.517	0.517	0.517
1.0	0.515	0.515	0.515	0.515
2.0	0.512	0.512	0.512	0.513
2.5	0.511	0.510	0.511	0.511
3.0	0.510	0.510	0.510	0.511

Table 8.1: Fraction of fluid flow through the wider gap ($y > 0$) as a function of z position ($z = 0$ is the center of each cylinder). Cylinders are misplaced by 0.5% of the channel width with the wider gap distance in the positive y direction. The reported volume fractions are for OLDB model fluid calculations $\beta = 0.59$.

dimensional numerical solution for the creeping flow of a Newtonian fluid past widely spaced cylinder arrays with aspect ratios of $H = 2$ and $L = 6$. For $We \leq 0.25$, the agreement between the Newtonian calculations and the LDV measurements is extremely good near both the upstream and downstream stagnation flow. At low We, the streamwise velocity is symmetric about $y = 0$. As the Weissenberg number is increased to $We \approx 0.5$, elastic effects result in a progressive modification to the velocity field around the cylinder, as indicated by the $v_z / <v_z>$ profile in Fig. 8-7(b). The different symbols in the figure denote the number of the cylinder where the streamwise velocity was measured. Upstream of the first cylinder, the streamwise velocity profiles remain unchanged from the Newtonian results when scaled with the average velocity $<v_z>$ and the cylinder radius R. This is consistent with the previous single cylinder experiments by McKinley (1991) and Byars (1995). The polymer molecules are in an unextended, near equilibrium state close to the centerline upstream of the stagnation point at $\zeta = -1$. However, in the wake of the first cylinder, and inbetween the cylinders thereafter, polymer molecules close to the symmetry line experience approximately planar elongational flow leading to the development of large molecular extensions and high elongational stresses (Liu *et al.* , 1997), which results in the pronounced shift of the velocity profile *downstream*, as shown in Fig. 8-7(b). In a linear array of cylinders, the decrease in

the streamwise velocity is observed both upstream ($\zeta \leq -1$) and downstream ($\zeta \geq 1$) of the interior cylinders. In addition, v_z is no longer symmetric about the cylinder center ($\nu = 0$). The calculated flow field is weakly affected by the constitutive equation (Liu *et al.* , 1997); FEM calculations for a viscoelastic model fluid, such as an OLDB model, capture very well the decrease in $v_z / < v_z >$. Another interesting observation in v_z is that the streamwise velocity reaches a periodic state after the second cylinder, since the velocity profiles along the symmetry line ($y = 0$) inbetween the first and second, fifth and sixth, and sixth and seventh cylinders are superimposed, and this also holds for the streamwise velocity across the channel at constant ζ.

The pointwise LDV measurements across the periodic plane $\zeta = \pm 3$ are compared with the OLDB FEM calculations in Fig. 8-8. At low $We \leq 0.25$, v_z lies between the Newtonian results given by the dotted line and the fully developed channel flow denoted by the solid line. Increasing We to 0.5, the streamwise velocity becomes asymmetric about $y = 0$. The degree of asymmetry in v_z is in good agreement with the FEM predictions for the cylinder 0.5% off-center in the positive y-direction.

Modifications in the streamwise velocity across the channel at other parts of the flow are shown in Fig. 8-9 for $We = 0.22$. The streamwise velocity in the downstream region at $\zeta = 2.5$ is slightly asymmetric. This asymmetry in v_z is amplified at $\zeta = -2$. There is excellent agreement of the streamwise velocity with OLDB finite element calculations; slight deviations are caused by two reasons, one is related to experimental error as the velocity measurements are accurate to 2% of the mean fluid velocity, and secondly the cylinder arrays are not uniformly off-centered in the flow domain.

8.2.2 Flow transition in linear array of cylinders

McKinley *et al.* (1993) and Byars (1995) examined the viscoelastic wake instability of a 0.31 wt% PIB/PB/C14 solution flowing past a confined cylinder for a wide range of cylinder radius to channel height ratios. In this section, we first review the flow transition for a single cylinder, then present results for viscoelastic flow around widely and closely spaced linear arrays of cylinders.

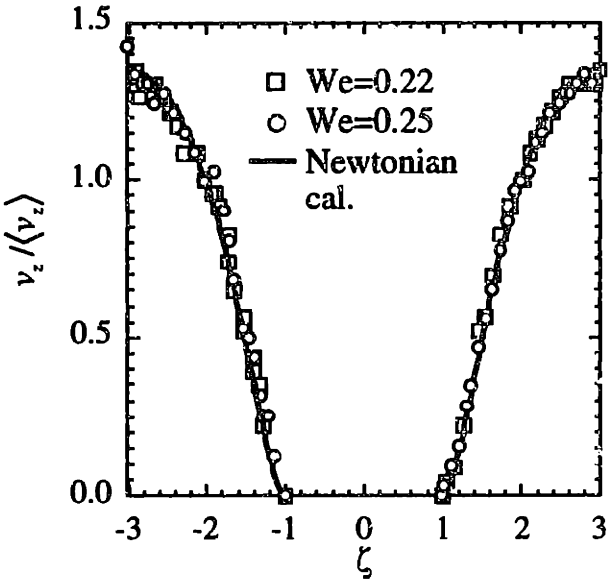

(a)

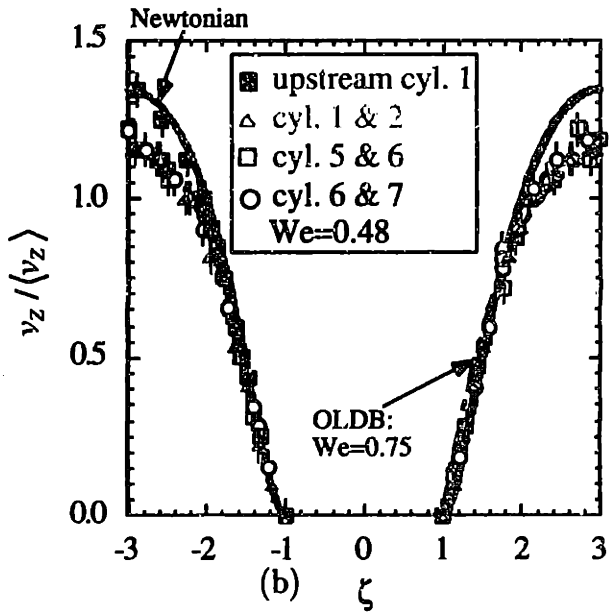

(b)

Figure 8-7: Streamwise velocity along the symmetry plane for viscoelastic flow around a widely spaced cylinder array. The solid lines are Newtonian FEM results. (a) The symbols '□' and 'o' denote v_z measurements between the fifth and sixth cylinders at $We = 0.22$ and $We = 0.25$, respectively. (b) v_z measurements between the first and second, fifth and sixth, and sixth and seventh cylinders at $We = 0.48$. The symbols, '■', '△', '□' and 'o' denote measurements between the subsequent pairs of cylinders. The dashed line is for an OLDB FEM calculation at $We = 0.75$. The shear-rate dependent We reported in the experiment, $We = 0.48$ is equivalent to the zero-shear-rate $We = 0.75$, as there is no shear thinning in Ψ_1 for the OLDB calculations.

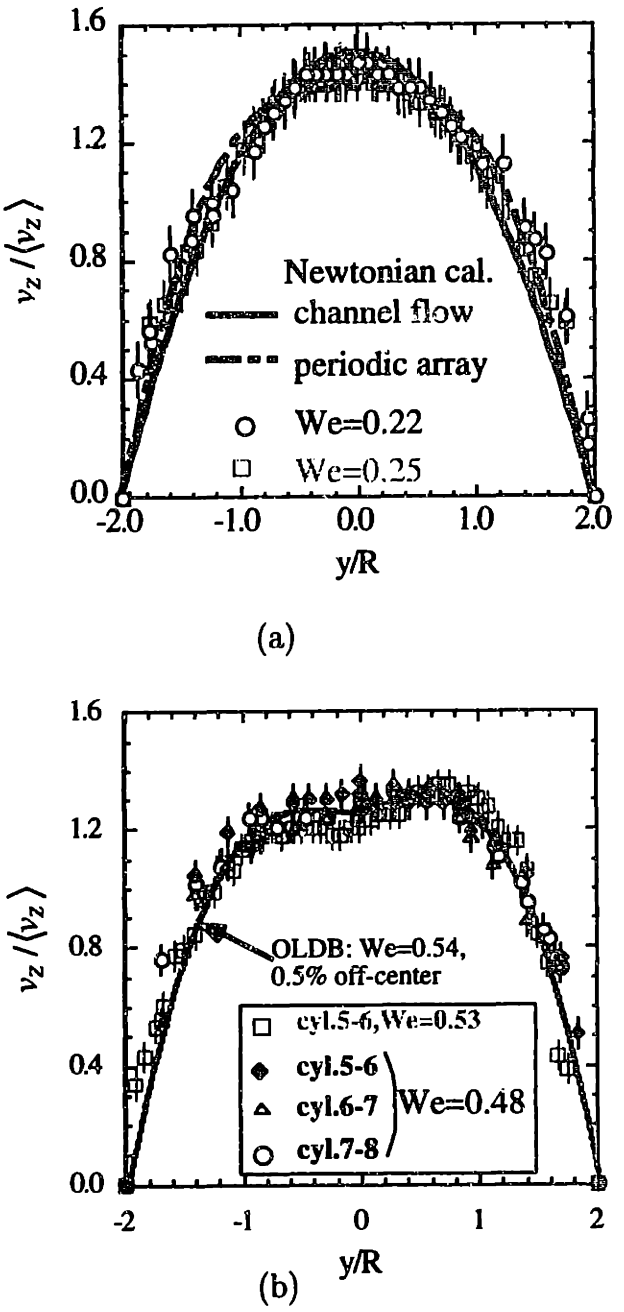

Figure 8-8: Streamwise velocity across the midway between neighboring cylinders. (a) the symbol '○' represents velocity measurements taken between the fifth and sixth cylinders at $We = 0.22$, and the symbol '□' corresponds to $We = 0.25$. The solid line is the fully developed channel flow data, and the dashed line corresponds to the Newtonian results. (b) Comparison between finite element OLDB model predictions with pointwise LDV measurements. The symbol '□' represents data collected at $We = 0.53$, the symbols '◈', '△', and '○' represents velocity measurements midway between the fifth and sixth, sixth and seventh, and seventh and eighth cylinders, respectively. The dotted line is FEM calculations with 0.5% off-centering.

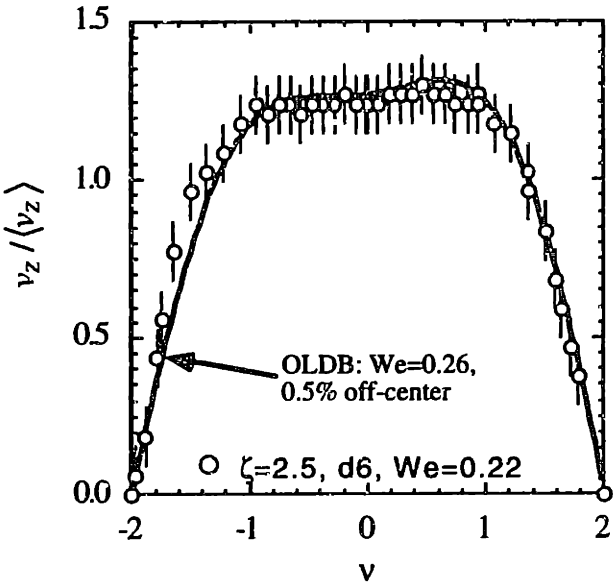

(a)

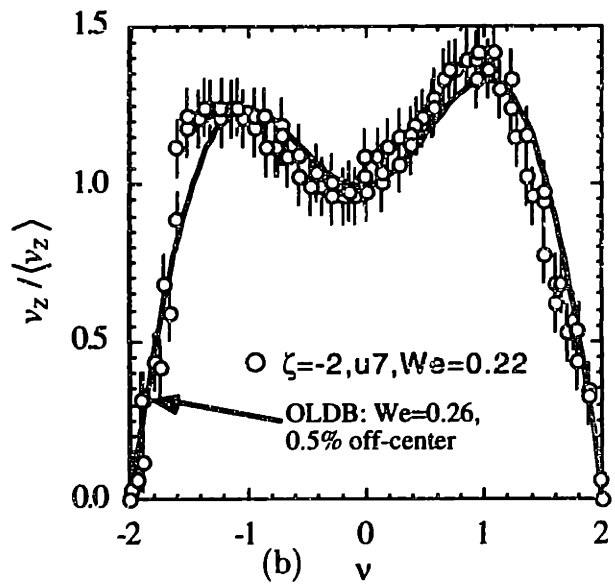

(b)

Figure 8-9: Modification of the streamwise velocity across the channel at (a) $z = 2.5R$ downstream of the sixth cylinder, and (b) $z = -2R$ upstream of the seventh cylinder in a widely spaced cylinder array.

8.2.2.1 Viscoelastic flow transition in a confined cylinder

Viscoelastic flow stability for flow past a single cylinder has been extensively studied by both McKinley (1993) and Byars (1995). McKinley *et al.* (1993) applied LDV to study the flow stability of 0.31 wt% PIB/PB/C14 past a centrally mounted cylinder in a rectangular channel, where the channel half height to cylinder radius ratio $H = H_c/R$ varied from 2 to 4. Combined flow visualization and LDV measurements indicate that beyond a critical $We = \lambda(\dot{\gamma}) < v_z > /R$, with $\dot{\gamma} = < v_z > /R$, the flow undergoes a transition from a steady 2D to steady 3D flow: the instability has the form of a cellular structure in the wake of the cylinder (McKinley *et al.* , 1993). Figure 8-10 is a reproduction of the flow visualization results where a plane sheet of laser light illuminates the centerplane of the flow cell. For an aspect ratio of $H = 2$, at $We \geq 0.34$, the transition from steady 2D flow to steady 3D flow occurs with spatially periodic fluctuations in the streamwise velocity. The instability originates in the wake at $z = 1.5R$, and propagates downstream for approximately four radii, beyond which the flow is again two-dimensional. The periodically spaced bright bands are the faster moving zones corresponding to the regions of higher scattering particle density. The wavelength of the three-dimensional instability depends on H. In particular, for $H = 2$, the wavelength, λ_x, is around $0.95R \pm 0.05R$.

Later experiments conducted by Byars (1995) show that critical We_{crit} for flow transition increases as $(H/R)^{0.4}$. The wavelength of the streamwise velocity fluctuation is a function of H/R. The We_{crit} and λ_x for $1.5 \leq H \leq 20$ are shown in Fig. 8-11 (Byars, 1995). The instability is observed slightly away from the centerplane of the geometry. As discussed below, a similar kind of flow transition is also observed in an linear array of cylinders, but at a different wavelength and We_{crit}. We are interested in knowing how the presence of a linear array of cylinders modifies the flow stability.

8.2.2.2 Flow transition in a widely spaced cylinder array ($L = 6, H = 2$)

Based on flow visualization experiments, it was found that the global flow field undergoes the same type of transition as for a single cylinder. The structure of the instability in widely spaced cylinder array is similar to the single cylinder geometry, but the wavelength of the

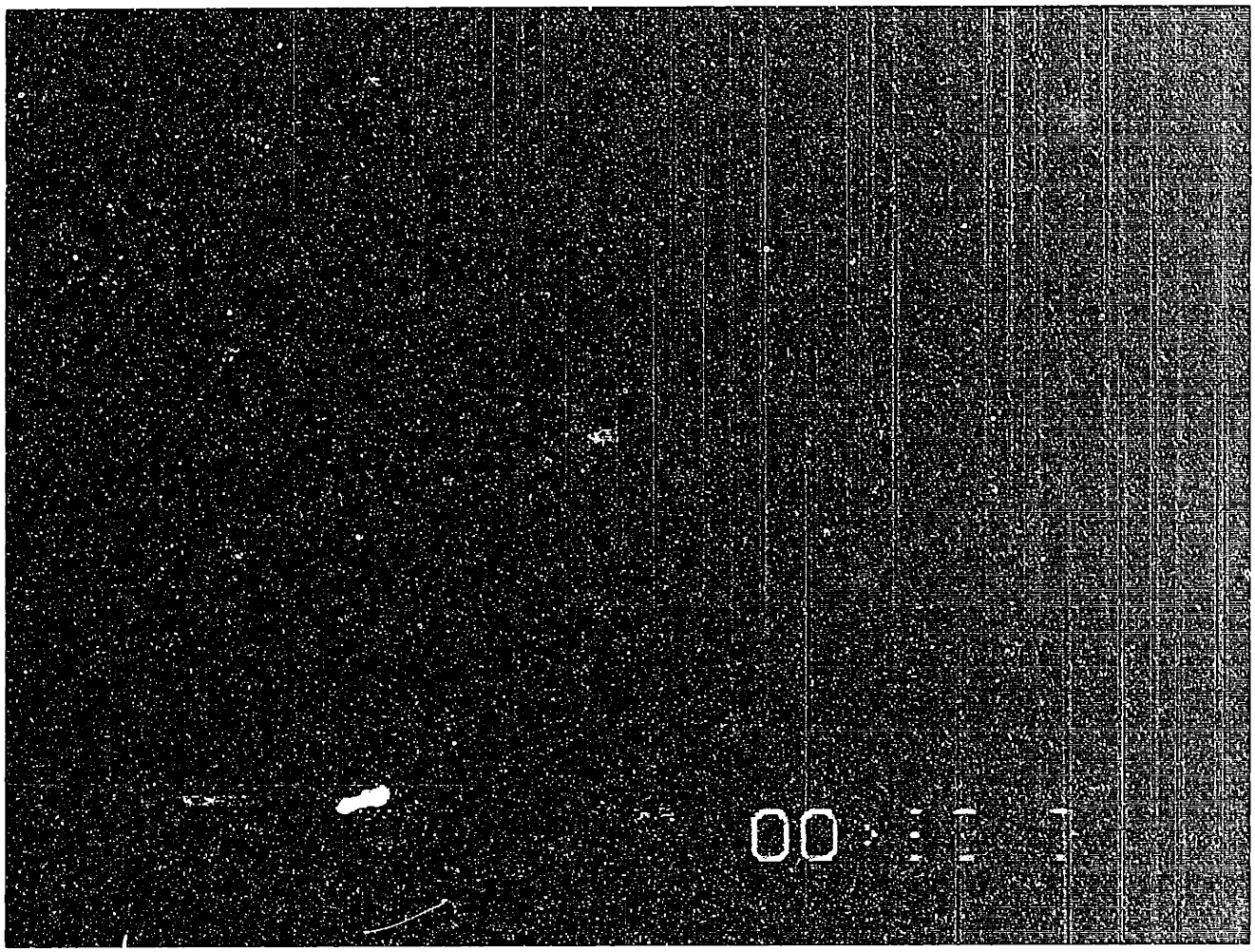

Figure 8-10: Elastic wake instability for 0.31 wt% PIB/PB/C14 solution flowing past a confined cylinder with an aspect ratio of $H = 2$. The flow is from top to bottom. Above a critical flow rate, video-imaging shows the formation of a steady cellular structure in the downstream wake of the cylinder at $We = 0.5$ and $Re = 0.028$ (McKinley *et al.* , 1993).

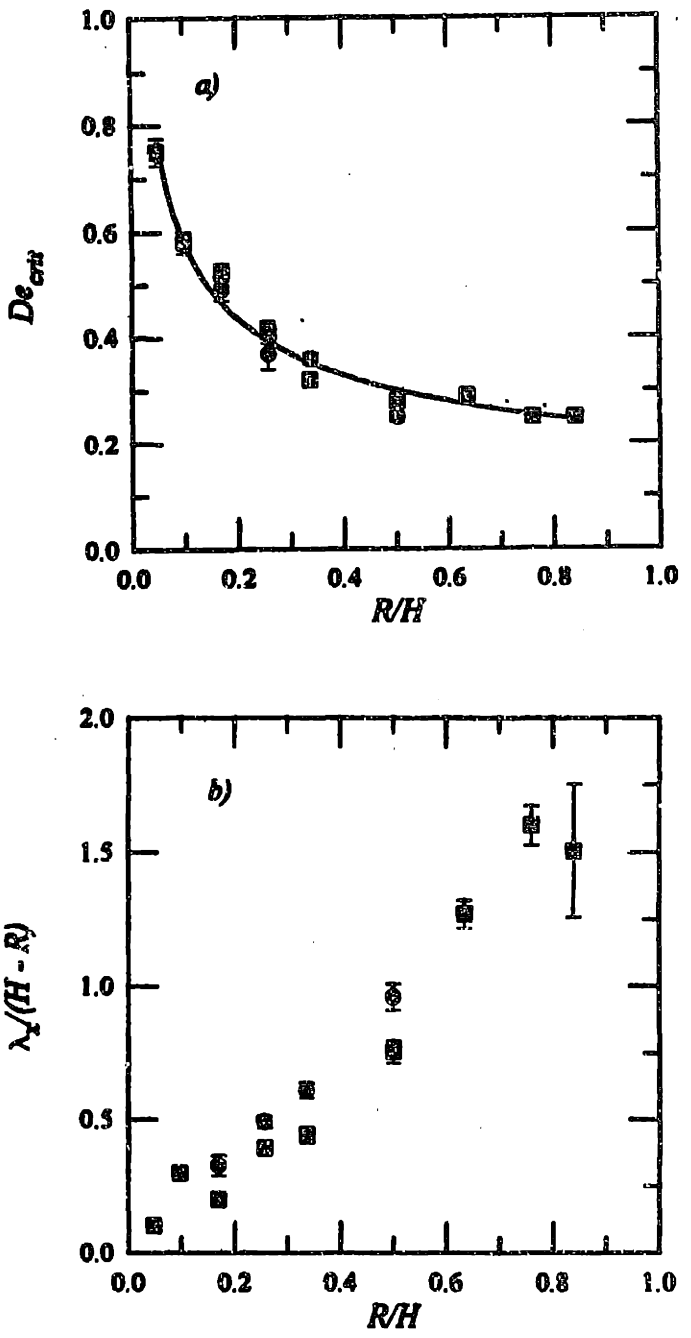

Figure 8-11: Critical condition for flow transition in a single cylinder flow. (a) The Deborah number, $De_{crit} = \lambda(\dot{\gamma}) < v_z > /R$, and (b) the wavelength at the three-dimensional flow instability, λ_x, as a function of cylinder radius to half-channel width ratio, R/H (Byars, 1995).

streamwise velocity fluctuation is much greater, and the flow is time dependent. Quantitative measurements to identify the critical We where the flow undergoes the transition are obtained by velocity scans along the neutral x-axis of the cylinder.

A series of streamwise velocity profiles is presented in Fig. 8-12 for increasing We. These profiles are measured in the neutral x-direction along the centerplane of the flow cell at $z = -2.5R$ upstream of the second cylinder. At low flow rates, the streamwise velocity profiles are flat because v_z is uniform along the length of the cylinder for a steady, two-dimensional stagnation flow. However, as the Weissenberg number is increased to a critical value, $We_{1,crit} = 1.14 \pm 0.03$, the flow undergoes a transition where periodic oscillations in the streamwise velocity appear along the length of the cylinder. Careful measurements near the critical conditions show that for increments of $\Delta We = 0.01$, there is no hysteresis in the flow, and thus the instability is supercritical. The instability is purely elastic in nature, since the Reynolds number at the critical $We_{1,crit} = 1.14 \pm 0.03$ is only $Re = 0.008$.

The axial extent of this instability at the first local transition is examined by scanning v_z across the neutral x-axis at the centerplane for various z positions. The results are shown in Fig. 8-13. The streamwise velocity measurements indicate that spatial fluctuations originate at $z = 1.5R$ downstream of the first cylinder, and propagate $3R$ downstream reaching $z = -1.5R$ upstream of the second cylinder. Beyond this point, the rest of the flow remains two-dimensional and steady. Starting from the rear stagnation point of the first cylinder, as z increases, the amplitude of the velocity fluctuation increases until $z = 3R$ is reached. At $z = 3R$, the amplitude of the fluctuation in v_z decreases. As z continues to increase past the $z = 3R$ downstream of the sixth cylinder (equivalently $z = -3R$ upstream of the seventh cylinder), the amplitude of the v_z fluctuations increases again, and then decreases, essentially disappearing at $z = -1.5R$ upstream of the second cylinder. Because the LDV measurements at $z = -2.5R$ and $-2R$ upstream of the second cylinder give rise to the strongest signals, the flow transition in the array of cylinders is identified by scanning the streamwise velocity along the neutral x-direction at $y = 0$ and $z = -2.5R$ upstream of each cylinder. The first local flow transition in a widely spaced cylinder array is very similar to the case of a single cylinder (McKinley *et al.* , 1993; Byars, 1995) where the velocity fluctuations originate in the wake of the cylinder and propagate downstream. In contrast

with the single cylinder flow transition, the wavelength of this 3D instability in a widely spaced cylinder array is $\lambda_x = 5.56 \pm 0.83\, mm = 3.5R \pm 0.5\, R$ along the x-axis. The large error in the wavelength is due to the fact that the velocity scan is restricted to the central region $-12 \leq x \leq 12$ to avoid end effects, and thus only six peaks are captured. This limited data set restricts the accuracy of the FFT in the computation of the dominant wavelength.

The wavelength of the perturbations in the streamwise velocity is determined by applying Fourier analysis to the velocity profile $v_z(x)$. The power spectrum of the signal measures the spectral contributions of the oscillations with a spatial wavelength of λ_x (mm). The FFT spectrum for the velocity profile measured at $We = 1.14$ is given in Fig. 8-14(a). The characteristic wavelength of the velocity fluctuation is determined to be $\lambda = 5.5 \pm 0.83 mm = 3.5R \pm 0.5R$. The temporal stability of the flow at this critical $We_{1,crit}$ is examined by monitoring the streamwise velocity at a single point in the flow. A velocity time series $v_z(0, 0, -2.5R, t)$ is presented in Fig. 8-14(b) for the same flow conditions reported at the critical condition. Oscillations in the streamwise velocity extend spatially across the length of the cylinder, while the velocity measured at a single point oscillates $\pm 5\%$ around the mean arising from random noise in the tracker, and is accordingly considered to be steady and time independent to within experimental error. Therefore, in the wake of the first cylinder, the transition from a steady, planar extensional flow to a steady three-dimensional cellular structure in a widely spaced cylinder array is very similar to the single cylinder case, but with a different critical We and wavelength.

Propagation of the three-dimensional instability downstream of the second cylinder is examined by scanning the streamwise velocity along the length of this cylinder with increasing flow rate as depicted in Fig. 8-15. At low We, the flow is steady and two-dimensional until a critical $We_{2,crit} = 1.19$, where spatial oscillations in the v_z profile become apparent. The three-dimensional instability persists downstream for a distance of one radius, beyond which the rest of the flow is steady and two-dimensional. Further increasing We to 1.28 leads to equally spaced v_z fluctuations convecting further into the linear array, reaching the upstream of the fourth cylinder. The wavelengths of the instability at the two different We are obtained from the FFT spectrum. At $We = 1.19$, two wavelengths are significant, one at $\lambda_x = 4.1R \pm 0.5R$ and the other at $\lambda_x = 7.3R \pm 1.4R$. Increasing the flow rate

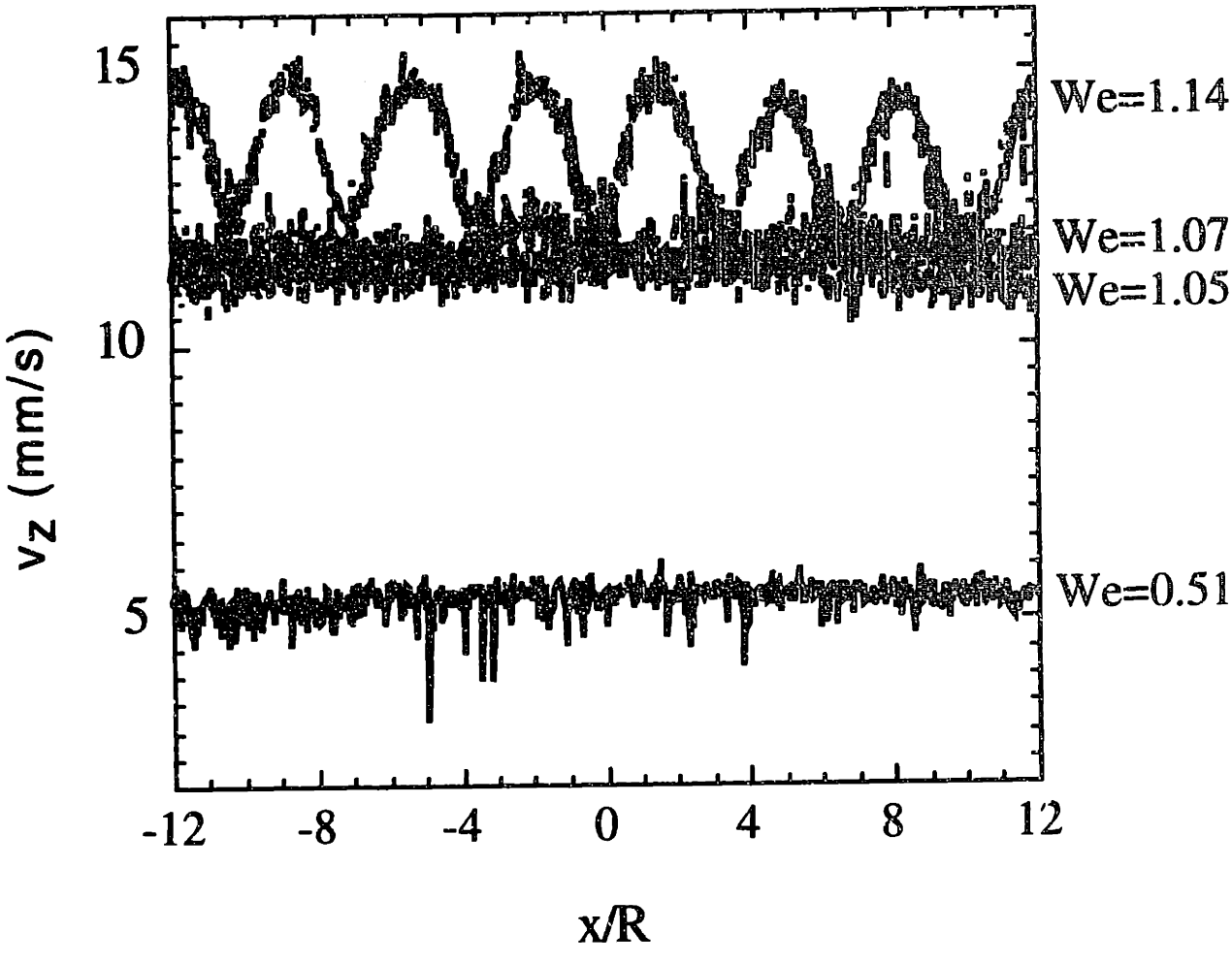

Figure 8-12: Streamwise velocity profile, $v_z(x, 0, -2.5R)$ across the width of the channel at fixed $y = 0$ and $z = -2.5R$ upstream of the second cylinder as the Weissenberg number is increased from $We = 0.51$ to 1.14.

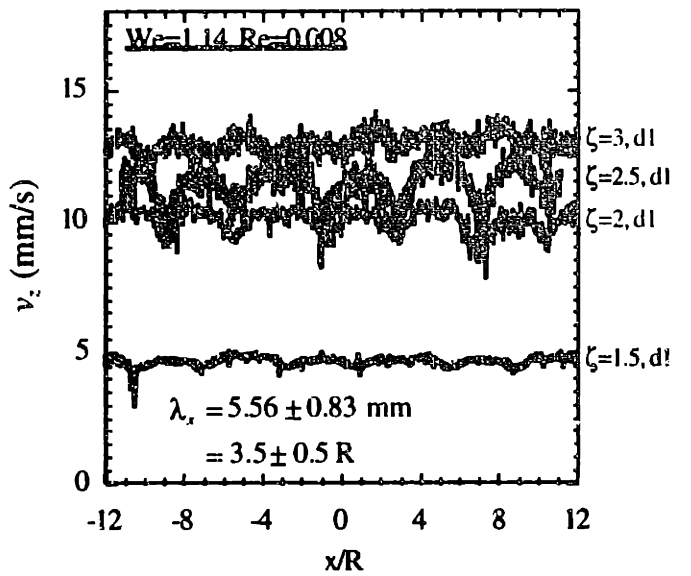

(a)

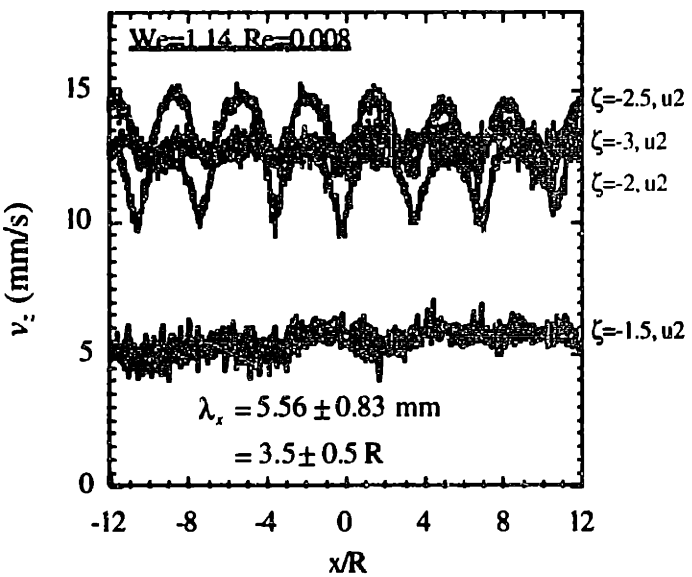

(b)

Figure 8-13: Axial extent of the flow instability at $We_{1,crit} = 1.14$ (a) downstream of the first and (b) upstream of the second cylinders in a widely spaced cylinder array. All streamwise velocity scans were carried out at $y = 0$. 'd1' indicates data collected downstream of the first cylinder, and 'u2' indicates a region upstream of the second cylinder. The instability has an unique wavelength of $3.5R \pm 0.5R$.

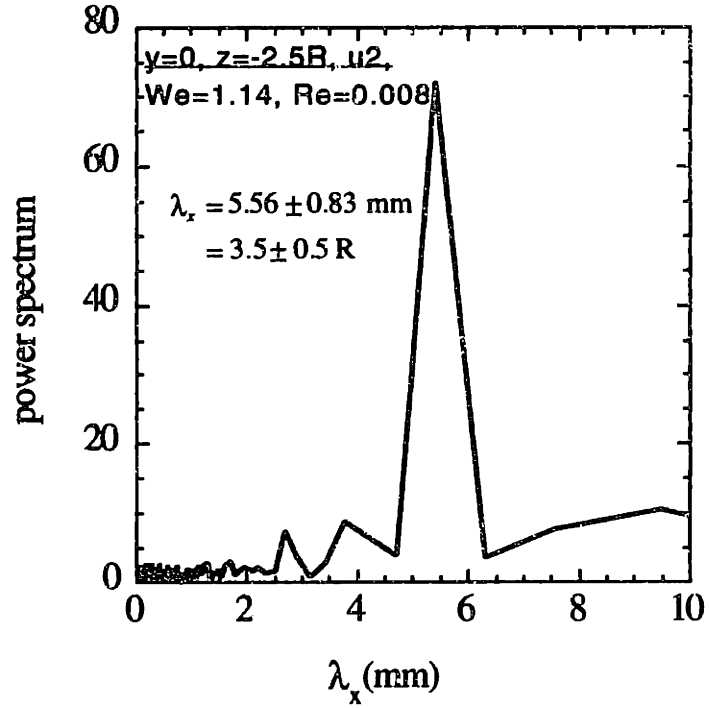

(a)

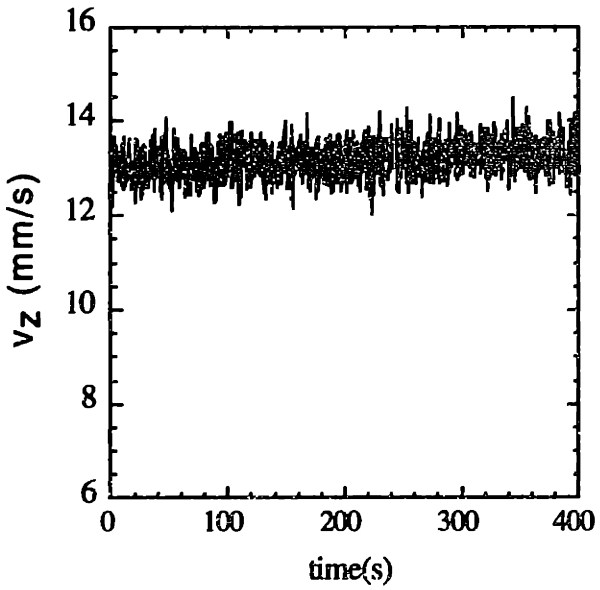

(b)

Figure 8-14: (a) Power spectrum of spatial fluctuations in the streamwise velocity $v_z(x, 0, -2.5R)$ measured at $z = -2.5R$ upstream of the second cylinder at the critical $We_{1,crit} = 1.14$. (b) Time series of the streamwise velocity $v_z(0, 0, -2.5R)$ at $z = -2.5R$ upstream of the second cylinder.

causes the fluctuations in v_z to become more selective, and at $We = 1.28$, the instability has a fixed wavelength of $3.9R \pm 0.4R$. The streamwise velocity scan along the neutral x-axis is used to characterize the spatial wavelength shown in Figs. 8-16(a) and (b), and the time characteristics of the second local flow transition are measured by monitoring the streamwise velocity at a single point $(-14R, 0, -2.5R)$ upstream of the third cylinder (Fig. 8-16(c)). The streamwise velocity v_z remains steady in time. Thus, the second local flow transition is from a steady two-dimensional to a steady three-dimensional flow. The onset of the first flow transition in a linear array of cylinders occurs at $We_{1,crit} = 1.14$, as compared to $We_{crit} = 0.34$ in a single cylinder flow, and the flow instability downstream of the second cylinder occurs at higher $We_{2,crit} = 1.19$ than the first local transition ($We_{1,crit} < We_{2,crit}$). This suggests that the presence of neighboring cylinders actually stabilizes the flow. Thus, the flow transition in a linear array of cylinders occurs at much higher We than in the single cylinder case.

Although the flow undergoes local transitions between the first and second, and second and third cylinders, these transitions are not of interest to us because we are mainly concerned with flow past an "infinite" linear array of cylinders, i.e. a flow transition that propagates throughout the entire array. Thus, we are interested in flow around the interior cylinders, not the first or the last few cylinders in the channel. As the flow rate of the fluid increases further to $We = 1.36$ and $Re = 0.01$, the streamwise velocity profiles along the centerplane of the flow cell at $z = -2.5R$ upstream of the fifth, sixth, seventh, and eighth cylinders become spatially periodic along the neutral x-axis, as shown in Fig. 8-17. The wavelength of the disturbance upstream of those cylinders is $4.0R \pm 0.6R$. Thus, the flow undergoes a transition from steady 2D to 3D spatially periodic at the critical $We_{crit} = 1.36$ in the widely spaced array ($L = 6, H = 2$).

Flow instabilities in linear periodic arrays of cylinders are characterized in terms of temporal and spatial extent. At a fixed point in the flow domain $(0, 0, -2.5R)$ upstream of the seventh cylinder, the streamwise velocity v_z is monitored as a function of time. Figure 8-18 clearly indicates that v_z evolves with time, and thus the flow undergoes a transition from steady 2D to transient 3D at critical $We_{crit} = 1.36$ in the widely spaced cylinder array. The time period cannot be determined by the current experimental setup due to the limitations

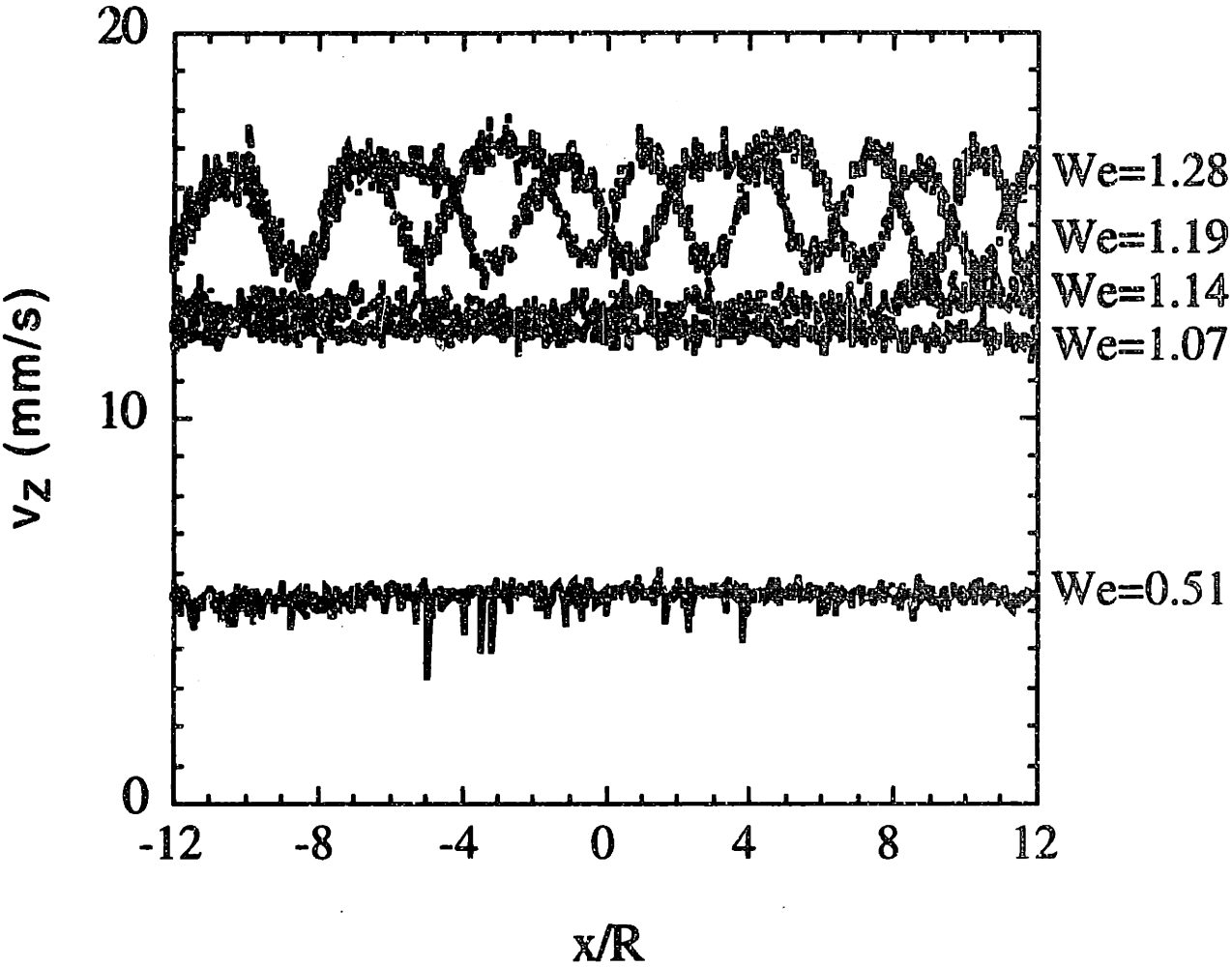

Figure 8-15: Streamwise velocity profile, $v_z(x, 0, -2.5R)$ across the width of the channel at fixed $y = 0$ and $z = -2.5R$ upstream of the third cylinder as the Weissenberg number is increased from $We = 0.51$ to 1.28.

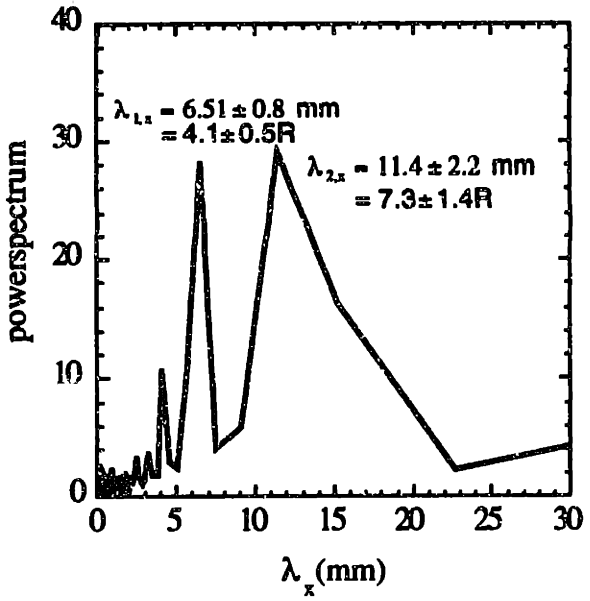

(a)

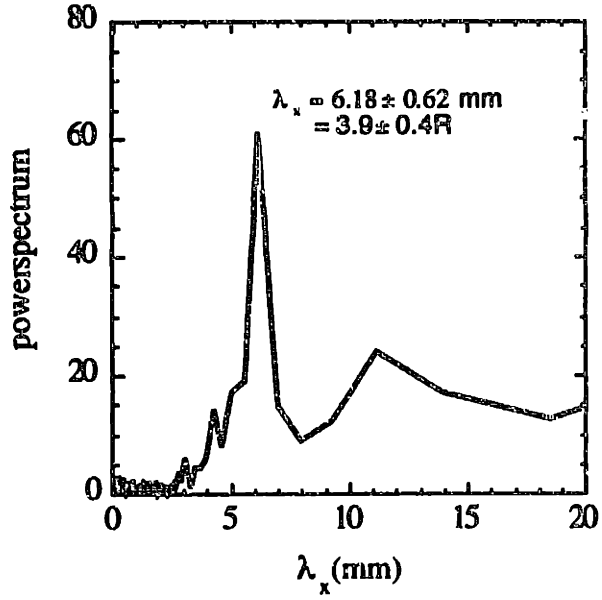

(b)

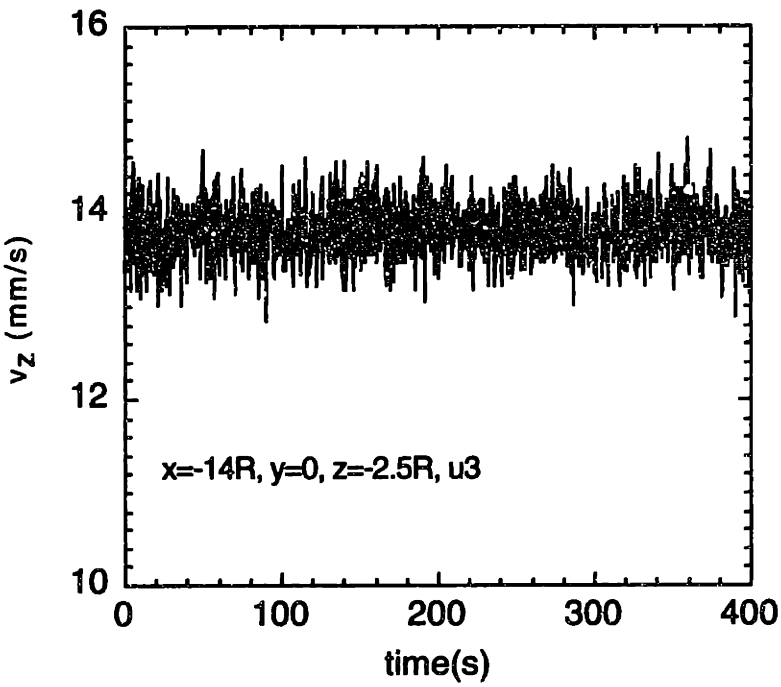

(c)

Figure 8-16: Power spectrum of spatial fluctuations in the streamwise velocity $v_z(x, 0, -2.5R)$ measured at $z = -2.5R$ upstream of the third cylinder at (a) the second critical Weissenberg number, $We_{2,crit} = 1.19$, (b) and third critical Weissenberg number, $We_{3,crit} = 1.28$. (c) time characteristic of the second flow transition at $We_{2,crit} = 1.19$.

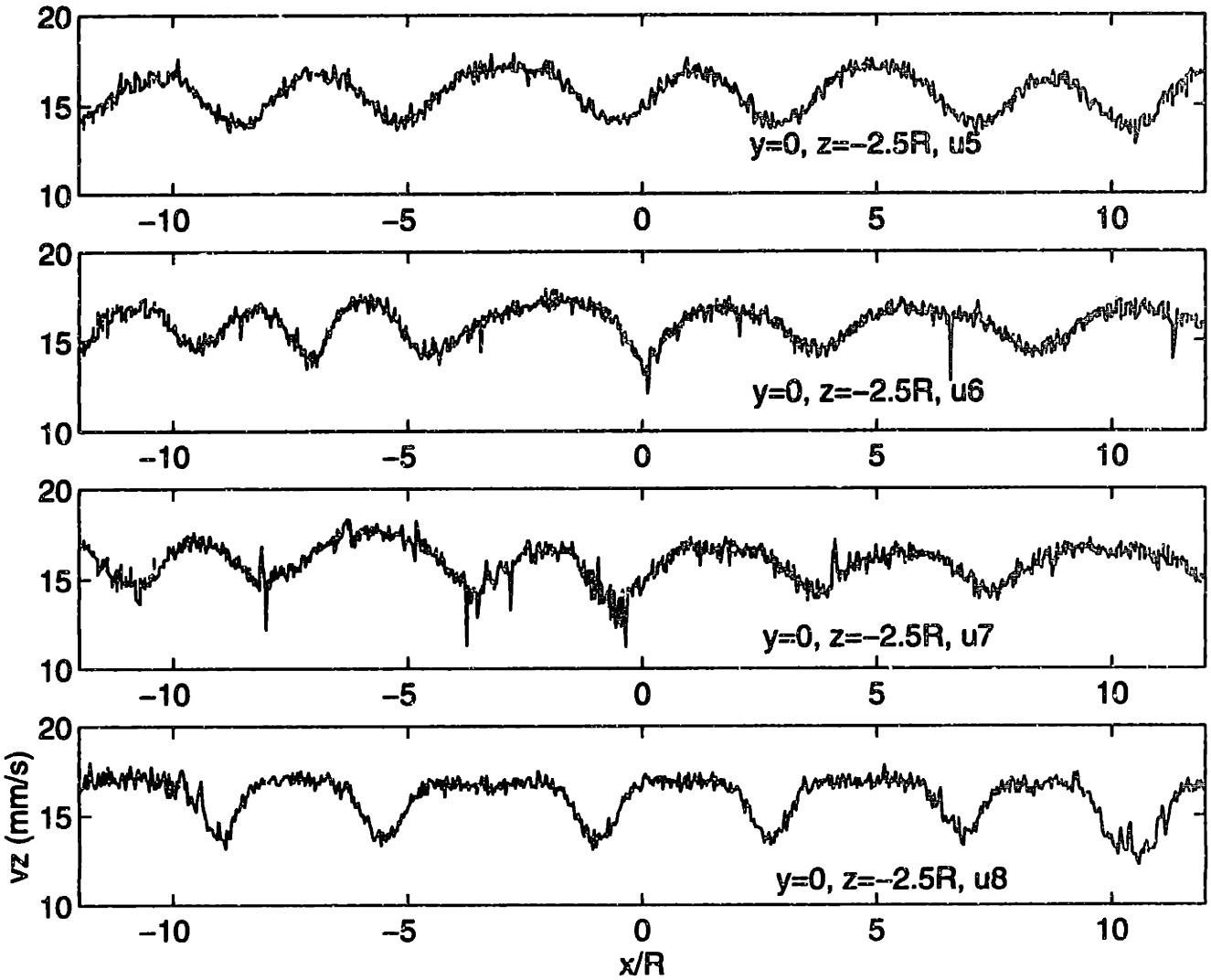

Figure 8-17: Streamwise velocity profile, $v_z(x)$, along neutral x-axis at fixed $y = 0$ and $z = -2.5R$ upstream of the fifth (u5), sixth (u6), seventh (u7) and eighth (u8) cylinders at critical Weissenberg number, $We_{crit} = 1.36$, where the flow in the entire linear array undergoes a transition. The wavelengths of the instabilities are $\lambda_{x,u5} = \lambda_{x,u6} = \lambda_{x,u7} = \lambda_{x,u8} = 6.33 \pm 0.91\ mm = 4.0R \pm 0.6R$.

of the analyzer. At the onset of the flow instability, $Re = 0.01 \ll 1$, and the inertial effects are negligible. The pressure drop across the flow unit is carefully controlled and monitored by a pressure controller to within ± 0.1 psi during the experiment; therefore, the time dependent three-dimensional flow is caused purely by fluid elasticity, not by inertia or pressure variations leading to oscillations in volumetric flow rate.

The spatial extent of the flow instability was examined by scanning the streamwise velocity along the neutral x-axis between the sixth and seventh cylinders at fixed z and y positions. At the center of the flow geometry, $y = 0$, streamwise velocity scans were performed between $z = 1.5R$ downstream of the sixth cylinder and $z = -1.5R$ upstream of the seventh cylinder, as shown in Fig. 8-19(a) and (b). The wavelength of the three-dimensional instability along the length of the cylinder increases from $3.0R \pm 0.3R$ at $z = 1.5R$ to $4.0R \pm 0.6R$ at $z = 2R$ and $z = 2.5R$ downstream of the sixth cylinder. At $z = 3R$, the spatial period decreases to $3.5R \pm 0.5R$, then increases back to $4.0R \pm 0.6R$ upon reaching $z = -2.5R$ upstream of the seventh cylinder. The wavelength of the instability is again $4.0R \pm 0.6R$ at $z = -2R$ and changes to $4.4R \pm 0.6R$ at $z = -1.5R$ upstream of the seventh cylinder. The instability disappeared at the front stagnation point of the seventh cylinder as the velocity approached zero. The dependence of wavelength on axial position is weak because of the large error ($0.6R$) in the discrete Fourier power spectrum. This arises from the fact that the instability has a wavelength of order $4R$, while the channel width in the neutral direction is only $40R$. To resolve more accurately the dependence of spatial wavelength in the streamwise direction, one needs to design a wider channel, which in turn decreases the velocity for a fixed maximum flow rate. Therefore, a compromise has to made in resolving the spatial characteristics of the instability in the linear array of cylinders.

The cross-channel extent of the flow instability was examined at $z = -2.5R$ upstream of seventh cylinder and various y positions. Unlike the case of the single cylinder where the instability is highly localized in the centerplane, in the linear array of cylinders, the instability extends to $y = 0.6R$ on either side of the centerplane. The wavelength of the fluctuation remains constant across the width of the channel; for example, at $y = 0.4R$ and $z = -2.5R$ upstream of the seventh cylinder, $\lambda_x = 4.0R \pm 0.6R$, as shown in Fig. 8-19(c). The amplitude of the flow instability decreases with increasing y and essentially disappears

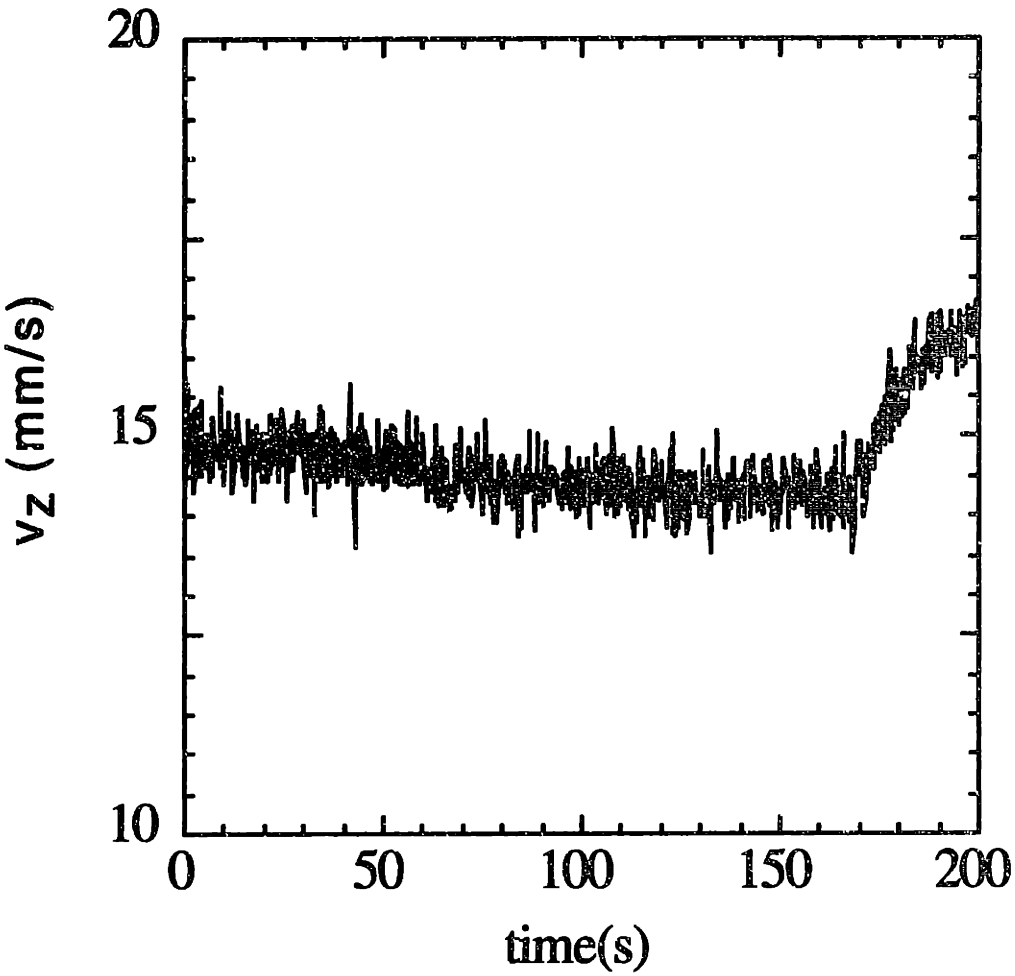

Figure 8-18: Streamwise velocity at a fixed point $(0, 0, -2.5R)$ upstream of the seventh cylinder as a function of time at critical $We_{crit} = 1.36$.

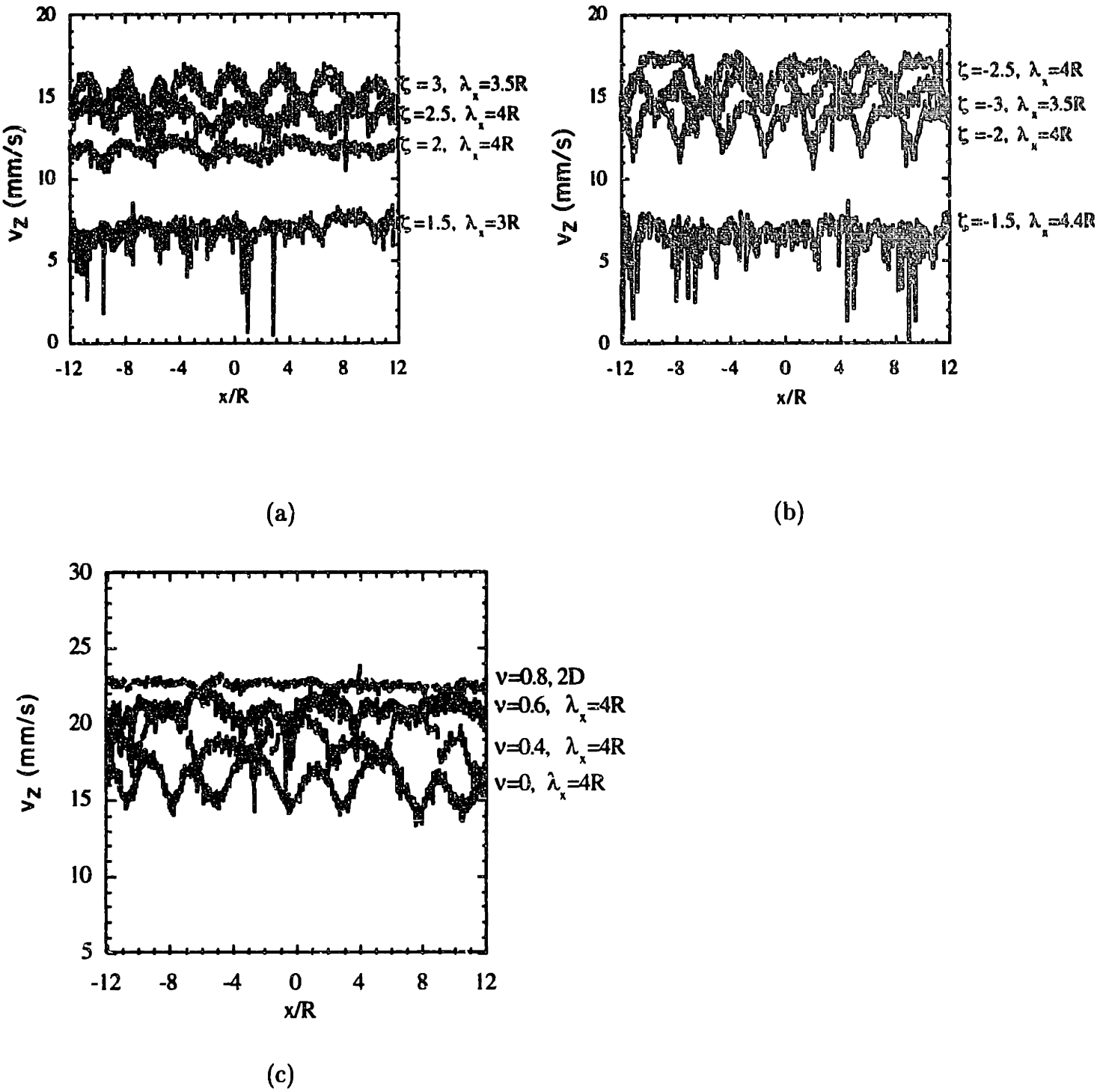

Figure 8-19: Spatial extent of the flow instability in a widely spaced linear array of cylinders. $v_z(x)$ is plotted for $y = 0$ and (a) $z = 1.5R$ to $3R$ downstream of the sixth cylinder and (b) $z = -3R$ to $-1.5R$ upstream of the seventh cylinder. Wavelength of the instability: $\lambda_{x,\zeta=-1.5} = 4.4R \pm 0.6R$, $\lambda_{x,\zeta=1.5} = 3.0R \pm 0.3R$, $\lambda_{x,\zeta=\pm2} = \lambda_{x,\zeta=\pm2.5} = 4.0R \pm 0.6R$, and $\lambda_{x,\zeta=\pm3} = 3.5R \pm 0.5R$ (c) $v_z(x)$ is plotted for $z = -2.5R$ upstream of the seventh cylinder and $y = 0$ to $0.8R$ at critical $We_{crit} = 1.36$. Wavelength is $\lambda_{x,\nu<0.8} = 4.0R \pm 0.6R$.

at $0.8R$. The wavelength of the instability depends on the streamwise position, with the largest fluctuation occurring at the center of the flow geometry ($y = 0$). Although the flow is time dependent, the wavelength of the streamwise velocity fluctuations along the neutral x-axis is time independent; therefore, the transient flow is time periodic.

Measurements of the v_x component of velocity at critical $We = 1.36$ also show periodic fluctuations about zero as shown in Fig. 8-20. The FFT spectrum shows a single peak at $\lambda_x = 12.6 \pm 1.9\,mm = 7.94R \pm 1.2R$, indicating that the wavelength of oscillations in v_x is doubled from $4R$ in the streamwise velocity fluctuation in v_z.

The measurements presented in this section are the first experimental observations of a three-dimensional elastic instability occurring in the widely spaced cylinder array. The LDV technique has proven to be an extremely powerful method for characterizing spatial characteristics of the elastic wake instability. At a critical Weissenberg number $We_{1,crit} = 1.14$, the flow locally undergoes a transition from steady 2D to steady 3D inbetween the first and second cylinders. This flow instability propagates into the subsequent cylinders as the flow rate is increased. The critical flow transition for interior cylinders, which resembles the flow past an infinite array of cylinders, does not occur until $We = 1.36$. The flow visualization (Liu *et al.* , 1996) indicates that the structure of the instability corresponds to spatially periodic cells of fluid that have alternating fast and slow streams. LDV measurements confirm that the steady two-dimensional flow undergoes a bifurcation to a time-dependent, three-dimensional spatially periodic cellular structure that extends between two neighboring cylinders. The instability originates at $z = 1.5R$ downstream of each cylinder and persists for a distance of $3R$, extending to $z = -1.5R$ upstream of the next cylinder. The wavelength of such an instability weakly depends on the z position and extends spatially from the centerplane to $y = 0.6R$ on either side. The spatial fluctuation in the streamwise velocity at $|z| > 1.5R$ of each cylinder has a wavelength of $4.0R \pm 0.6R$, and the wavelength is doubled in v_x.

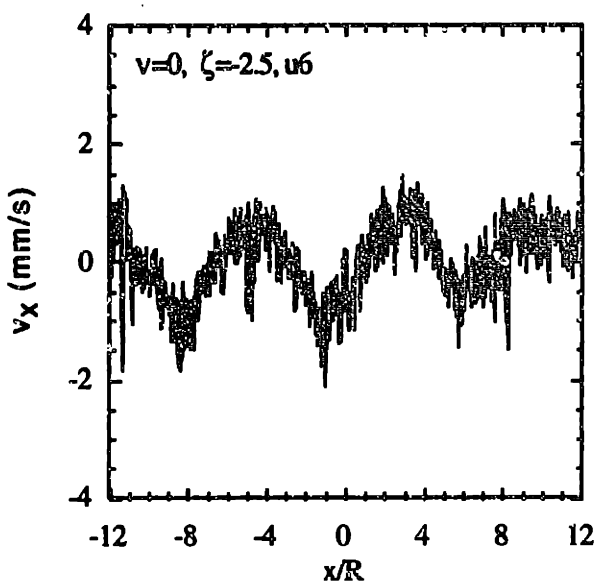

(a)

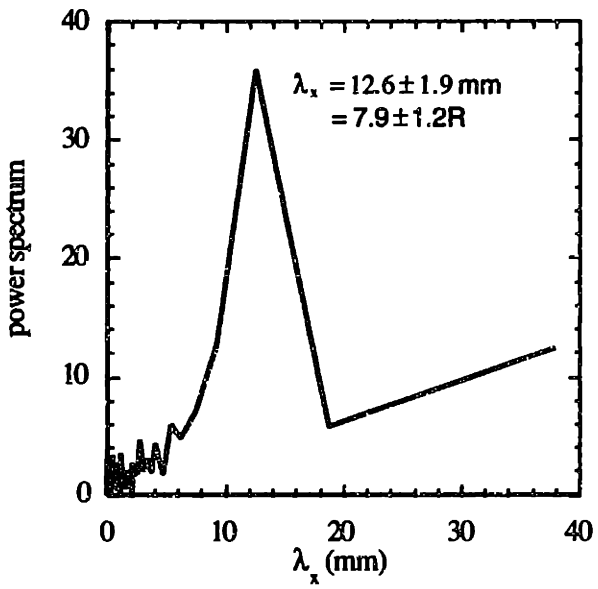

(b)

Figure 8-20: (a) $v_x(x)$ profiles along the neutral x-axis at $y = 0$ and $z = -2.5R$ upstream of the sixth cylinder at the critical flow transition $We_{crit} = 1.36$ in a linear array of cylinders. (b) The FFT spectrum used to resolve the x-component instability.

8.3 Creeping flow in closely spaced cylinder arrays ($L = 2.5$, $H = 2$)

In this section, results of laser Doppler velocimetry investigations of viscoelastic flow around closely spaced cylinder arrays are described. In section 8.3.1, the steady two-dimensional streamwise velocity measurements are compared with the finite element calculations reported in chapter 5. Excellent agreement in v_z between numerical predictions and measurements are obtained. Slight asymmetries in the streamwise velocity profiles are caused by the off-centering of the cylinders. In addition to the steady state flow results, at a critical Weissenberg number, the two-dimensional steady flow undergoes a transition to become three-dimensional and time periodic. Details of the onset condition, the spatial extent and time period of this instability is provided are section 8.3.2.

8.3.1 Steady flow in closely spaced cylinder arrays ($L = 2.5$, $H = 2$)

When the center-to-center cylinder spacing is $2.5R$, the flow is separated between the neighboring cylinders. The steady two-dimensional viscoelastic calculations predict that the streamwise velocity across the width of the channel is weakly dependent on ζ for $|\zeta| \geq 1$, and the v_z profiles are insensitive to We.

Fig. 8-21 presents the streamwise velocity across $\zeta = 1.25$ downstream of the first, second, and fifth cylinders at $We = 0.37$. There is a slight asymmetry in the $v_z / \langle v_z \rangle$ profiles because the cylinders are not positioned exactly in the center of the channel. The steady two-dimensional Newtonian calculation with 0.25% off-centering in the negative y direction captures the asymmetry in the velocity field to within 4%, which is within the accuracy of the LDV measurements. As indicated in Fig. 8-22, the streamwise velocity across $\zeta = 1.25$ downstream of each cylinder does not deviate from the Newtonian results even at $We = 0.7$. Even when the Weissenberg number is increased to $We = 1.48$, which is below the onset of any flow transition, the $v_z / \langle v_z \rangle$ profile across the width of the channel remains Newtonian. This observation agrees with the steady two-dimensional finite element calculations reported in chapter 5. In a closely spaced two-dimensional array of cylinders, flow visualization stud-

ies conducted by Chmielewski and Jayaraman (1993) concluded that the flow is basically identical to that of the Newtonian case prior to flow transition. Furthermore, the dimensionless velocity $v_z / \langle v_z \rangle$ does not depend on ζ because of the small separation between cylinders. In particular, at $\zeta = -1.05$ upstream of the sixth cylinder, the velocity field is identical to that of the flow across $\zeta = 1.25$ downstream of each cylinder. For this reason, in the flow stability studies, we used the streamwise velocity across $\zeta = 1.25$ downstream of each cylinder to identify the occurrence of flow transition.

The recirculating flow between neighboring cylinders is only $O(10^{-3} \langle v_z \rangle)$, and this small negative velocity cannot be measured by the LDV system. It is more reasonable to examine v_z outside of the flow separation region. Fig. 8-23 presents the streamwise velocity across $y = R$ and $y = 1.35R$. At $We = 0.33$, the measured v_z at fixed $y = R$ is symmetric about the center of the cylinder ($z = 0$), and agrees very well with the Newtonian results. Moving farther away from the flow recirculation region at $y = 1.35R$, the streamwise velocity is no longer symmetric about $z = 0$. The slight shift in v_z is accurately predicted by the OLDB model. The shift in v_z is more pronounced at $y = 1.35R$ than $y = R$ for two reasons. First, because the cylinders are so close to each other, polymer molecules do not have sufficient time to relax before they reach the next cylinder in the array. Second, the presence of recirculating flow between cylinders eliminates the wake extensional region, and the largest molecular extension remains in the minimum gap between the cylinder and channel wall. Therefore, for polymer molecules further away from the cylinder ($y = 1.35R$), the large nonhomogeneous shear flow results in large molecular extensions and high stresses (Liu *et al.* , 1997), which in turn are reflected as a pronounced shift of the velocity profile.

8.3.2 Flow transition in closely spaced cylinder arrays ($L = 2.5$, $H = 2$)

In section 8.2, we saw that in widely spaced cylinder arrays ($L = 6, H = 2$), the flow undergoes a transition from a steady two-dimensional to a transient three-dimensional flow at a critical $We = 1.36$. The structure of this wake instability is very similar to the case of single cylinder flow. Now the question becomes, how is the flow stability modified when cylinders are closely spaced and flow is separated between them?

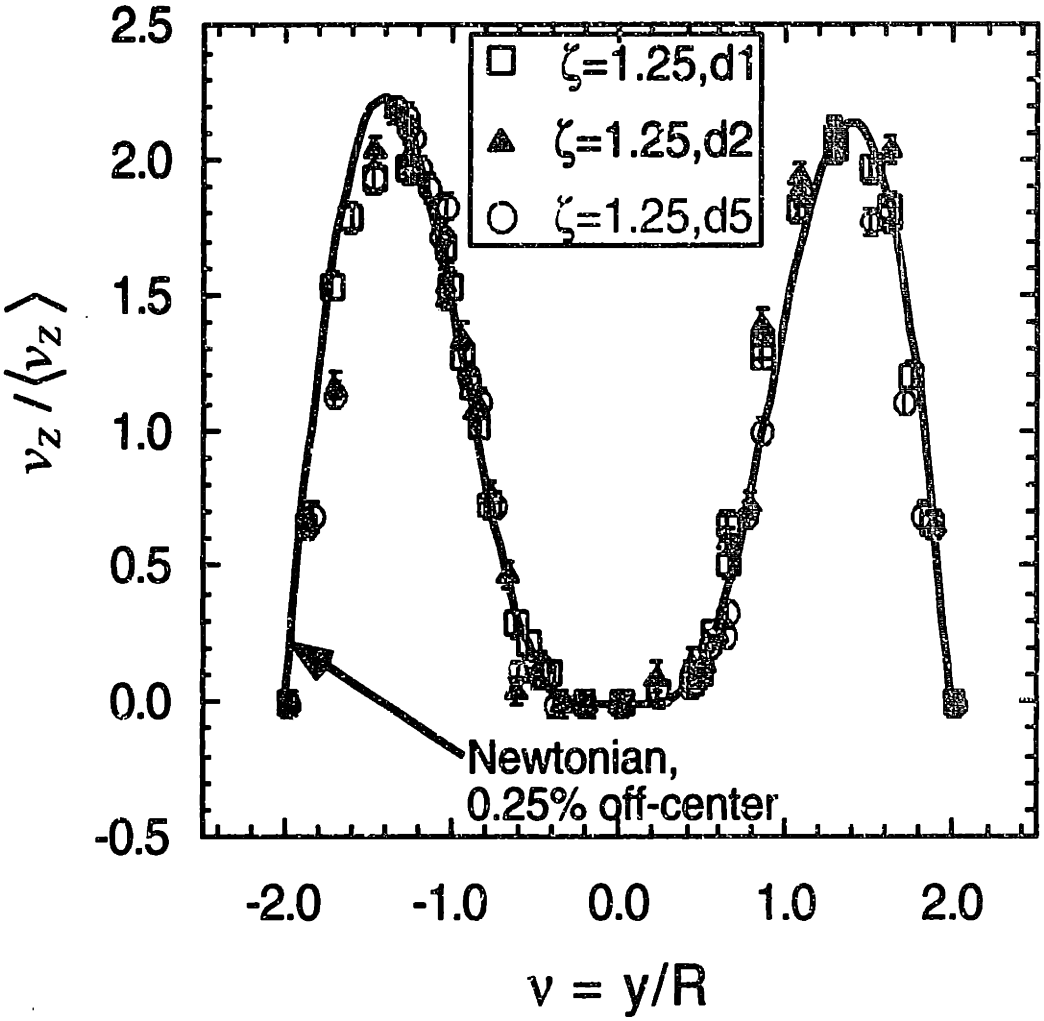

Figure 8-21: Streamwise velocity profile across $\zeta = 1.25$ mideway between two adjacent cylinders at $We = 0.37$ in a closely spaced cylinder array. The symbols '□', ▲', and 'o' denote measurements downstream of the first, second, and fifth cylinders, respectively. The solid line corresponds to the Newtonian calculations with 0.25% off-centering in the negative y-direction.

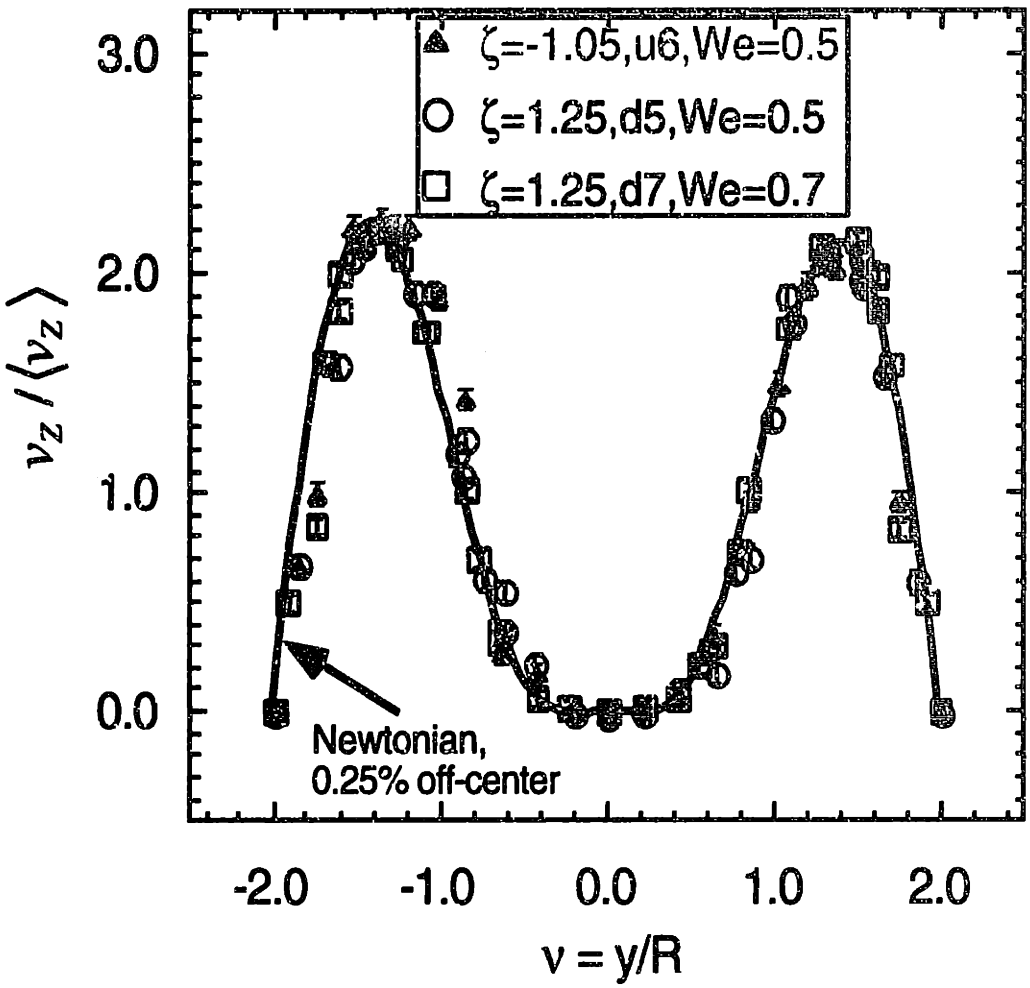

Figure 8-22: Streamwise velocity profile across the channel. The symbols '▲' and 'o' denote measurements at $-1.05R$ upstream of the sixth, and $1.25R$ downstream of the fifth cylinder, respectively at $We = 0.54$. The symbol '□' corresponds to data at $We = 0.72$ obtained $z = 1.25R$ downstream of the seventh cylinder. The solid line corresponds to the Newtonian calculations with 0.25% off-centering in the negative y-direction.

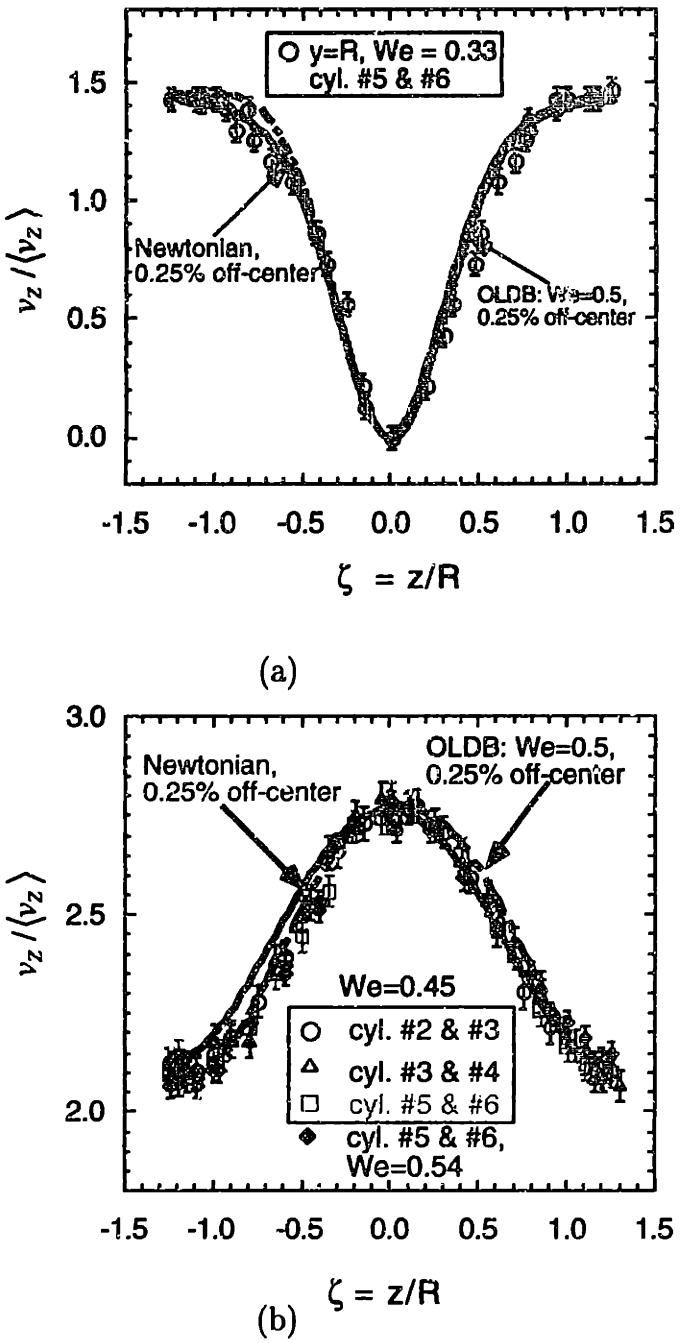

Figure 8-23: Streamwise velocity profile at fixed y. The solid line is for Newtonian results and the dotted line corresponds to viscoelastic calculations with 0.25% off-centering in the negative y direction. (a) $v_z / \langle v_z \rangle$ along $y = R$. (b) $v_z / \langle v_z \rangle$ along $y = 1.35R$. The symbols '$\circ$', '$\triangle$' and '$\square$' denote measurements between the second and third, the third and forth, the fifth and sixth cylinders, respectively, at $We = 0.45$. The symbol '$\blacklozenge$' corresponds to $We = 0.54$.

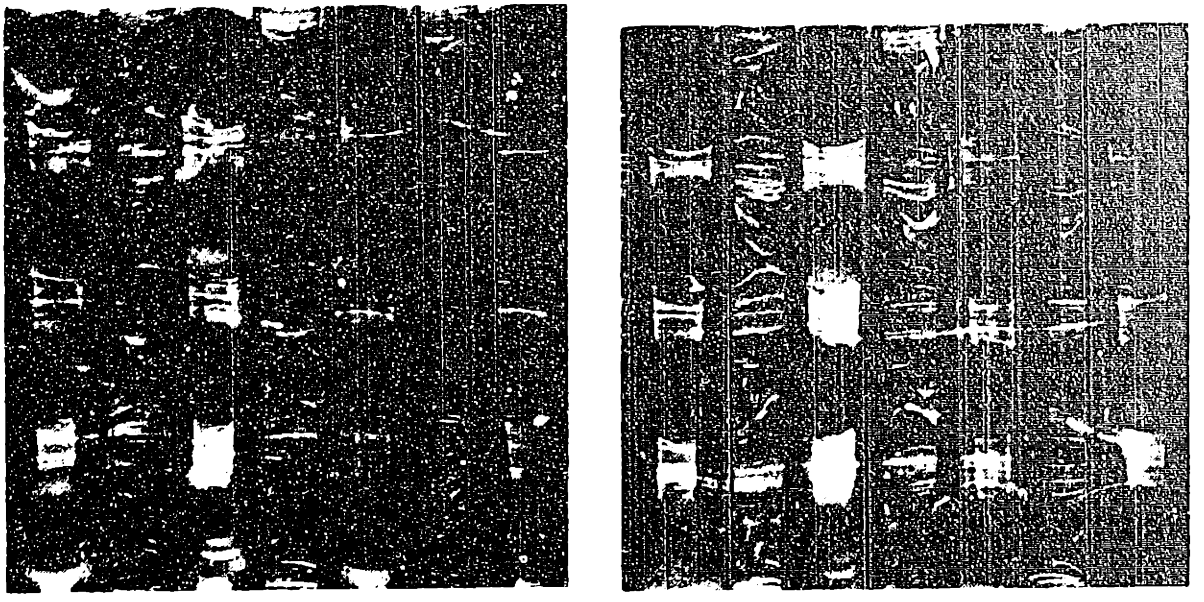

Figure 8-24: Streak photographs of 0.25 wt% PIB/PB/Kerosene Boger fluid flow through a 2-D square array of cylinders with a void fraction of 70% (from Chmielewski & Jayaraman, 1993). The flow is from left to right. (a) At $Re = 0.039$ and $We = 0.31$, the flow is essentially Newtonian. (b) At $Re = 0.19$, $We = 1.59$, the flow is asymmetric and time periodic. The recirculation regions oscillate up and down, as can be seen from the recirculation region behind several cylinders.

Viscoelastic flow instability in a two-dimensional square array of cylinders has been observed by Chmielewski & Jayaraman (1993). Flow visualization indicates that the flow undergoes a transition from a steady, two-dimensional, symmetric to a time-dependent, three-dimensional, asymmetric flow pattern. Streak photographs reproduced in Fig. 8-24 clearly show that above a critical $We = 1.5$, the recirculation region between the centers of the cylinders along the flow direction exhibited periodic oscillations. Neither the structure nor the time period of this instability was investigated by these authors.

Video imaging of the flow was used by us to examine the flow stability in a closely spaced cylinder array. There was no detectable change in the streaklines as the flow rate was increased because the bulk flow is always steady, and the flow rate within the recirculating region is only 0.1% of the mean fluid velocity, making it is very difficult to detect any flow transition. The LDV system, on the other hand, can resolve small changes (to $\pm 0.3\, mm/s$)

in the velocity field. At a given flow rate, two kinds of measurements are carried out: the streamwise velocity is scanned along the neutral x-axis at various values of y lying on the periodic boundary; and at a single point, v_z is monitored with time. These measurements are performed in the wake of the first, second, and sixth cylinders.

Figure 8-25 presents the streamwise velocity at four values of We at a fixed point $(0, 0.68R, 1.25R)$ downstream of the first cylinder. At low flow rates, the streamwise velocity profiles are essentially independent of time, as expected for a steady flow. At a critical $We = 1.53$, v_z is no longer steady but becomes time periodic. At $y = 0.68R$, just $0.2R$ outside of the recirculating region, the time averaged streamwise velocity at $We = 1.53$ is approximately 5.5 mm/s, which is near the lower end of the detection range of the LDV system. Therefore, it is not surprising that the noise in v_z can be as large as 40% of the time averaged velocity. The time period at the onset of the flow transition as shown in $\lambda_{1,t} = 100 \pm 33\ s$ (see the FFT spectrum in Fig. 8-26). The instability is solely the result of the elasticity of the polymer, because the Reynolds number at the onset of the flow transition is only $Re = 0.02$. Similar measurements in the wake of the second and sixth cylinders indicate that the flow transition took place at the critical $We = 1.53$. Therefore, in closely spaced cylinder arrays, flow instabilities appearing in the wake of the first cylinder propagate quickly into the entire array. This is in contrast to the flow transitions in widely spaced cylinder arrays, where streamwise velocity fluctuations appear in the wake of successive cylinders at incremental values of We. The presence of recirculating flow in closely spaced cylinder arrays actually helps the propagation of the flow instability into the entire array.

Along the neutral x-direction, $0.68R$ off the centerplane of the flow cell, a series of streamwise velocity profiles at various We are presented in Fig. 8-27. At $We \leq 1.47$, the streamwise velocity profiles are flat as the flow is essentially two-dimensional and v_z is uniform along the length of the cylinder. However, as the Weissenberg number is increased to a critical value $We_{crit} = 1.53$, periodic oscillations are observed along the neutral x-axis. Careful measurements near the critical conditions show that for an increment of $\Delta We = 0.02$, there is no hysteresis in the flow, and thus the instability is supercritical. The streamwise velocity fluctuation has two wavelengths, one at $\lambda_x = 1.89mm \pm 0.19mm = 1.2R \pm 0.1R$ and

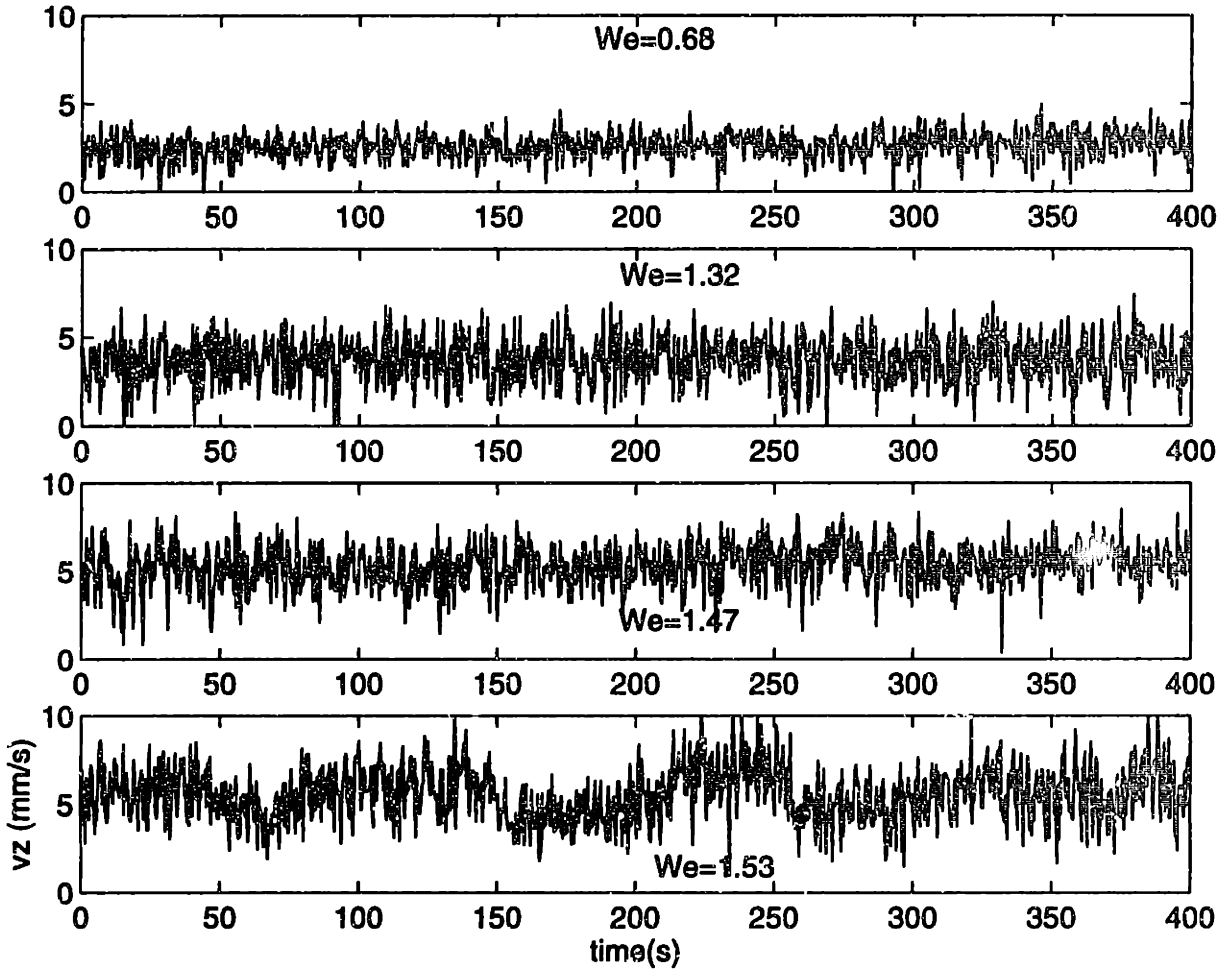

Figure 8-25: The time evolution of the streamwise velocity, $v_z(t)$ at a fixed point $(0, 0.68R, z = 1.25R)$ downstream of the first cylinder, as the Weissenberg number is increased from $We = 0.68$ to 1.53.

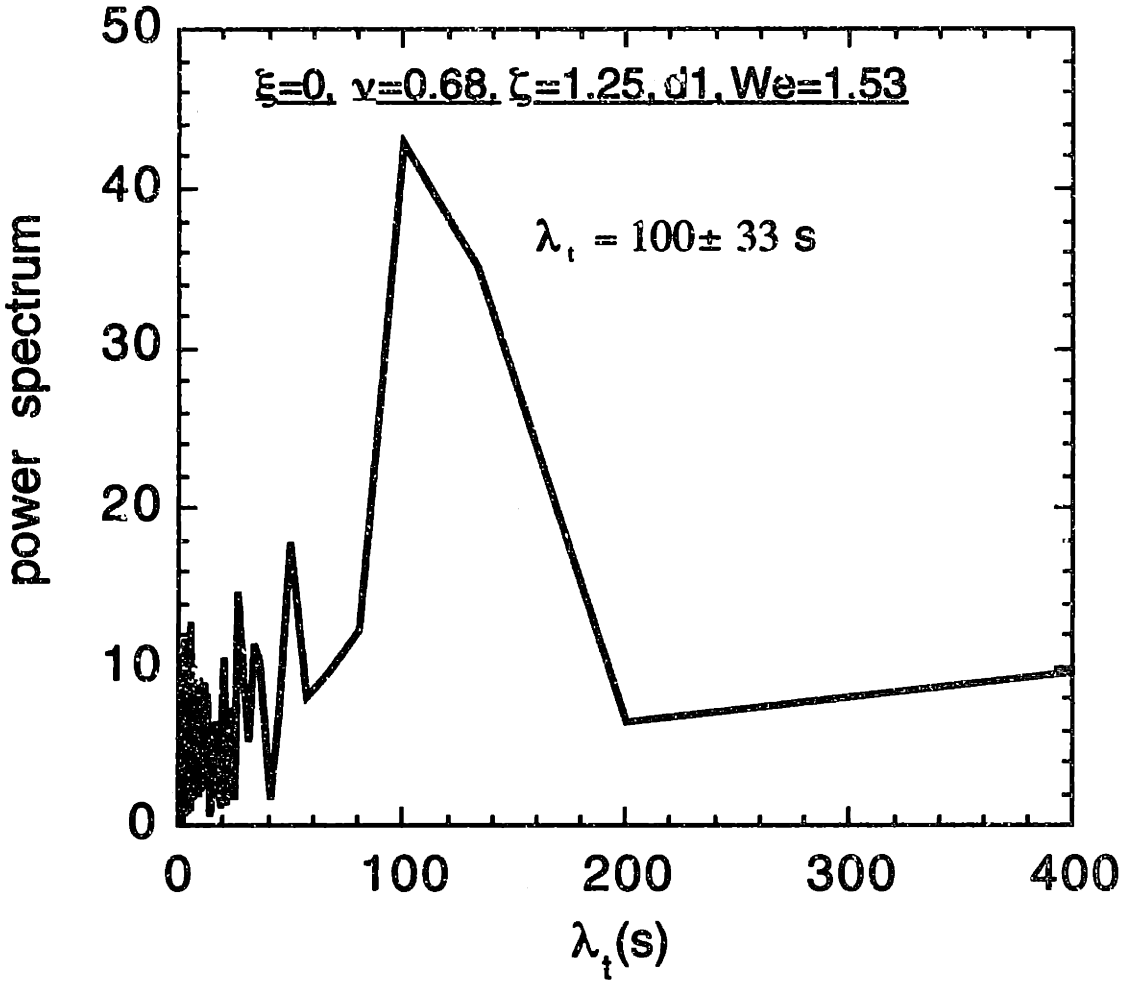

Figure 8-26: The FFT power spectrum used to resolve the time period of the instability at a fixed point $(0, 0.68R, 1.25R)$ downstream of the first cylinder at $We = 1.53$.

the other at $\lambda_x = 3.78\,mm \pm 0.34\,mm = 2.4R \pm 0.2R$ as shown by the FFT spectrum in Fig. 8-28. The first peak corresponds to the wavelength of the instability for ($|x| \geq 6R$), and the second peak corresponds to the flow instability in the middle of the channel ($-6R \leq x \leq 6R$). In the central region, $-6R \leq x \leq 6R$, wall effects are negligible. At the critical $We = 1.53$, streamwise velocity measurements in the wake of the second and sixth cylinders reveal that the spatial wavelength of the v_z fluctuation is $\lambda_x = 3.15 \pm 0.63\,mm = 1.98R \pm 0.4R$ (see Fig. 8-32). Therefore, in a closely spaced cylinder array, the flow undergoes a transition from a steady, two-dimensional to a time-periodic, three-dimensional flow at critical $We = 1.53$.

The spatial extent of the flow instability is examined by monitoring the evolution of the streamwise velocity over time at $x = 0$, and fixed y and z positions. Figure 8-29 presents the time evolution of v_z at $x = 0$, $z = 1.25R$ downstream of the sixth cylinder, and y between $0.30R$ and $1.32R$. Very close to the centerplane $y = 0.3R$, the flow is separated between the neighboring cylinders. Slight variations in v_z are due to noise in the LDV measurements, and thus the time period is infinite. At the boundary between the recirculation and bulk flow zones ($y = 0.48R$), variations in v_z are much more pronounced, indicating that the flow is time dependent, and the FFT spectrum shows the time period of $100 \pm 33\,s$. Away from the flow recirculation zone at $y = 0.68R$, fluctuations in the streamwise velocity increase, and a clear time period of $\lambda_t = 133 \pm 50\,s$ is determined from the FFT analysis shown in Fig. 8-30. Moving further away from the centerplane to $y = 0.86R$, where the flow is still in the shadow of the preceding cylinder, v_z is time dependent and has the same time period of $133 \pm 50\,s$. At $y = 1.32R$, fluctuations in v_z are significantly smaller than those at $y = 0.68R$, and the time period is around $200 \pm 100\,s$. Farther away, the instability disappears and the flow is steady. In a closely spaced cylinder array, the flow instability thus appears outside of the flow recirculation zone. Streamwise velocity evolution at a fixed point $(0, -0.68R, 1.25R)$ downstream of the sixth cylinder gives rise to the same time period.

In addition to the streamwise velocity fluctuations, measurements of the v_x component of velocity at the critical $We = 1.53$ were also carried out. Figure 8-31 shows that v_x fluctuates about zero and has a time period of $133s \pm 50s$. Various scans of v_z and v_x along the neutral x-axis were performed to determine the range of spatial wavelengths of the instability. Figure 8-32 indicates that the spatial periods of v_z and v_x were $\lambda_{x,v_z} = 3.15 \pm 0.63\,mm = 2.0 \pm 0.4R$

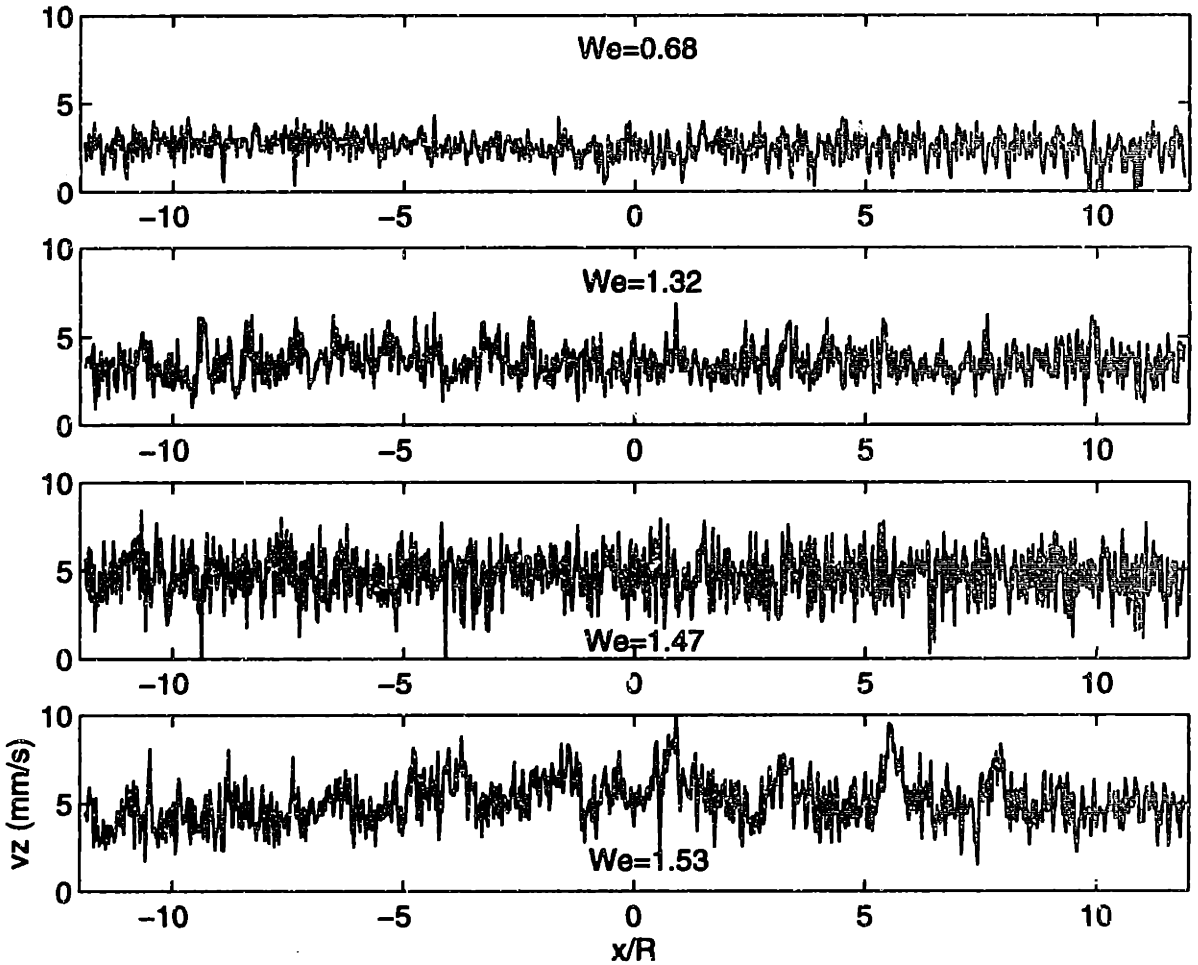

Figure 8-27: The streamwise velocity profile, $v_z(x)$, along the length of the cylinder at fixed $y = 0.68R$ and $z = 1.25R$ downstream of the first cylinder as the Weissenberg number is increased from $We = 0.68$ to 1.53.

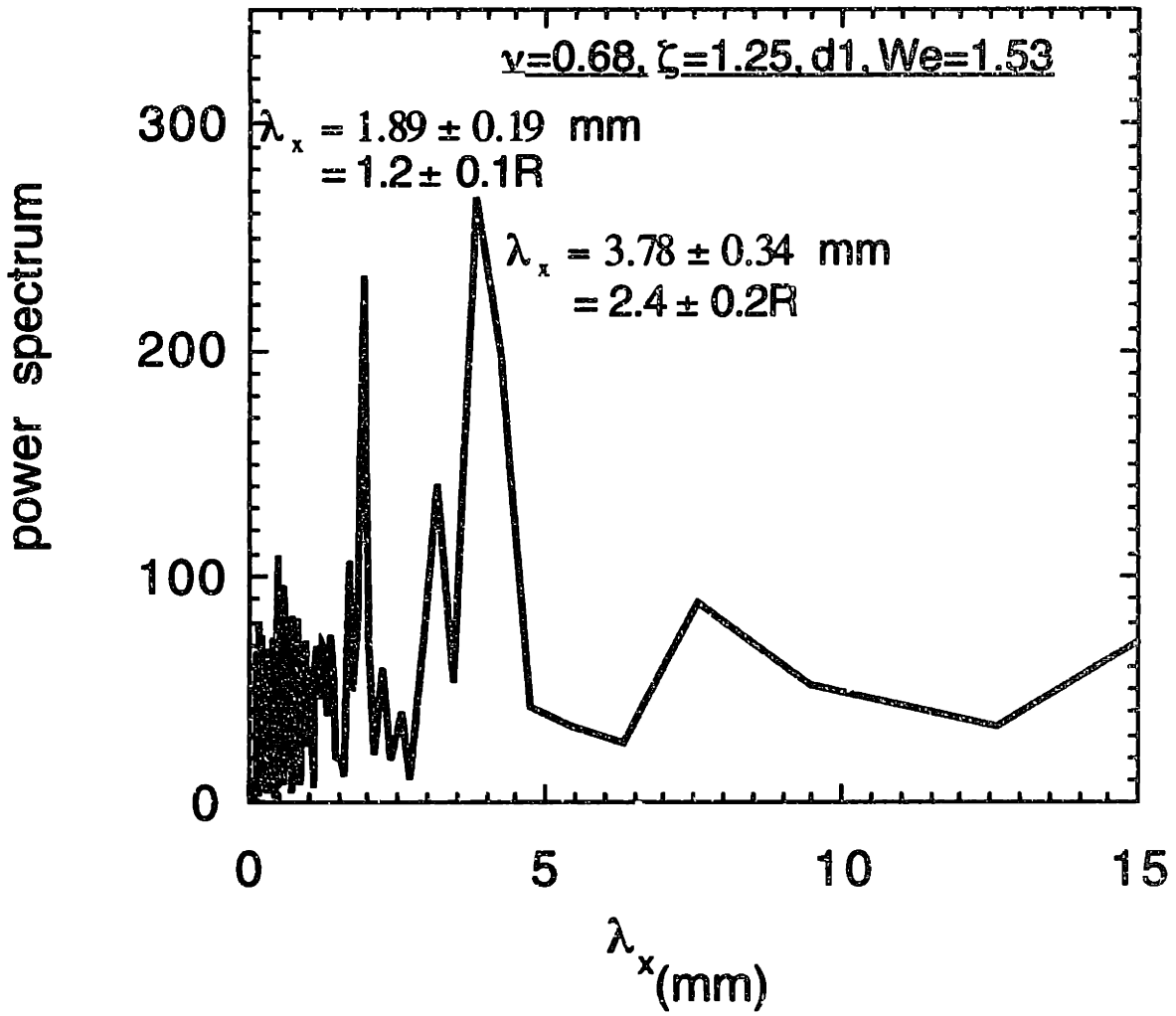

Figure 8-28: The FFT power spectrum used to resolve the spatial period of the instability at fixed $y = 0.68R$ and $z = 1.25R$ downstream of the first cylinder at $We = 1.53$.

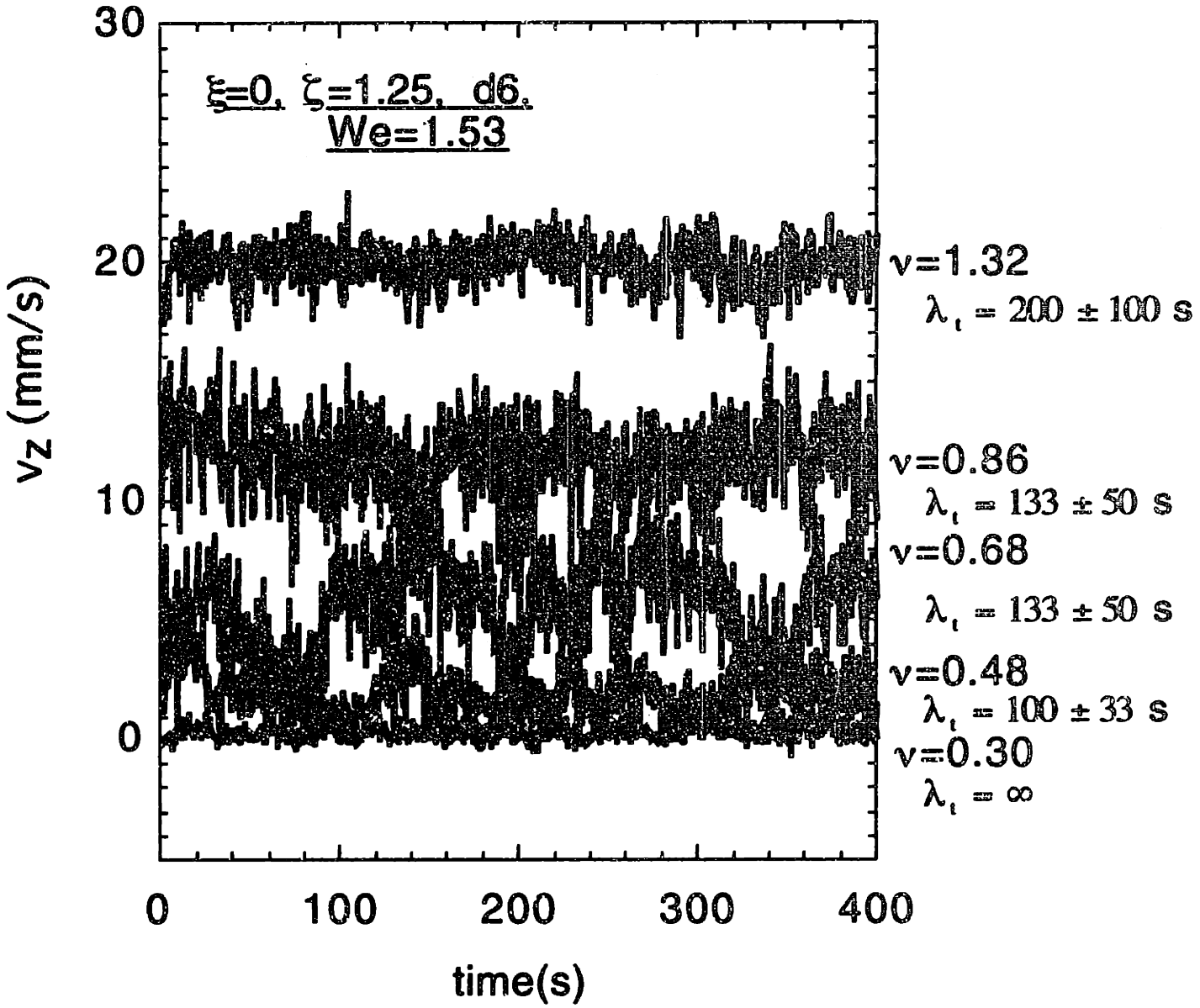

Figure 8-29: Extent of viscoelastic instability in a closely spaced cylinder array. The streamwise velocity, v_z is monitored at $x = 0$, $y = 0.3R$ to $1.32R$ and $z = 1.25R$ downstream of the sixth cylinder at $We = 1.53$.

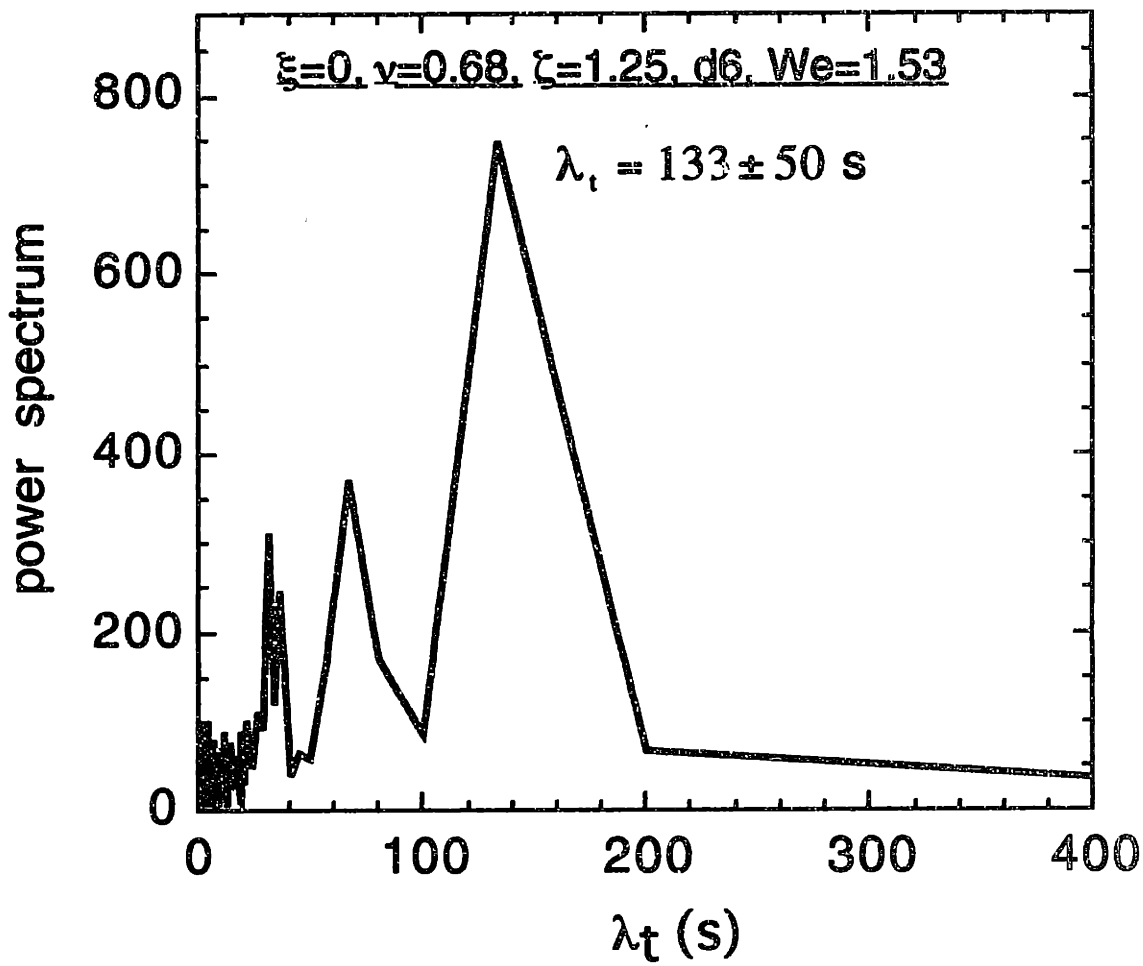

Figure 8-30: The FFT spectrum used to resolve the time period of the flow instability at $(0, 0.68R, 1.25R)$ downstream of the sixth cylinder at $We = 1.53$.

and $\lambda_{x,v_x} = 3.78 \pm 0.63\, mm = 2.4 \pm 0.5R$, respectively. Compared to the widely spaced cylinder array of $L = 6$, $H = 2$, where the spatial period is around $4R$, flow separation apparently decreases the spatial period of the flow instability.

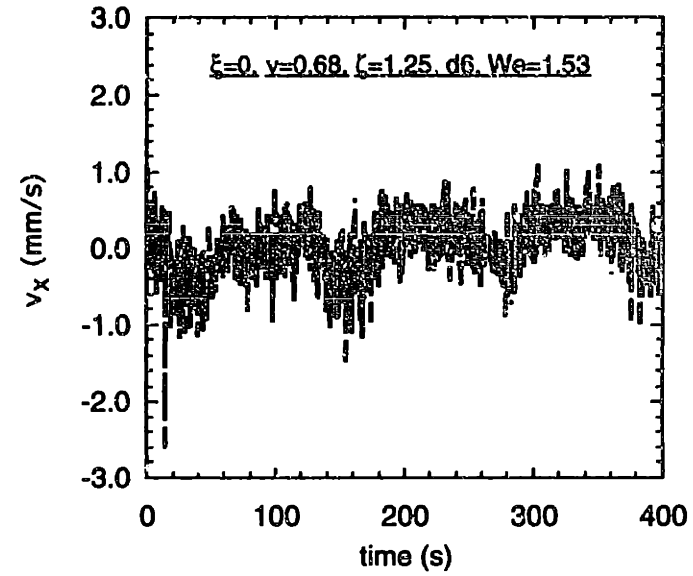

(a)

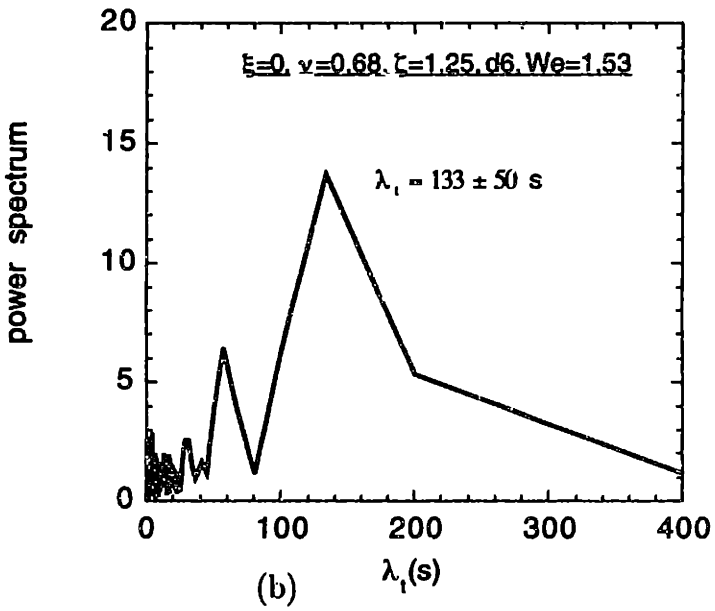

(b)

Figure 8-31: (a) The time evolution of v_x at $(0, 0.68R, 1.25R)$ downstream of the sixth cylinder at $We = 1.53$. (b) The FFT power spectrum used to determine the time period in (a).

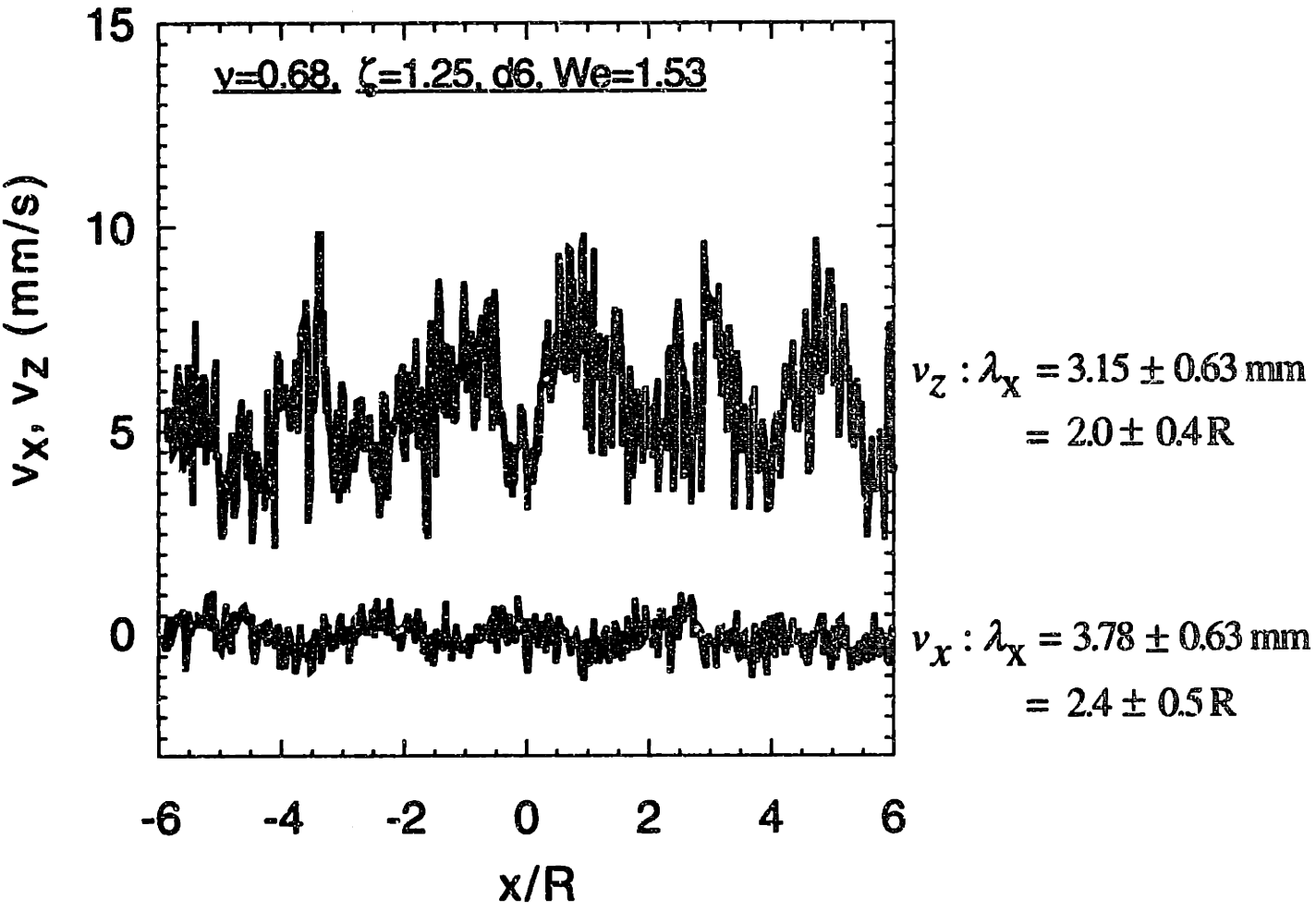

Figure 8-32: The spatial period of v_z and v_x along the length of the cylinder at $y = 0.68R$ and $z = 1.25R$ downstream of the sixth cylinder at $We = 1.53$.

8.4 Drag force on a cylinder

In this section, the drag force on a cylinder is reported as the Weissenberg number is increased. First, the drag force on a single cylinder in a confined rectangular channel with an aspect ratio of ($H = 2$) is presented. Second, the drag force on the seventh cylinder in a widely spaced cylinder array with aspect ratio of ($L = 6, H = 2$) is reported. Third, the drag response in a closely spaced cylinder array with $L = 2.5, H = 2$ is monitored as the flow rate is increased.

8.4.1 Single cylinder flow

Here, we consider viscoelastic flow around a confined cylinder, with the flow geometry designed by McKinley *et al.* (1993). The cylinder has a radius of $R = 3.188 \pm 0.013$ mm and the channel-cylinder ratio is $H = 0.5036 \pm 0.050$ mm. The drag force on the cylinder is measured by the force/torque (F/T) transducer described in section 7.4. Calibration of the F/T transducer with standard weights is illustrated in Fig. 8-33. The slope is 0.8273 instead of unity because the presence of o-ring seals actually restricts the movement of the stainless steel rod. The intercept is 0.013 N, which is within the tolerance level of the transducer (0.02 N). The x and y components of the force are all within ± 0.02 N.

The drag force on the cylinder as a function of Weissenberg number is presented in Fig. 8-34 for flow of the 0.31 wt% PIB/PB/C14 fluid around a single, confined cylinder. The Newtonian drag force at a given We is computed from the mean fluid velocity across the channel. The average flow rate is nonlinear with the Weissenberg number, because We is defined as a function of the shear-rate dependent relaxation time, $\lambda(\dot{\gamma}) = \Psi_1(\dot{\gamma})/2(\eta(\dot{\gamma}) - \eta_s)$, $We = a_T\lambda(\dot{\gamma})\dot{\gamma}$. It is not surprising that the Newtonian drag force, $F_{D,N}$, is a nonlinear function of We. The viscoelastic drag force is calculated by multiplying the Newtonian drag force by the drag enhancement factor which was determined by fitting a fourth order polynomial to the drag enhancement factor versus We data generated from finite element calculations (Liu *et al.* , 1997). It was found that $R^2 = 0.9986$ for the worst fit. The drag response for low $We \leq 0.5$ is given in Fig. 8-34. For $We \leq 0.33$, drag measurements are in good agreement with the Newtonian calculations, within the accuracy of the force trans-

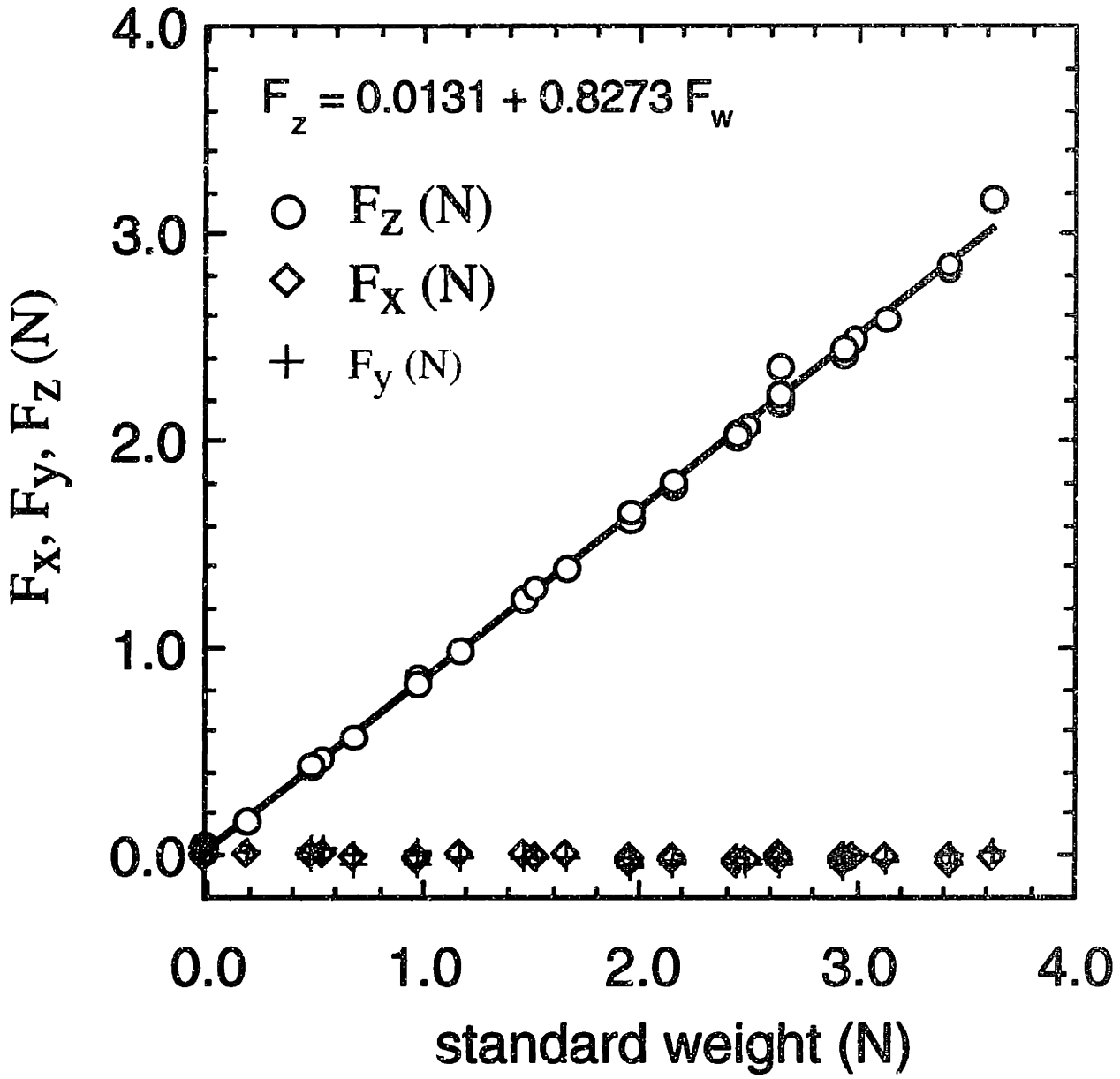

Figure 8-33: Calibration curve for mounting of F/T transducer at the end of a cylinder of radius $R = 3.175$ mm and half channel height to cylinder radius, $H/R = 2$.

ducer ($\pm 0.02N$). Deviation from the Newtonian values occurs at the critical Weissenberg number, $We_{crit} = 0.35$, where the flow undergoes a transition from a steady, two-dimensional to a steady, three-dimensional flow. At $We \leq 0.33$, viscoelastic constitutive models such as the OLDB, the Giesekus, the FENE-P and CR models all predict that the drag force enhancement factor monotonically decreases with We, but the predicted drag force is slightly smaller than the Newtonian results with a maximum difference of $0.03N$. Therefore, prior to flow transition, all four constitutive models predict fairly accurately the drag force on the cylinder. As the Weissenberg number is increased to $We = 0.35$, the measured drag force is lower than the computed Newtonian value, and this discrepancy is captured by the viscoelastic FENE-P, OLDB, Giesekus and CR models. Because of limitations in the resolution of the F/T transducer, and also because the flow is no longer steady and two-dimensional, we cannot distinguish which constitutive model is the most suitable to describe the 0.31 wt% PIB/PB/C14 fluid flow around a confined cylinder at higher We.

The onset of the three-dimensional instability modifies the drag response on the cylinder. At first, the resistance experienced by the cylinder is lower than if the fluid were Newtonian; but at higher Weissenberg numbers, $We \geq 0.4$, the drag force on the cylinder is greater than the two-dimensional finite element calculations for the Newtonian, OLDB, Giesekus, FENE-P and CR models. As expected, the two-dimensional steady viscoelastic constitutive models fail to predict this increase in the drag force. For a falling sphere in PIB/PB Boger fluids, the drag force enhancement has been reported by various investigators (Tirtaatmadja *et al.* , 1990; Chmielewski *et al.* , 1990; Becker *et al.* , 1993). Experiments conducted by Chmielewski *et al.* (1990) showed that the ratio of the measured drag force on the sphere to the Newtonian result, $\chi = F_{D,v}/F_{D,N}$, initially decreases with increasing We up to $We = 0.3$. Beyond $We = 0.3$, χ starts to increase, and at $We = 0.7$, a 15% drag enhancement was measured. Therefore, a comparison of experimental results reported here for a single cylinder with results for a falling sphere (Chmielewski *et al.* , 1990), reveals that the two cases are similar.

The flow transition also results in a lift force, F_y. At low $We \leq 0.5$, the lift force is essentially zero because the flow is symmetric about the centerplane prior to any flow transition. This indicates that the cylinder is centrally mounted, and no measurable lift

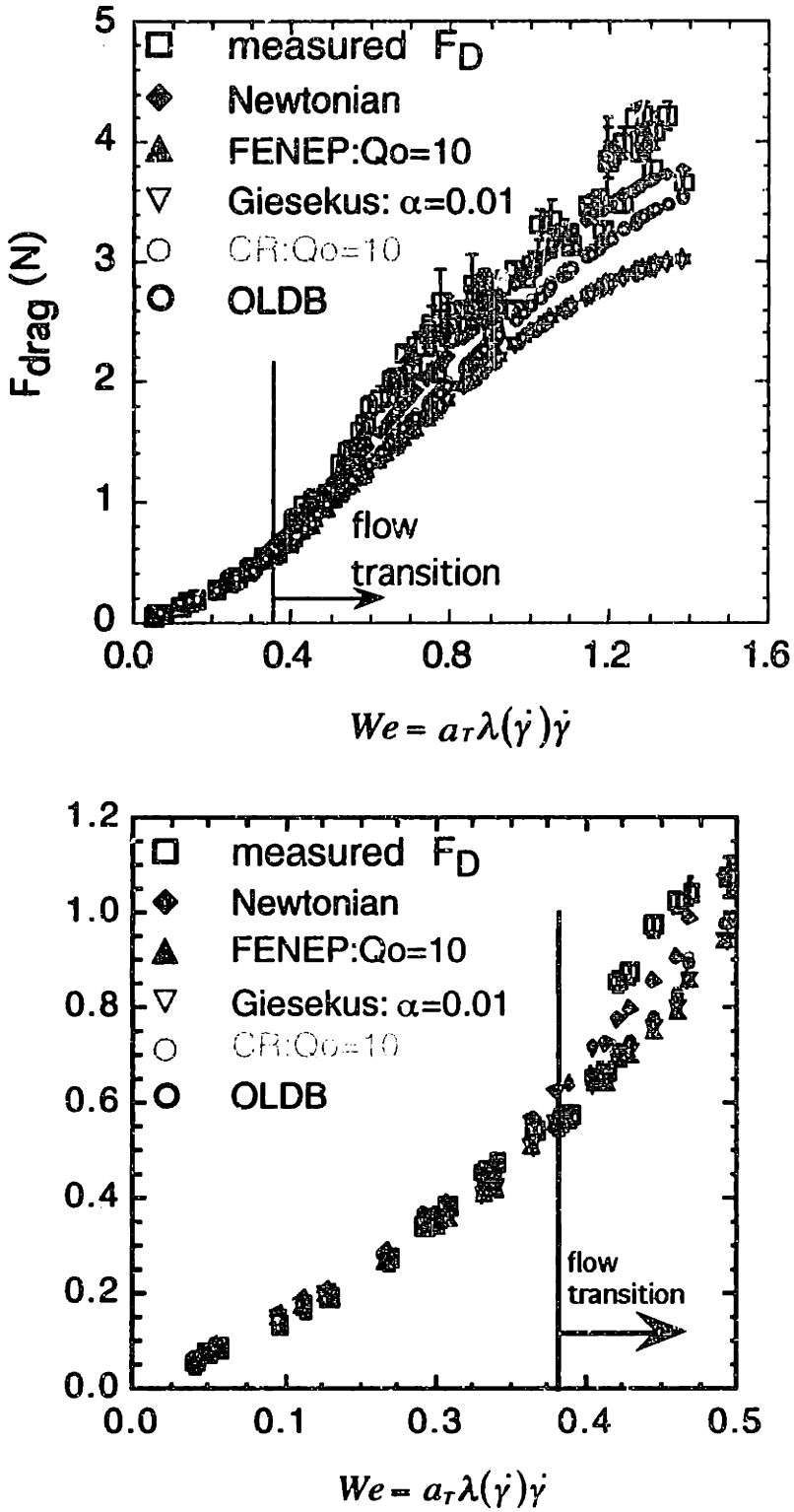

Figure 8-34: Drag force on a confined cylinder with an aspect ratio of $H = 2$. The symbol '□' denotes measured drag force with error bars in We and F_D. 'Newtonian', 'FENEP', 'Giesekus', 'CR' and 'OLDB' denote Newtonian, FENE-P, Giesekus, CR and Oldroyd-B FEM calculations. Model parameters for viscoelastic calculations are $\beta = 0.59$ and $Q_0^2 = 1/\alpha = 100$.

force is expected. With increasing We, the lift force becomes negative, as illustrated in Fig. 8-35. This is consistent with the fact that the streamwise velocity across the width of the channel becomes increasingly asymmetric about the centerplane as the flow rate is increased (Byars, 1995), leading to a continuous increase in the magnitude of the lift force. Because there are four screws that rigidly fix the transducer housing to the side channel wall, the lift force is not due to any slight rotation of the cylinder axis. The calibration of the transducer was carried out in vitro with the cylinder axis perfectly aligned with that of the flow cell. Attachment of the side panel was completed using additional screws, so there is no possibility of cylinder axis rotation. Additional force calibration inside the flow cell revealed that the maximum F_y for an applied load of 5 N was 0.04 N, leading to a maximum axis of rotation 0.5°. Taking into account 0.5° rotation, the magnitude of the lift force for $We = 1.4$ is only 0.03 N, an order-of-magnitude smaller than the measured value of 0.3 N.

Scatter in the experimental measurements is caused by uncertainties in both the fluid temperature and mean fluid velocity. All recorded temperatures are at the ambient conditions. Since fluid viscosity and the relaxation time of the polymer are very sensitive to temperature, for the 0.31 wt% PIB/PB/C14 solution, a maximum increase in temperature during the course of the experiment of $1°C$ corresponds to a 10% decrease in solution viscosity. The temperature shift factor, a_T, for superposition of material functions at any T for the 0.31 wt% PIB/PB/C14 fluid was found to depend on temperature according to an Arrhenius expression (Quinzani *et al.* , 1990),

$$a_T = exp[(\frac{\Delta H}{R}(\frac{1}{T} - \frac{1}{T_0})], \tag{8.2}$$

where T_0 is the reference temperature, $R = 8.314\, J/mol \cdot K$ and ΔH is the activation energy for flow (Ferry, 1980) determined to be $\Delta H/R = 7362\ K$ (McKinley, 1992). To account for the temperature dependence of the solution viscosity, Newtonian drag force calculations are corrected by multiplying the zero-shear-rate solution viscosity at reference temperature $T_0 = 25°C$ by the shift factor a_T. In later experiments on widely and closely spaced cylinder arrays, a thermocouple was installed to monitor the solution temperature. The difference between the ambient and solution temperature was less than $0.2°C$ at the beginning of each

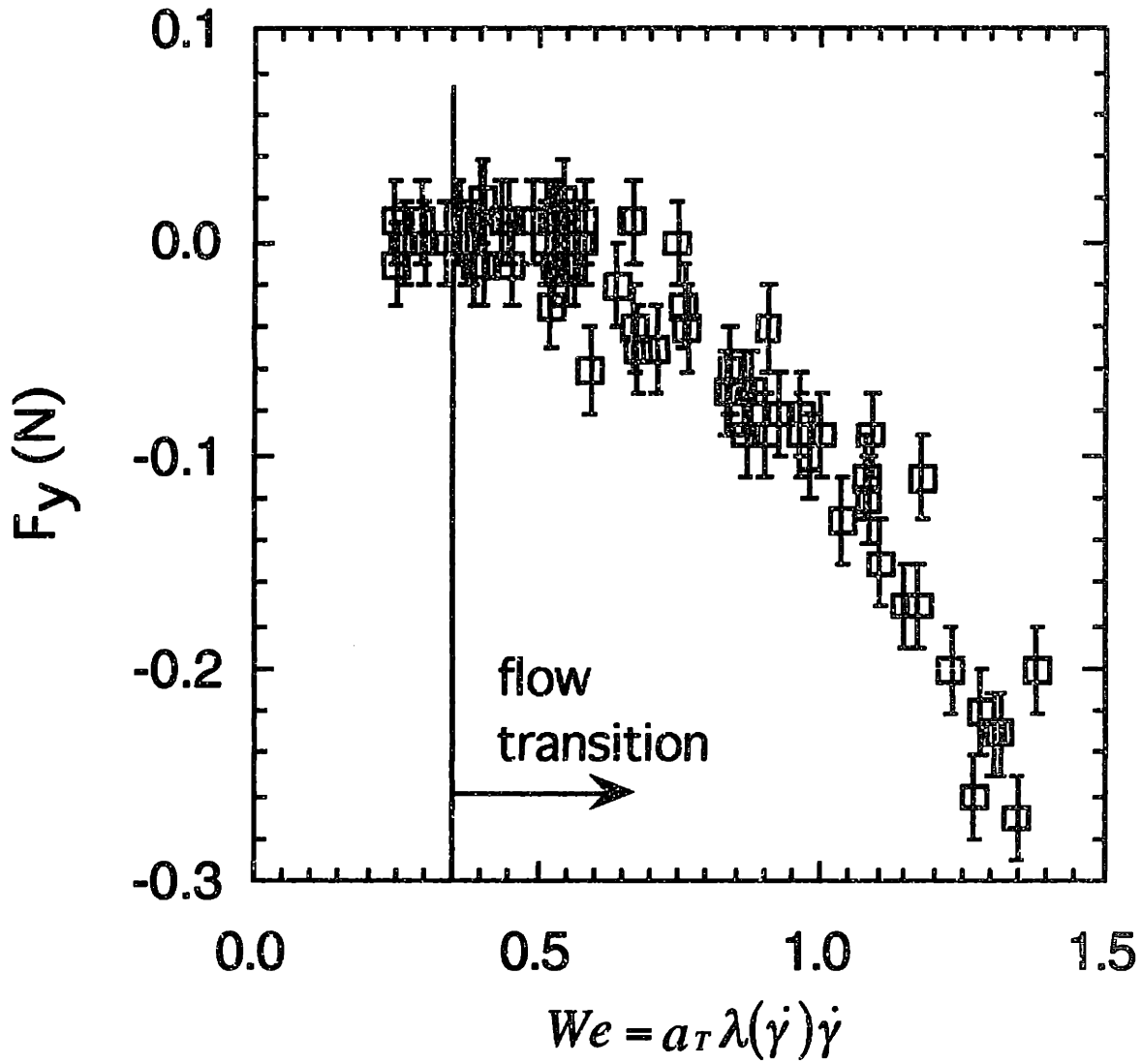

Figure 8-35: Lift force on a confined cylinder with a channel to cylinder ratio of $H = 2$.

experiment; thus ambient temperature is a good estimate of solution temperature.

Errors in Fig. 8-34 for the drag force measurements correspond to either the accuracy of the F/T transducer or the shift in the bias after the valve is closed for fifteen minutes, whichever is greater. The bias is shifted because of the prolonged application of the external force and temperature increases during the experiment. The maximum temperature increase was found to be $0.7°C$. The steady-state reading varies less than $\pm 0.02N$ during the course of the experiment. Figure 8-36 is a representative plot of the evolution of the drag force on the cylinder at $We = 0.67$. At $t = 0$, the valve begins to open and at $t = 7$ s, it is completely open. The drag force on the cylinder, F_z, rises quickly from zero to the steady-state value of $1.8N$, while the lift force, F_y, decreases quickly to a steady value of $-0.05N$. Small fluctuations in F_z are observed, but these variations are within the sensitivity range of the F/T transducer. Fifteen minutes after the valve is closed, the bias is shifted to $0.08\,N$ because of the $0.5°C$ rise in the fluid temperature during the course of the experiment. The bias eventually returns to zero when the fluid temperature cools to the ambient temperature after 60 minutes.

8.4.2 Drag behavior in widely spaced cylinder arrays

Fluid is handled by pressurizing the holding tank as discussed in section 7.4. For a fixed maximum pressure, the maximum mean fluid velocity (or equivalent maximum We) that can be attained experimentally is inversely related to the cross-sectional area of the channel. For this reason, we use a smaller cylinder radius of $R = 1.5875\,mm$ and channel-cylinder ratio of $H/R = 2$. The F/T transducer is mounted at the end of the seventh cylinder, with a mounting that is identical to the single cylinder case. Since cylinder size and associated o-rings are smaller than in the single cylinder case, the F/T transducer must be recalibrated, as illustrated in Fig. 8-37. The slope is 0.83, slightly greater than for the single cylinder case. The intercept is $0.015\,N$, within the accuracy of the transducer ($0.02\,N$). To monitor better the fluid temperature, a K-type thermocouple from Omega Technologies with a resolution of $\pm 0.1°C$ was installed right before the 1" hose adapter of the flow cell.

In order to verify the important role temperature plays in the drag force measurements,

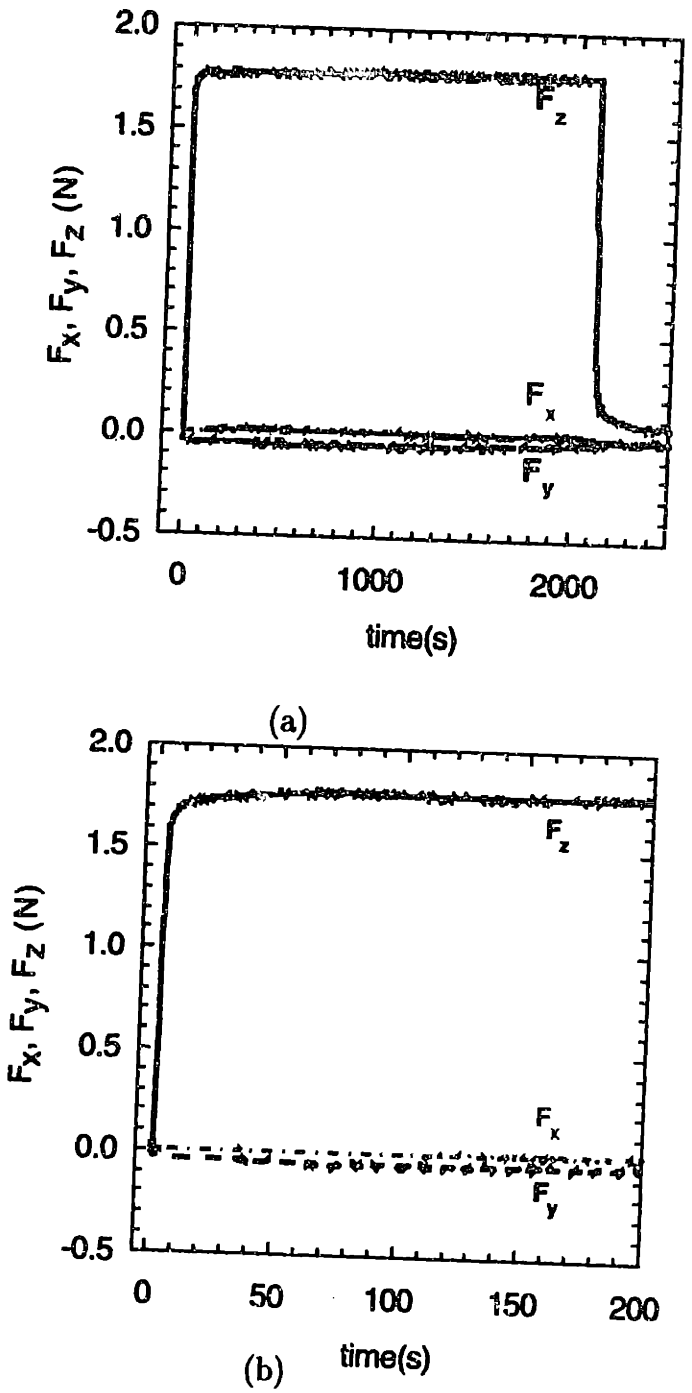

Figure 8-36: (a) Evolution of drag and lift forces on the cylinder during startup, steady-state, and shutdown. Experiments take place for 0.31 wt% PIB/PB/C14 fluid flowing around a single, confined cylinder at $We = 0.67$. (b) Enlargement of evolution of the drag and lift forces during startup.

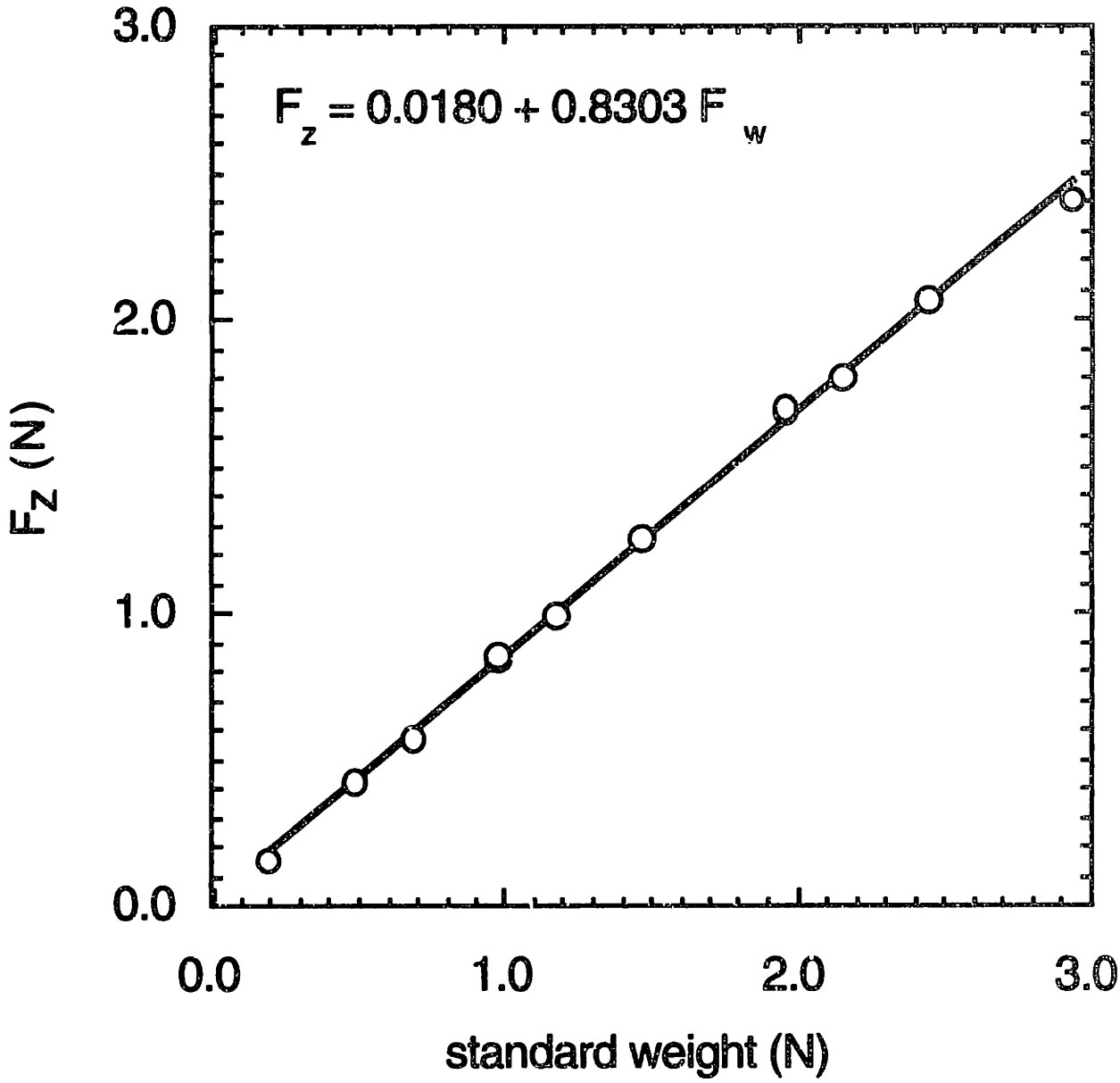

Figure 8-37: Calibration curve for mounting of F/T transducer at the end of the seventh cylinder in a linear array of cylinders.

we designed an experimental protocol as depicted in Fig. 8-38(a). At the beginning of the experiment, the pressure drop is set at 4 psi. At an incremental time of 450 seconds, the pressure is increased by adjusting the pressure controller to a different setpoint. The corresponding drag force evolution is given in Fig. 8-38(b). The largest variations in the drag force at the steady-state condition is only $\pm 0.02N$, within the resolution of the F/T transducer. The entire experiment lasts 50 minutes and a temperature rise of $0.1°C$ is noted. The mean flow rate and the measured force as a function of pressure are given in Figs. 8-39(a) and (b). The mean fluid velocity varies linearly with pressure. Note that the intercept is non-zero because pressure loss in the tubing is around 1 psi, and the fluid does not flow when the applied pressure is only 1 psi. The drag force on the cylinder is also linearly related to the pressure, and once again at $\Delta p = 1$ psi, the drag force is zero.

Fig. 8-40 presents the measured and computed drag force on the cylinder as a function of Weissenberg number. The accuracy of the F/T transducer is $\pm 0.02N$, and the error in the Weissenberg number is also presented in Fig. 8-40. For $We \leq 0.51$, drag force measurements agree extremely well with the Newtonian results. Deviations from the Newtonian case were first noted at $We = 0.70$. As the Weissenberg number continues to increase, the measured force is consistently greater than the Newtonian case. The difference between the experimental and Newtonian results increases with increasing We until $We = 1.14$. At this point, the first flow transition occurs locally between the first and second cylinders, and the difference between the measurements and the Newtonian calculations increases to $0.49N$, a 38% rise in the drag force compared to the Newtonian case. Further increases in the flow rate result in an increase in the difference between the measured and computed Newtonian drag force. During the propagation of the flow instability throughout the linear array, deviations of the measurements from the Newtonian values continue to increase. At $We = 1.36$, where the flow undergoes a transition throughout the entire array, the deviation is as large as $0.62\,N$. As the We continues to increase, the difference between the measurements and the calculated Newtonian force increases. The drag force enhancement at the onset of the flow transition is consistent with the experimental findings of Chmielewki *et al.* (1993a, 1993b) for a two-dimensional array of cylinders, where a 2% increase in the pressure drop was noted at the onset of the flow instability.

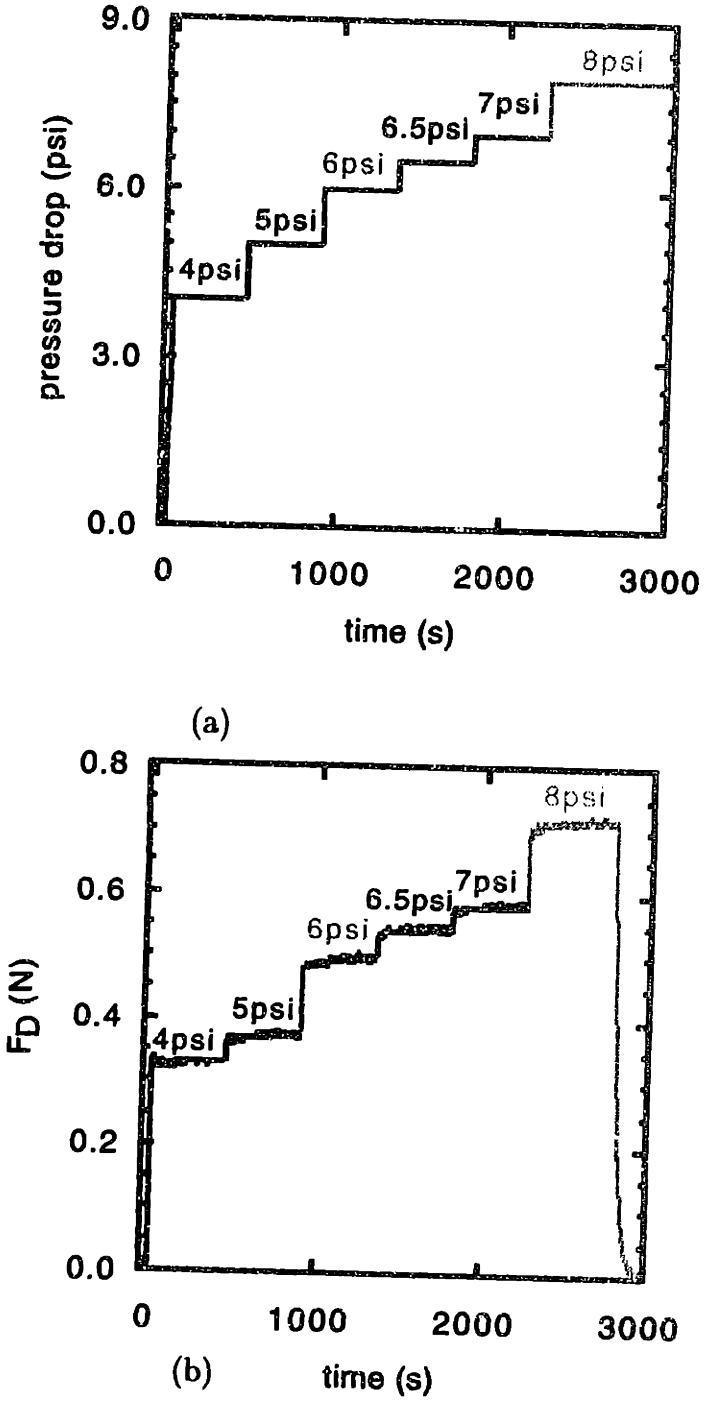

Figure 8-38: (a) Experimental protocol for increments of pressure at an interval of 450 seconds. (b) Drag force on the cylinder as a function of time as the pressure increases from 4 psi to 8 psi.

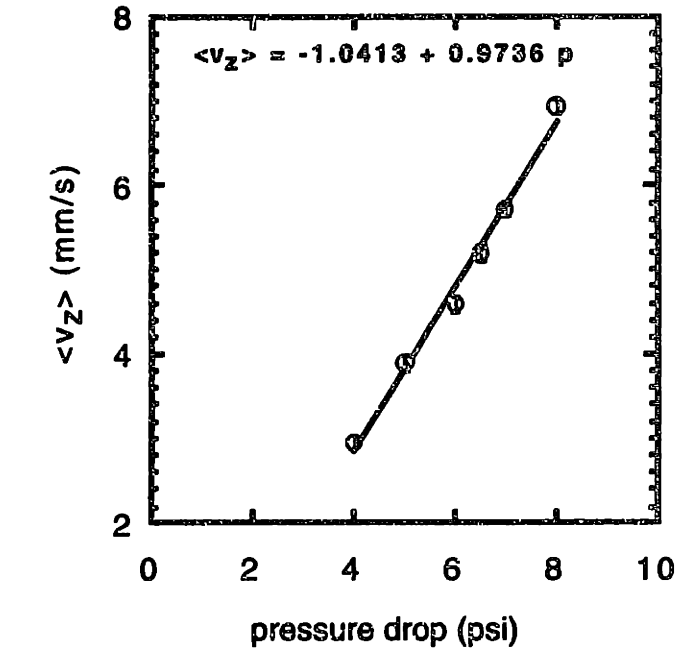

(a)

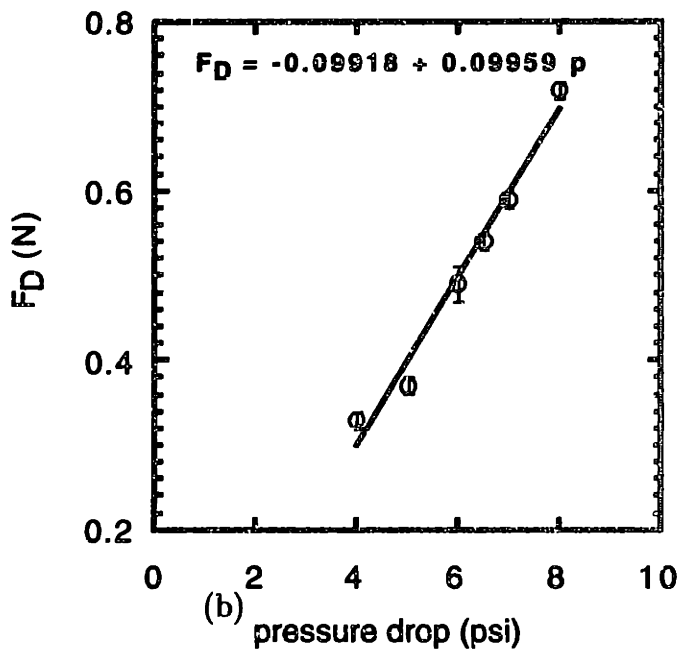

(b)

Figure 8-39: (a) Mean flow rate as a function of pressure drop. (b) Drag force on the cylinder as a function of pressure drop.

The lift force is nonzero because the cylinders are not perfectly aligned in the center of the flow channel. The measured lift force is shown in Fig. 8-41 as compared with the OLDB model calculations with 0.5% off-centering in the positive y-direction. For $We \leq 0.8$, the computed lift force agrees reasonablely well with the measurements; but for $We > 0.85$, the viscoelastic model underestimates the lift force, as it did for the drag force. The percentage differences between the measured and computed drag and lift forces are not the same. Prior to any flow transition, the measured drag force is 1.5 N at $We = 1.0$, while the computed value from the OLDB model is 1.0 N, resulting in a 50% difference in the drag force, whereas for the lift force, the measured value is from the OLDB model is 0.18 N as compared to the computed value of 0.01 N. As discussed in section 8.4.1, the lift force is not due to misalignment of the cylinder axes and the interactions with fluid elasticity. For a Newtonian fluid the off-centering does not result in any lift force, but for an Oldroyd-B model, the lift force monotonically increases with increasing We. Therefore, the non-zero lift force is due not only to off-centering of the cylinders, but also to the elasticity of the fluid. Neither Newtonian nor viscoelastic constitutive models predict precisely the drag and lift forces on the cylinder. The deviation of the measured lift force from the computed value increases with increasing We.

At the first flow transition for $We = 1.14$, the lift force rises to $0.23N$ while the computed lift force is only $0.03N$. The lift force, F_y, continues to rise and reaches a maximum around $We = 1.5$, beyond which it decreases rapidly and monotonically towards zero for $We = 2.0$ and becomes negative for $We > 2.0$. Since there is a slightly wider gap between the cylinder and channel in the positive y direction, viscoelasticity results in the lift force in the direction of the narrow portion of the flow cell. Two-dimensional steady-state calculations predict that the lift force monotonically increases with increasing We, and thus the drop in the lift force is due purely to the combined effects of viscoelasticity and three-dimensional flow. As in the case of a single cylinder flow, the effect of fluid elasticity is to enhance the drag force on the cylinder. The effect of the flow transition is to exert a lift force in the direction of the side of the channel with the slightly narrower gap between the cylinder and channel, as indicated by the rapid decrease in the lift force past We_{crit} shown in Fig. 8-41.

Viscoelastic constitutive models such as the OLDB, the Giesekus, the FENE-P and CR

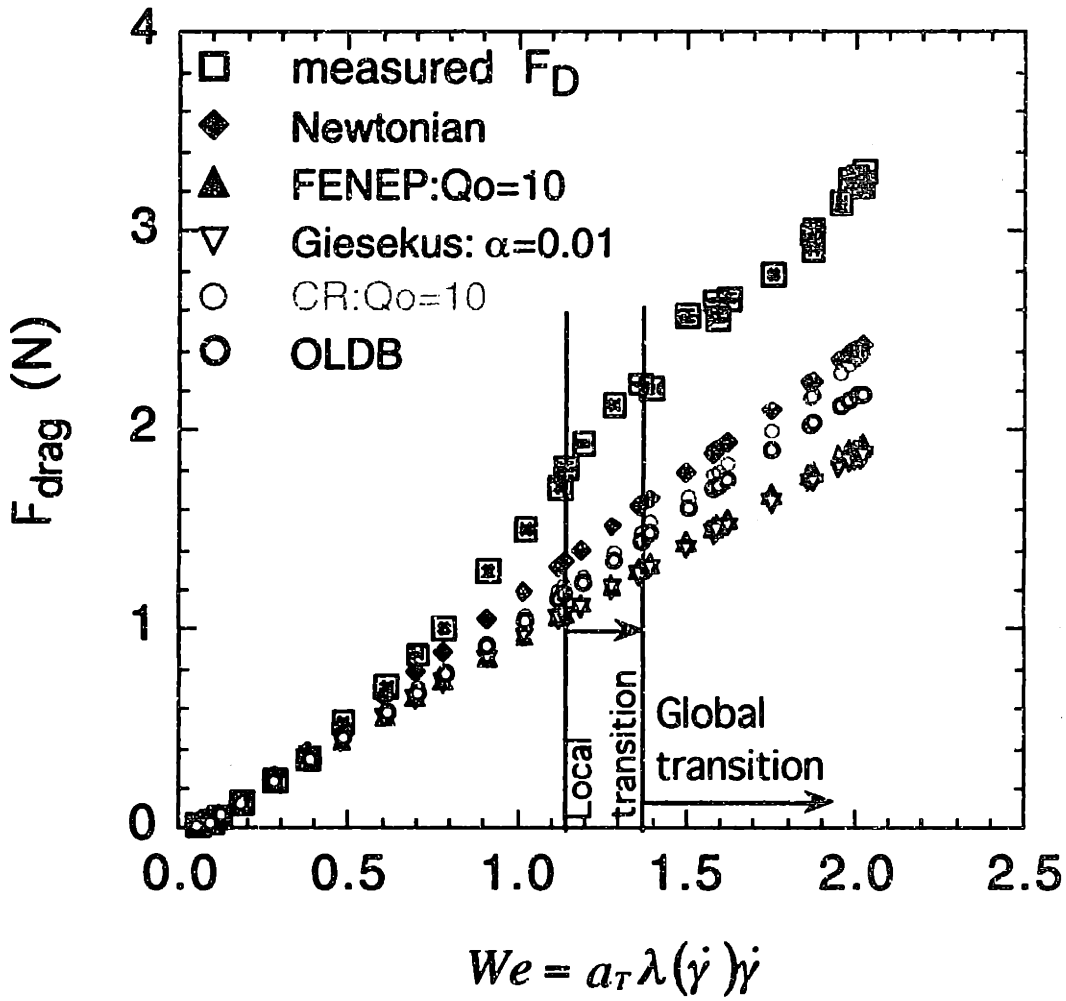

Figure 8-40: Drag response on a cylinder in a widely spaced cylinder array ($L = 6, H = 2$).

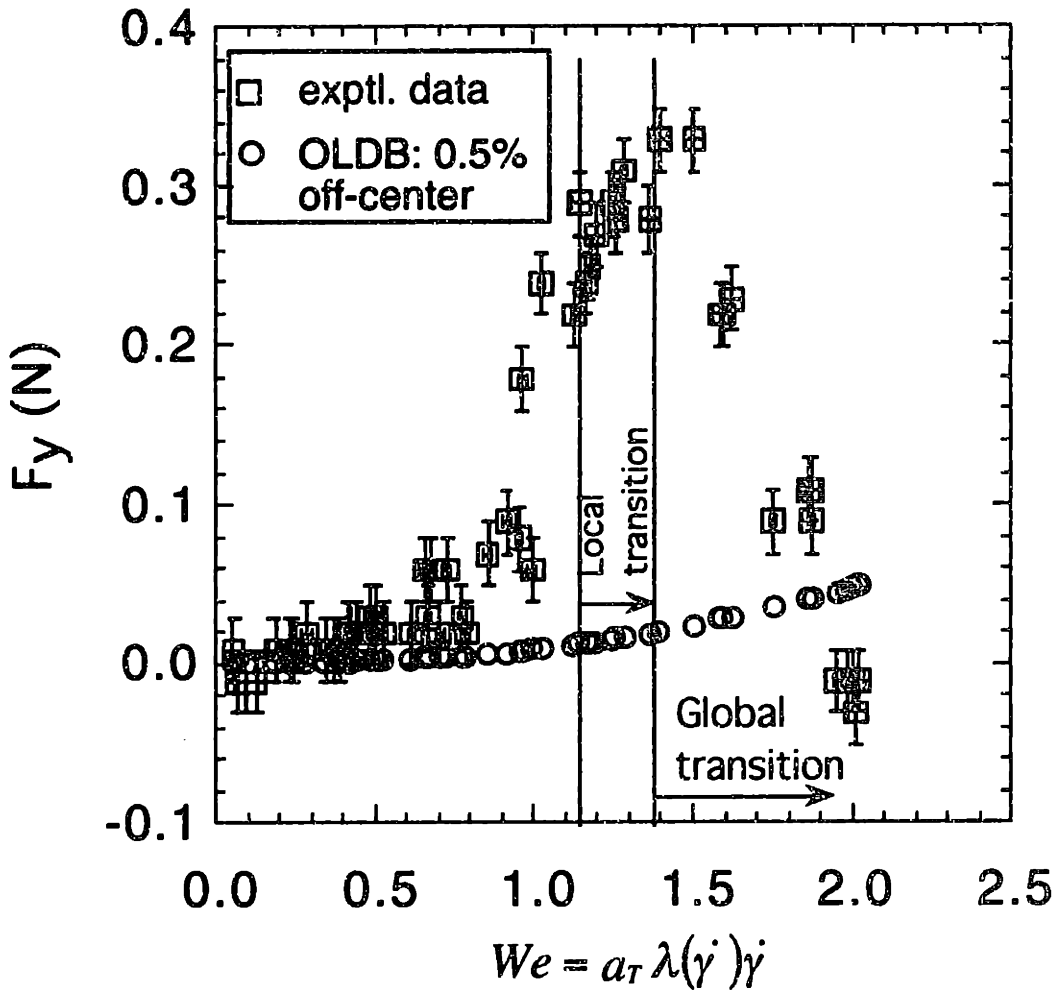

Figure 8-41: Lift force on a cylinder in a widely spaced array of cylinders. The symbols '□' and '△' denote experimental and OLDB FEM predictions with 0.5% off-centering with $\beta = 0.59$.

models all predict Newtonian like drag behavior for $We \leq 0.12$. When the Weissenberg number increases to $We = 0.18$, viscoelastic models consistently underestimate the drag force on the cylinder. However, a simple Newtonian model predicts the drag force response fairly well for $We < 0.7$. Among the four constitutive models considered in this work, the CR model predicts the largest drag force on the cylinder, followed by the OLDB model, the Giesekus, and finally the FENE-P model. For all $We > 0.7$ considered in this work, the drag force computed from any of the four constitutive models is consistently lower than the Newtonian case, so none of the models is suitable for describing the drag behavior in widely spaced cylinder arrays.

Although viscoelastic constitutive equations such as the OLDB model accurately predict the steady velocity field, all models fail to predict the drag force enhancement in comparison with the Newtonian results. Finite element calculations presented in chapter 5 indicated that the largest tensile stress is in the highest shear rate region in the narrow gap between the cylinder and channel wall. To investigate if the deviation between the measurements and predictions is caused by underestimation of the stress field, Fig. 8-42 compares the $v_z / <v_z>$ profile across the minimum gap at $We = 0.68$. The steady two-dimensional $v_z / <v_z>$ profile is independent of We, as shown by the overlapping of the Newtonian and viscoelastic calculations in Fig. 8-42. The measured streamwise velocity agrees very well with the FEM predications. Therefore, the failure of viscoelastic models in estimating the drag force on the cylinder is possibly due to the fact that neither the OLDB, nor the Giesekus, CR and FENE-P constitutive equations can accurately describe the stress-strain relationships in complex flow geometries (Quinzani, 1991; Baaijens, 1994). Quinzani (1991) examined a 5 wt% PIB/PB/C14 fluid in planar contraction and observed extensional thinning behavior at high flow rate, and only the Phan-Thien-Tanner model could qualitatively, though but not quantitatively, fit the experimental results. Baaijens (1994) used the same 5 wt% PIB/PB/C14 solution in the study of flow around a single cylinder; the measured velocity profile agreed very well with model predictions, but the agreement of the normal and shear stresses was not good even at $We = 0.25$. Other experimental investigations of viscoelastic flow of a sphere falling in a PIB-based Boger fluid conducted by Tirtaatmadja *et al.* (1990), Chmielewski *et al.* (1990), and Becker *et al.* (1993) consistently showed a pronounced drag

enhancement over the Newtonian results at high We. The only way to resolve whether the aforementioned viscoelastic constitutive equations can accurately describe the stress-strain relationship in a linear array of cylinders is to measure the components of the stress tensor at each point in the flow domain using flow induced birefringence, and compare those with the model predictions. It is definitely an interesting and exciting problem to investigate, but it is beyond the scope of this thesis.

Even though the flow transition in a linear array of cylinders corresponds to the three-dimensional transient flow, the drag force on the cylinder remains steady, as illustrated in Fig. 8-43. This is because the force transducer measures the integral of all differential forces exerted by the fluid over the entire length of the cylinder and is time independent. Figure 8-43 shows the evolution of three components of the force vector at $We = 1.30$. Both the drag and lift force experienced by the cylinder increase rapidly as the valve opens. Figure 8-43(b) is a plot of the startup of the experimental run. The drag force, F_z, shows a noticeable overshoot of 0.05 N during the startup process. Both the drag and lift forces reach steady-state values with slight variations of $\pm 0.01N$ within the resolution of the F/T transducer. The third component of the force, F_x, remains zero at all times. Upon shutdown of the valve, both F_z and F_y decrease quickly to the no applied load condition, with the same rate of decrease.

8.4.3 Closely spaced array of cylinders ($L = 2.5, H = 2$)

A comparison between drag force measurements and finite element calculations for a widely spaced cylinder array ($L = 6, H = 2$) indicates that under steady flow conditions, the Newtonian model more accurately describes the drag response than the viscoelastic constitutive models as the flow rate is increased. As shown in Fig. 8-44, prior to the onset of flow instability ($We = 1.53$), the CR model best fits the experimental results for a closely spaced cylinder array. At low $We \leq 0.6$, Newtonian and all four constitutive models describe accurately the resistance experienced by the cylinder. It is difficult to determine which constitutive model is best suited for describing the drag force on the cylinder. As We increases, the FENE-P model underestimates the drag force on the cylinder, while the differences between the

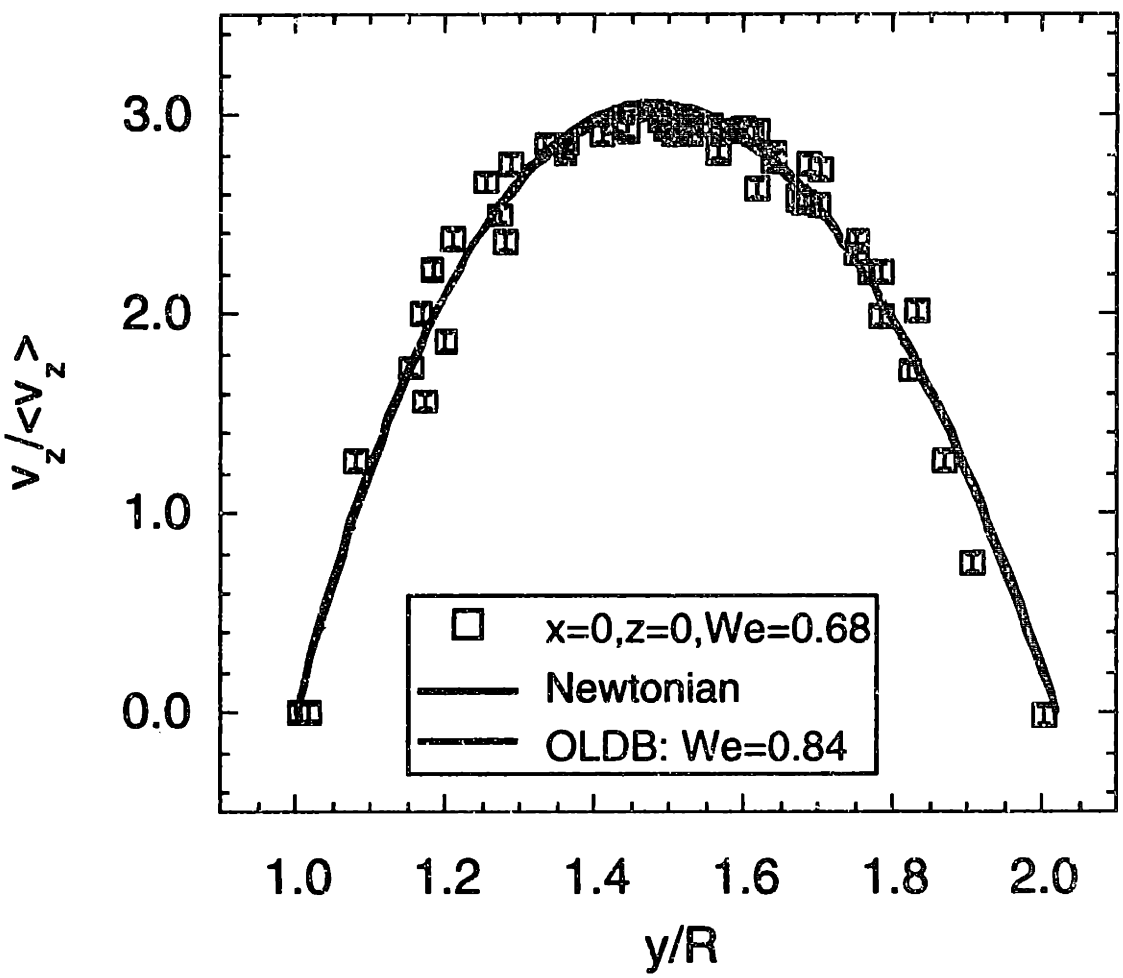

Figure 8-42: Streamwise velocity across the minimum gap between the cylinder and the channel wall. The symbol '□' denotes velocity measurements at fixed $x = 0$, $z = 0$ (the center of the fifth cylinder) and $We = 0.68$. The black and green lines corresponds to the Newtonian and OLDB FEM calculations at $We = 0.84$.

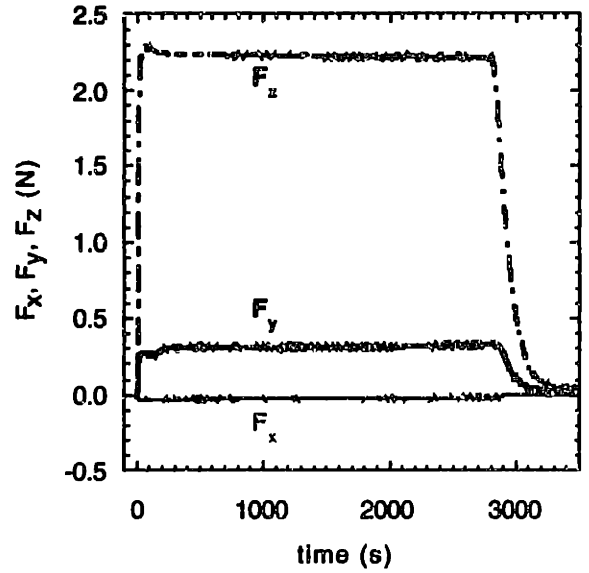

(a)

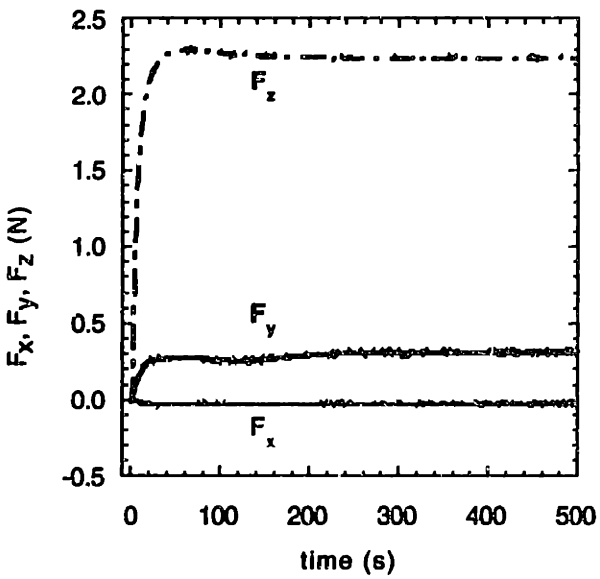

(b)

Figure 8-43: (a) Evolution of the drag and lift forces on the cylinders during startup, steady-state, and shutdown. The valve begins to open at $t = 0$, and is fully open at $t = 7\ s$. The experiment was carried out for a 0.31 wt% PIB/PB/C14 fluid flowing around a linear array of cylinders at $We = 1.3$. (b) Evolution of the drag and lift forces on the cylinder during startup.

Newtonian, Giesekus, CR and OLDB models are small ($\leq 0.04\,N$) until $We = 1.35$, where the CR model predicts a larger drag force. As the flow rate continues to increase beyond the critical $We = 1.53$, the flow undergoes a transition and the drag force on the cylinder is significantly greater than the values predicted by the steady two-dimensional FEM calculations. After the flow transition takes place, deviations between the measurements and steady FEM calculations increase. Since the pressure drop across the channel is carefully controlled by a pressure controller to ± 0.1 psi, the sudden rise in the drag force is caused by the presence of an elastic instability. Hence, the assumption of a steady flow field appears to be untenable for computing the drag force, and comparisons between the experiments and predictions are no longer valid. Chmielewski and Jayaraman (1993) investigated elastic flow instabilities in a square array and observed a 2% rise in the downstream pressure fluctuations corresponding to the onset of a flow transition. Although the flow undergoes a transition from steady two-dimensional to time periodic three-dimensional at the critical $We = 1.53$, the drag force on the cylinder remains time independent.

The asymmetry in the streamwise velocity field caused by off-centering of the cylinders suggests a non-zero lift force. Figure 8-45 indicates that the lift force is negative, i.e., the force is in the direction of the side of the channel with the slightly wider gap between the cylinder and channel. The magnitude of the lift force increases with increasing We, consistent with the fact that the flow becomes increasingly asymmetric about the centerplane. For both the single cylinder and the linear array of cylinders, the fluid elasticity tends to enhance drag force on the cylinder relative to the Newtonian fluid. Prior to flow transition a perfectly centered cylinder experiences no lift force. This is the case in the single cylinder geometry. However, in both the widely and the closely spaced cylinder arrays, it is observed that the off-centering causes a lift force in the direction of the wider gap between the cylinder and the channel wall. The effect of the flow transition is to impose a negative lift force on the cylinders. This explains the behavior seen in Fig. 8-41 for widely spaced cylinder arrays, where the lift force on the cylinder is initially positive due to off-centering and subsequently negative due to the effects of the flow transition. The closely spaced cylinder arrays exhibit similar behavior with initially negative lift force on the cylinder due to off-centering and subsequently more negative after flow transition takes place as shown in Fig. 8-45.

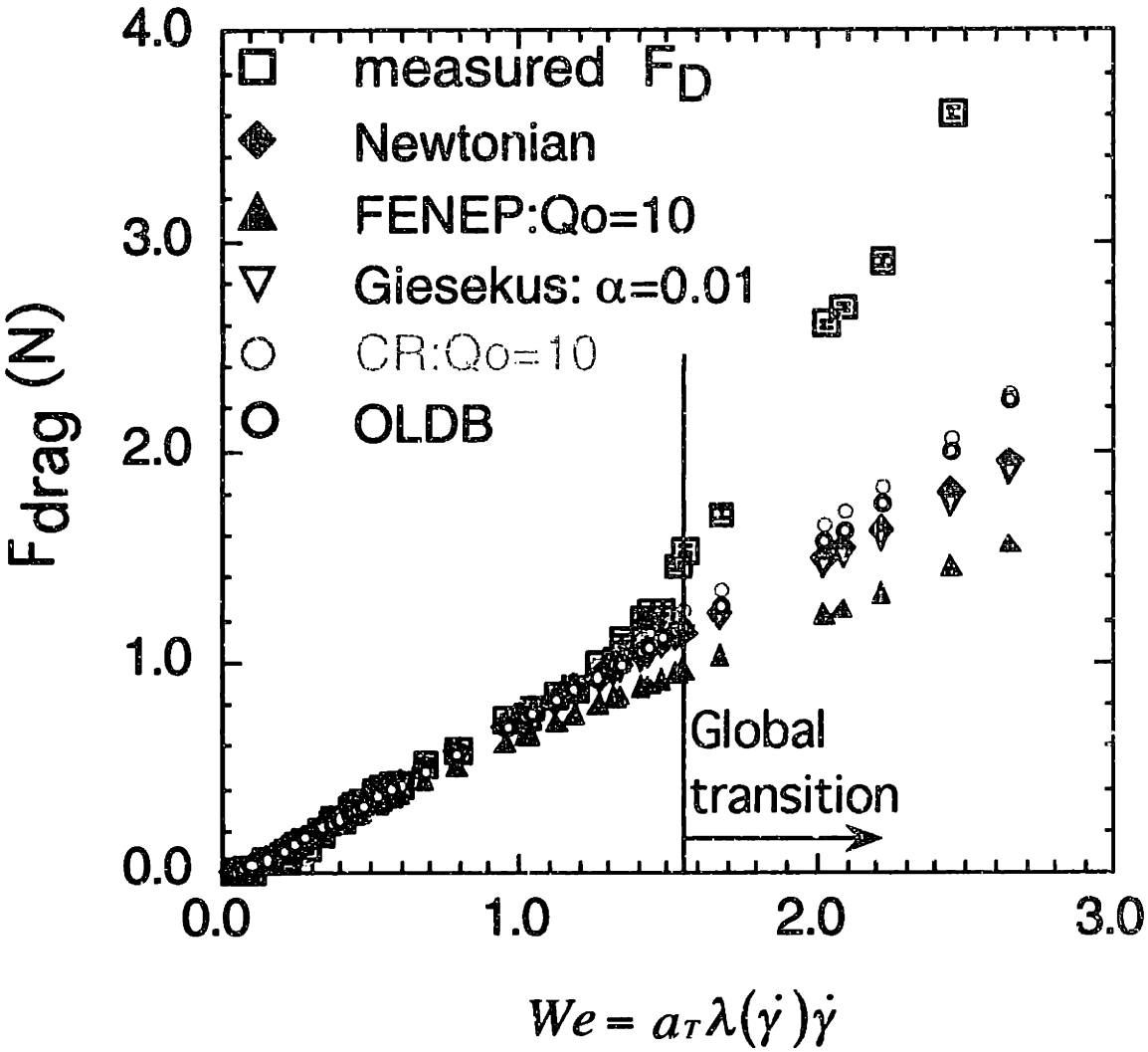

Figure 8-44: Drag force on a cylinder in a closely spaced array. The symbol '□' denotes experimental data points with error bars for both We and drag force measurements. Different colors correspond to the Newtonian, FENE-P, OLDB, CR, and Giesekus FEM calculations.

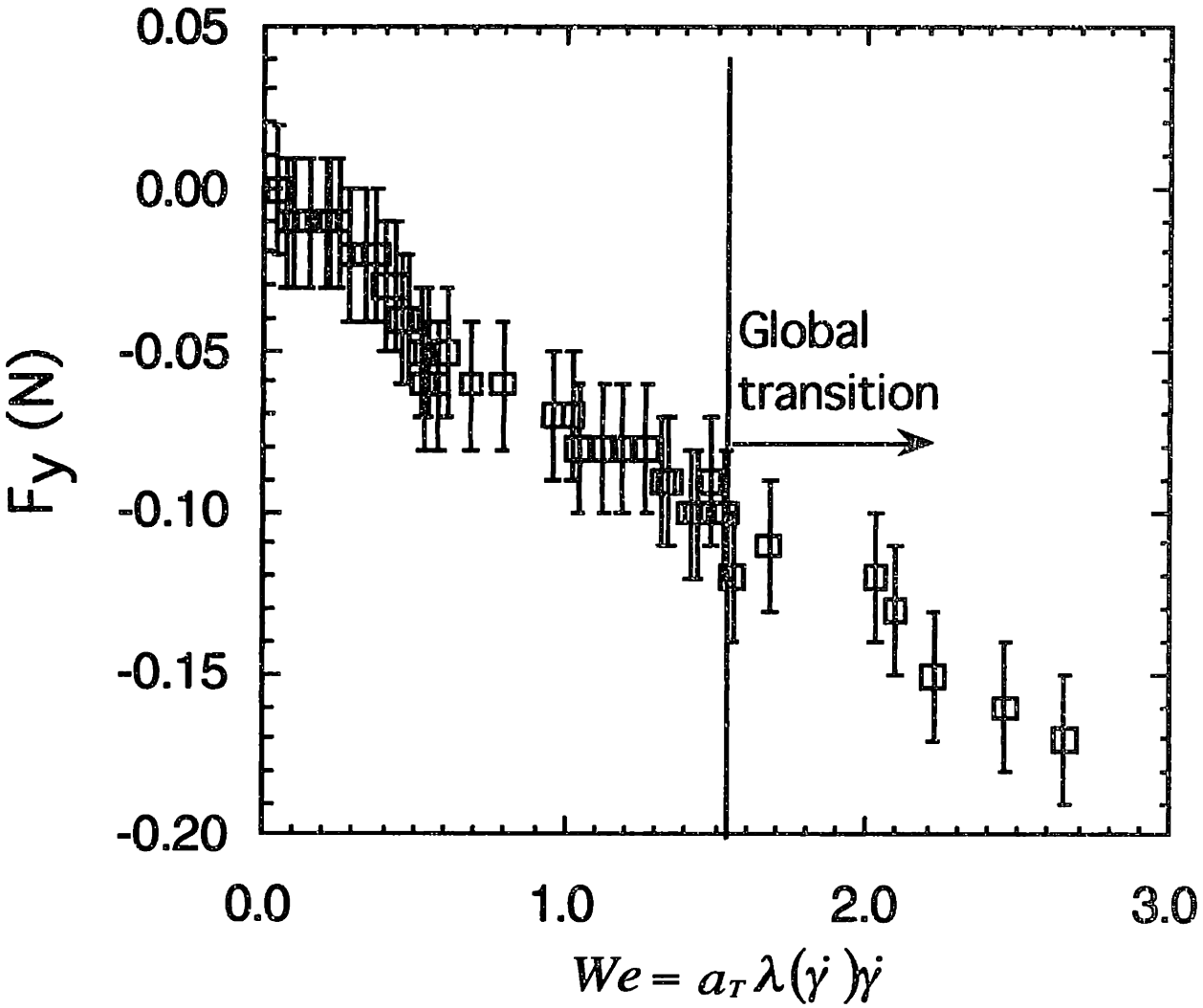

Figure 8-45: Lift force experienced by the seventh cylinder in a closely spaced array. The symbol '□' denotes experimental data points with error bars for both We and force measurements.

Chapter 9

Conclusions

The properties of products manufactured from polymers are sensitive to the underlying arrangement of the polymer molecules in the products. This molecular arrangement is a direct consequence of the interaction between the dynamics of the polymer and the fluid flow during the forming process. By understanding the effects of fluid flow in polymer processing, we are thus able to optimize the design and operating conditions of the forming process. Therefore, this thesis is concerned with both developing accurate and convergent finite element simulations of steady viscoelastic flows in complex flow geometries, and measuring experimentally pointwise velocity by laser Doppler velocimetry (LDV) and macroscopic forces by the use of a force transducer.

Viscoelastic flow past a periodic array of cylinders has received considerable attention in the last several years because it is a simple model system for polymeric flow in porous media, which is of interest for such engineering applications as enhanced oil recovery and composite and textile coating operations. In particular, we examine through both simulations and experiments the flow of polymer solutions around a periodic, linear array of cylinders, and two-dimensional arrays.

Finite element simulations are performed with three different constitutive models: the Giesekus model, the FENE-P model, and the Chilcott and Rallison model. All three constitutive models treat the macromolecules as dumbbells consisting of two point mass beads connected by a spring immersed in a Newtonian solvent. In the Giesekus model, intramolec-

ular forces are described by a Hookean spring, whereas a finitely extensible spring whose modulus is given by a Warner approximation is used in both the FENE-P and Chilcott-Rallison (CR) models. Hydrodynamic drag on the beads is taken to be anisotropic in the Giesekus model and isotropic in the other two models. The FENE-P and CR models differ subtly in their approximate treatment of the nonlinear force law. All three models exhibit very similar rheological behavior in viscometric flow and steady elongational flow, with the notable exception that the viscosity for the Chilcott-Rallison model is shear-rate independent.

Numerical solution techniques incorporate two different formulations: the Elastic-Viscous Split-Stress Gradient (EVSS-G) method and a new variant of this formulation, the Discrete EVSS-G (DEVSS-G) formulation, in which the elliptic stabilization term is added only to the discrete version of the momentum equation, and the constitutive equation is solved directly in terms of the polymer contribution to the stress tensor.

Calculations of steady two-dimensional flow in a periodic array of cylinders were performed. For closely spaced cylinders, the flow is separated between adjacent cylinders. This is not the case for more widely spaced cylinders. In both arrangements, the structure of the stress and molecular extension fields predicted by all three constitutive models are qualitatively similar. A "birefringent strand" of highly stretched polymer molecules which appears to emanate from the rear stagnation point of a cylinder in a widely spaced cylinder array ($L = 6, H = 2$), strengthens as the flow rate is increased. For a closely spaced cylinder array ($L = 2.5, H = 2$), the presence of flow recirculation between neighboring cylinders eliminates the wake extensional flow. The computed drag force on the cylinders differs among the models. Perhaps the most surprising result of this study is that, despite the fact that the presence of fore and rear stagnation points in the widely spaced cylinder array implies the existence of strong elongational flows in the wake of the cylinders, the results are clearly dominated by the shear flow behavior of the models in both intercylinder spacings. This is manifest in at least three ways: First, the normal stress contours for τ_{pxx} are very similar in both flow geometries; however, the slight variation in the magnitude of the minimum τ_{pxx} among the models follows the same trends as Ψ_1 in steady shear flow. Second, the contours of molecular extension also are similar (apart from the very large elongations possible for the Giesekus

Linear array ($H = 2$)	flow type	transition sequence	We_{crit}	type of transition	$\lambda_{x,v_z}, \lambda_{x,v_x}, \lambda_t$
$L \to \infty$	no flow separation	at once	0.34	steady 2D $\to$ steady 3D	$\lambda_{x,v_z} = \lambda_{x,v_x} = 0.95R \pm 0.05R$
$L = 6$	no flow separation	sequence of transitions	1.36	steady 2D $\to$ time dependent 3D	$\lambda_{x,v_z} = 4.0R \pm 0.6R$ $\lambda_{x,v_x} = 7.9R \pm 1.2R$
$L = 2.5$	flow separation	at once	1.53	steady 2D $\to$ time periodic 3D	$\lambda_{x,v_z} = 2.0 \pm 0.4R, \lambda_{x,v_x} = 2.4 \pm 0.5R$, $\lambda_t = 133 \pm 50s$

Table 9.1: Critical conditions for the onset of a wake instability in linear cylinder arrays.

model), and the trend in $<Q^2>_{max}$ is consistent with the response of $<Q^2>$ in simple shear flow. Third, the viscoelastic drag enhancement factor, χ, is very sensitive to shear thinning in the viscosity. This is seen in the dramatic difference in χ between the constant viscosity models, which show a minimum in χ with increasing We, and the shear thinning models, which show a monotonically decreasing drag force. The effects of inter-cylinder spacing, L, are also interesting. As L decreases from 6 to 2.5, flow separation appears even for the Newtonian fluid. When the flow is separated between adjacent cylinders, the interaction between adjacent cylinders has a much greater effect on molecular extension than when L is larger.

Experimental investigations also are presented for the creeping motion of a highly elastic, constant viscosity 0.31 wt% polyisobutylene (PIB) in polybutene (PB) and tetradecane (C14) Boger fluid past a linear array of cylinders. Along the symmetry plane, the $v_z / <v_z>$ profile shifts downstream as the Weissenberg number is increased. This shift is very well captured by the Oldroyd-B (OLDB) FEM calculations. Excellent agreement was achieved between the measured steady two-dimensional streamwise velocity field and the numerical predictions in the widely spaced ($L = 6, H = 2$) cylinder array. For a closely spaced ($L = 2.5, H = 2$) cylinder array, the $v_z / <v_z>$ is independent of axial position when $|z| \geq 1$. In addition to the steady-state results, flow transitions were observed in both flow geometries. Two-color laser Doppler velocimetry and flow visualization were used to characterize the spatial extent, and time period of the instability.

The critical conditions for flow transitions in a linear array of cylinders are summarized

in Table 9.1. When the center-to-center cylinder spacing is infinite (i.e. $L \to \infty$), the flow undergoes a transition from steady 2D to steady 3D at $We = 0.34$. The center-to-center cylinder spacing of $L \approx 8$ appears to be the limit where the streamwise velocity v_z, is still fully developed channel flow across $z = 3R$ downstream of each cylinder. At $L = 6$, v_z approaches 92% of the fully developed channel flow across $z = 3R$ downstream of each cylinder, and the steady 2D flow becomes transient 3D at a critical $We = 1.36$. Prior to this flow transition, a sequence of local flow transitions in the wake of the first, second, third and subsequent cylinders are observed. The first flow transition occurs locally in the wake of the first cylinder at a critical $We_{1,crit} = 1.14$; beginning $1.5R$ downstream of the first cylinder, periodic oscillations in the streamwise velocity appear along the entire length of the cylinder. The 3D instability is steady and has a wavelength of $3.5R \pm 0.5R$. The instability persists downstream for a distance of three radii, beyond which the rest of the flow is steady and 2D. As the flow rate increases to the second critical $We_{2,crit} = 1.19$, spatial oscillations in the v_z profile become apparent in the wake of the second cylinder, and once again, the instability starts at $z = 1.5R$ downstream of second cylinder and persists for three radii downstream, beyond which the rest of the flow is again steady and two-dimensional. Further increasing We to 1.36 leads to equally spaced v_z fluctuations appearing throughout the entire linear array. The transition is from a steady 2D to time dependent 3D flow. As the cylinders are moved closer to each other, flow separation appears between neighboring cylinders, and the flow undergoes a transition from a steady 2D to time periodic 3D at critical $We = 1.53$. At this critical condition, a flow transition takes place in the entire array. Therefore, decreasing L actually stabilizes the flow, and as a result the critical We shifts to higher values.

The structure of the flow instability also depends on L. For a single cylinder ($L \to \infty$), the wake instability is in the form of a three-dimensional cell along the length of the cylinder. The instability originates at $z = 1.5R$ downstream of the cylinder and is highly localized around the centerplane. For $L = 6$, the wake instability has a similar cellular structure as for $L \to \infty$, but the flow is now time dependent while the wavelength of the instability remains steady. A local flow transition occurs first in the wake of the first cylinder, then in the wake of subsequent cylinders as the flow rate is increased. The instability originates at $z = 1.5R$ downstream of each cylinder, propagates $3R$ downstream reaching $z = -1.5R$ upstream of

the next cylinder. The instability extends to $y = \pm 0.8R$ across the channel. The wavelength of the instability is weakly dependent on the axial position z, with the largest variations in v_z at the centerplane $y = 0$ and $z = -2R$, $z = -2.5R$ upstream of each cylinder (with the exception of the first cylinder). For $L = 2.5$, where a flow recirculation zone is established between neighboring cylinders, the flow transition is from steady two-dimensional to time periodic three-dimensional, and the instability is found for $0.48R \leq y \leq 1.32R$.

The drag and lift forces on the cylinder were measured as as a function of flow rate (We) using a specially mounted transducer at the seventh cylinder. Although the flow undergoes a transition at critical We in all three flow geometries, the measured drag force is time independent. For a single cylinder, drag experienced by the cylinder follows the Newtonian result for $We \leq 0.34$; deviations from the Newtonian value first appear at $We = 0.35$, after the flow transition has taken place. For $0.35 \leq We \leq 0.39$, the measured drag force is lower than those for the Newtonian case; this discrepancy is captured by the the OLDB, Giesekus, FENE-P, and CR viscoelastic models. Because of limitations in the sensitivity of the force transducer, and also because the flow is no longer steady and two-dimensional, no conclusions can be drawn as to which constitutive model is more suitable to describe the flow of the 0.31 wt% PIB/PB/C14 fluid around a confined cylinder. For $We \geq 0.4$, greater drag force is measured than is predicted by the finite element calculations using the Newtonian, OLDB, Giesekus, FENE-P, and CR models. As expected, the two-dimensional steady viscoelastic calculations fail to predict this increase in the drag force, which is likely due to the effects of the flow transition. Prior to flow transition a perfectly centered cylinder experiences no lift force. This is the case as the lift force on the cylinder is essentially zero for $We \leq 0.5$. The appearance of 3D flow instabilities causes the streamwise velocity across the channel width to become more and more asymmetric about the centerplane (Byars, 1995), leading to a measurable lift force, F_y. As We continues to increase, the lift force becomes more negative due to the increasing asymmetry in the streamwise velocity profile (Byars, 1995).

In a widely spaced cylinder array, $(L = 6, H = 2)$, the measured drag forces agree extremely well with the Newtonian results at low flow rates. Deviations from the Newtonian flow were first noted at $We = 0.70$. As the Weissenberg number is increased, the deviations from Newtonian behavior become greater. Therefore, fluid elasticity tends to enhance the

drag force on the cylinder relative to that for a Newtonian fluid. Since viscoelastic constitutive equations such as the OLDB, Giesekus, FENE-P, and CR models all predict the drag force to be lower than the Newtonian values, these models underestimate the drag force on the cylinder for $We > 0.6$. Although all four constitutive models accurately predict downstream shifts in the streamwise velocity along the symmetry line ($y = 0$) as We is increased, none of the models accurately predict the stress field around the cylinder (as discussed in section 8.4.2). The simple Newtonian model actually does a reasonable job in predicting the drag force on the cylinder at these higher flow rates. In addition to the drag force, a lift force is measured and exists because of slight off-centering of the cylinder which causes asymmetry in the velocity profile. It is observed that the off-centering of the cylinders causes a lift force in the direction of the wider gap between the cylinder and the channel wall. The effect of the flow transition is to impose a negative lift force on the cylinders. This explains the behavior seen in Fig. 8-41 for widely spaced cylinder arrays, where the lift force on the cylinder is initially positive due to off-centering and subsequently negative due to the effects of the flow transition.

For a closely spaced cylinder array, both the Newtonian and all four constitutive models accurately describe the drag force on a cylinder when $We \leq 0.6$. At higher We, a comparison between drag force measurements and finite element calculations indicates that the CR model best fits the experimental results prior to the onset of the flow instability ($We = 1.53$). At the onset of the flow transition; the drag force on the cylinder is significantly greater than the values predicted by the steady two-dimensional FEM calculations. All constitutive models, including the Newtonian model, fail to predict this significant increase in drag force caused by the three-dimensional motion. For $We > We_{crit}$, deviations between the measurements and steady-state FEM calculations increase with increasing We. Because the cylinders are not mounted exactly in the center of the channel, asymmetry in the streamwise velocity field results in a non-zero lift force. The lift force on the cylinder is initially negative due to off-centering and subsequently more negative after the flow transition takes place as shown in Fig. 8-45. For both the single cylinder and linear array of cylinders, the effect of fluid elasticity is to enhance the drag force on the cylinder relative to Newtonian values, and the effect of the flow transition is to exert a negative lift force as indicated in Figs. 8-35, 8-41

and 8-45.

Although viscoelastic constitutive models can predict accurately the changes in the flow kinematics, all of them fail to predict drag force enhancement relative to the Newtonian values prior to the flow transition; and the difference between the measurement and predictions increases with increasing We. Because polymer fluids have a fading memory, the stress tensor at time t at some point in space is given as the integral of the rate-of-strain tensor multiplied by the memory function at that same point in space but for all previous times t' (Bird *et al.* , 1987). Since increasing the Deborah number (De) lengthens the memory history of the deformation, the stress is integrated over a longer time period, and the differences between the measured and predicted stress values at each past time contribute to a larger difference at the present time. Also, the behavior of macromolecules in complex flow is not clear because an actual polymer molecule is an extremely complex mechanical system with an enormous number of degrees of freedom (Bird *et al.* , 1987). The dumbbell models considered in this thesis are crude mechanical models to describe polymer behavior in complex flow, but the their simplicity minimizes the mathematics and allows us to obtain a quantitative result, and can act as the basis for the study of much more realistic molecular models.

To study this problem one step further with a more realistic constitutive model, we would need to examine multi-mode constitutive equations. The existence of a molecular weight distribution suggests that a single relaxation time is inadequate to characterize many different modes of relaxation available to long flexible polymer chains. This difficulty is overcome by the introduction of multiple modes of relaxation (Bird *et al.* , 1987). Quinzani (1991) found that a multi-mode Phan-Thien-Tanner model gave rise to the best fit of the experimental results for concentrated 5 wt% PIB/PB/C14 fluid in a 4:1 planar contraction. More recent experiments on concentrated 5 wt% PIB/PB/C14 fluid in flow around a cylinder confirmed that the use of multi-mode Phan-Thien-Tanner model was best suited to describe the stress field in complex flow geometry (Baaijens *et al.* , 1994). Therefore, the use of multi-mode constitutive models should be considered for flow around a linear array of cylinders.

The underestimation of the stress in relationship with the rate-of-strain can be verified experimentally by measuring the pointwise stress field around the cylinder directly using

flow induced birefringence. However, some experimental modifications to the current system would be necessary. Quinzani (1991) has observed beam divergence during FIB measurements on 0.31 wt% PIB/PB/C14 Boger fluid in a Couette cell. However, beam divergence was not detected in subsequent LDV measurements in the axisymmetric contraction, a single cylinder (McKinley, 1991; Byars, 1995) and the present study in a linear array of cylinders in a rectangular channel. McKinley (1991) postulated that the discrepancy was due to the degree of mixing. Insufficient mixing in a shear dominated Couette flow cell may lead to the formation of separate fluid phases, whereas in the case of contraction flow, the fluid is uniformly mixed. Recent experiments on 0.31 wt% PIB/PB in a Couette cell indicated no beam divergence up to a shear rate of $\dot{\gamma} = 13\,s^{-1}$ (Genieser, 1993). This seems to suggest that C14 may be responsible for beam divergence. Thus, the combined LDV and FIB methods for validating the accuracy of the constitutive models should be carried out for 0.31 wt% PIB/PB fluids. Genieser (1995) has developed a batch process to produce PIB/PB solution efficiently. The two-component PIB/PB fluid is formed by dissolving PIB in hexane (C6), then mixing the PIB/C6 into solvent PB. After forming PIB/PB/C6 ternary mixture, the hexane is driven off by evaporation. In addition, a low parasitic birefringence glass window should be used to improve the resolution of the FIB system.

The experimental work in this thesis has shown that viscoelastic flow transitions in both widely and closely spaced cylinder arrays take place at critical We. The results are reported only for a single highly elastic fluid consisting of 0.31 wt% PIB dissolved in PB/C14 solution. Further work is required to understand the precise role of the fluid rheology on the stability of the flow. Previous theoretical and experimental work has shown that in general, shear-thinning tends to stabilize viscoelastic instabilities (Baaijens, 1994; Öztekin and Brown 1993; McKinley *et al.* 1991b, 1995; Cable and Boger, 1979). The effects of polymer additives also needs to be addressed because previous investigations show that these additives inhibit the onset of inertial instabilities (Larson, 1989). Another issue that needs to be addressed is the importance of elongational effects on flow stability. Experiments with polyacrylamide- (PAC) and polyisobutylene-based Boger fluids in falling sphere, and axisymmetric contraction flow experiments have revealed significant differences in the drag coefficient on the sphere with De (Muller, 1986; Chmielewski *et al.* , 1990; McKinley, 1991). The deviation must arise from

differences in the extensional rheology of the PAC and PIB solutions because the viscometric properties η and Ψ_1 of the two fluids are similar.

With continuing advances in computer architecture and algorithms, it is possible to perform large-scale numerical modeling that examines more complex flow problems to include transient, non-isothermal, free surface and three-dimensional effects (Burdette, 1989; Northey *et al.* , 1990; Szady, 1995; Caola, 1995; Smith, 1996; Sureshkumar *et al.* , 1997). Therefore it is feasible at least qualitatively to examine computationally the flow transition in a linear array of cylinders, to address the effect of cylinder center-to-center spacing on the onset of the flow instabilities for a fixed value of H and to search for the cause and origin of these instabilities.

This thesis only concerns linear arrays with a fixed $H = 2$, where the largest shear rate is in the minimum gap between the cylinder and channel wall, and the high shear and velocity gradients are found both around the cylinder surface and on the channel wall. This makes the computation very expensive because local mesh refinement is needed in those two regions. To minimize the effect of the channel and examine the modification of flow due to the presence of cylinders, future experiments on large H values need to carried out. Previous experimental investigations of Byars (1995) for a cylinder in a channel indicate that as the distance between the channel wall and the cylinder is increased, the onset of the instability occurs at higher We. Similar experiments need to be performed for a linear array of cylinder.

Bibliography

[1] R. C. Armstrong, and G. H. McKinley, *Class notes for Summer professional program PST102s: Rheological behavior of polymeric liquids with laboratory workshop* (1995)

[2] R. C. Armstrong, and S. Ishikawa, "A rheological equation of state for dilute Solutions of nearly-Hookean dumbbells", *J. Rheo.*, **24:2** (1980), 143-165

[3] A. Acrivos, D. D. Snowden, A. S. Grove and E. E. Peterson, "The steady separated flow past a circular cylinder at large Reynolds numbers", *J. Fluid Mech.*, **21** (1965), 737-760

[4] F. P. T. Baaijens, H. P. W. Baaijens, G. W. M. Peters, and H. E. H. Meijer, "An experimental and numerical investigation of a viscoelastic flow around a cylinder", *J. Rheol.*, **38** (1994), 351-376

[5] H. P. W. Baaijens, *Evaluation of constitutive equations for polymer melts and solutions*, Ph.D. Thesis, Eindhoven University of Technology (1994)

[6] H. P. W. Baaijens, G. W. M. Peters, F. P. T. Baaijens, and H. E. H. Meijer, "Viscoelastic flow past a confined cylinder of polyisobutylene", *J. Rheol.*, **39** (1995), 1243-1277

[7] I. Babuska and W. C. Rheinboldt, *In elliptic problem solvers II*, edited by G. Brikhoff and A. Schoenstadt, Academic Press, New York (1984)

[8] I. Babuska, J. T. Oden, and J. K. Lee, "Mixed-hybrid finite element approximations of second-order elliptic boundary value problems", *Comp. Meth. App. Mech. Eng.*, **14** (1977), 175-206

[9] I. Babuska, "The theory of small changes in the domain of existence in the theory of partial differential equations and its applications", in A. C. Giffin and J. F. Johnson, editors, *Differential equations and their applications*, Academic Press, New York (1963)

[10] L. Bairstow, "The two-dimensional slow motion of viscous fluids", *Proc. Roy. Soc.*, **A100** (1922), 394-413

[11] G. K. Batchelor, *An introduction to fluid mechanics*, Cambridge University Press (1967)

[12] R. E. Bank, *In elliptic Problem Solvers*, edited by Schultz Martin, Academic Press, New York (1981)

[13] G. Barakos, and E. Mitsoulis, "Numerical Simulation of viscoelastic flow around a cylinder using an integral constitutive equation", *J. Rheol.*, **39** (1996), 1279-1292

[14] H. A. Barnes, J.F. Hutton and K. Walters, *An introduction to Rheology*, Elsevier Science Publishers (1989)

[15] L. E. Becker, G. H. McKinley, H. K. Rasmussen, and O. Hassager, "The unsteady motion of a sphere in a viscoelastic fluid", *J. Rheo.*, **38** (1994), 377-403

[16] T. G. Beckwidth, R. D. Marangoni and J. H. Lienhard, *Mechanical measurements*, Addison-Wesley Publishing, 5th Ed. (1993)

[17] M. A. Behr, L. P. Franca, T. E. Tezduyar, "Stabilized finite element methods for the velocity-pressure-stress formulation of incompressible flows", *Computer Methods in App. Mech. Eng.*, **34** (1993), 31-48

[18] A. V. Bhave, R. C. Armstrong, and R. A. Brown, "Kinetic theory and rheology of dilute, nonhomogeneous polymer solutions", *J. Chem. Phys.*, **95** (1991), 2988-3000

[19] R. B. Bird, W. E. Stewart and E.N. Lightfoot, *Transport Phenomena*, John Wiley and Sons (1960)

[20] R. B. Bird, P. J. Dotson, and N. L. Johnson, "Polymer solution rheology based on a finitely extensible bead-spring chain model", *J. Non-Newtonian Fluid Mech.*, **7** (1980), 213-235

[21] R. B. Bird, R. C. Armstrong, and O. Hassager, *Dynamics of Polymeric Liquids. Vol. 1: Fluid mechanics*, 2nd Ed., Wiley Interscience, New York (1987)

[22] R. B. Bird, R. C. Armstrong, and O. Hassager, *Dynamics of Polymeric Liquids. Vol. 2: Kinetic Theory*, 2nd Ed., Wiley Interscience, New York (1987)

[23] R. B. Bird, and J. R. Deaguiar, "An encapsulated dumbbell model for concentrated polymer solutions and melts, I. theoretical development and constitutive equation", *J. Non-Newtonian Fluid Mech.*, **13** (1993), 149-160

[24] C. Bisgaard, "Velocity fields around spheres and bubbles investigated by laser-Doppler anemometry", *J. Non-Newtonian Fluid Mech.*, **12** (1983), 283-302

[25] D. V. Boger, "A highly elastic constant-viscosity fluid", *J. Non-Newtonian Fluid Mech.*, **3** (1977), 87-91

[26] D. V. Boger, D. U. Hur, and R. J. Binnington, "Further observations of elastic effects in tubular entry flows", *J. Non-Newtonian Fluid Mech.*, **20** (1986), 31-49

[27] D. V. Boger, "Viscoelastic flows through contractions", *Ann. Rev. Fluid Mech.*, **19** (1987), 157-182

[28] D. V. Boger, and R. J. Binnington, "Circular entry flow of fluid M1", *J. Non-Newtonian Fluid Mech.*, **35** (1990), 339-360

[29] D. V. Boger, *Rheological phenomena in focus*, Elsevier, Amsterdam (1993)

[30] R. A. Brown, M. J. Szady, P. J. Northey, and R. C. Armstrong, "On the numerical stability of mixed finite-element methods for viscoelastic flows governed by differential constitutive equations", *Theoret. Comput. Fluid Dynamics*, **5** (1993), 77-106

[31] R. A. Brown, G. H. McKinley, "Report on the VIIIth international workshop on numerical methods in viscoelastic flows", *J. Non-Newtonian Fluid Mech.*, **52** (1994), 407-413

[32] J. M. Broadbent, and B. Mena, "Slow flow of an elastico-viscous fluid past cylinders and spheres", *Chem. Eng. J.*, **8** (1985), 11-19

[33] M. B. Bush, "The stagnation flow behind a Sphere", *J. Non-Newtonian Fluid Mech.*, **49** (1993), 103-122

[34] M. B. Bush, "On the stagnation flow behind a sphere in a shear-thinning viscoelastic liquid", *J. Non-Newtonian Fluid Mech.*, **49** (1993), 103-122

[35] S. R. Burdette, "Development of the velocity field in transient shear flows of viscoelastic fluids", *J. Non-Newtonian Fluid Mech.*, **32** (1989), 269-294

[36] J. A. Byars, A. Öztekin, R. A. Brown, and G. H. McKinley, "Spiral instabilities in the flow of highly elastic fluids between rotating parallel disks", *J. Fluid Mech.*, **271** (1994), 173-218

[37] J. A. Byars, *Experimental characterization of viscoelastic flow instabilities*, Ph. D. thesis (1995)

[38] P. J. Cable, and D. V. Boger, "A comprehensive experimental investigation of tubular entry flow of viscoelastic fluids: part 3, Unstable flow", *AIChE J.*, **25** (1979), 152-159

[39] A. E. Caola, *The solution of large viscoelastic flow problems using parallel techniques*, Ph. D. Thesis proposal (1995)

[40] C. A. Cathey, and G. G. Fuller, "The optical and mechanical responses of flexible polymer solutions to extensional flow", *J. Non-Newtonian Fluid Mech.*, **34** (1990), 63-88

[41] E. A. Cerutti, R. B. Kinney, and M. A. Paolino, "Numerical predictions for unsteady viscous flow past an array of cylinders", *Int. J. Numerical Methods in Fluids*, **6** (1986), 715-731

[42] E. A. Cerutti, R. B. Kinney and M. A. Paolino, "Numerical predictions for unsteady viscous flow past an array of cylinders", *Int. J. Num. Methods Fluids*, **6** (1986), 715-731

[43] R. Chandra, "Recent progress in the degradation of polyisobutylene", *Prog. Polym. Sci.*, **11** (1985), 1-22

[44] R. P. Chhabra, P. H. T. Uhlherr and D. V. Boger, "The influence of fluid elasticity on the drag coefficient for creeping flow around a sphere", *J. Fluid Mech.*, **6** (1980), 187-199

[45] R. P. Chhabra, and P. H. T. Uhlherr, "The influence of fluid elasticity on wall effects for creeping sphere motion in cylindrical tubes", *Can. J. Chem. Eng.*, **66** (1988), 154-157

[46] M. D. Chilcott, and J. M. Rallison, "Creeping flow of dilute polymer solutions past cylinders and spheres", *J. Non-Newtonian Fluid Mech.*, **29** (1988), 381-432

[47] C. Chmielewski, C. A. Petty, and K. Jayaraman,"Crossflow of elastic liquids through arrays of cylinders", *J. Non-Newtonian Fluid Mech.*,**35** (1990), 309-325

[48] C. Chmielewski, K. L. Nichols, and K. Jayaraman, "A comparison of the drag coefficients of spheres translating in corn-syrup-based and polybutene-based Boger fluids", *J. Non-Newtonian Fluid Mech.*, **35** (1990), 37-49

[49] C. Chmielewski, *Crossflow permeation of viscous and viscoelastic liquids through arrays of circular cylinders*, Ph.D. Thesis, Michigan State University (1991)

[50] C. Chmielewski, and K. Jayaraman, "The effect of polymer extensibility on crossflow of polymer solutions through cylinder arrays", *J. Rheol.*,**36** (1992), 1105-1126

[51] C. Chmielewski, C. A. Petty, and K. Jayaraman, "Elastic instability in crossflow of polymer solutions through periodic arrays of cylinders", *J. Non-Newtonian Fluid Mech.*,**48** (1993), 285-301

[52] A. Chow, A. Keller, A. J. Müller, and J. A. Odell, "Entanglements in polymer solutions under elongational flow: a combined study of chain stretching, flow velocimetry, and elongational viscosity", *Macromolecules*, **21:1** (1988), 250-256

[53] Z. M. Cielak and R. B. Kinney, "Analysis of unsteady viscous flow past an airfoil: part II-numerical formulation and results", *AIAA J.*, **16** (1978), 105-110

[54] P. J. Coates, *Simulation of the flow of viscoelastic fluids in contraction geometries*, PhD thesis, Massachusetts Institute of Technology (1992)

[55] S. H. Crandall, N. C. Dahl and T. J. Lardner, *An introduction to the mechanics of solids*, McGraw-Hill, 2nd ed., 1978

[56] R. Cressely, and R. Hocquart, "Birefringence d'ecoulement localisee induite a larriere d'obstracle", *Opt. Acta*, **27** (1979), 699-711

[57] P. K. Currie, "Constitutive equations for polymer melts predicted by the Doi-Edwards and Curtiss-Bird kinetic theory models", *J. Non-Newtonian Fluid Mech.*, **11** (1982), 53-68

[58] J. W. Dally, and W. F. Riley, *Experimental stress analysis*, 2nd Ed., McGraw-Hill, New York (1978)

[59] D. L. Davidson, W.W. Graessley, and W.R. Schowalter, "Velocity and stress fields of polymeric liquids flowing through periodically constricted channel. Part 1. Experimental methods and straight channel validation", *J. Non-Newtonian Fluid Mech.*, **49** (1993a), 317-344

[60] D. L. Davidson, W. W. Graessley, and W. R. Schowalter, "Velocity and Stress Fields of polymeric liquids flowing through periodically constricted channel. Part 2. Observations of non-Newtonian behavior", *J. Non-Newtonian Fluid Mech.*, **49** (1993b), 345-375

[61] P. G. De Gennes, "Coil-stretch transition of dilute Flexible polymers under ultrahigh velocity gradients", *J. Chem. Phys.*, **60** (1974), 5030-5042

[62] P. G. DeGennes, *Scaling Concepts in Polymer Physics*, Cornell University Press, New York (1987)

[63] S. A. Dhahir, and K. Walters, "On non-Newtonian flow past a cylinder in a confined flow", *J. Rheol.*, **33** (1989), 781-804

[64] J. E. Drummond, and M. I. Tahir,"Laminar viscous flow through regular Arrays of parallel solid cylinders", *Int. J. Multiphase Flow*, **10:5** (1984), 515-540

[65] P. N. Dunlap, and L. G. Leal, "Dilute polysteyrene solutions in extensional flows Birefringence and flow modifications", *J. Non-Newtonian Fluid Mech.*, **23** (1987), 5-48

[66] E. C. Eaton, "Resistance strain gage measures stresses in concrete" *Eng. News Rec.*, **107** (1931), 615-616

[67] O. Emersleben, "Das Darcysche Filtergesetz", *Physikalische Zeitschrift*, **26** (1925), 601-610

[68] O. H. Faxens,"Forces exerted on a rigid cylinder in a viscous fluid between two parallel fixed plane", *Proc. Roy. Swedish Acad. Eng. Sci.*, **187** (1946), 1-13

[69] S. Flew, "Non-Newtonian flow in porous media - a laboratory study of polyacrylamide solutions", *J. Non-Newtonian Fluid Mech.*, **47** (1993), 169-210

[70] H. Fujikawa, "The forces acting on two circular cylinders of arbitrary radii placed in a uniform stream at low values of Reynolds number", *J. Phys. Soc. Japan*, **11** (1956), 690-701

[71] H. Fujikawa, "The force acting on two equal circular cylinders placed in a uniform stream at low values of Reynolds number", *J. Phys. Soc. Japan*, **11** (1957), 558-569

[72] G. G. Fuller, and L. G. Leal, "The effects of conformation-Dependent friction and internal viscosity on the dynamics of the nonlinear dumbbell model for a dilute polymer solution", *J. Non-Newtonian Fluid Mech.*, **8** (1981), 271-310

[73] L. H. Genieser, "Investigation of viscoelastic elongational flow phenomena in the planar contraction", Ph.D. Thesis proposal, MIT (1993)

[74] G. Georgiou, S. Momani, M. J. Crochet, and K. Walters, " Newtonian and non-Newtonian flow in a channel obstructed by an antisymmetric array of cylinders", *J. Non-Newtonian Fluid Mech.*,**40** (1991), 231-260

[75] D. Gordon, "Numerical calculations on viscous flow field through cylinder arrays", *Comp. Fluids*, **6** (1978), 1-13

[76] F. O. Griffin and A. Meisen, "Impaction of spherical particles on cylinders at moderate Reynolds numbers", *Chem. Eng. Sci.*, **28** (1973), 2155-2164

[77] R. Guenette, A. Zine, A. Fortin, P. Carreau, and M. Grmela, "Simulation of viscoelastic flows using a conformation tensor model", *J. Non-Newtonian Fluid Mech.*,**45** (1992), 187-208

[78] R. Guenette, and M. Fortin, "A new mixed finite element method for computing viscoelastic flows", *J. Non-Newtonian Fluid Mech.*, **60** (1995), 27-52

[79] M. D. Gunzburger, *Finite element methods for viscous incompressible flows*, Academic Press (1989)

[80] A. E. Hamielec and J. D. Raal, "Numerical studies of viscous flow around circular cylinders", *Phys. Fluids*, **12** (1969), 11-17

[81] J. Happel, "Viscous flow relative to arrays of cylinders", *Am. Inst. Chem. Eng. J.*, **5** (1959), 174-177

[82] J. Happel and H. Brenner, *Low Reynolds number hydrodynamics*, 2nd ed. Noordhoff International Publishing (1973)

[83] O. G. Harlen, "High Deborah number flows of dilute polymer solutions past a sphere falling along the axis of a cylindrical tube", *J. Non-Newtonian Fluid Mech.*, **37** (1990), 157-173

[84] O. G. Harlen, J. M. Rallison, and M. D. Chilcott, "High Deborah number flows of dilute polymer solutions", *J. Non-Newtonian Fluid Mech.*, **34** (1990), 319-349

[85] O. G. Harlen, E. J. Hinch, and J. M. Rallison, "Birefringent pipes: the steady flow of a dilute polymer solution near a stagnation point", *J.Non-Newtonian Fluid Mech.*, **44** (1992), 229-265

[86] O. J. Harris, J. M. Rallison, "Start-up of a strongly extensional flow of a dilute polymer solution", *J. Non-Newtonian Fluid Mech.*, **50** (1993), 89-124

[87] W. H. Harrt, and D. G. Baird, "Flow of viscoelastic fluids through banks of cylinders", 65th Annual Society of Rheology Meeting (1993)

[88] H. Hasimoto, "On the Periodic Fundamental Solutions of the Stokes' Equations and Their Application to Viscous Flow Past a Cubic Array of Spheres", *J. Fluid Mech.*, **5** (1959), 317-328

[89] H. Hasimoto, "On the flow of a viscous fluid past a thin screen at small Reynolds numbers", *J. Phys. Soc. Japan*, **13** (1958), 633-639

[90] O. Hassager, "Working group on numerical techniques", *J. Non-Newtonian Fluid Mech.*, **29** (1988), 2-5

[91] O. Hassager, and C. Bisgaard, "A Lagrangian finite element method for the simulation of flow of Non-Newtonian liquids", *J. Non-Newtonian Fluid Mech.*, **12** (1983), 153-164

[92] M. Herrchen and H. C. Öttinger, "A detailed comparison of various FENE dumbbell models", *J. Non-Newtonian Fluid Mech.*, **68** (1997), 17-42

[93] E. J. Hinch, "Mechanical models of dilute polymer solutions for strong flows with large Polymer deformations", *Colloques Internationaux. du C.N.R.S.*, **233** (1971), 241-247

[94] E. J. Hinch, "An averaged-equation approach to particle interactions in a fluid suspension", *J. Fluid Mech.*, **83:4** (1977), 695-720

[95] E. J. Hinch, "The flow of an Oldroyd fluid around a sharp corner", *J. Non-Newtonian Fluid Mech.*, **50** (1993), 161-171

[96] P. Hood, "Frontal solution program for unsymmetric matrices", *Int. J. Numer. Methods Eng.*, **10** (1976), 379-399

[97] P. Hood, "Note on frontal solution program for unsymmetric matrices", *Int. J. Numer. Methods Eng.*, **11** (1977), 1055

[98] N. E. Hudson, and T. E. R. Jones, "The A1 project-an overview", *J. Non-Newtonian Fluid Mech.*, **46** (1993), 69-88

[99] M. A. Hulsen, "A sufficient condition for a positive definite configuration tensor in differential models", *J. Non-Newtonian Fluid Mech.*, **38** (1990), 93-100

[100] S. Huzarewicz, R. K. Gupta, and R. P. Chhabra, "Elastic effects in flow of fluids through sinuous tubes", *J. Rheo.*, **35** (1991), 221-235

[101] I. Imai, "On the asymptotic behavior of viscous fluid flow at a great distance from a cylindrical body, with special reference to Filon's paradox", *Proc. Roy. Soc. London, Series A*, **208** (1951), 487-516

[102] I. Imai, "On the asymptotic behavior of viscous fluid flow at a great distance from a cylindrical body, with special reference to Filon's paradox", *Proc. Roy. Soc. London, Series A*, **208** (1951), 487-516

[103] I. Imai, "A new method of solving Oseen's equations and its application to the flow past an inclined elliptic cylinder", *Proc. Roy. Soc. London, Series A*, **224** (1954), 141-160

[104] S. Ishigai, E. Nishikawa, K. Nishimura and K. Cho, "Experimental study on structure of gas flow in tube banks with tube axes normal to flow (Part 1, Karman vortex flow around two tubes at various spacings)", *Bulletin Japan Soc. Mech. Eng.*, **15** (1972), 949-956

[105] D. F. James, and D. R. Mclaren, "The Laminar flow of dilute polymer solutions through porous media", *J. Fluid Mech.*, **70** (1975), 733-752

[106] H. Jin, N. Phan-Thien, and R. I. Tanner, "A finite element analysis of the flow past a sphere in a cylindrical tube: PTT fluid model", *Comp. Mech.*, **8** (1991), 409-422

[107] C. Johnson, *Numerical solution of partial differential equations by the finite element method*, Cambridge University Press, New York (1987)

[108] D. D. Joseph, M. Renardy and J.C. Saut, "Hyperbolicity and change of type in the flow of viscoelastic fluids", *Arch. Rat. Mech.*, 87 (213-251), 1985

[109] D. M. Jones, and K. Walters, "The behaviors of polymer solutions in extension-dominated flows with applications to enhanced oil recovery", *Rheol. Acta*, **28** (1989), 482-498

[110] S. Kaplun, "Low Reynolds number flow past a circular cylinder", *J. Math. Mech.*, **6** (1957), 595-603

[111] H. H. Kausch, T. Q. Nguyen, "Chain scission in strong flows", *Xth International Congress on Rheology*, (1988), 20-21

[112] M. Kawaguti, "Numerical solution of the Navier-Stokes equations for the flow around a circular cylinder at Reynolds number 40", *J. Phys. Soc. Japan*, **8** (1953), 747-757

[113] M. Kawaguti, "On the viscous shear flow around a circular cylinder II. Oseen's approximation", *J. Phys. Soc. Japan*, **11** (1956), 570-583

[114] M. Kawaguti and P. Jain, "Numerical study of viscous fluid flow past a circular cylinder", *J. Phys. Soc. Japan*, **21** (1966), 2055-2062

[115] R. A. Keiller, "Extending filaments of an Oldroyd fluid", *J. Non-Newtonian Fluid Mech.*, **42** (1992), 37-48

[116] R. A. Keiller, "Modeling of the extensional flow of the M1 fluid with the Oldroyd equation", *J. Non-Newtonian Fluid Mech.*, **42** (1992), 49-64

[117] R. A. Keiller, "Entry flow calculations for the Oldroyd-B and FENE equations", *J. Non-Newtonian Fluid Mech.*, **46** (1993), 143-178

[118] A. Keller, A. J. Müller, and J. A. Odell, "Entanglements in semi-dilute solutions as revealed by elongational flow studies", *Progr. Colloid Polym. Sci.*, **75** (1987), 179-200

[119] H. B. Keller, H. Takami and D. Greenspan, *Numerical solutions of nonlinear differential equations*, Wiley, New York (1966), p. 115

[120] R. Keunings, "Simulation of viscoelastic fluid flow", from C. L. Tucker, Computer modeling for polymer processing, Hanser publishers (1989)

[121] R. Keunings, "Progress and challenges in computational rheology", *Rheol. Acta*, **29** (1990), 556-570

[122] B. Khomami, K. K. Talwar, and H. K. Ganpule, "A comparative study of higher- and lower-order finite element techniques for computation of viscoelastic flows", *J. Rheol.*, **38** (1994), 255-289

[123] R. C. King, *Stable and convergent finite element methods for the calculation of viscoelastic flows in smooth geometries*, PhD thesis, M.I.T (1987)

[124] R. C. King, M. R. Apelian, R. C. Armstrong, and R. A. Brown, "Numerically stable finite element techniques for viscoelastic calculations in smooth and singular geometries", *J. Non-Newtonian Fluid Mech.*, **29** (1988), 147-216

[125] R. B. Kinney and Z. M. Cielak, "Analysis of unsteady viscous flow past an airfoil: part I-theoretical development", *AIAA J.*, **15** (1977), 1712-1717

[126] A. A. Kirsch and N. A. Fuchs, "The fluid flow in a system of parallel cylinders perpendicular to the flow direction at small Reynolds numbers", *J. Phys. Soc. Japan*, **22** (1967), 1251-1255

[127] L. S. G. Kovasznay, "Hot-wire investigation of the wake behind cylinders at low Reynolds number", *Proc. Roy. Soc. London, series A*, **198** (1949), 174-190

[128] S. Kuwabara, "The forces experienced by two circular cylinders in a uniform flow at small Reynolds numbers", *J. Phys. Soc. Japan*, **12** (1957), 291-299

[129] S. Kuwabara, "The forces experienced by randomly distributed parallel circular cylinders or spheres in a viscous flow at small Reynolds numbers", *J. Phys. Soc. Japan*, **14** (1959), 527-532

[130] Y. Kwon, and A. I. Leonov, "On 1D instabilities in simple shear and extensional flows as predicted by some Maxwell-like constitutive equations", *J. Rheol.*, **36:8** (1992), 1515-1528

[131] H. Lamb, *Hydrodynamics*, 6th ed. Cambridge: Cambridge University Press (1932)

[132] R. G. Larson, *Constitutive equations for polymer melts and solutions*, Butterworths, Boston (1988)

[133] R. G. Larson, *Instabilities in viscoelastic flows*, *Rheol. Acta*, **31** (1992), 213-263

[134] A. I. Leonov, "On a class of constitutive equations for viscoelastic liquids", *J. Non-Newtonian Fluid Mech.*, **25** (1987), 1-59

[135] F. M. Leslie, and R. I. Tanner, "The slow flow of a viscoelastic liquid past a sphere", *Quart. J. Mech. Appl. Math.* **14** (1961), 36-48

[136] A. W. Liu, D. E. Bornside, R. C. Armstrong and R. A. Brown, "Viscoelastic Flow of Polymer Solutions Around a Periodic, Linear Array Cylinders: Comparisons of Predictions for microstructure and Flow fields", accepted for publication J. Non-Newtonian Fluid Mech., (1997)

[137] A. W. Liu, R. C. Armstrong and R. A. Brown, "Experimental Investigation of Viscoelastic Flow Around a Periodic Array of Cylinders", *Proceedings of XIIth International Congress on Rheology*, (1996)

[138] A. W. Liu, D. E. Bornside, R. C. Armstrong and R. A. Brown, "Viscoelastic Flow around a 2-dimensional Periodic Array of Cylinders", in preparation

[139] A. S. Lodge, "Variation of flow Birefringence with stress", *Nature*, **176** (1955), 838-839

[140] A. S. Lodge, "A network theory of flow Birefringence and stress in concentrated polymer solutions", *Trans. Faraday Soc.*, **52** (1956), 120-130

[141] W. J. Lunsmann, L. Genieser, R. C. Armstrong, and R. A. Brown, "Finite element analysis of steady viscoelastic flow around a sphere in a tube: calculations with constant viscosity models", *J. Non-Newtonian Fluid Mech.*, **48** (1993), 63-99

[142] M. E. Mackay, and C. J. S. Petrie, "An unusual prediction utilizing FENE-P rheological models in the fiber-spinning problem", *J. Non-Newtonian Fluid Mech.*, **41** (1992), 365-373

[143] J. E. Matta, and R. P.Tytus, "Liquid stretching using a falling cylinder", *J. Non-Newtonian Fluid Mech.*, **35** (1990), 215-229

[144] G. H. McKinley, A. Öztekin, J. A. Byars, R. A. Brown, and R. C. Armstrong, "Self-similar spiral instabilities in elastic flows between a cone and a plate", *J. Fluid Mech.*, **285** (1995), 123-164

[145] G. H. McKinley, R. A. Brown, and R. C. Armstrong, "The wake instability in viscoelastic flow past confined circular cylinders", *Phil. Trans. Royal Soc.*, **344** (1993), 265-304

[146] G. H. McKinley, *Nonlinear dynamics of viscoelastic flows in complex geometries*, Ph.D. Thesis, MIT (1991a)

[147] G. H. McKinley, J. A. Byars, R. A. Brown, and R. C. Armstrong, "Observation on the elastic instability in cone-and-plate and parallel-plate flows of a polyisobutylene Boger fluid", *J Non-Newtonian Fluid Mech.*, **40** (1991b), 209-229

[148] B. Mena, and B. Caswell, "Slow flow of an elastic-viscous fluid past an immersed body", *Chem. Eng. J.*, **8** (1974), 125-134

[149] E. Mitsoulis, "Numerical Simulation of planar entry flow for a polyisobutylene solution using an integral constitutive equation", *J. Rheol.*, **37** (1993), 1029-1040

[150] T. Miyagi, "Viscous flow at low Reynolds numbers past an infinite row of equal circular cylinders", *J. Phys. Soc. Japan*, **13** (1958), 493-496

[151] H. Mizumoto, "A note on the numerical treatment of Navier-Stokes equation", *J. Phys. Soc. Japan*, **34** (1973), 1396-1401

[152] A. J. Müller, J. A. Odell, and A. Keller, "Elongational flow and rheology of monodisperse polymers in solution", *J. Non-Newtonian Fluid Mech.*, **30** (1988), 99-118

[153] S. J. Muller, Experimental analysis of flow through an axisymmetric sudden contraction: rheological characterization and LDV measurements, Ph.D thesis, MIT (1986)

[154] P. Morley, personal communication (1997)

[155] C. Norberg, "An experimental investigation of the flow around a circular cylinder: influence of aspect ratio", *J. Fluid Mech.*, **258** (1994), 287-316

[156] P. J. Northey, *Numerical simulation of time-dependent, two-dimensional viscoelatic fluid flows*, Ph.D. Thesis, MIT (1991)

[157] "Practical strain gage measurements", *Omega complete pressure, strain and force measurement handbook and encyclopedia*, **Vol. 28**, (1996), E31-E58

[158] H. C. Öttinger, "Gaussian approximation for Rouse chains with hydrodynamic interaction", *J. Chem. Phys.*, **90** (1989), 463-473

[159] A. Öztekin, and R. A. Brown, "Instability of a viscoelastic fluid between rotating parallel disks: analysis of the Oldroyd-B fluid", *J. Fluid Mech.*, **255** (1993), 473-502

[160] A. Öztekin, R. A. Brown, and G. H. McKinley, "Quantitative prediction of the viscoelastic instability in cone-and-plate flow of a Boger fluid using a multi-mode Giesekus model", *J. Non-Newtonian Fluid Mech.*, **54** (1994), 351-377

[161] A. Öztekin, J. A. Byars, A. W. Liu, R. C. Armstrong, R. A. Brown, "Three-dimensional wake instability in viscoelastic flow past a cylinder: theory and experiment", in preparation

[162] J. R. Pannell, E. A. Griffiths and J. D. Coales, "Experiments on the interference between pairs of aeroplane wires of circular and circular cross section", British Advisory Committee for Aeronautics, Reports and Memoranda No. 208 (1915), Annual reports for 1915-1916, **7**, 219-221

[163] A. C. Payatakes, C. Tien and R. M. Turian, "Part II. Numerical solution of steady state incompressible Newtonian flow through periodically constricted tubes", *A.I.Ch. E Journal*, **19** (1973), 67-76

[164] F. L. Penna, *New mixed finite element methods*, Ph.D. thesis, UMI (1987)

[165] A. Perta, class notes for computational fluid dynamics (1995)

[166] C. C. Perry and H. R. Lissner, *The strain gage primer*, McGraw-Hill, New York (1962)

[167] N. Phan-Thien, O. Manero, and L. G. Leal, "A study of conformation-dependent friction in a dumbbell model for dilute solutions", *Rheol. Acta*, **23** (1984), 151-162

[168] N. Phan-Thien, H. Jin, and R. Zheng, "On the flow past a needle in a cylindrical tube", *J. Non-Newtonian Fluid Mech.*, **47** (1993), 137-155

[169] W. H. Press, B. P. Flannery, S. A. Teukolasky and W. T. Vetterling, *Numerical recipes*, Cambridge university Press, Cambridge (1986)

[170] I. Proudman and J. R. A. Pearson, "Expansions at small Reynolds numbers for the flow past a sphere and a circular cylinder", *J. Fluid Mech.*, **2** (1957), 237-262

[171] L. M. Quinzani, G. H. McKinley, R. A. Brown, and R. C. Armstrong, "Modeling the rheology of polyisobutylene solutions", *J. Rheo.*, **34:5** (1990), 705-748

[172] L. M. Quinzani, *Birefringence studies of entry flows of concentrated polymer solutions*, Ph.D. Thesis, MIT, 1991

[173] J. M. Rallison, and M. D. Chilcott, "Do we understand the physics in the constitutive equation?" *J. Non-Newtonian Fluid Mech.*, **29** (1988), 37-55

[174] D. Rajagopalan, R. C. Armstrong, and R. A. Brown, "Calculation of steady viscoelastic flow using a multimode Maxwell model: application of explicitly elliptic momentum (EEME) formulation", *J. Non-New. Fluid Mech.*, **36** (1990a), 135-157

[175] D. Rajagopalan, R. C. Armstrong, and R. A. Brown, "Finite element methods for calculation of steady, viscoelastic flow using constitutive equations with a Newtonian viscosity", *J. Non-New. Fluid Mech.*, **36** (1990b), 159-192

[176] D. Rajagopalan, *Convergent finite-element calculation of steady, viscoelastic flow using nonlinear, multimode constitutive models*, Ph.D. Thesis, MIT (1991)

[177] M. Renardy, "Existence of slow steady flows of viscoelastic fluids with differential constitutive equations", *Z. Agnew. Math. u. Mech.*, **65** (1985), 449-451

[178] M. Renardy, "The stresses of an upper-convected Maxwell fluid in a Newtonian velocity field near a re-entrant corner", *J. Non-Newtonian Fluid Mech.*, **50** (1993), 127-134

[179] H. K. Rasmussen, and O. Hassager, "Simulation of transient viscoelastic flow", *J. Non-Newtonian Fluid Mech.*, **46** (1993), 298-305

[180] J. Rosenberg, and R. Keunings, "Numerical integration of differential viscoelastic models", *J. Non-Newtonian Fluid Mech.*, **39** (1991), 269-290

[181] T. R. Salamon, *Finite element simulations of steady viscoelastic free-surface flows*, PhD thesis, MIT (1995)

[182] A. S. Sangani, and A. Acrivos, "Slow flow past periodic arrays of cylinders with application to heat transfer", *Int. J. Multiphase Flow*, **8:3** (1982), 193-206

[183] R. W. G. Shipman, M. M. Denn, and R. Keunings, "Mechanics of the 'falling plate' extensional rheometer", *J. Non-Newtonian Fluid Mech.*, **40** (1991), 281-288

[184] P. Singh, and L. G. Leal, "Computational studies of FENE dumbbell model in a co-rotating two-roll mill", *J. Rheo.*, **38** (1993), 485-517

[185] P. Singh, and L. G. Leal, "Finite element simulation of the start-up problem for a viscoelastic fluid in an eccentric rotating cylinder geometry using a third-order upwind scheme", *Theoret. Comput. Fluid Mech.*, **5** (1993), 107-137

[186] L. Skartsis, B. Khomami and J. L. Kardos, "Polymeric flow through fibrous media", *J. Rheo.*, **36** (1992), 589-620

[187] L. Skartsis, J. L. Kardos, and B. Khomami, B., "Resin flow through fiber beds during composite manufacturing processes. Part I: review of Newtonian flow through fiber beds", *Polym. Eng.* and *Sci.* (1992), **32:4**, 221-239

[188] L. Skartsis, J. L. Kardos, and B. Khomami, "Resin flow through fiber beds during composite manufacturing processes. Part II: numerical and experimental studies of Newtonian flow through ideal and actual fiber beds", *Polym. Eng.* and *Sci.* (1992), **32:4**, 231-239

[189] M. D. Smith, *Nonisothermal viscoelastic fluid mechanics*, Thesis proposal, MIT (1995)

[190] M. J. Solomon, S. J. Muller, "Flow past a sphere in polystyrene-based Boger fluids: the effect on the drag coefficient of finite extensibility, solvent quality and polymer molecular weight", *J. Non-Newtonian Fluid Mech.*, **62** (1996), 81-94

[191] A. Souvaliotis, and A. N. Beris, "Spectral collocation domain decomposition method for viscoelastic flow simulations in model porous geometry", *Comp. Meth. App. Mech. Eng.* **129** (1996), 9-28

[192] A. Souvaliotis, and A. N. Beris, "Applications of domain decomposition spectral collocation methods in viscoelastic flows through model porous media", *J. Rheol.*, **36:7** (1992), 1417-1453

[193] S. H. Spiegelberg, D. C. Ables, and G. H. McKinley, "The role of end-effects on measurements of extensional viscosity in filament stretching rheometers", *J. Non-Newtonian Fluid Mech.*, **64** (1996), 229-267

[194] L. Speilman and S. L. Goren, "Model for predicting pressure drop and filtration efficiency in fibrous media", *Environ. Sci. Tech.*, **2** (1968), 279-287

[195] H. M. Spivack, "Vortex frequency and flow pattern in the wake of two parallel cylinders at varied spacing normal to an air stream", *J. Aero. Sci.*, **13** (1946), 289-297

[196] T. Sridhar, V. Tirtaatmadja, D. A. Nguyen, and R. K. Gupta, "Measurement of extensional viscosity of polymer solutions", *J. Non-Newtonian Fluid Mech.*, **40** (1991), 271-280

[197] J. F. Stevenson, and R. B. Bird, "Elongational viscosity of nonlinear elastic dumbbell suspensions", *Trans. Soc. Rheol.*, **15:1** (1971), 135-145

[198] F. Sugeng, and R. I. Tanner, "The drag on spheres in viscoelastic fluids with significant wall effects", *J. Non-Newtonian Fluid Mech.* **20** (1986), 281-292

[199] J. S. Sun, N. Phan-Thien, and R. I. Tanner, "Viscoelastic flow between two opposing orifices", *J. Non-Newtonian Fluid Mech.* **58** (1995), 219-242

[200] R. Sureshkumar, M. D. Smith, R. A. Brown and Rober C. Armstrong, personal communication (1997)

[201] B. A. Szabo, *In accuracy estimates and adaptive refinements in finite element computation*, edited by Babuska, I, Zienkiewicz, O. C., Gago, J., and E. R. de A. Oliverira, Wiley, New York (1986)

[202] M. J. Szady, T. R. Salamon, A. W. Liu, D. E. Bornside, R. C. Armstrong, and R. A. Brown, "A new mixed finite element method for viscoelastic flows governed by differential constitutive equations", *J. Non-Newtonian Fluid Mech.*,

[203] M. J. Szady, *Finite element methods for the time dependent simulation of viscoelastic fluid flows*, Ph.D. thesis, MIT (1996)

[204] K. K. Talwar, and B. Khomami, "Application of high order finite element methods to viscoelastic flow in porous Media", *J. Rheol.*, **36:7** (1992), 1377-1416

[205] K. Tamada, and H. Fujikawa, "The steady two-dimensional flow of viscous fluid at low Reynolds numbers passing through an infinite row of equal parallel circular cylinders", *Quart. J. Mech. Applied Math.*, **10:4** (1957), 425-432

[206] S. Taneda, "Experimental investigation of the wakes behind cylinders and plates at low Reynolds numbers", *J. Phys. Soc. Japan*, **11** (1956), 302-307

[207] G. I. Taylor, "The singing of wires in a wind", *Nature*, **113** (1924), 536-536

[208] A. Thom, "The flow past circular cylinders at low speeds", *Proc. Roy. Soc. London, series A*, **14** (1933), 651-669

[209] D. G. Thomas and K. A. Kraus, "Interaction of vortex streets", *J. Applied Phys.*, **35** (1964), 3458-3459

[210] W. Thomson, "On the electro-dynamic qualities of metals", *Phil. Trans. Roy. Soc.*, **146** (1856), 649-751

[211] V. Tirtaatmadja, P. H. T. Uhlherr and T. Sridhar, "Creeping motion of spheres in fluid M1", *J. Non-Newtonian Fluid Mech.*, **35** 327-337

[212] V. Tirtaatmadja, and T. Sridhar, "A filament stretching device for measurement of extensional viscosity", *J. Rheol.*, **37** (1993), 1081-1102

[213] P. Townsend, and K. Walters, "Expansion flows of non-Newtonian liquids", *Chem. Eng. Sci.*, **49:5** (1994), 749-763

[214] K. Tsiveriotis, and R. A. Brown, "Solution of free-boundary problems using finite element/Newton methods and locally refined grids: application to analysis of solidification microstructure", *Int. J. Numer. Meths. Fluids*, **16** (1993), 827-843

[215] J. S. Ultman,and M. M. Denn, "Slow viscoelastic flow past submerged objects", *Chem. Eng. J.*, **2** (1971), 81-89

[216] A. Umemura, "Matched-asymptotic analysis of low-Reynolds-number flow past two equal circular cylinder", *J. Fluid Mech.*, **121** (1982), 345-363

[217] J. Vorwerk, and P. O. Brunn, "Porous medium flow of the fluid A1: effects of shear and elongation", *J. Non-Newtonian Fluid Mech.*, **41** (1991), 119-131

[218] J. L. S. Wales, *The application of flow Birefringence to rheological studies of polymer melts*, Delft University Press (1976)

[219] L. E. Wedgewood, and H. C. Öttinger, "A model of dilute polymer solutions with hydrodynamic interaction and finite extensibility II. shear flows", *J. Non-Newtonian Fluid Mech.*, **27** (1988), 245-264

[220] L. E. Wedgewood and R. B. Bird, "From molecular models to the solution of flow problems", *Ind. Eng. Chem. Res.*, **27** (1988), 1313-1320

[221] L. E. Wedgewood, D. N. Ostrov, and R. B. Bird, "A finitely extensible bead-spring chain model for dilute polymer solutions." *J. Non-Newtonian Fluid Mech.*, **40** (1991), 119-139

[222] C. Wieselsberger, *Physik. Z.*, "Nwuere Feststellungen uber die Gesetze des Flussigkei -und Luftwiderstandes", **22** (1921), 321-328

[223] C. Wieselsberger, *Physik. Z.*, "Weitere Feststellungen uber die Gesetze des Flussigkeits- und Luftwiderstandes", **23** (1922), 219-224

[224] J. M. Wiest, L. E. Wedgewood, and R. B. Bird, "On coil-stretch transitions in dilute polymer solutions", *J. Chem. Phys.*, **90** (1989), 587-594

[225] E. H. Wissler, "Viscoelastic effects in the flow of non-Newtonian fluids through a porous Medium", *Ind. Eng. Fundam.* (1971), **10:3**, 411-417

[226] X. L. Wu, D. J. Pine and P. K. Dixon, "Enhanced concentration fluctuations in polymer solutions under shear flow", *Phys. Review Letters*, **66** (1991), 2408-2411

[227] H. Yano and A. Kieda, "An approximate method for solving two-dimensional low-Reynolds-number flow past arbitrary cylindrical bodies", *J. Fluid Mech.*, **97** (1980), 157-179

[228] D. P. Young, R. G. Melvin and M. B. Bieterman, "A locally refined rectangular grid finite element methods: application to computational fluid dynamics and computational physics", *J. Comp. Phy.*, **92** (1-66), 1991

[229] R. J. Young, *Introduction to polymers*, Chaapman and Hall, New York (1981)

[230] S. Vossoughi, and F. A. Seyer,"Pressure drop for flow of polymer solution in a model porous geometry", *Canadian J. Chem. Eng.*, **52**, (1974), 666-669

[231] M. M. Zdravkovich, "Smoke observations of wake of a group of three cylinders at low Reynolds number", *J. Fluid Mech.*, **32** (1968), 339-351

[232] M. M. Zdravkovich, "Smoke observations of wakes of tandem cylinders at low Reynolds number", *Aero. J.*, **76** (1972), 108-114

[233] M. M. Zdravkovich, "Review of flow interference between two circular cylinders in various arrangements", *J. Fluids Eng.*, **99** (1977a), 618-633

[234] M. M. Zdravkovich, "Interference between two circular cylinders; Series of unexpected discontinuities", *J. Ind. Aerodynamics*, **2** (1977b), 255-270

[235] R. Zheng, N. Phan-Thien, and R. I. Tanner, "The flow past a sphere in a cylindrical tube: effects of inertia, shear-thinning and elasticity", *Rheol. Acta*, **30** (1991), 499-510

[236] W. Zylka, and H. C. Öttinger, "A Comparison between simulations and various approximations for Hookean dumbbells with hydrodynamic interaction", *J. Chem. Phys.*, **90** (1989), 474-480